Time Domain Imaging of Transient and Variable Radio Sources

Yvette Nora Cendes

Time Domain Imaging of Transient and Variable Radio Sources

Proefschrift

ter verkrijging van
de graad van Doctor aan de Universiteit Leiden,
op gezag van de Rector Magnificus Prof. mr. C. J. J. M. Stolker,
volgens besluit van het College voor Promoties
te verdedigen op 12 mei, 2020
om 16.30 uur

door
Yvette Nora Cendes
geboren te Pittsburgh, PA, USA
in MJD 46453.7375

Promotiecommissie

Promotor:	Prof. dr. A. G. G. M. Tielens
Promotor:	Prof. dr. B. M. Gaensler *(University of Toronto)*
co-Promotor:	Dr. M. R. Drout *(University of Toronto)*
Overige leden:	Prof. dr. H. Rottgering
	Prof. dr. H. J. van Langevelde
	Prof. dr. P. Chandra
	Prof. dr. F. Israel
	Dr. S. Ryder
	Dr. C. Stockdale
	Dr. R. van Weeren

For my family– családomnak

Egy lángot adok, ápold, add tovább;
Csillaggal álmodik az éjszaka,
És lidércfénnyel álmodik a láp
És öröktűzzel álmodik a szívem.
Egy lángot adok, ápold, add tovább,
És gondozd híven.
— Reményik Sándor, Öröktűz

I'm giving you a flame, tend it, and pass it on;
The night is dreaming with stars,
As the marsh dreams with will-o'-the-wisp
And my heart burns with an eternal fire.
I'm giving you a flame, tend it, and pass it on,
And to this be true.
— Reményik Sándor, Eternal Fire

Introduction

The Transient Radio Sky

The most extreme physics of our universe occurs in transient events. These exotic phenomena can range from stars exploding in fiery deaths to compact objects merging to produce gravitational waves detected billions of light years away, to black holes that rip apart matter that wanders too close to them. These events allow us to probe the physics of environments which are impossible to reproduce on Earth, and can play out over time scales ranging from a fraction of a second to longer than a human lifetime. This thesis focuses on the physics that occurs in transients on the long time scales of years to decades, and on the technical challenges that we face to identify them.

This thesis is possible because we live in a golden age of transient astronomy. What began with the occasional "guest stars" recorded by Chinese astronomers thousands of years ago has evolved into a period where hardly a day passes without an interesting transient event. Satellites have made the observation and rapid follow-up of Gamma-Ray Bursts (GRBs) two decades ago routine. Surveys like the All Sky Automated Survey for SuperNovae (ASAS-SN) and Zwicky Transient Facility (ZTF) discover new optical transient events every night. And a large fraction of the world's astronomical resources are used routinely to follow up gravitational wave alerts from the Laser Interferometer Gravitational-Wave Observatory (LIGO).

Compared to other parts of the electromagnetic spectrum, studies of the transient and variable radio sky have lagged.[1] This is due to limits with traditional radio telescopes. However, this is rapidly changing with advances in the field, such as increased computation and sensitivity. The maturing nature of radio astronomy is also an asset: while the field was pioneered in the 1930s, mJy level astronomy only became more routine in the 1970s. This means that transients that occur over long time scales can be subject to monitoring over their full transient because data is now available over a period of decades.

[1]The words transient and variable are used somewhat interchangeably in this thesis, as they are in much of the literature. Typically "transient" refers an event where the radio flux appears and disappears, and "variable" is when the flux is always present, but varies.

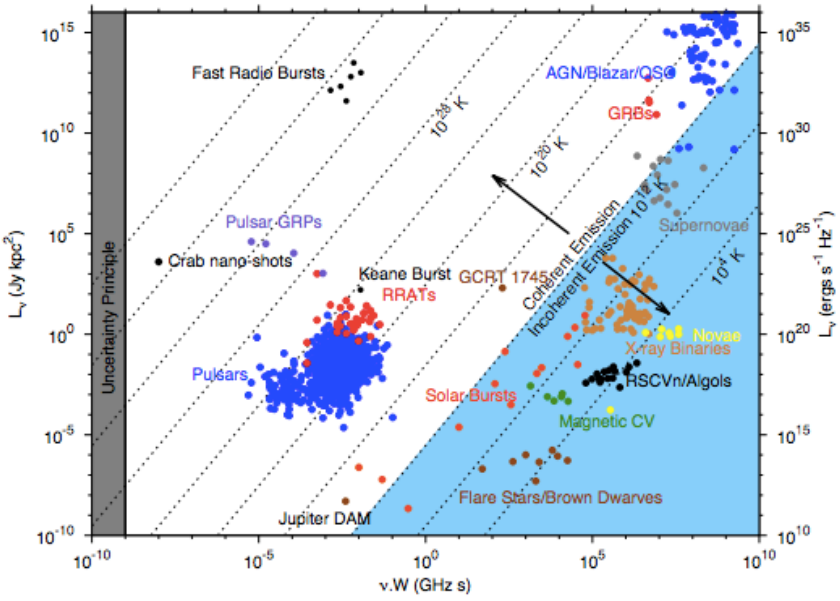

Figuur 1 The phase space for various radio transients from Pietka et al. [2015], where radio luminosity is plotted against the time-scale of the various included events. The dividing line between coherent (white) and incoherent (blue) emission is the brightness temperature $T_b \sim 10^{12}$ K. It should be noted that the shortest time scales are dominated by coherent emission, whereas emission on longer time scales is dominated by incoherent emission.

Radio-Emitting Transients

Many radio transients emit through a process called called synchrotron emission. It is produced by the acceleration of ultra-relativistic electrons spiraling in a magnetic field due to the Lorentz force, and is powered by shock interaction between fast ejecta and the ambient medium. The frequency for synchrotron radiation depends on the electron energy and strength of the magnetic field.

Synchrotron radiation is a form of incoherent emission, meaning that the electrons are acting independently from one another and that the resulting emission has no phase relationship. A coherent emission process occurs when electrons instead accelerate in phase, and in turn produce photons with the same direction and phase. Coherent and incoherent processes are separated by the maximum constant brightness temperature, $T_b \sim 10^{12}$ K, which is the theoretical upper limit for incoherent emission (Figure 1).

Typically, radio transients with coherent emission have a brief duration of < 1 second, such as pulsars and fast radio bursts (FRBs; see section below), and are typically observed through time-series techniques. On the other hand, transients with incoherent emission evolve over longer time scales, and are observed in the image plane. Beyond the type of emission, the duration of the transient depends on several factors, such as the energy scale of the initial event, whether the explosion was relativistic or non-relativistic, the type of outflow, the density in the surrounding region, ejecta profile, and whether the explosion is on or off axis in the direction of Earth. The

phase space in luminosity, time, and frequency of these various transients can be seen in Figure 1. Additionally, interstellar scattering and scintillation of radio waves can also be observed, due to a turbulent interstellar medium (ISM) along the line of sight [Rickett, 1977]. This phenomenon is independent of the transients themselves, but can result in observed variations on the order of seconds to centuries.

There are several types of radio transients, both on short and long time scales. Those covered in this thesis are listed below, roughly in order of time scales associated with the event. We define short term transients as those occurring on time scales ranging from a fraction of a second to months-long time scales, and long-term transients are events longer than those.

Short Term

Pulsars are rapidly rotating neutron stars which produce beamed radio emission from their magnetic poles. As the pulsar rapidly rotates, this beam briefly crosses our line of sight on Earth, like a cosmic lighthouse. Pulsars are a famous example of coherent emission, and as mentioned above are typically observed via time series techniques [Hewish et al., 1968]. Pulsars can have a period as short as milliseconds, and the longest known duration for a pulsar is 23.5 seconds [Tan et al., 2018].

In more recent years, an enigmatic class of brief transients has emerged in FRBs. FRBs are brief pulses of coherent emission of millisecond duration, extragalactic origin, and high luminosity. Theories regarding the origins of FRBs are numerous, and range from diverse sources such as magnetars, supernova remnants, flare stars, black holes, and others. Although FRBs were first found using time series methods, the bursts can also be directly imaged [Chatterjee et al., 2017].

As of May 2019, less than 100 FRBs are in the published literature, and two repeating FRBs have been reported [Platts et al., 2018; Petroff et al., 2016].[2] It is not yet understood if the repeating and non-repeating FRBs have the same emission mechanism. It should be noted that so far only the first repeating FRB, known as FRB 121102, has been localized to a position of a star forming region in a faint dwarf galaxy (r = 25.1 mag) at a redshift of 0.19273 [Bassa et al., 2017; Tendulkar et al., 2017]. There also appears to be a persistent radio counterpart consistent with the star forming region to $\sim$40 pc [Chatterjee et al., 2017]. Finally, it should be noted that the spectral profile of FRBs is uncertain: although FRB emission has been detected down to 400 MHz [Platts et al., 2018], searches for FRBs at lower frequencies have so far been unsuccessful [Sokolowski et al., 2018; Houben et al., 2019]. As such, it is not clear if and where a spectral turnover occurs in FRB signals, which could be due to processes such as scintillation or an intrinsic property related to the FRB emission mechanism [Sokolowski et al., 2018].

Progress in this field is severely hampered by the limited number of FRBs known. Systematic radio surveys for them need to understand the technical details behind their radio telescopes to ensure they are correctly seen by the observer (see Chapter 3).

Supernovae

[2] The current number can be found at http://www.frbcat.org; see Petroff et al. [2016] for more info.

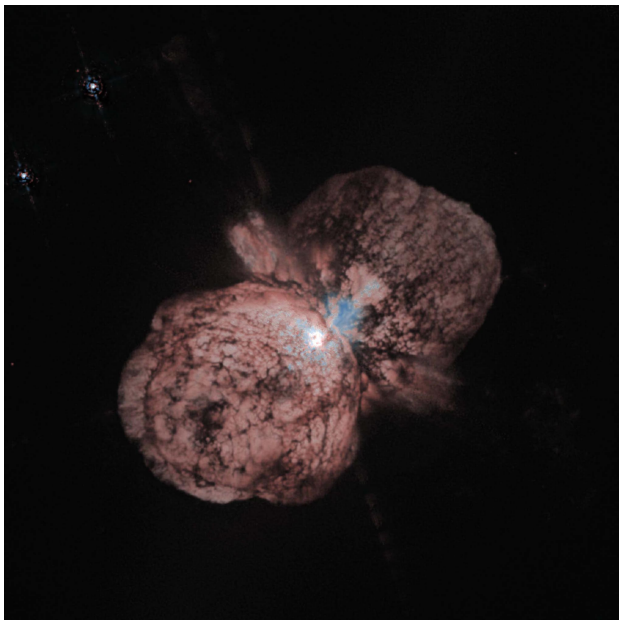

Figuur 2 An example of CSM surrounding the Eta Carinae nebula, as seen with the Hubble Space Telescope. It is thought that this system is near the end of its life, and will explode as a supernova on an astronomically soon time scale. Image credit: Jon Morse (University of Colorado) & NASA Hubble Space Telescope.

A supernova (SN) is the violent explosion of a star. A single supernova event can shine brighter in optical light than all the other stars in a galaxy. Many questions surround supernova events, particularly in relation to the circumstances leading up to the final explosion. Supernovae (SNe) also play an important role in their environments by triggering new star formation in their surroundings, and by enriching the surrounding interstellar medium with heavier mass elements.

Radio emission from SNe originates from synchrotron emission as the blast wave from the supernova interacts with surrounding material, with radio luminosity proportional to the density of material present [Chevalier, 1982a]. The material in the immediate surroundings is the circumstellar material (CSM) that was shed by the star itself before the SN explosion. This means that the CSM closest to the explosion was the material ejected the most recently, and older material ejected at earlier times is further out. After the prompt emission from the supernova fades, this shockwave/ CSM interaction can continue for decades.

Studying the CSM surrounding a supernova is important because mass loss is common in stellar evolution for supermassive stars that will explode in a supernova, especially for binary systems [Smith, 2014]. Further, eruptive mass loss does appear common in SNe- $36.5 \pm 6\%$ of all core collapse SNe are “stripped envelope"SNe which have lost much of their outer envelope before explosion, and $9 \pm 3\%$ are of Type IIn, which underwent a large amount of mass loss a few years before the SN [Li et al., 2011b]. These eruptions appear to be a prelude to the final core collapse, and may be due to severe instabilities during the star’s last stages, but details behind this process are not well understood [Smith, 2014]. Figure 2 shows an example of what the CSM surrounding such a star is thought to look like, surrounding η Carinae. It is a binary star 7,500 light years

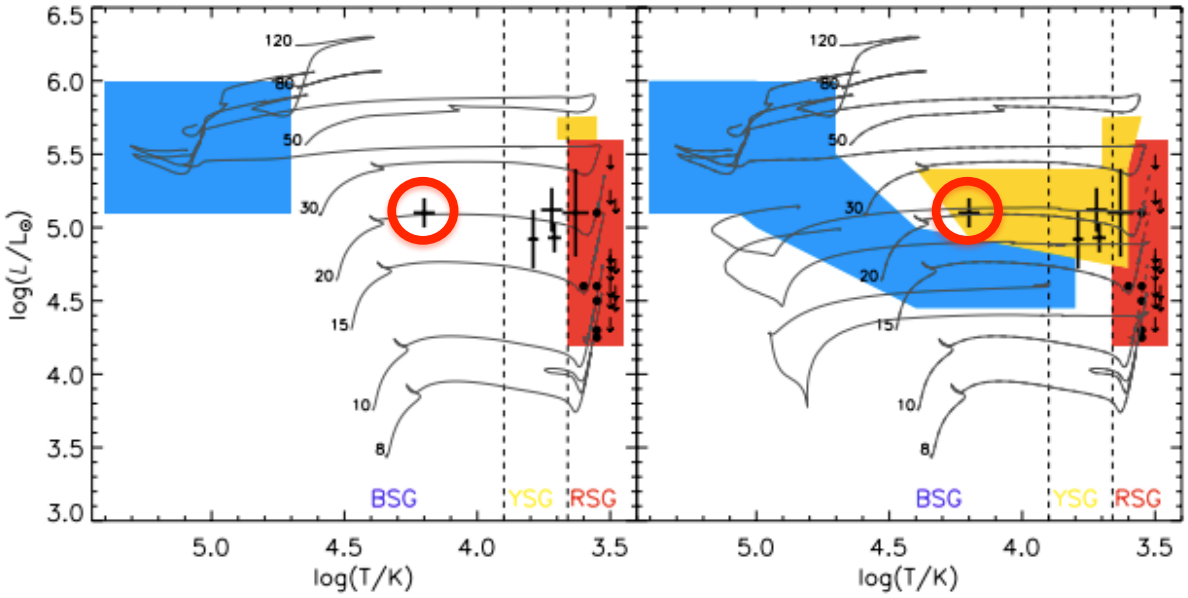

Figuur 3 Hertzsprung-Russell diagrams for SN progenitors, where the solid lines show evolution tracks for stars with their initial masses. Here, the the red, yellow, and blue regions are the expected locations for SN progenitors for Type IIP, other Type II, and Type Ib/c, respectively. The left hand panel shows the parameter space for a single star scenario, and the right hand shows scenarios for binary systems. In both plots, the points with errors show the locations of observed SN progenitors. I have circled the location of SN 1987A on both plots for reference. Image credit: Eldridge et al. [2013].

distant from us, thought to be in the end stages of its life, and it shed $\geq 12 - 20 M_{\odot}$ in under a decade during the 19th century [Smith & Owocki, 2006].

Another large factor in supernova dynamics is the system's binarity and subsequent effects stemming from the binary companion. This is because a binary system is often required to explain the CSM observed around the SN [Smith, 2014]. We can see an example of this in Figure 3, which shows cartoon Hertzsprung-Russell (HR) diagrams for SN progenitors and the expected locations for various SN progenitors assuming a single star (left) or binary (right) system. A binary star system model not only covers a greater section of the HR diagram, but can also the only way to explain the explosion of the progenitor in many cases and supernova types [Eldridge et al., 2013; Smith, 2014]. The nature of a binary companion is also crucial for producing a thermonuclear (Type Ia) SNe, as we shall cover below and in Chapter 2. However, much about these binary companions is still unknown.

Further, one of the great difficulties in supernova studies is their rarity: it is estimated that 2-3 SNe occur in the Milky Way every century [Li et al., 2011a]. Although several "guest stars" have been recorded over the centuries, the last supernova event observed in our own galaxy was Kepler's Supernova in 1604.[3] This luminosity means that most observed SNe are at great distances from

[3]This does not mean that this was the last supernova in the Milky Way: the bright radio remnant Cassiopeia A corresponds with an unrecorded supernova in the late 17th century, and the remnant G1.9+0.3 exploded sometime

Figuur 4 SN 1987A and its surrounding CSM structure, as seen with the Hubble Space Telescope. The complex ring structure is thought to originate from CSM loss from the progenitor prior to the supernova explosion. We note that the bright innermost yellow-white ring of emission is the equatorial ring in the shockwave interaction discussed in Chapter 1. Image credit: ESA/Hubble & NASA.

Earth.

The categories of SNe of interest to this thesis are as follows.

Core-Collapse Supernovae

A core-collapse supernova (CC SN) occurs when a massive star ($> 8M_{\odot}$) is at the end of its thermonuclear evolution and no longer creates the energy required to counteract gravitational forces. At this point, the star collapses, and depending on the mass of the star either a neutron star or black hole is created at the core. The supernova is triggered when the compressed inner core exceeds the Chandrasekhar mass limit ($\geq 1.4M_{\odot}$), and the outer layers rapidly collapse at $\sim 20\%$ the speed of light, bounce off the incredibly dense core, causing the infalling matter to rebound. This creates the light and heat from the supernova event, as well as the shockwave which subsequently interacts with surrounding CSM.

Radio emission has been observed from many nearby core collapse supernovae [Weiler, 2003]. However, the majority of SNe are typically detected at distances that make radio detection difficult. Most radio SNe appear as point sources, and to date there are less than 10 spatially resolved

between 1890 and 1908. In the case of both, large amounts of dust between the supernova and Earth was likely sufficient to block optical light from reaching us at the time.

radio SNe. This means much is still unknown about the shockwave/CSM interaction over time, and the supernova to supernova remnant (SNR) transition.

To date, our best picture of what a supernova and its surroundings look like are from SN 1987A, discovered on February 24, 1987 by University of Toronto astronomer Ian Shelton and Oscar Duhalde at Las Campanas Observatory, and independently by amateur astronomer Albert Jones in New Zealand [Kunkel et al., 1987]. Occurring in the Large Magellanic Cloud, ∼170,000 light years from Earth, it was the closest supernova to Earth and the first observed with the naked eye since the invention of the telescope. This has allowed us an unprecedented view into the process of how a supernova occurs, and how the SN shockwave interacts with its surroundings in the decades after the prompt emissions fade.

SN 1987A has also raised several questions about supernova physics that are still unresolved. It was for example the first time in history the progenitor star of a SN explosion was identified, a blue supergiant star named Sanduleak -69 202 [West et al., 1987], which shocked the astronomical world because a blue supergiant progenitor contradicted all stellar evolution theories at the time [Trimble, 1988]. SN 1987A was subsequently interpreted as having undergone a red supergiant phase prior to becoming a blue supergiant, as evidenced by its metallicity and mass loss [Arnett et al., 1989]. Further, SN 1987A was the first sub-luminous SN ($M_B \geq$ -15), and ultimately became the prototype for the Type II-pec (for "peculiar") sub-class of SNe [Smith, 2014].

Observations with the Hubble Space Telescope (Figure 4) show a complex CSM structure ejected in the tens of thousands of years prior to the supernova, possibly from a binary merger event [Morris & Podsiadlowski, 2007]. Such a merger would be doubly interesting in the context of occurring just before the supernova because, as seen in Figure 3, a single star system does not make sense in the context of stellar evolution. The CSM environment surrounding SN 1987A is the key to understanding what happened prior to the explosion. Radio observations play a key role in this by tracing the ejecta/CSM interaction, which can also be compared to observations in X-ray and radio. Understanding the details seen in radio due to factors such as clumps in the CSM, potential asymmetry in the shockwave, and changes in density are key to interpreting other radio SNe further away where seeing detail is impossible.

It should also be noted that, to date, a compact object has not been detected at the center of SN 1987A [Alp et al., 2018]. We do know a neutron star was *created* because SN 1987A was also the first time neutrinos were detected from outside the solar system. However, whether the compact object remained a neutron star, or collapsed further into a black hole, is unknown.

Type Ia Supernovae

A Type Ia Supernova (SN Ia) is caused by the explosion of a carbon-oxygen white dwarf [(WD); Nomoto et al., 1997]. Type Ia SNe have become an important cornerstone of cosmological studies as "standard candles" for cosmological distance calculations via the measured luminosity distances of SNe Ia as a function of redshift [Nomoto, 1982; Howell, 2011]. This has been used as evidence for an accelerating universe that is dominated by a mysterious dark energy [Perlmutter et al., 1999]. More recently, the Type Ia distance scale has been used to suggest a discrepancy in the Hubble Constant between local scales and that derived from the Cosmic Microwave Background [Riess et al., 2018; Burns et al., 2018].

Despite their importance in cosmology, both the progenitor systems and explosion mechanism of Type Ia SNe are still debated. There are two main scenarios, and both involve binary systems with a WD and second companion [Hillebrandt & Niemeyer, 2000; Wang, 2018]. The first is a single degenerate (SD) scenario, where a WD interacts with a non-degenerate, main sequence stellar companion [Holmbo et al., 2018]. The second is the double degenerate (DD) scenario, where the second companion is also a WD [Maoz et al., 2014]. The term "double degenerateïs broad and currently encompasses multiple possible combinations of progenitor binary systems and explosion mechanisms, such as a collision [Kushnir et al., 2013], hydrodynamic instability [Glasner et al., 2018], re-ignition as the combined mass post-merger exceeds the Chandrasekhar mass [Shen et al., 2012], and others. It is also unclear if the majority of Type Ia SN explode at the Chandrasekhar mass, or whether sub-Chandrasekhar WDs can also explode as SNe Ia while undergoing double detonations or violent mergers. Some observations show evidence for a population of sub-Chandra explosions [Nomoto, 1982; Scalzo et al., 2019].

Like core-collapse SNe, any radio emission from Type Ia SNe is expected to be from a shockwave interacting with CSM surrounding the blast. Such CSM could reflect the nature of the SN progenitor system, as it would be present due to mass transfer, or pre-supernova activity such as stellar winds or outbursts. However, for decades searches for CSM around SNe Ia in X-ray, optical, and radio have been consistent with very low-density environments, which would be the most constraining if the CSM is ejected in a stellar wind from a SD progenitor [Chomiuk et al., 2016; Margutti et al., 2014].

However, most of these observations have focused on detecting CSM just a few hundred days after the event [Chomiuk et al., 2016]. This is in spite of how we know that SNe Ia in our own galaxy have been observed to “turn on” in radio wavelengths as they transition to the supernova remnant (SNR) stage, although whether this is due to CSM ejected by the progenitor system, or ISM interaction not related with the original system, is still debated. For example, G1.9+0.3, a SN Ia which is the most recent supernova known within our galaxy, was first discovered by the VLA and is estimated between 125 and 140 years old [Reynolds et al., 2008]. Additionally, Kepler’s Supernova is radio bright ∼400 years after the event [DeLaney et al., 2002]. Most recently, [Sarbadhicary et al., 2019] made deep radio images of the SN 1885A area in the Andromeda Galaxy (M31; 0.785 ± 0.025 Mpc distant). The resulting upper limits constrain SN 1885A to be fainter than G1.9+0.3 at a similar timescale of ∼120 years post-explosion, placing strict limits on the density of the ambient medium and the transition to the SNR stage.

The question of the CSM environment surrounding SNe Ia has also become more complex in recent years as blue-shifted Na I D absorbing material has been detected in some SNe Ia spectra, which is interpreted as CSM surrounding the SNe Ia which has been ionized [Patat et al., 2007; Blondin et al., 2009]. Modeling has indicated the material is likely not distributed continuously with radius, as expected from a stellar wind centered at the explosion site, but instead is more likely distributed in a shell-like structure with a radius $\geq 10^{17}$ cm [Chugai, 2008]. Such absorbing material is estimated to have a total integrated mass of $\sim 1 M_{\odot}$ [Sternberg et al., 2011].

In addition, a small, new class of supernovae has been recognized (SNe Ia-CSM). These spectroscopically resemble SNe Ia but have strong hydrogen emission lines, as expected if there is significant interaction between the blast wave and a large amount (∼few $M_{\odot}$) of circumstellar

material [Silverman et al., 2013]. SNe Ia-CSM are very rare, and the most nearby (SN 2012ca; ∼80 Mpc distant) is the only SN Ia detected in X-ray to date [Bochenek et al., 2018]. Most recently, there has been evidence of CSM interaction surrounding SN 2015cp at ∼ 730 days post-explosion, consistent with a CSM shell [Graham et al., 2019], and the detection of Hα in a late-time nebular spectrum, which was interpreted as the signature of CSM excited by the SN ejecta slamming into it [Kollmeier et al., 2019].

While the very early and very late times after Type Ia SNe have been probed, the intermediate age period (∼10-100 years) for SNe Ia has not yet been examined in radio wavelengths. This is despite the fact that limits during this period could provide important evidence for or against various Type Ia progenitor models. We shall discuss this more in Chapter 2.

Other Transients

Active Galactic Nuclei (AGN)

The majority of radio sources in the sky with brightness $S > 1$ mJy at 1.4 GHz are active galactic nuclei [AGN; Becker et al., 1994], which are supermassive black holes at the centers of galaxies which are accreting material. In optical light, all types of broad-line AGN are known to vary by several factors on timescales ranging from weeks to years [Matthews & Sandage, 1963; Hovatta et al., 2008]. The same also holds for radio AGN, and low-luminosity or quiescent AGN activity accounts for ∼60% of all AGN [Padovani et al., 2011].

It is also possible to have variability over longer time scales due to the fueling of AGN, which can lead to larger variations by a factor of three or more [Tadhunter, 2016]. These are due to intermittencies in the fuel supply for the AGN, where a lack of fuel can trigger a phase where the central AGN has a lower luminosity, or even switches off altogether. The time scales of these changes depends on the sizes of the AGN components considered. For example, the torus of a typical radio AGN is ∼ 0.1–100 pc, corresponding with a light crossing time of ∼0.3–300 years, whereas the large AGN radio lobes are ∼0.05– 1 Mpc with a light crossing time of $1.5 - 3 \times 10^6$ light years. This means that if the fuel supply were to completely stop powering the AGN, an observer would see a significant decrease in radio flux from the torus in the first weeks or decades, but emission from the radio lobes would continue to last for thousands of years.

Other Transients

Tidal Disruption Events

A tidal disruption event (TDE) occurs when a star gets sufficiently close enough to a black hole's event horizon that it is pulled apart by the black hole's tidal forces. In this process, about half of the star becomes unbound from the system, while the remainder of the stellar mass is bound in highly eccentric orbits [Giannios & Metzger, 2011]. During the process, jets are formed that are detectable in the radio [Zauderer et al., 2011; Cenko et al., 2012]. Off-axis TDEs should also be visible at radio wavelengths [Generozov et al., 2017].

There are still many questions surrounding TDEs relating to the formation of the jet and their energy distributions, which observations over several years of a TDE would be able to constrain

[Generozov et al., 2017]. TDEs are, however, relatively rare when compared to GRBs and neutron star mergers [Metzger et al., 2015].

Radio Afterglows from Gamma-Ray Bursts (GRBs)

GRBs are very luminous and energetic bursts of gamma radiation that occur at cosmological distances. When one occurs– roughly once a day– it will briefly be the brightest source in the gamma-ray sky. There are two primary categories of GRBs, known as "long" and "short" GRBs, with the distinction between the two drawn at ∼2 seconds. Short GRBs are created during the merger process of two neutron stars [Eichler et al., 1989; Abbott et al., 2017]. Long GRBs, on the other hand, are created by some CC SNe when the core of a massive star collapses to form a black hole, and two very powerful, beamed relativistic jets are created [Mészáros & Rees, 1997].

The afterglow of a GRB can be observed at radio frequencies when the ejected matter collides with the surrounding environment, and forms a spherically expanding shell emitting via the synchrotron process [Frail et al., 1997; Chevalier & Li, 1999]. If the initial GRB beam is not pointed in the direction of Earth, it is still possible to detect the so-called "orphan" GRB afterglow. The first candidate orphan afterglow, FIRST J141919+394036, has confirmed an orphan GRB's radio emission evolves over a decades-long time scale [Law et al., 2018].

The Tools of the Radio Astronomy Trade

Radio Telescopes Used In This Thesis

In this thesis I have used several radio interferometers to study radio transients and to explore their technical challenges. We shall highlight the ones used below.

The Low Frequency Array (LOFAR)

The Low Frequency Array [LOFAR; van Haarlem et al., 2013a] is an interferometer located primarily in the Netherlands, although external stations are located across Europe. LOFAR operates between 10 MHz and 250 MHz, with the exception of the FM radio band from 80-120 MHz. This split also corresponds with the two different types of dipole antennas: the low band antennas (LBA, 10-80 MHz) and high band antennas (HBA, 120-250 MHz). The LBA stations (Figure 5) consist of 96 dipoles, of which 48 can be actively beamformed (Broekema et al.,2018). For the HBA, dipoles are in a 4 x 4 tile with an analog beamformer, and are grouped into stations where each one forms an independent phased array (Figure 6). There are 24 stations in the core of LOFAR, which are connected via fiber to a central clock, and thus their signals can be added coherently to form a telescope with a maximum baseline of 3.5 km. The stations in the innermost 350 m are known as the Superterp.

LOFAR is a "software telescope,"with no moving parts, and the radio signals arriving at the telescope are processed via the correlator for radio imaging. This makes LOFAR an excellent test case for the feasibility of the technical challenges for future radio telescopes such as the Square Kilometer Array (SKA), which will be heavily software reliant.

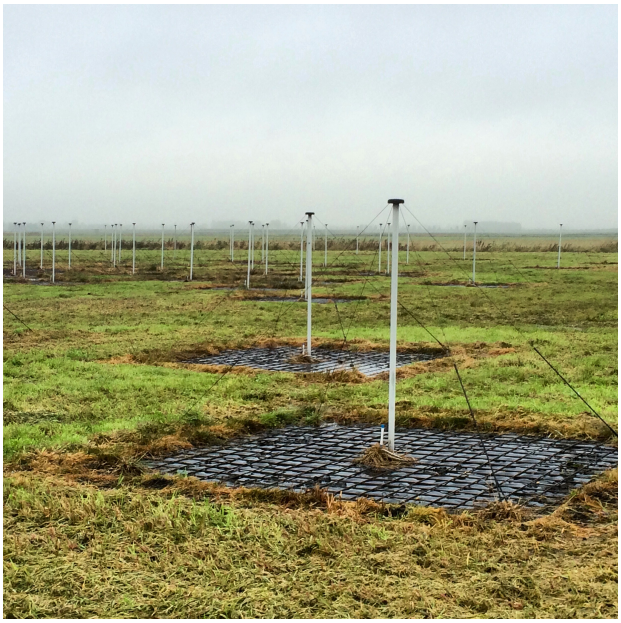

Figuur 5 LOFAR Low-Band Antennas near Exloo, NL.

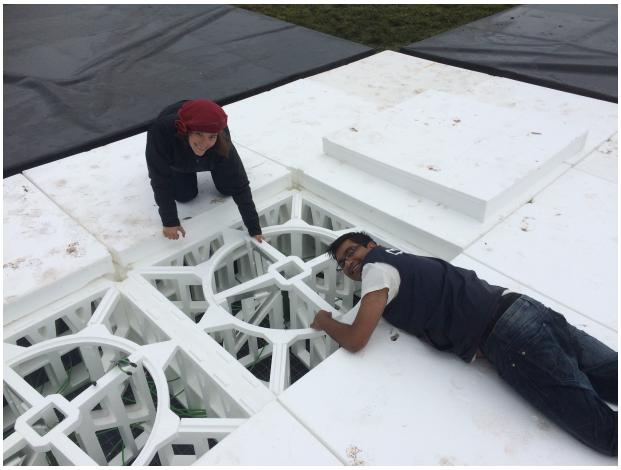

Figuur 6 Field work on LOFAR antenna CS013 on October 22, 2015, a high band antenna. Each square contains a low frequency dual-polarization dipole.

Figuur 7 Part of the VLA in New Mexico as seen on a site visit in November 2018, when it was in D configuration.

The Karl G. Jansky Very Large Array (VLA)

The Karl G. Jansky Very Large Array (VLA) is located 64 kilometers west of Socorro, New Mexico, USA. The telescope is an interferometer that consists of 27 individual antenna dishes, each of which is 25 meters in diameter and weighs about 200,000 kg (or 220 tons). A close-up of a VLA antenna, with part of the full array behind it, can be found in Figure 7.

The VLA antennas sit in three arms in a "Y" shape, and the length of the arms can be changed by moving the antennas on a rail track with a specially designed locomotive. There are four principal array configurations, A through D, along with hybrid configurations. A configuration has the longest baselines, where the telescopes extend over the full 21 kilometer length of each arm, and corresponds to the highest possible angular resolution observations at a given observing frequency. In D configuration, on the other hand, all the telescopes are within 0.6 km of the array center, which translates to a high surface brightness sensitivity. The layout seen in Figure 7 is D configuration.

The VLA was constructed in the 1970s, and inaugurated in 1980. It was upgraded in 2012, at which point the expanded VLA was renamed the Karl G. Jansky Very Large Array. As the upgrade significantly increased the telescope's sensitivity, to avoid confusion in this work we will refer to pre-upgrade observations as from the "historic VLA."

The VLA is an excellent telescope for transient astronomy due to its sensitivity and resolution. It has also conducted several surveys of the sky, including the NRAO-VLA Sky Survey [NVSS; Condon et al., 1998], the Faint Images of the Radio Sky at Twenty-cm [FIRST; Becker et al., 1994], and the currently ongoing Very Large Array Sky Survey (VLASS). Additional surveys of smaller areas of sky for transients have also been conducted over the years [see Hodge et al.,

2011, for one such example]. Further, all VLA data after an initial proprietary period are publicly available via the National Radio Astronomy Observatory's archival website. This means observations from approximately 1980 are accessible, which is an invaluable asset in the study of long-term transients.

The Australia Telescope Compact Array (ATCA)

The Australia Telescope Compact Array (ATCA) is a radio telescope located a few kilometers from Narrabri, New South Wales, Australia, which is about 500 kilometers northwest of Sydney. ATCA consists of six 22 meter antennas, and operates at frequencies from 1.1 to 105 GHz.

ATCA is a very useful telescope for long-term transient projects because it first opened in 1988, and for many years was the only such interferometer in the southern hemisphere. As such, observations on the long-term evolution of sources such as SN 1987A have been taken since this source was first visible by ATCA. However, care must be taken for observations from before 2009, which have much less bandwidth compared to the Compact Array Broadband Backend (CABB; Wilson et al. 2011) upgrade.

Radio Frequency Interference

Radio Frequency Interference (RFI) corresponds to radio signals of man-made origin detected by radio telescopes. RFI has been ubiquitous in radio astronomy since its earliest founding experiments, when Oliver Lodge abandoned his efforts to detect radio waves from the sun due to local interference, and Karl Jansky reported interference rendered observations at certain frequencies impossible [Lodge, 1900; Jansky, 1932]. RFI is of major concern in radio astronomy because man-made signals are typically many times brighter than the celestial signals of interest.

Several frequency bands of interest to radio astronomy are protected by regulation, such as the 21-cm HI line at 1420 MHz. However, as modern radio telescopes have a very large bandwidths, it is impossible to rely on spectrum management alone, and RFI is an inevitable complication in observations. For example, the RFI occupancy at LOFAR is 2% in the low band, and 3% in the high band, and originates from sources such as emergency pagers, radio transmitters, aircraft, and even reflected signals from windmill turbines [Offringa et al., 2013a]. Even radio telescopes in very remote locations are not immune to RFI, as such signals can originate from aircraft, meteor scatter, or satellites.

In practice, this means all radio telescopes have some processes in place for RFI mitigation. For smaller data sets, identifying and flagging RFI can be conducted by hand, which is common for radio telescopes such as ATCA (see Chapter 1). For larger data sets where manual flagging is unfeasible, RFI detection can be conducted using software. Such software is employed to find RFI contamination in frequency or time, and can flag sections of data that meet the criteria for RFI. These automatically flagged sections are then ignored in any further analysis.

This Thesis

This thesis focuses on two broad challenges for radio transient searches:

- What physical processes can we study on different time scales?
- What technical challenges do we face to identify transients on different time scales?

These questions are pertinent for several reasons. The first is defined by the physics, and how the processes that produce radio emission on different time scales can be vastly different from one another. Physics that occurs on short time scales in radio (seconds to months) has been the focus of much research in the past in the form of pulsars, flaring stars, FRBs, and others. However, due to the nature of the time scales involved, it is much less understood how events on the scale of years to decades unfold (supernovae, AGN variability, TDEs, orphan GRBs, etc).

The technical challenges relate to our successful observations of the processes outlined by the first paragraph. The technical challenges in studying these objects are particularly imperative to understand the physical results at *all* radio telescopes, but all radio telescopes and their instruments are different and located in unique environments. Considerations can also change at the same radio telescope over different time scales- one second of interference in a several hour observation causes minimal issues, for example, but could be enough to ruin the data of someone searching for brief transients if not properly considered.

With this motivation, the thesis is divided as follows:

Chapter 1 focuses on radio results from the most famous astronomical transient of the 20th century, SN 1987A. Although our data set covers over 25 years of observations, we will focus primarily on the most recent observations (2013-2017) during which the supernova entered a new phase in its evolution in a remnant, in order to understand how changes on shorter time scales contribute to long term variability. We discover the shockwave from SN 1987A has left the dense equatorial ring of CSM, and is re-accelerating as it begins to interact with CSM beyond the dense inner ring.

Chapter 2 continues this trend by focusing on two nearby intermediate aged Type Ia SNe, SN 1895B and SN 1972E, and establishing a data set of VLA archival observations covering > 30 years. We constrain the surrounding CSM to levels consistent with ISM, and shells $> 0.1 M_{\odot}$ surrounding SN 1972E, which allows us to eliminate several progenitor scenarios for these Ia SNe.

Chapter 3 transitions to the technical challenges of transient radio astronomy searches in the form of automatic RFI flagging algorithms. We discuss the effects of RFI flagging on transient searches such as those undertaken by the LOFAR Transients Key Science Project, and describe a potential solution for detecting when the flagging algorithms may be mistakenly flagging genuine transients as RFI.

Finally, **Chapter 4** discusses the technical challenges in monitoring for long-term transients and variability that occur over several years at minimum, by reporting our results for the monitoring of a catalog of luminous radio sources seen toward galaxies using data from VLASS and other radio telescope surveys. I also cover the difficulties in identifying variable sources hidden amongst more mundane sources on these time scales, and consider how multiple radio surveys over decades can be used to monitor long-term behavior.

Future Outlook

As this thesis shows, radio astronomy has now matured as a field to the point where we can study transient events over decades. This trend will continue to the future as more data are taken over longer time scales and the sensitivity of radio telescopes improves. The evolution of the transients that we have studied will also continue: SN 1987A continues to brighten in radio wavelengths, and is now entering a new phase of its evolution as the shockwave continues to expand into new areas of CSM. It will continue to be the best picture of the supernova to supernova remnant transition until a new supernova is detected in our own galaxy. In the case of Type Ia SNe, we have raised the question as to whether emission may be detected at later times via dedicated observations. VLA time is secured for a dozen of the nearest Ia SNE that are 20-120 years post-SNe (project code: 19A-398), which will yield a statistical sample of the environments surrounding intermediate-aged SNe Ia for the first time.

The future of radio astronomy will also present its own technical challenges with the next generation of radio telescopes, such as the Next Generation VLA (ngVLA) and the SKA. As we increasingly rely on automatic data pipelines to process prodigious amounts of data, automatic RFI mitigation will play a crucial role. Care will have to be taken to ensure at these stages that no astronomical signals are flagged that are of interest to the astronomer. Consideration will also have to be given on how data storage will occur with such large volumes, particularly in the context of long transient events over many years that rely on data over a long range of time.

In the far future, radio astronomy on the far side of the moon may also eliminate some current technical challenges in radio astronomy. For example, such a radio telescope would be shielded from terrestrial RFI by the moon itself. Data collected by the Netherlands-China Low-Frequency Explorer [NCLE; Jia et al., 2018] – the first radio astronomy experiment on the far side of the moon, currently ongoing– will hopefully demonstrate the feasibility of such a radio telescope.

Hoofdstuk 1

The Reacceleration of the Shock Wave in the Radio Remnant of Supernova 1987A

Y. Cendes, B. M. Gaensler, C.-Y. Ng, et al.

The Astrophysical Journal, Volume 867, Issue 1, article id. 65, 15 pp. (2018)

Abstract

We report on updated radio imaging observations of the radio remnant of Supernova 1987A (SN 1987A) at 9 GHz, taken with the Australia Telescope Compact Array (ATCA), covering a 25-year period (1992-2017). We use Fourier modeling of the supernova remnant to model its morphology, using both a torus model and a ring model, and find both models show an increasing flux density, and have shown a continuing expansion of the remnant. As found in previous studies, we find the torus model most accurately fits our data, and has shown a change in the remnant expansion at Day 9,300 ±210 from 2,300 ±200 km/s to 3,610 ±240 km/s. We have also seen an increase in brightness in the western lobe of the remnant, although the eastern lobe is still the dominant source of emission, unlike what has been observed at contemporary optical and X-ray wavelengths. We expect to observe a reversal in this asymmetry by the year ∼2020, and note the south-eastern side of the remnant is now beginning to fade, as has also been seen in optical and X-ray data. Our data indicate that high-latitude emission has been present in the remnant from the earliest stages of the shockwave interacting with the equatorial ring around Day 5,000. However, we find the emission has become increasingly dominated by the low-lying regions by Day 9,300, overlapping with the regions of X-ray emission. We conclude that the shockwave is now leaving the equatorial ring, exiting first from the south-east region of the remnant, and is reaccelerating as it begins to interact with the circumstellar medium beyond the dense inner ring.

1.1 Introduction

Supernova 1987A (SN 1987A) is the closest observed supernova to Earth since the invention of the telescope. The initial supernova event was observed on February 23, 1987, and since then monitoring of the supernova remnant (SNR) at multiple wavelengths has provided crucial information in understanding the remnant's evolution [McCray & Fransson, 2016]. The SNR has been shown to evolve on a time scale of months to years, and its relatively near distance in the Large Magellanic Cloud ($\sim$ 50 kpc) has allowed for many details in the structure to be visible.

The progenitor star for SN 1987A, Sanduleak -69°202, was surrounded by an unusual structure of material, believed to be emitted by the progenitor before the supernova explosion. The most striking optical feature consists of two outer rings forming an hourglass structure and one dominant equatorial ring (ER) [Burrows et al., 1995]. The origin of these rings is unclear, but it is thought they could originate from a binary merger some $\sim$20,000 years ago [Urushibata et al., 2018; Menon & Heger, 2017; Morris & Podsiadlowski, 2009, 2007], or perhaps a fast-rotating progenitor star [Chita et al., 2008]. These rings became visible during the ionizing flash of photons released by the supernova event [Burrows et al., 1995], and the ER is located on the shock front boundary between the HII region of the red supergiant (RSG) progenitor and the RSG free wind [Chevalier & Dwarkadas, 1995]. The density in the polar directions is thought to be somewhat lower, and little is known about the region beyond the ER [Chevalier & Dwarkadas, 1995; Mattila et al., 2010a].

The first radio emission from SN 1987A was detected two days after the supernova event (February 25, 1987) by the Molonglo Observatory Synthesis Telescope (MOST) [Turtle et al., 1987]. This emission reached a peak four days after the explosion, then faded below a 3σ detection limit some $\sim$ 200 days after the explosion [Ball et al., 1995]. Emission was then detected again $\sim$1,200 days after the supernova event (mid-1990), both with MOST and the Australia Telescope Compact Array [ATCA; Ball et al., 1995; Staveley-Smith et al., 1992]. Since then, constant monitoring in the 9 GHz band shows that the radio remnant has steadily increased in radio emission, thought to originate from synchrotron emission as electrons are accelerated by the expanding shockwaves from the original supernova explosion [Ball & Kirk, 1992]. Continuous multi-wavelength monitoring suggests that the shockwave reached the optical inner ring around day 5,500-6,500, which corresponded with an increase in observed radio luminosity [Zanardo et al., 2010].

Recent data at both visible and X-ray wavelengths suggest that the SNR is now reaching the end of its current phase of passing through the ER. Fransson et al. [2015] reported that the most dense clumps of the emission region have been fading since Day $\sim$8,000, with diffuse emission and hot spots appearing outside the optical ring around Day $\sim$9,500. They predicted that the inner ring of the supernova will be destroyed by $\sim$2025. In the X-ray, Frank et al. [2016] report that the 0.5-2 keV light curve has remained constant since Day 9,500, and that the south-eastern side of the ER is fading, which is consistent with optical observations. This suggests that the blast wave is indeed leaving the ER, and that the SNR is expanding into the surrounding region. Potter et al. [2014] recently presented a model for radio emission which included the fact that the shock is expanding above and below the ER.

In this paper, we are interested in the most recent evolution of the SN 1987A radio remnant at

9 GHz, as part of a series of continuing monitoring [Gaensler et al., 1997; Ng et al., 2008; Zanardo et al., 2013; Ng et al., 2013]. The most recent observations of the SNR showed a potential break in the expansion of the remnant, which was perhaps due to a change in emission morphology [Ng et al., 2013]. Furthermore, a decreasing trend in the east-west surface emissivity of the remnant was observed, with predictions that the western lobe of the SNR would soon dominate in radio emission [Ng et al., 2013; Potter et al., 2014]. The eastern side of SN 1987A has always been brighter in earlier epochs, typically attributed to faster shocks in the east [Gaensler et al., 1997; Zanardo et al., 2010], which were possibly caused by an asymmetric explosion [Zanardo et al., 2013]. Ng et al. [2013] first noted the decrease in the ER asymmetry at Day 7,000, which was attributed to these faster shocks in the east encountering the ER, then slowing down and exiting the ER faster than shocks in the west. We seek to identify whether these trends have continued, and also whether there is evidence of the shockwave leaving the ER as was reported at optical and X-ray wavelengths.

In this paper, we report on the updated radio observations of SN 1987A through Day 10,942 after the supernova explosion, using 9 GHz ATCA data from January 1992 to February 2017. In Section 3.3.1, we discuss our observations and data reduction. In Section 3, we show our resulting images, and discuss our analysis of the remnant including Fourier modeling techniques, and the subsequent results. In Section 4.4 we discuss the physical implications of our results, and compare SN 1987A to the handful of other spatially resolved radio supernovae.

1.2 Observations and Data Reduction

Our radio observations are part of a continuing ATCA imaging project at 9 GHz of SN 1987A, which has been bright enough for imaging since Day 1,786 [Staveley-Smith et al., 1993]. These observations are taken using 6-km configurations only, with typically $\sim$ 10 hr of on-source time. This publication covers all observations taken to February 2017 of the source, with observations prior to 2013 July 18 also discussed by Ng et al. [2013]. Our new observations are summarized in Table 1.1.

Observations before 2009 in this monitoring campaign were made in two bands centered at 8.512 GHz and 8.896 GHz, respectively, with a usable bandwidth of 104 MHz each. Since the Compact Array Broadband Backend [CABB; Wilson et al., 2011] upgrade, which enables observations on 2-GHz bandwidth on each band, we have restricted the analysis of 9-GHz monitoring data to two 104-MHz sub-bands that match the older observation settings.

The data were reduced using the MIRIAD software package [Sault et al., 1995], first using standard flagging and calibration techniques, and then implementing self-calibration [see Gaensler et al., 1997; Ng et al., 2008]. We averaged the visibility data first in one-minute intervals, and formed intensity maps from the visibility data using a maximum entropy algorithm [Gull & Daniell, 1978]. Finally, we applied a super resolution technique by restoring the cleaned maps with a FWHM beam of 0.4"based on the method outlined by Briggs [1994, 1995].

Observing Date	Days since Supernova	Array Configuration	Center Frequency (MHz)	Time on Source (hr)	Epoch Shown in Figure 1.1
2013 July 18	9642	6A	8512, 8896	10	2013.5
2013 Nov 09	9756	6A	8512, 8896	9	2013.9
2014 Apr 16	9915	6A	8512, 8896	8	2014.3
2016 Mar 03	10601	6B	8512, 8896	8	2016.2
2017 February 7	10942	6D	8512, 8896	9	2017.2

Tabel 1.1 Observations and parameters new to this study. Data prior to Day 9,642 is available in the electronic version of the journal article for this chapter.

1.3 Results

1.3.1 Images

The 9 GHz images of the remnant derived since 1992 are shown in Figure 1.1. The remnant forms a circular shell, with brightness varying between different regions. The left (east) side of the shell is consistently brighter than when it was first observed in 1992, and has steadily increased in brightness until the present day. The right (west) side of the shell is increasing in brightness, but is less bright than the eastern side at all epochs. Emission is also present but more limited in the top (north) and bottom (south) regions. While emission is not uniform, we can see that all of the shell is increasing in brightness during our observations.

We can also see a clear expansion in the shell from 1992 to present day. In 1992, the radius of the emission region from the center of the SNR to the edge of emission in the eastern side can be measured directly from the image as ∼0.6", and the 2017 image shows expansion to ∼1.4". A quantitative analysis of this expansion can be found in Section 1.3.3.

We have also included contour plots of the images that are new to this paper in Figure 1.2. We can see that the circular structure of the remnant is present at all epochs, and that the remnant is getting brighter. We also see that the south-eastern part of the remnant is the only region decreasing in brightness, which can be seen in the final two most recent observations. Specifically, the average flux density in our first three images measured at a 135 degree angle, which is measured from north to east, (from Day 9,642, 9,756, and 9,915 respectively), is 10.0 ± 0.1 mJy, which fades to 9.0 ± 0.1 mJy by the observation on Day 10,061 and 8.2 ± 0.1 mJy on Day 10,942. We acquired these values by measuring the flux density along the south-western region by drawing a box in the image plane using KVIS, which is marked in Figure 1.2.

1.3.2 Fitting

The resolution of imaging data allows us to fit various models to the supernova shell structure and to obtain several parameters for its expansion. For this, we used the Fourier modeling script outlined by Ng et al. [2008] and Ng et al. [2013], which assesses the geometry of the remnant in the visibility (uv) plane, which is defined by a 2D Fourier transform of the sky brightness. The fitting was done using a modified UVFIT task in MIRIAD, which in addition to the parameter

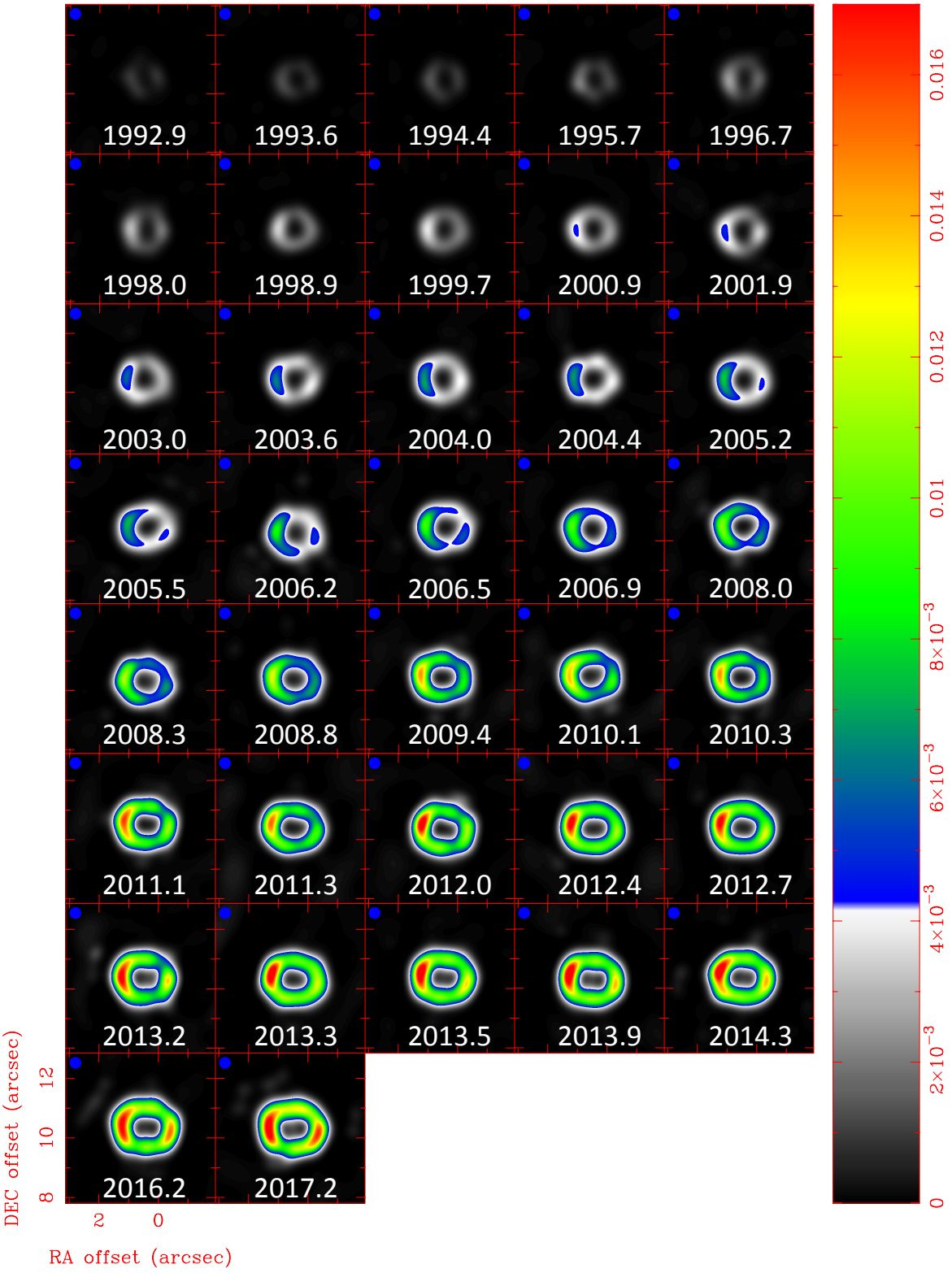

Figuur 1.1 Super-resolved false color pixel images of SN 1987A at 9 GHz with ATCA data from 1992-2017. North is up and east is left. The scale on the right hand side is the intensity in Jy/beam, and we have provided the beam size for each image (blue circle, upper left hand corner) for reference.

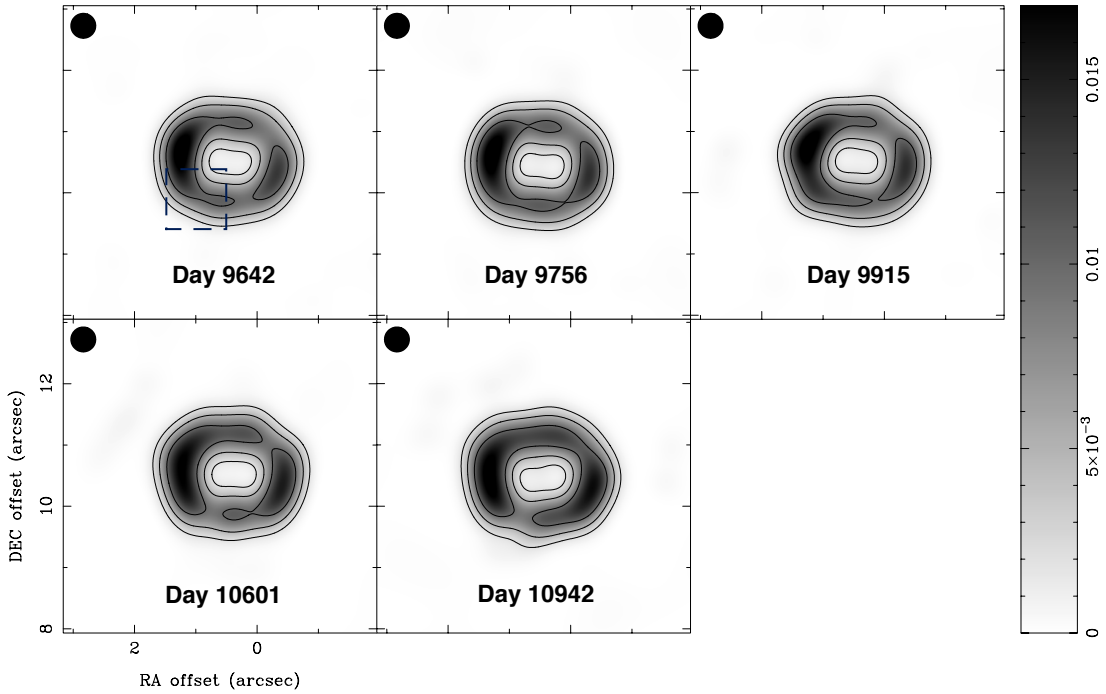

Figuur 1.2 Contour plots of the last five images in Figure 1.1, by epoch of observation. The contour levels correspond with 2, 5, 10, and 20 mJy/beam, respectively. The circle in the upper left hand corner of each image is the beam size, and the dark blue box in the Day 9,642 image is the southeast corner region.

Day	Flux (mJy)	Radius (")	Half-opening Angle θ (°)	Thickness (%)	Asymmetry	ϕ(°)
9,642	175.81 ± 0.04	0.9464 ± 0.0002	29.68 ± 0.05	<1	21.30 ± 0.04	99.6 ± .2
9,756	179.87 ± 0.04	0.9508 ± 0.0002	30.84 ± 0.06	<1	21.98 ± 0.05	103.5 ± 0.2
9,915	185.96 ± 0.0005	0.9583 ± 0.0003	30.55 ± 0.06	<2	20.57 ± 5	94.7 ± 0.3
10,601	199.45± .06	0.9857 ± 0.0003	32.48 ± 0.07	<7	15.42 ± 0.5	88.6 ± 0.4
10,942	216.43 ± 0.06	0.9975 ± 0.0002	28.36 ± 0.05	9 ± 8	10.36 ± 6	87.5 ± 0.5

Tabel 1.2 Best-fit Parameters for the Torus Model with Statistical Uncertainties at 68% Confidence Level. This table contains observations new to this publication. The full data set for all values are available in the electronic journal article.

Day	Flux (mJy)	Radius (")	Half-opening Angle θ (°)	Thickness (%)	Asymmetry	ϕ(°)
9642	171.54± .04	0.8781 ± 0.0002	0.6580 ± 0.0002	19.28 ± 0.04	81.7 ± 0.2	
9756	176.54± .04	0.8810 ± 0.0002	0.669 ± 0.0003	19.53 ± 0.04	93.1 ± 0.1	
9915	181.69 ± .05	0.8916 ± 0.0003	0.663 ± 0.0003	18.87 ± 0.05	89.1 ± 0.3	
10601	195.68± .06	0.9182 ± 0.0003	0.691 ± 0.0003	14.61 ± 0.06	74.1 ± 0.4	
10942	209.78 ± .06	0.9348 ± 0.0003	0.634 ± 0.0003	10.64 ± 0.07	64.1 ± 0.4	

Tabel 1.3 Best-fit Parameters for the Ring Model with Statistical Uncertainties at 68% Confidence Level. This table contains observations new to this publication. The full data set for all values are available in the journal article.

values for the model also provides χ^2 values in order to confirm the reliability of the fit.

We fit two geometries to the remnant: a 3D torus model and a 2D ring model. Based on previous studies of 9-GHz observations [e.g., Ng et al., 2008, 2013] and the complex remnant geometry (see simulations by [Potter et al., 2014]), we fit the data with two geometrical model: a 2D ring and a 3D torus. The 2D models allow us to compare to the model used in X-ray studies [Racusin et al., 2009; Helder et al., 2013; Frank et al., 2016]. For the torus model, we fit for eight parameters: flux density, center position (in RA and Dec), radius, half-opening angle (θ), thickness (as a fraction of the radius), asymmetry (as a percentage), and direction of a linear gradient in surface emission (ϕ) [see Section 3, Ng et al., 2013]. The parameters we obtained can be seen in Table 2 along with the confidence intervals from the χ^2 distribution.

For the ring model, we fit the semi major axis (R_1) and semi-minor axis (R_2), as well as the flux density and center position[see Section 3 of Ng et al., 2013]. The obtained parameters can be seen in Table 3 with the χ^2 fit.

1.3.3 Expansion

The obtained radii for the torus model, and for the ring model, can be seen in Figure 1.3. We also included the X-ray radius reported by Frank et al. [2016] for reference, who fit their data with a ring model using a single radius. All three of our models show a clear increase in the radius over the entire time period.

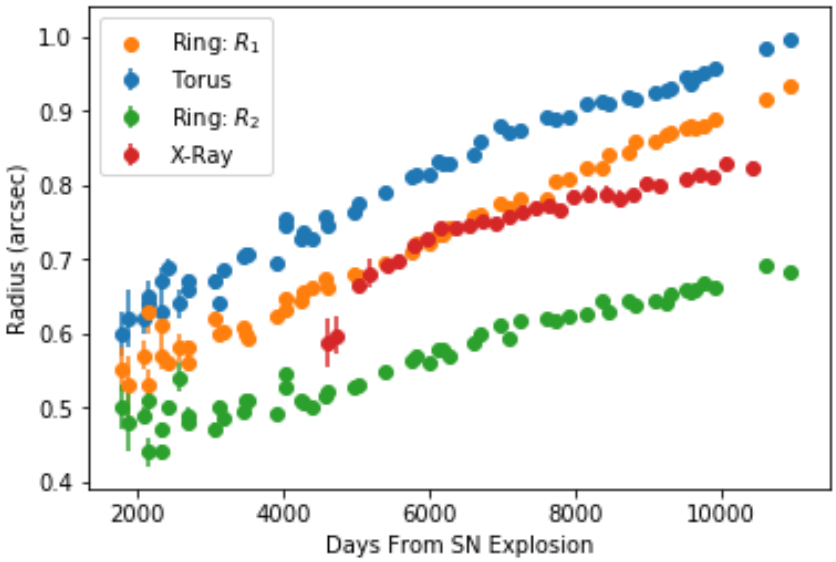

Figuur 1.3 The radius of SN 1987A as a function of time, as measured using the torus model (blue), and the semi-major (R_1) and semi-minor (R_2) axes for the ring model (yellow and green, respectively). The radius as measured in the X-ray by Chandra (red) is provided for reference from Frank et al. [2016].

Model	Type	BIC
Torus	Piecewise	-368.7
Torus	Linear	-325.1
Ring (R_1)	Piecewise	-373.7
Ring (R_1)	Linear	-378.8
Ring (R_2)	Piecewise (semi-minor axis)	-365.6
Ring (R_2)	Linear (semi-minor axis)	-338.7

Tabel 1.4 Bayes factors calculated via the Bayesian Information Criterion (BIC) for six linear and multi-linear (piecewise) models of the radio remnant that rely on three radius geometry parameters (torus, semi-major radius R_1, semi-minor radius R_2). All models fit data from Day 7200 to Day 10942. Smaller BIC values indicate more accurate fits.

Model	Transition Date (Days From SN)		Velocity (km/s)		
	Transition 1	Transition 2	v_1	v_2	v_3
Torus	7,000 ± 200	9,300 ±200	4,600±200	2,300±200	3,610±240
Ring: semi-major axis (R_1)	—	—	3,800 ±460	—	—
Ring: semi-minor axis (R_2)	7,000 ±300	—	3,300±200	2,120±40	—

Tabel 1.5 Expansion velocities and errors of the radio remnant from Day 4,000 over time. Values for v_1 were obtained from Ng et al. [2013], v_2 corresponds with the velocity after the first transition date, and v_3 corresponds with the velocity after the second transition date. A dash corresponds with when no transition to a different velocity was observed.

Ng et al. [2013] analyzed the SNR expansion data from Day 4,000, and reported a break in the expansion rate for the torus model at Day 7,000 ± 200 to a lower speed (with a similar break occurring at the same time in R_2), and a linear trend in R_1. Thus, when examining our most current data, first we examined data from Day 4,000 onwards in our analysis, as we were most interested in recent changes in the expansion of the emission. For each of our models, we considered both a linear fit from Day 4,000 to present, and a break in expansion where the initial rate of linear expansion of the emission region changes to a second rate of expansion. In the latter case, we fit a piecewise function consisting of two different linear slopes, and the transition day where the slope changed was fit as a free parameter. This data fit is consistent with the earlier analysis of Ng et al. [2013], and should emphasize that we do not believe these times don't necessarily refer to physical events, but rather this method was used in order to identify roughly where changes in the expansion rate occurred. For each fit, we then calculated the Bayesian Information Criterion [BIC; Hogg et al., 2010] so we could compare the two models for each data set (Table 1.4), where the lower value indicates a more accurate fit. We chose this over the χ^2 fit because the broken linear fit has an extra parameter when compared to a simple linear fit, and the BIC takes into account potential overfitting with this method. As in [Kass & Raftery, 1995], given $\Delta B_i j = |B_i - B_j|$, where B_i and B_j are the BIC values associated with two statistical models, if $3 < \Delta B_i j < 10$, the smaller BIC value provides *substantial* evidence that the associate model is more accurate. For $\Delta B_i j > 10$, the smaller BIC value provides *strong* evidence that the associate model is more accurate. Therefore, the BIC values listed in Table 1.4 indicate that the torus model is the most accurate representation of the data after Day 7000, since $\Delta B_i j = |B_4 - B_2| = 43.6$.

From this, our results for the expansion velocities can be seen in Table 1.5, where we assumed a distance to the supernova of 51.4 kpc to obtain expansion velocities in km/s. We found that during this entire period, R_1 has continued expanding linearly of 3,800 ±460 km/s, which is in agreement with the reported value in Ng et al. [2013] of 3,890±50 km/s. Our test also confirmed the break previously observed at Day 7,000 in the cases of both the torus model and R_2. Based on this, we further examined the data from Day 7,000 to the present with another BIC test comparing a broken linear versus linear model. In this case, linear expansion was the best model for R_2 from Day 7,000, with a velocity of 2,120±40 km/s, which is greater than the previously reported value for Day 7,000-9,568 from Ng et al. [2013] of 1,750±300 km/s). For the torus model, we identified a second break in the expansion velocity that best fits our data from Day 7,000 to the present

Model	K	t_0 (days)	β
Torus	1.5 ± 0.1	6,540 ± 80	0.59 ± 0.02
Ring	2.0 ± 0.12	6,680 ± 80	0.55 ± 0.02

Tabel 1.6 Parameters for the exponential fits seen in Figure 1.6.

period. This occurred at Day 9,300 ± 200, where the expansion rate of the torus model changed from 2,300±200 km/s to 3,610±240 km/s. For reference, the best fits to our data are in Figure 1.4.

1.3.4 Radio Light Curve

The integrated flux densities obtained via the torus and ring models are compared in Figure 1.5. We chose to measure and list the flux of the model, not the source itself, because this value is tied to the overall geometry versus the individual fluctuations and our goal was to understand how the models can change. For consistency, we checked the flux of the source in kvis for the first and last natural images in our data set. For the Day 1,786 date, we found a flux density of 4.3 ± .1 mJy, which can be compared to 4.2 ± .2 mJy for the torus model and 3.70 ± .12 in the ring model. On Day 10,942, we measure 212 ± 3 mJy with this method, compared to 216.43 ± .06 mJy for the torus model and 209.78 ± .06 mJy for the ring model. This shows our using this method to measure total flux is consistent with measuring it for the entire source region, and can even be more accurate.

We find that the ring and torus flux density were in agreement, except the ring model is lower than the flux density measurement when compared to the torus measurement in later epochs. The discrepancy between the two values, which begins at Day ∼6,000, has increased over time, to a ∼7 mJy difference in 2017, or 3% of the total. Measuring the flux density using another method such as the peak flux value using a conventional software package like kvis could not distinguish between the two models, as the uncertainty from this method is larger than the difference in flux density between the two models. Instead, we examined the maps of the residual visibilities (i.e., our data minus the model) for both the torus and ring models. We found the torus model accounted for the emission more accurately than the ring model by showing less residual flux. This leads us to conclude that the flux emission from the torus model is more accurate than the ring model, although we include values for the ring model here for completeness.

Ng et al. [2013] reported that the fluxes obtained were lower than expected from the exponential fit given by Zanardo et al. [2010] from Day ∼7,500. After this time, our data confirm a continuation of this trend. As such, we considered data from Day 7,500 onward to derive a new modified power law fit. The radio light curve of SN 1987A can be parameterized by

$$\mathrm{S(mJy)} = \mathrm{K}\left(\frac{\nu}{5\ \mathrm{GHz}}\right)^{\alpha}\left(\frac{t-t_0}{1\ \mathrm{day}}\right)^{\beta}, \tag{1.1}$$

where K is the parameter fit due to the flux density, ν is the frequency of observation, α is the spectral index, and β is the modified power law fit for the light curve [Weiler et al., 2002]. Using $\nu = 9$ GHz, $\alpha = -0.74$ [Zanardo et al., 2013] , and the curve fitting package in [SciPy;

Model	a	t_0 (days)	β
Torus	4.0 ± 0.1	6,540 ± 80	-1.129×10^{-6} ± 9 × 10^{-9}
Ring	4.6 ± 0.2	6,680 ± 80	-8.71×10^{-7} ± 9 × 10^{-9}

Tabel 1.7 Parameters for the asymmetry fits seen in Figure 1.8.

Jones et al., 2001], we obtained the parameter values seen in Table 1.6. The data generated with this model along with the relevant fits can be seen in Figure 1.6 for both models.

We also did the same fitting routine by dividing the flux values for each model by the number of days since the supernova explosion (Figure 1.7), in order to see whether there are changes in the increase in flux density itself. Here, we can see that from Day 7,500, the rate of brightness increase has been growing more slowly over time.

1.3.5 Morphological Behavior

Although the remnant of SN 1987A is increasing in brightness on a power law scale, this is not evenly distributed throughout the entire ring. Surface brightness asymmetry has been apparent in the remnant since the earliest radio observations, with the eastern (left) lobe the brightest area. We confirm that the eastern lobe is still increasing in flux, although emission from the southeastern quadrant is fading (Figure 1.2).

On the western side of the source, emission is increasing at a faster rate than previous years when compared to the eastern side. This is particularly visible in the east-west asymmetry of surface emissivity, defined as the slope of the gradient of flux in the image plane (north to east), as seen in Figure 1.8. We note this decrease is greater in the ring model than in the torus model. We provide a fit for the change in asymmetry gradient over time, the parameters for which can be seen in Table 1.7.

The torus model also provides us with the half-opening angle (θ). A plot of these data can be seen in Figure 1.9. The orientation of the half opening angle has become more stable after Day 4,000, and between Day 4,000 and 7,700 has a mean value $\theta = 41.4°$. From this point, θ begins to rapidly decrease, until stabilizing again at Day 8,800 with a new mean value of $\theta = 29.9°$.

In the case of the ring model, Ng et al. [2013] noted that the ratio of R_2/R_1 closely follows the trends seen in θ. Results for this ratio over time can be seen in Figure 1.10. We find that during the Day 4,000- 7,700 period, the R_2/R_1 ratio is 0.78 ± 0.01, and after Day 8,800 (when θ stabilizes), the ratio is 0.74 ± 0.02. As such, our findings are consistent with the results from Ng et al. [2013], and have continued to Day 11,000.

1.4 Discussion

The current radio emission from SN 1987A at 9 GHz is dominated by the interaction of the supernova shockwave with the ER, which is a smooth ring interspersed with denser clumps, plus an unknown contribution of polar emission from outside the dense ring. We are currently witnessing the forward shock from the supernova explosion leaving the ER as the reverse shock is driven back into this ring. We first discuss the picture of the SN 1987A CSM during the

period when the supernova blast wave pushed through the CSM (Day 4,000-9,300), both in the morphological and physical contexts.

Our breakdown of the Day 4,000-9,300 period in Section 4.4 is as follows. First, in Section 1.4.1.1 we discuss the expansion index of both the ring and torus models, which indicates that the increased expansion rate during this period is caused by shockwaves at high latitudes in the SNR. In Section 1.4.1.2, we discuss the coupling between θ and the expansion of the remnant. In Section 1.4.1.3, we compare our radio observations to X-ray data, and discuss how the difference in size between the two is likely physical. In Section 1.4.1.4, we discuss the delayed change in the asymmetry between the eastern and western lobes of the SNR as predicted from theory and seen at other wavelengths. And in Section 1.4.1.3, we discuss our increasing flux brightness in the context of potential high latitude emission, and a potential change in emission region within the ER.

After this, in Section 1.4.2 we will discuss the observed changes in SN 1987A from Day 9,300 onwards, which we interpret as the time at which the shockwave left the ER. In Section 2.5.4, we will discuss our future predictions for the SNR, including factors such as high latitude emission and the unknown composition of the region beyond the ER, and make future predictions for the change in asymmetry in emission. Finally, in Section 4.4.5, we compare SN 1987A to other resolved radio supernovae, and discuss in this context how SN 1987A can be used to contrast features such as hotspots and expansion rates in various SNR.

1.4.1 Day 4,000- Day 9,300

1.4.1.1 Rate of Expansion

In Section 1.3.3 and Figure 1.3, we presented our results from the expansion of both the torus and ring models of SN 1987A. When comparing our two models for the SNR expansion, there is a discrepancy in the values for the radius measurement between the torus model radius and R_1, where the torus values are consistently larger than R_1 (and R_2). This discrepancy was first noted by Ng et al. [2013], who described the cause of this phenomenon in more detail and presented two explanations for it. The first is that the torus model, unlike the ring model, is dependent on the half-opening angle, θ (see Section 1.4.1.2). This then creates a projection effect, as the torus model approximates a ring when $\theta = 0°$, but is a shell as θ increases to 90°, and the shell model can have its emission peak inside the shell's radius. Another proposed explanation is that because the shockwave travels faster in the lower density regions above the ER [Blondin et al., 1996], any high-latitude material present would manifest in a higher radius measurement for the 3D-sensitive torus model.

In the case of spherical symmetry in the SNR and a power law density distribution, one can model the expansion of the supernova remnant as $R \propto t^m$ [Chevalier, 1982a,b]. This is because we expect the forward and reverse shocks to drive our observed expansion, and we can expect these shocks to slow down over time as the ejecta transfer some amount of their kinetic energy into the swept-up material. We can assume the shockwave entered the ER by Day 5,600 [Helder et al., 2013], and from this point to the transition observed at Day 9,300 (see Section 1.4.2), we find m= 0.30± 0.01 for the torus data, and 0.41 ± 0.01 for R_1.

1.4.1.2 Expansion and Half-Opening Angle

When considering the expansion rate of the radio remnant, we already explained in Section 1.4.1.1 that the torus and ring models give us different values for the radius. However, the ratio between the torus radius and R_1 is not constant, due to the changing velocity of the torus radius (Figure 1.3). Figure 1.12 shows the changing ratio of the torus radius divided by R_1 from Day 4,000. For reference, we have indicated the deceleration at Day 7,000 and re-acceleration at Day 9,300 (as measured from the torus model) with black dashed lines (See Table 1.5).

Before Day 7,000, we find that the ratio is 1.13 ± 0.01. This corresponds with a period during which Ng et al. [2013] reports that the torus model velocity is higher than the R_1 velocity, at 4,600 ± 200 km/s compared to 3,890 ± 50 km/s, respectively. These faster initial velocities in the torus model imply that higher latitude radio emission played a large contribution during this period. From Day 7,000 to 9,300, we see the Torus/R_1 ratio decrease as emission from the low-lying areas begins to dominate, which corresponds with the period when the torus velocity decreases to 2,300 ± 200 km/s and R_1 remains constant at 3,800 ± 460 km/s in our analysis.

The system re-stabilized at Day 9,300 before the ring and torus models could converge, meaning emission from high latitudes continues to be a factor in the radio remnant. The existence of such emission would also help explain the expansion of both the torus and R_1 sizes beyond the optically observed ER before the shockwave interacted with it [Plait et al., 1995]. Further, there is a clear correlation between the expansion of the torus radii and θ during this time period, as shown in Figure 1.13.

We also see a coupling between the torus/R_1 radius ratio and the half opening angle, as shown in Figure 1.14. This implies that the radio emission has become more ring-like and two dimensional in nature over time, and that the emission is increasingly dominated by lower latitudes. This could be due to one of two reasons. First, it is possible that there previously was a higher amount of high-latitude emission, which has steadily decreased over time. The second option is that while high-latitude emission is still present, the emission from lower latitudes has increasingly dominated, as the shockwave interacted with increasingly dense regions of the ER [Potter et al., 2014].

Finally, we should note that this occurred in conjunction with a decrease in the R_2/R_1 ratio from 0.78 ± 0.01 to 0.74 ± 0.02, respectively (Figure 1.10). The ER region is known to have an orientation of 41° to the line of sight [Sugerman et al., 2005], which would imply a ratio of ∼0.70. This supports the interpretation that some high latitude emission has been persistent, but that emission from the ER has dominated more recently.

1.4.1.3 Size Comparison to X-ray

The ring model allows us to compare the size of the remnant with X-ray data, which appears to follow a ring model fit [Frank et al., 2016]. When comparing the ring model to the X-ray data, the radio emitting region has consistently been larger than the X-ray emitting region since Day 7,500, which was first noted by Ng et al. [2013]. Since this date, the trend has continued (Figure 1.3). This difference is likely physical as opposed to a difference in measuring technique between X-ray and radio [Gaensler et al., 2007; Ng et al., 2009, 2013].

Ng et al. [2009] applied the torus spatial model to Day 7736 X-ray observations, and found a value of $\theta = 26^\circ \pm 3^\circ$. We note that radio observations at this time yielded a value for θ of 36.2°– that is, at the beginning of the transition of θ from a higher value to its lower one (Figure 1.9). Further, the X-ray emission at this time is believed to originate from the shockwave interacting with the dense clumps in the ER [Orlando et al., 2015; Frank et al., 2016]. The fact that θ derived from our torus model from Day 8,800 is in agreement with the θ obtained by Ng et al. [2009] suggests the radio emission also largely originates from the same half opening angle region as is the X-ray radiation during this time, although the overall emission torus may be larger in radio.

1.4.1.4 Asymmetry

The morphological changes in SN 1987A have also included a reduction in the asymmetry of surface brightness between the eastern and western parts of the remnant (Figure 1.8). A 3D simulation of SN 1987A by Potter et al. [2014] used this assessment, and predicted that the faster shocks would first depart the eastern lobe at Day 7,000, and shocks from the western lobe would later emerge at Day 8,000. At this point, the model predicted that the asymmetry between the two lobes should pass parity (where the emission is equally bright between the eastern and western lobes), and ultimately the asymmetry should be brighter in the western side by Day 9,000-10,000. However, we do not observe this in our data; instead, it appears that we are only beginning to approach parity between the eastern and western lobes (where both are equally bright) by Day 11,000. This could be attributed to several possibilities, such as an over-density compared to what was used in theoretical models in the eastern lobe, which would delay the egress of the shock from this area. Another possibility is that the assumed distribution in emission used by Potter et al. [2014] between the forward and reverse shocks is incorrect, and that there is instead a longer exit phase as different shocks leave the ring. It should be noted, however, that despite the delay, our observations show a trend which is consistent with model predictions.

We can also compare the asymmetry to what we see in X-ray data. Although it is not known whether the X-ray and radio emission necessarily originate from the same region, Frank et al. [2016] note that the radio emission evolves similarly to the X-ray and optical data, but is delayed by ∼2,000 days, which appears consistent with our findings (Figure 1.1). They further suggest that the 'hard' component (∼2-10 keV) best matches the radio data in morphology, and that the east-west asymmetry only began to reverse in this X-ray band around Day ∼9,500. This delay would be consistent with what we see in our data, where by Day 11,000 we have not yet reached parity in the brightness between the eastern and western lobes. As such, it does appear that there is some similarity in the emission region from the ER between the radio and X-ray data.

1.4.1.5 Flux Density

Radio emission in SN 1987A is thought to be distributed between the forward and reverse shocks [Jun & Norman, 1996], although the exact distribution between these is still unknown. In the case of SN 1987A, the picture is further complicated by potential emission from multiple components [Blondin et al., 1996], such as a component arising from the ER and emission from high latitudes. Our residuals when the model was subtracted from the data favored the torus model over the ring model. This fact suggests the picture including high-latitude emission is more accurate.

Radio emission in the period from Day 5,000 to 7,500 increases exponentially (Figure 1.5), and was thought to be caused by interactions between the shockwave and the ER [Zanardo et al., 2010]. From Day 7,500, we still see an increase in brightening of the remnant, but at a reduced rate compared to that in earlier epochs (Figure 1.6). This transition likely corresponds with a decrease of material interacting with the shockwave during this time, likely corresponding to the shockwave beginning to leave the ER. If the asymmetry of the ER is caused by faster shocks in the east (see Section 1.4.1.4), as the shockwave leaves the eastern lobe a part of the shockwave would still be interacting with the western lobe, and this would cause the overall flux of the ER to continue increasing until the entire shockwave leaves the ring completely.

1.4.1.6 Summary of Day 4,000-9,300

The Day 4,000-9,300 period was clearly a time of transition in SN 1987A, with many changes observed over the epoch. First, our observed expansion rate in both torus and ring models isconsistent with the shockwave interacting with the dense ER. Second, there is a coupling between θ and the torus radii, as shown in Figure 1.13, whereby the decrease in the rate of expansion of the torus radii at Day 7,000 corresponds with the half-opening angle for the emission decreasing. The expansion rate for the torus radii then begin to increase again once θ stabilizes. We attribute this to high latitude emission being present from earlier stages, and then later the lower latitudes begining to dominate the emission profile. The size of the radio remnant also appears to be larger than that of the X-ray remnant. Further, the radio remnant appears to lag in flux density over time compared to what is seen in the X-ray by $\sim$2,000 days.

The asymmetry observed between the eastern and western limbs of the ER is delayed compared to predictions in theoretical models, which during this period predicted parity between brightness in both sides, and that the western limb would become subsequently brighter. Instead, we see the eastern limb remaining brighter than the western limb. Finally, the flux density of the SNR has continued to increase, but from Day 7,500, the increase has continued at a lower rate than what was measured for Days 4000-7500. This could be due to the shockwave leaving the ring from this period, but the contribution of any emission from high latitudes that has been present since the ER was first encountered is unknown.

1.4.2 Day 9,300 Onwards

From Day 9,300, the supernova remnant has undergone several changes. These include the re-acceleration to a faster expansion rate in the torus model fits to the data to 3,610 $\pm$ 240 km/s (Table 1.5 and Figure 1.3). This is in agreement with the velocity value obtained for R_1, as well as θ stabilizing at 29.9 $\pm$ 0.1 degrees, as seen in Figure 1.13. This re-acceleration has corresponded with an expansion rate $R \propto t^m$ of $m = 0.43\pm$ 0.02 for the torus model, and 0.44 $\pm$ 0.02 for R_1. This indicates that a transition occurred around Day 9,300, which we interpret as the forward shock leaving the ER.

As the SN expands beyond the ER, high-latitude emission components of the radio remnant become more prominent (Potter et al. 2014). Given the hourglass structure of the nebula and its inclination along the line of sight, emission components above and below the equatorial plane have been identified as extended bright sites in the northern and southern sectors of the SNR

[Zanardo et al., 2018]. At 9 GHz, although we cannot distinguish the specific contribution of high-latitude emission from that of emission sites specifically located within the equatorial plane, i.e., where the dense CSM is located, we measured a marked increase of the emission from the northern and southern sites. In particular, within 1,000 days (Day 9,915-10,942), the emission observed in the northern and southern sectors has undergone an increase of 20%, compared to the 10% increase across the eastern lobe (see flux density contours in Figure 2). At day 11,000, the integrated flux density over the northern and southern sites is 12 mJy, while the emission from the brightest eastern sites is 18 mJy. Further, Ng et al. [2013] predicted that if shocks from the lower latitudes continue to dominate the emission, the radius measurements between both the torus and ring measurements should converge. With the re-acceleration of the torus expansion rate, we do not see that this will be the case in the future.

The southern part of the emission paints a more complex picture, as we can see by Day 10,600 that the southeastern area of the ring has begun to fade (Figure 1.2). This is consistent with the break-up seen in the X-ray and optical data [Fransson et al., 2015; Frank et al., 2016]. Hotspots beyond this area have also been observed in the optical, interpreted as due to the direct interaction of the shockwave with gas beyond the ER [Fransson et al., 2015].

1.4.3 Future Predictions

The SN 1987A remnant is transitioning into a new phase. Much of what happens next in SN 1987A depends on the density of the area beyond the visible emission region which the shockwave is now entering. Mattila et al. [2010a] estimated a mass for the ring, but emphasized that this calculation only included the mass ionized by the initial shock breakout from the supernova. As such, it is possible that the density beyond the visible ER could be greater than expected, assuming that the shockwave will enter a region where the CSM will originate from a free RSG wind emitted by the progenitor star [Chevalier & Dwarkadas, 1995].

Observations of hotspots appearing beyond the ER at optical wavelengths [Fransson et al., 2015] also indicate that the structure beyond the ER may be more complex than expected. Understanding this structure is particularly important if the CSM is from a binary progenitor model [Urushibata et al., 2018; Menon & Heger, 2017; Morris & Podsiadlowski, 2009], as the distribution of material could shed light on slow and fast merger scenarios. Radio observations should tell us more about this environment, as a further increase in shockwave velocity over the next few thousand days would indicate that the density of gas with which the shockwave is interacting is decreasing. Simulations from Potter et al. [2014] predicted a velocity at a few thousand days as high as 6,000 km/s, although this is dependent on the temperature and density for the region.

When it comes to the asymmetry of the SN emission, if we extrapolate the rate of asymmetry decrease seen in Figure 1.8, we expect the asymmetry to reach parity (where the east and west sides are equally bright), on Day 11,650 $\pm$ 60 using the torus model, and Day 12,300 $\pm$ 60 with the ring model. This prediction is also consistent with the picture seen in X-rays, which is typically 2,000 days ahead of the radio [Frank et al., 2016]. We also expect this asymmetry to then increase as the western limb increases in brightness and the eastern limb continues to fade, although we note that the rate of asymmetry may change depending on the rate of destruction of the ER in

the east, and on whether there are notable amounts of unionized or neutral gas beyond the ER which may be as dense as the ER, but not visible. The picture on the western limb may also be more complex, as analysis by Zanardo et al. [2014] suggested residual emission in the western region at higher frequencies that may be attributed to a pulsar wind nebula (PWN).

High latitude emission may also play a factor in the asymmetry, although we note that the difference in brightness between these two nodes matches very well the picture seen in X-ray data, which indicates that the two bright eastern and western nodes are likely originating from the same region. Currently, the asymmetry values between the torus and ring models are in agreement, which also indicates that the emission creating the asymmetry comes from this region. A divergence in the future asymmetry between the two models would indicate the presence of emission from higher latitudes. Further, if there are notable amounts of polar emission emerging in the next few thousand days, we expect to see further brightening in both the northern and southern areas of the ER. Such emission would be accompanied by an increase in θ.

Finally, the radio flux for the SNR will provide a good indicator for any future high latitude emission beyond the ER. Little is known of this region, although its contents are thought to be from the RSG wind of the progenitor [Chevalier & Dwarkadas, 1995; Mattila et al., 2010a]. If the material in the SNR is concentrated wholly in the ER, we expect the radio flux to plateau in the next few thousand days as the reverse shock leaves the ER, similar to what was seen in the X-ray emission [Potter et al., 2014; Frank et al., 2016]. New material interacting with the shockwaves, however, could contribute to a further increase in radio flux.

1.4.4 Comparison to Other Supernovae

SN 1987A provides a unique opportunity for comparisons between different radio supernovae, as its proximity means details in the structure can be seen which can only be resolved in a handful of other radio supernovae. Although these other radio supernovae are brighter and have a different CSM density, these comparisons over time allow us to learn how common features such as asymmetry and changes in shockwave velocity are in young supernova environments. In order to highlight these similarities, in this section we will compare our observations of SN 1987A with those of two other spatially resolved radio supernova remnants, SN 1986J and SN 1993J.

1.4.4.1 SN 1986 J

SN 1986J was first detected in 1986 via its radio emission, although it is estimated that its explosion epoch is 1983.2 $\pm$1.1 [Rupen et al., 1987; Bietenholz et al., 2002]. It is a Type IIn supernova located at a distance of $\sim$10 Mpc [Rupen et al., 1987]. Radio emission from the expanding shell of the SNR was the dominant observed emission for many years [Bietenholz et al., 2010], but at present the emission of the shell is decreasing, with the brightness of the outer edge fading faster than the edge near the center [Bietenholz & Bartel, 2017]. This is because SN 1986J also has an observable central component at its center, first detected at t $\simeq$ 20 years, which is now approximately ten times brighter than the shell component.

Radio observations of the SN 1986J shell have included a hotspot region brighter than the rest of the shell once resolution was sufficient to observe it [Bietenholz et al., 2002]. This is consistent with other spatially resolved radio supernovae, such as SN 1993J [Bietenholz et al., 2010], SN

2011dh [de Witt et al., 2016], and SN 2014C [Bietenholz et al., 2018], where the brighter hotspot regions have expanded homologously with the SNR as the shockwave expanded through the surrounding regions. Further, the SN 1986J shell was reported by Bietenholz & Bartel [2017] as expanding at a velocity of 2,810 ± 750 km/s, which is consistent with the velocities observed in SN 1987A. As such, it appears that the expansion in both remnants is dominated by the forward shock of the supernova event itself. However, it is likely that the CSM surrounding SN 1986J is much more dense than that of SN 1987A based on the former's optical spectral lines [Filippenko, 1997].

Overall, the expansion of the ring, and the expansion of homologous hotspots with this area of the remnant in SN 1986J are consistent with our observations of SN 1987A. However, the CSM surrounding SN 1986J is distributed very differently, as evidenced by how radio luminosity was likely created by material in the CSM and that the ring is now fading. In the future of SN 1987A, however, any potential increase in radio luminosity detected on the inner edge of the observed ring may be evidence of a compact object. If the compact object in SN 1987A is off-center in the SNR, as suggested by Zanardo et al. [2014], such a brightening would most likely be visible on the inner western lobe.

1.4.4.2 SN 1993J

SN 1993J, at a distance of 3.62 Mpc in M81, is the second brightest supernova observed in the last century after SN 1987A. A Type IIn supernova, its progenitor is believed to have had a significantly different mass loss history compared to SN 1987A, with a simple $\rho \propto r^{-2}$ CSM during its first few hundred days [Weiler et al., 2007; Staveley-Smith et al., 1993]. A radio shell was first observed 175 days after the explosion using Very Long Baseline Interferometry (VLBI) imaging, with multiple hotspots that shift in orientation through 2,787 days [Bietenholz et al., 2010].

In the SN 1993J disc, an asymmetry in brightness is first seen when the disc appears, in the south-east, but this hotspot appears to shift within a few hundred days and disappear altogether by ∼1,000 days after the supernova explosion [Bietenholz et al., 2003]. This is much faster than what we observe for hotspots in SN 1987A, and may imply greater density disparities in the SN 1993J ejecta than that seen in the ER for SN 1987A. Further, asymmetry has been suggested for the SN 1993J explosion based on optical spectra [Lewis et al., 1994], which may also cause radio hotspots similar to those observed for SN 1987A.

Bietenholz et al. [2001] fit the observed SN 1993J remnant with an optically thin spherical shell model, which they felt was accurate as the radio emission was circular to within 4%. If we compare our R_2/R_1 ratio for a two dimensional model of the emission ring, where we expect a 0.70 ratio based on the inclination of the system, we find that the emission from SN 1987A was more asymmetric during the period when the shockwave was interacting with the ER. This value decreased, however, to 0.74 ± 0.02 in recent observations, meaning that the emission has become more circular over time. This shows that the CSM emitted by the SN 1993J progenitor was more uniform than the complex structure surrounding SN 1987A.

1.5 Conclusions

We have reported our imaging results of SN 1987A at 9 GHz using ATCA, covering a 25-year period from 1992 to 2017. We have also carried out Fourier modeling of the visibilities, with a torus model and ring model used to describe the evolving remnant. Both models have shown the continued expansion of SN 1987A through February 2017, as well as an increasing flux density. Our data are most consistent with a torus model where high latitude emission is present from soon after the shockwave encountered the ER. This is based on the rate of expansion of the remnant, the observed changes in the evolution of the torus radius at Day 7,000 and Day 9,300, and how this data is also coupled with the decrease of the half-opening angle of the remnant during this period. Lower latitude emission then dominates during the later stages as the shockwave continues to plow through the ER. We should note that the radio remnant appears to be larger than the X-ray remnant, although the radio remnant appears to lag 2,000 days after the morphology seen in X-ray data, which may be due to the magnetic fields in the remnant increasing in strength after the shockwave has passed through the medium.

Unlike at other wavelengths, we have not yet seen the western side of the radio remnant become brighter than the eastern side. We have also seen the southeastern side of the SNR begin to fade, which, combined with the similar fading seen in X-ray and optical data, suggests that the shockwave has left at least this region of the ER.

In the future, we expect the western side of the SNR to become the brightest region as the eastern continues to fade, and we also expect a further plateau in radio emission as the shockwave leaves the ER completely. Our observations will also help us understand the structure of material beyond the ER, which is from the progenitor star's stellar wind and about which little is known. Because of its proximity, studies of SN 1987A will also be useful for the comparison to other radio supernovae and their surrounding CSM.

1.6 Acknowledgements

We would like to thank the referee for their helpful comments in the preparation of this manuscript. We thank K. Frank for recent Chandra data. The Australia Telescope Compact Array is part of the Australia Telescope, which is funded by the Commonwealth of Australia for operation as a National Facility managed by CSIRO. The Dunlap Institute is funded through an endowment established by the David Dunlap family and the University of Toronto. B.M.G. acknowledges the support of the Natural Sciences and Engineering Research Council of Canada (NSERC) through grant RGPIN-2015-05948, and of the Canada Research Chairs program.

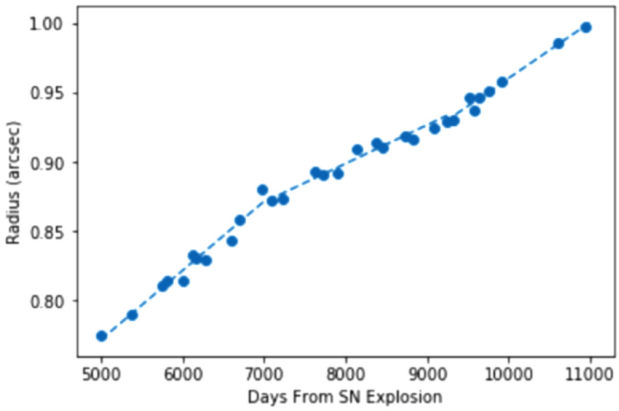

(a) Torus Radii

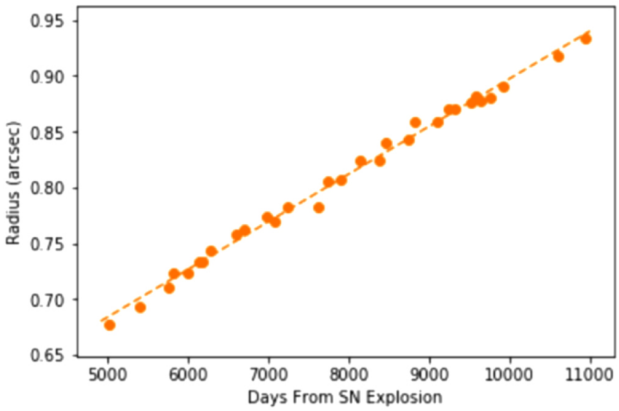

(b) Semi-Major Axis in Ring fit (R_1)

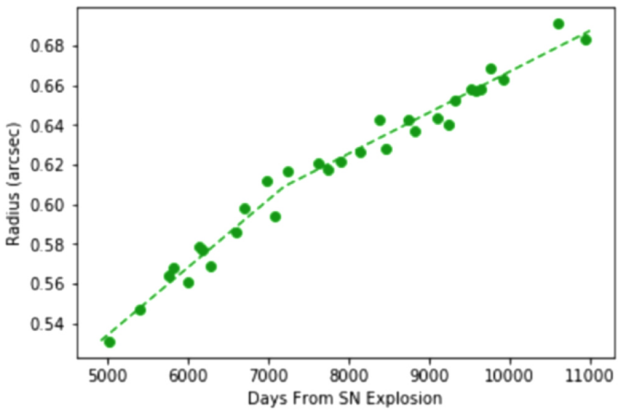

(c) Semi-Minor Axis in Ring (R_2)

Figuur 1.4 A subset of data shown in Figure 1.3 to highlight the difference in fit between the torus radii, R_1, and R_2. Here, we show the multi-linear fit for the torus radius from Day 7,500, and the linear fit to R_1 and R_2 from Day 7,000.

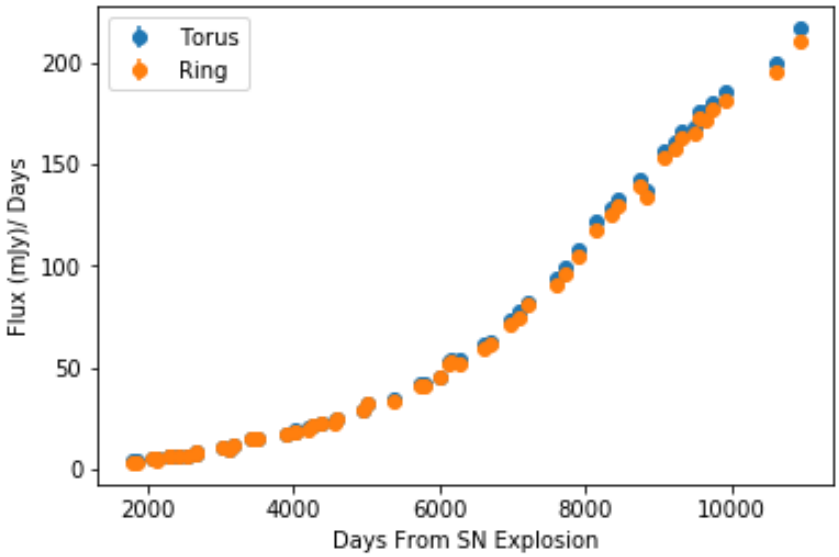

Figuur 1.5 The measured flux densities for the SN 1987A emission region for both the torus and ring models. Note that the errors are included in this plot, but are too small to be visible.

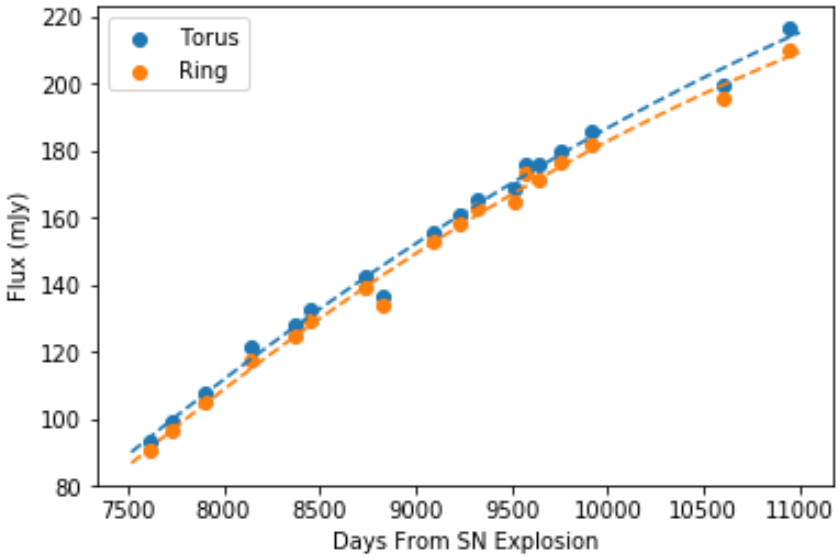

Figuur 1.6 The measured flux densities for the SN 1987A emission region for both the torus and ring models from Day 7,500, along with the exponential fits to the data following Equation 1.1 and Table 1.6.

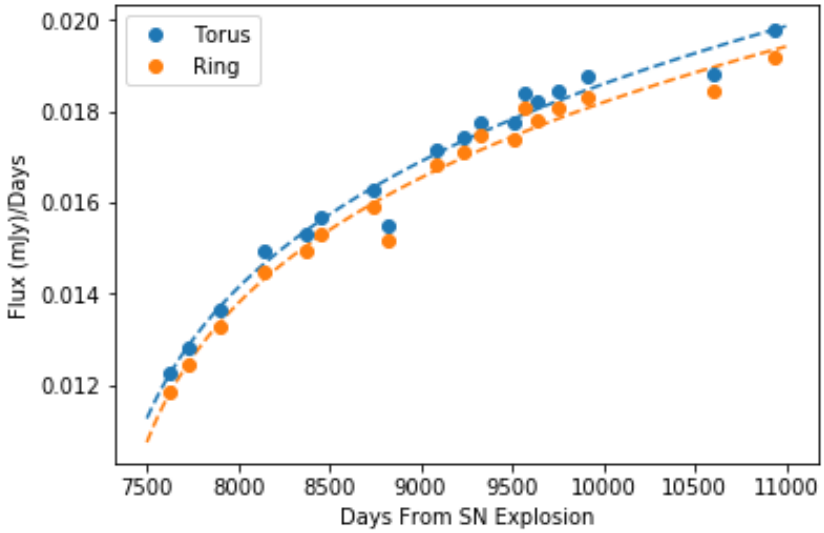

Figuur 1.7 The same plot as Figure 1.6, but with the fluxes divided by the day number. This is done to highlight the fact that the rate of brightening in both models has been growing more slowly with time.

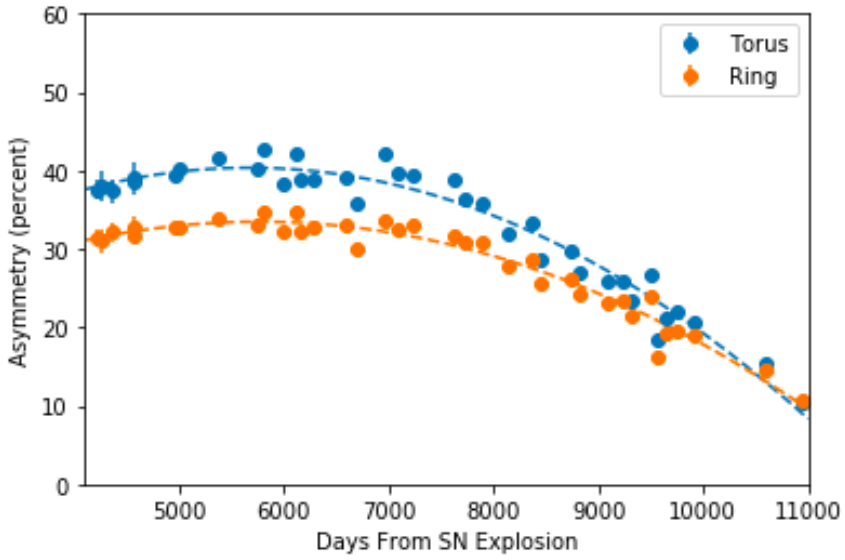

Figuur 1.8 The east-west asymmetry in the SN 1987A emission region for both the torus and ring models, modeled as a linear gradient in emissivity across the the equatorial plane. The parameters for the fits can be found in Table 1.7

.

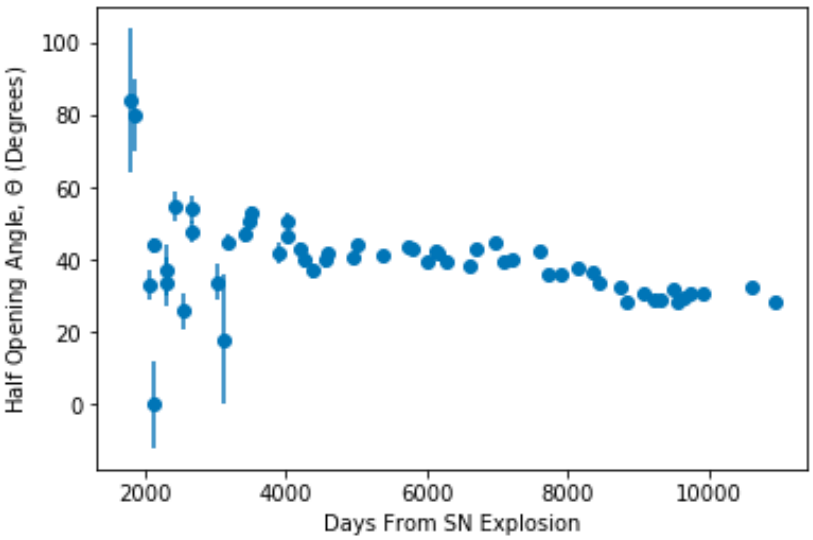

Figuur 1.9 The measured half-opening angle (θ) in the the SN 1987A remnant for the torus model.

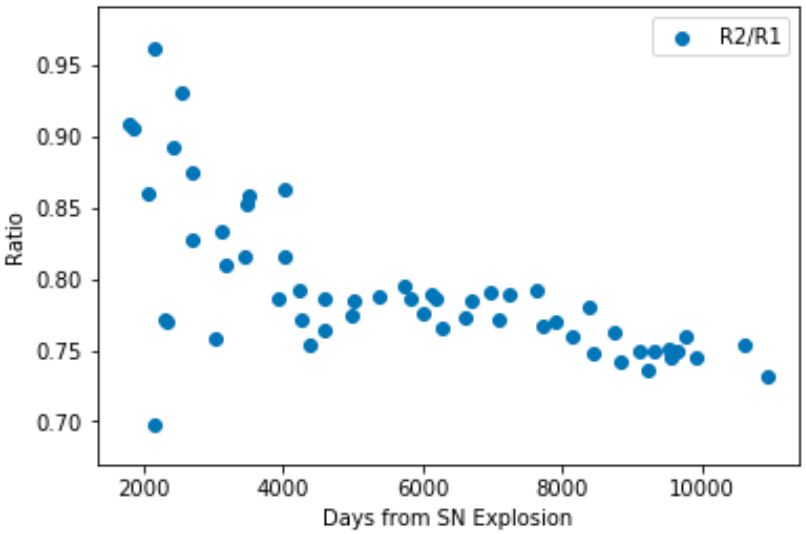

Figuur 1.10 The measured ratio for R_1/R_2 for the ring model. We will note that in this plot the errors are included, but are too small to be visible.

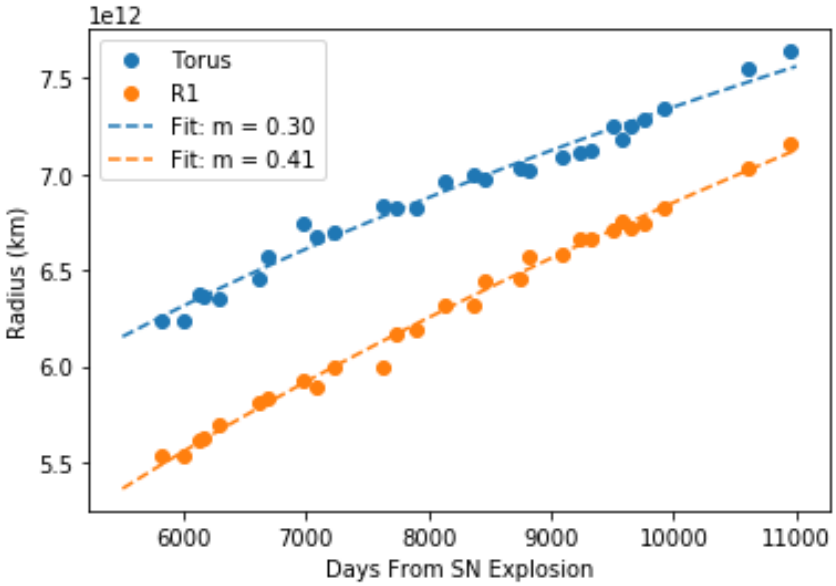

Figuur 1.11 Radius as a function of time during the period when the shockwave was interacting with the ER. We fit the data to $R \propto t^m$, which resulted in a value for m= 0.30 ± 0.01 for the torus model m= 0.41 ± 0.01 for R_1.

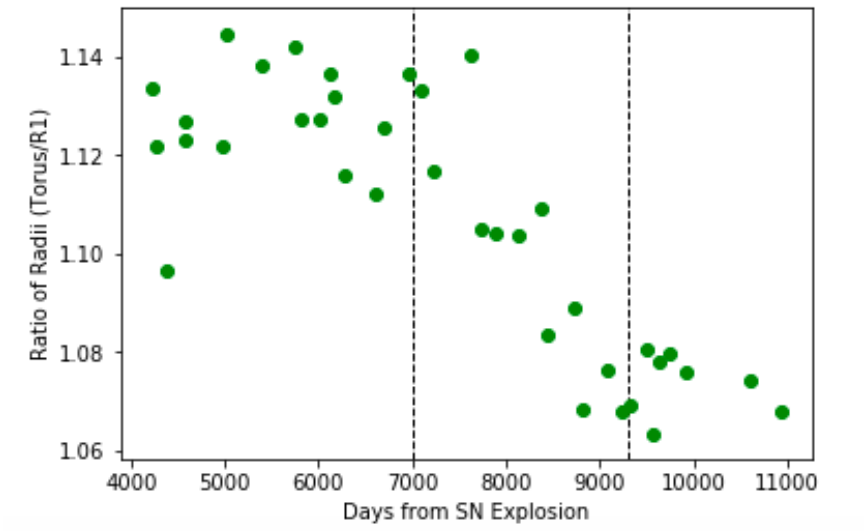

Figuur 1.12 The ratio of the torus radii to R_1 from Day 4,000 to present. The black dashed lines are at the two breaks in velocity detected in the torus radius at Day 7,000 and Day 9,300, respectively.

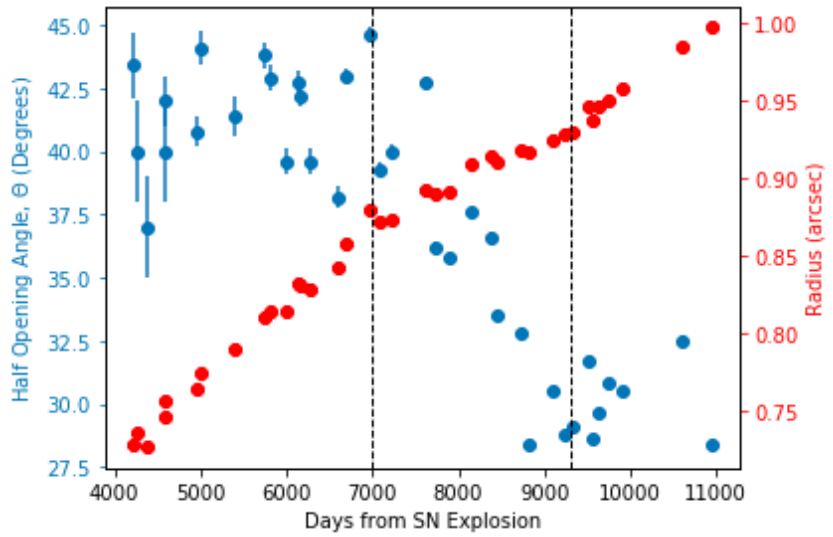

Figuur 1.13 The measured half-opening angle (θ, blue) in the SN 1987A remnant compared with the radii measured in the torus model (red). Black dashed lines are provided for reference at the two changes in expansion seen in the torus radii at Day 7,000 and Day 9,300, respectively.

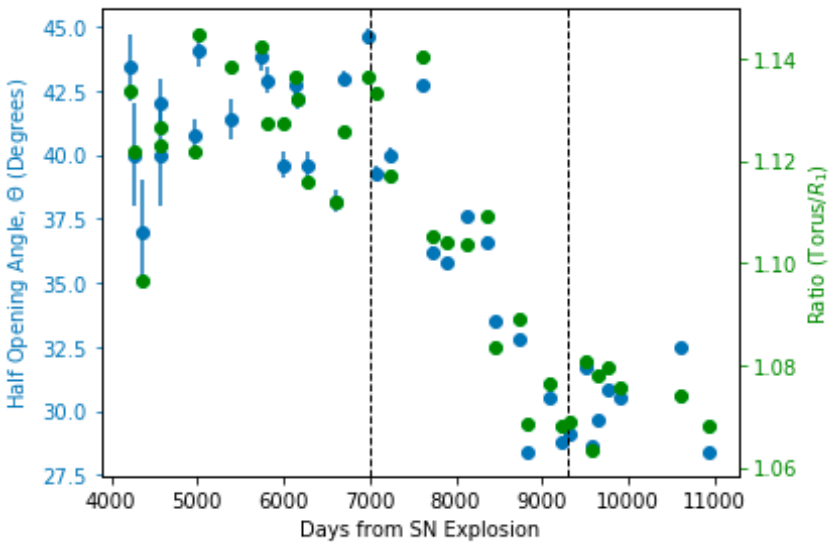

Figuur 1.14 As for Figure 1.13, but with the measured half-opening angle plotted with the ratio between the torus model and R_1 (green).

Hoofdstuk 2

Thirty Years of Very Large Array Observations of Type Ia Supernovae 1972E and 1895B: Constraints on the Presence of Circumstellar Shells

Yvette Cendes, Maria Drout, Laura Chomiuk, Sumit Sarbadhicary

The Astrophysical Journal, in press. [arxiv:2001.03558]

Abstract

We have imaged over 35 years of archival Very Large Array (VLA) observations of the nearby (d_L = 3.15 Mpc) Type Ia supernovae SN 1972E and SN 1895B between 9 and 121 years post-explosion. No radio emission is detected, constraining the 8.5 GHz luminosities of SN 1972E and SN 1895B to be $L_{\nu,8.5GHz} < 6.0 \times 10^{23}$ erg s^{-1} Hz^{-1} 45 years post-explosion and $L_{\nu,8.5GHz} < 8.9 \times 10^{23}$ erg s^{-1} Hz^{-1} 121 years post-explosion, respectively. These limits imply a clean circumstellar medium (CSM), with $n < 0.9$ cm^{-3} out to radii of a few $\times 10^{18}$ cm, if the SN blastwave is expanding into uniform density material. Due to the extensive time coverage of our observations, we also constrain the presence of CSM shells surrounding the progenitor of SN 1972E. We rule out essentially all medium and thick shells with masses of 0.05−0.3 $M_\odot$ at radii between $\sim 10^{17}$ and 10^{18} cm, and thin shells at specific radii with masses down to $\lesssim$0.01 $M_\odot$. These constraints rule out swaths of parameter space for a range of single and double degenerate progenitor scenarios, including recurrent nova, core-degenerate objects, ultra-prompt explosions and white dwarf (WD) mergers with delays of a few hundred years between the onset of merger and explosion. Allowed progenitors include WD-WD systems with a significant ($> 10^4$ years) delay from the last episode of common envelope evolution and single degenerate systems undergoing recurrent

nova—provided that the recurrence timescale is relatively short and the system has been in the nova phase for $\gtrsim 10^4$ years, such that a large ($> 10^{18}$ cm) cavity has been evacuated. Future multi-epoch observations of additional intermediate-aged Type Ia SNe will provide a comprehensive view of the large-scale CSM environments around these explosions.

2.1 Introduction

Type Ia supernovae (SNe) are caused by the explosion of a carbon-oxygen white dwarf [WD; Nomoto, 1982]. They have become an important cornerstone of cosmological distance calculations as "standardizable candles" for measuring the expansion of the universe via their measured luminosity distances as a function of redshift [Reiss et al., 1998 Perlmutter et al., 1999]. However, despite their importance, debates still remain regarding both the progenitor systems and explosion mechanism of Type Ia SNe [Maoz et al., 2014].

There are two broad scenarios in which a carbon-oxygen WD can explode as Type Ia SNe, and both involve binary systems [Hillebrandt & Niemeyer, 2000; Wang, 2018]. The first is the single degenerate (SD) scenario, in which the WD accretes material from a non-degenerate stellar companion [Holmbo et al., 2018]. The second is the double degenerate (DD) scenario, where the secondary companion is also a WD [Maoz et al., 2014; Liu et al., 2018]. The term "double degenerate" is broad and currently encompasses multiple combinations of progenitor binary systems and explosion mechanisms, including direct collisions [Kushnir et al., 2013], mergers [Shen et al., 2012], and double detonations due to accretion from a helium WD companion [Shen et al., 2013; Glasner et al., 2018]. It is also debated whether Type Ia SN can only be produced near the Chandrasekhar Mass (M_{Ch}), or if sub-M_{Ch} WDs can also produce normal Type Ia SNe while undergoing double detonations or violent mergers[Shen et al., 2018]. Some observations show evidence for a population of sub-M_{Ch} explosions [e.g. Scalzo et al., 2019].

One strategy to shed light on these open questions is to search for circumstellar material (CSM) surrounding Type Ia SNe. The CSM is produced by the pre-explosion evolution of binary system—including winds, outbursts and episodes of mass transfer—and can therefore reflect the nature of the SN progenitor. However, for decades searches for CSM around Type Ia SNe in the X-ray and radio have yielded non-detections [Panagia et al., 2006; Hancock et al., 2011; Margutti et al., 2012; Chomiuk et al., 2012; Russell & Immler, 2012; Margutti et al., 2014; Chomiuk et al., 2016], implying low-density environments. Most of these observations were taken within a few hundred days of the SN explosion, constraining the density of the CSM at distances $\lesssim 10^{16}$ cm from the progenitor star. Of these, observations of three nearby events—SN 2011fe, SN 2014J, and SN 2012cg—have constrained the pre-explosion mass-loss rates of the progenitor systems to $\dot{M} < 10^{-9} M_{\odot}$ yr^{-1}, ruling out all but the lowest mass SD systems [Margutti et al., 2012; Chomiuk et al., 2012; Margutti et al., 2014; Chomiuk et al., 2016]. At the same time, larger samples of more distant events systematically rule out winds from more massive or evolved stellar companions [Russell & Immler, 2012; Chomiuk et al., 2016].

In recent years, however, other types of observations have painted a more complex picture of the CSM surrounding Type Ia SNe. First, a new class of SNe (SNe Ia-CSM) spectroscopically

resemble SNe Ia but have strong hydrogen emission lines [Silverman et al., 2013]. This has been interpreted as the SN shockwave interacting with a significant amount of CSM (∼few $M_{\odot}$) located directly around the explosion site (distributed out to radii of $\sim 10^{16}$ cm). SNe Ia-CSM are rare, and the most nearby (SN 2012ca; $d_L \sim 80$ Mpc) is the only Type Ia SN detected in X-rays to date [Bochenek et al., 2018].

Additionally, blue-shifted Na I D absorbing material has been detected in some normal Type Ia SNe spectra, which is interpreted as CSM surrounding the SNe that has been ionized [Patat et al., 2007; Blondin et al., 2009; Sternberg et al., 2011; Maguire et al., 2013]. Modeling has indicated the material is not distributed continuously with radius, but is more likely located in shell-like structures at radii $\geq 10^{17}$ cm [Chugai, 2008]. Such absorbing material is estimated to have a total mass of up to $\sim 1 M_{\odot}$, and is thought to be present in ≥20% of SNe Ia in spiral galaxies [Sternberg et al., 2011]. Most recently, Graham et al. [2019] reported evidence of CSM interaction surrounding SN 2015cp at ∼ 730 days post-explosion, consistent with a CSM shell that contains hydrogen at distances $\geq 10^{16}$ cm, and Kollmeier et al. [2019] reported the detection of Hα in a late-time nebular spectrum of ASASSN-18tb, interpreted as the signature of CSM interaction.

Despite these intriguing results, constraints on the CSM surrounding Type Ia SNe at radii $\gtrsim 10^{17}$cm have been relatively sparse. These distances can be probed by radio observations obtained between ∼5 and 50 years post-explosion. These timescales have typically been neglected because the deepest constraints on the presence of a stellar wind density profile can be made in the first ∼year post-explosion. However, if an uniform density medium is present, deeper limits on CSM would be possible via radio observations at greater times post-SN, as the shockwave continues to interact with the ambient material [Chevalier, 1998]. Additionally, if multiple observations are taken over the course of several years, the presence of CSM shells at a range of radii can be probed.

On even longer time scales (∼100 years) radio observations can yield information on the CSM density and structure as a SN transitions to the SN remnant (SNR) stage. In our own galaxy, young Type Ia SNRs have been observed in radio wavelengths. For example, G1.9+0.3, was first discovered by the Very Large Array (VLA) and is estimated to be between 125 and 140 years old [Reynolds et al., 2008]. Additionally, Kepler's SNR is radio bright ∼400 years after the explosion [DeLaney et al., 2002]. However, whether this emission is due to interaction with CSM ejected by the progenitor system, or the interstellar medium (ISM), is still debated. In contrast, Sarbadhicary et al. [2019] made deep radio images of the SN 1885A area in the Andromeda Galaxy (M31; 0.785 ± 0.025 Mpc distant). The resulting upper limits constrain SN 1885A to be fainter than G1.9+0.3 at a similar timescale of ∼120 years post-explosion, placing strict limits on the density of the ambient medium and the transition to the SNR stage. This appears to favor a sub-M_{Ch} model for the explosion.

While observations of SNe within our Local Group (e.g. SN 1885A) can provide the deepest *individual* limits on the CSM density surrounding the progenitors of Type Ia SNe, the number of Type Ia SNe with ages $\lesssim$100 years is limited. Therefore, in order to build up a statistical sample of intermediate-aged SNe, we must look to galaxies farther afield. In this paper, we have compiled over 30 years of radio observations of NGC 5253 for this purpose. NGC 5253 offers an

ideal example for such studies because (i) it has hosted two Type Ia SNe in the past ∼150 years (SN 1972E and SN 1895B), (ii) it is located at very close proximity (d=3.15 Mpc; Freedman et al. 2001), and (iii) it has been observed with the historic VLA and upgraded Karl G. Jansky VLA multiple times between 1981 and 2016. Such a data set over so many years allows us to probe the density of the CSM out to large radii from the SNe, constrain the presence of CSM shells, and provide insight into various progenitor scenarios for Type Ia SNe.

This paper is structured as follows. In Section 2.2, we summarize information known on SN 1895B and SN 1972E. In Section 3.3.1, we describe 30 years of archival radio observations of these systems. In Section 2.4, we use these observations to place deep limits on the density of a uniform ambient medium and the presence of CSM shells surrounding SN 1972E and SN 1895B at radii between 10^{17} and 10^{18} cm. In Section 4.4, we discuss these results in the context of multiple Type Ia SN progenitor scenarios, and the future of SN 1972E and SN 1895B as they transition to the SNR stage.

2.2 Background: SN 1895B and SN 1972E

Two independent Type Ia SNe, SN 1895B and SN 1972E, occurred within a century of each other in the nearby blue compact dwarf galaxy, NGC 5253. NGC 5253 is located within the M83/Centaurus A Group, and throughout this work we adopt the Cepheid distance of 3.15 Mpc from Freedman et al. [2001][1]. NGC 5253 is currently undergoing a starburst phase with a compact, young star forming region at its center [Monreal-Ibero et al., 2010].

SN 1895B (J2000 Coordinates: RA = 13:39:55.9, Dec = −31:38:31) was discovered by Wilhelmina Fleming on December 12, 1895 from a spectrum plate taken on July 18, 1895 [Pickering, 1895]. Throughout this manuscript, we adopt the discovery date as the explosion epoch for our analysis, although the explosion likely occurred some days earlier. Three direct image plates and one spectrum plate taken within the first five months of the SN are available. Re-analysis of these plates with a scanning microdensiometer have resulted in a light curve that is consistent with a normal Type Ia SN ∼15 days after maximum light [Schaefer, 1995]. From this analysis, it is estimated that SN 1895B peaked at a visual magnitude of $< 8.49 \pm 0.03$ mag.

Significantly more information is available for SN 1972E, which was the second-brightest SN of the 20th century. Discovered on May 13, 1972 (J2000 coordinates: RA = 13:39:52.7, Dec = −31:40:09), SN 1972E was identified just prior to maximum light, peaked at a visual of 8.5 mag and was observed for 700 days after initial discovery [Kirshner & Oke, 1975; Ardeberg & de Groot, 1973; Bolton et al., 1974]. As with SN 1895B, we adopt the discovery date as the explosion date for the analysis below[2]. The exquisite late-time coverage of SN 1972E at optical wavebands played a key role in our understanding of the link between Type Ia SNe and nucleosynthesis [Trimble, 1982] as it was shown that the energy deposition during the optical-thin phase was consistent with the radioactive decay of ^{56}Ni and ^{56}Co [Axelrod, 1980]. SN 1972E is now considered an archetype for Type Ia SN, and was one of the events used to define the spectroscopic features of "Branch normal" events [Branch, 1993].

[1]This distance includes a metallicity correction factor.

[2]We note that differences of ∼1 month in adopted explosion epoch will not influence our results, as our observations take place tens to 100 years after the explosion.

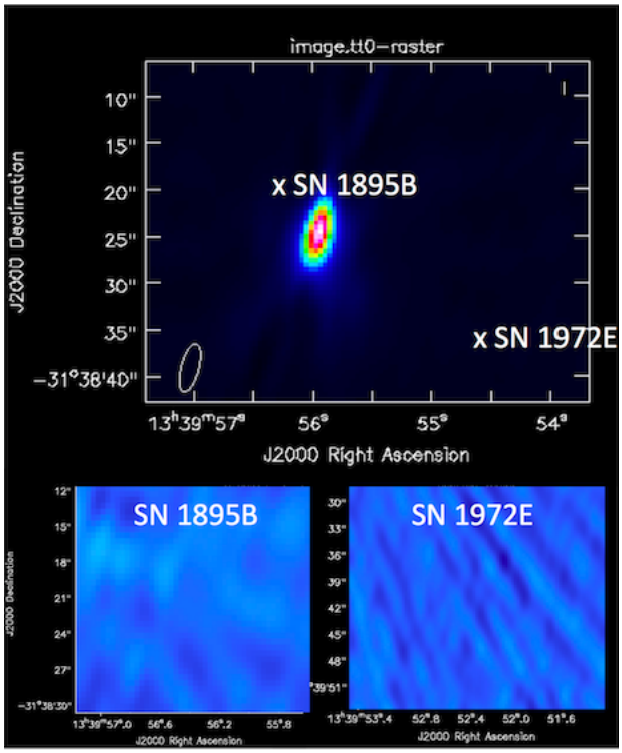

Figuur 2.1 *Top:* Radio image of NGC 5253 from a December 2016 VLA observation at 8.35 GHz, with the positions SN 1972E and SN 1895B marked. The bright central radio source in NGC 5253 is a compact star forming region in the galaxy core [Monreal-Ibero et al., 2010]. The synthesized beam is drawn as an ellipse in the lower left corner. *Bottom:* Close-ups of the regions surrounding each SN.

After the initial optical light faded, neither SN 1895B nor SN 1972E has been detected at any wavelength. Observations of NGC 5253 with the *Chandra* X-ray observatory yielded non-detections at the locations of both SNe [Summers et al., 2004]. In the radio, two upper limits for the SNe have been published to date, which are listed in the electronic journal article for this chapter. Cowan & Branch [1982] observed both SN 1895B and SN 1972E with the VLA for 3 hours at 1.45 GHz in April 1981. They report non-detections with upper limits of 0.9 mJy for both SNe. Subsequently, Eck et al. [2002], reported upper limits on the radio flux from both SNe of 0.15 mJy based on 9.1 hours of VLA data obtained in November 1984, also at 1.45 GHz. Modeling these limits assuming a CSM with a $\rho \propto r^{-2}$ density profile, Eck et al. [2002] find upper limits on mass-loss rates of the progenitor systems of SN 1972E and SN 1895B of $< 8.60 \times 10^{-6}$ $M_\odot$ yr^{-1} and $< 7.2 \times 10^{-5}$ $M_\odot$ yr^{-1}, respectively. These mass-loss rate estimates, which assumed wind speeds of 10 km s^{-1}, are not strongly constraining in the context of Type Ia SN progenitors, ruling out only a few specific Galactic symbiotic systems [Seaquist & Taylor, 1990].

These two SNe are worthy of further study at radio wavelengths for several reasons. First, at 3.15 Mpc, SN 1972E and SN 1895B are among the closest known extragalactic SNe. Second, while radio observations of SNe years after explosion are generally not constraining in the content of a $\rho \propto r^{-2}$ wind environments, even comparatively shallow limits can provide useful constraints on the presence of a constant density CSM [Sarbadhicary et al., 2019] and low-density CSM shells [Harris et al., 2016]—physical models that were not considered in the analysis of Eck et al. [2002]. Third, NGC 5253 has been observed multiple times by the VLA since 1984, and these observations are currently in the VLA archive. This gives us the unique opportunity of being able to set limits at multiple epochs for two SNe, as the shockwave has traversed a wide range of radii—and potentially, CSM environments.

2.3 Observations and Data Reduction

2.3.1 VLA Observations

For our study, we examined all archival VLA observations of the galaxy NGC 5253. While over 85 observations of NGC 5253 have been obtained since 1979, the location of SN 1972E [approximately 56"west and 85"south of the nucleus of NGC 5253 Jarrett, 1973] is too far to be visible in higher frequency images centered on the galaxy core. As a result, we initially restrict ourselves to 24 observations that contain either SN 1895B or SN 1972E within their primary beam, and occurred in C and X bands (4-12 GHz).

Subsequently, we further restrict ourselves to observations that can provide constraints on constant density CSM surrounding the SNe, as described by the model outlined in Section 2.4.2.1. In particular, while a higher density CSM will lead to brighter overall radio emission, it will also cause the SN to enter the Sedov-Taylor phase (and therefore fade at radio wavelengths) at an earlier epoch. Thus, in the context of this physical model, there is a maximum radio luminosity that can be achieved at a given time post-explosion. This translates to a minimum image sensitivity that must be achieved for a given intermediate-aged SN. For the cases of SN 1972E and SN 1895B, we find that we require radio images with RMS noise less than 85 mJy/beam. After performing a number tests with historical VLA data of NGC 5253, we find that observations with

total on-source integration times less than 20 minutes do not meet this threshold. After applying these cuts, we are left with two historical (pre-2010) VLA observations in addition to the observations published in Cowan & Branch [1982] and Eck et al. [2002], and three observations taken with the upgraded Karl G. Jansky VLA (post-2012).

The information for each observation including date, project code, exposure time, configuration, frequency, and band are shown in Table 1 in the electronic journal version of the article. Overall, these observations provide constraints on the radio luminosity from SN 1972E and SN 1895B between 9−44 years and 86−121 years post-SN, respectively.

2.3.2 Data Reduction and Imaging

All VLA data were analyzed with the Common Astronomy Software Applications (CASA; McMullin et al. 2007). For the 2012 and 2016 data, taken with the ungraded VLA, CASA tasks were accessed through the python-based `pwkit` package[3] [Williams et al., 2017], while historical data was reduced manually. We flagged for RFI using the automatic AOFlagger [Offringa et al., 2012]. After calibration, we imaged the total intensity component (Stokes I) of the source visibilities, setting the cell size so there would be 4−5 pixels across the width of the beam. All data was imaged using the CLEAN algorithm [Cornwell, 2008], and for post-2010 data we utilize mfsclean [Rau, 2011] with nterms = 2. Due to the large distance of SN 1972E from the galaxy center (and thus image pointing) we also image using the w-projection with wprojplanes = 128. Finally, images were produced setting robust to 0 and for all observations, we used the flux scaling as defined by Perley & Butler [2017].

For all observations, the center of the radio image is dominated by the bright central radio source in NGC 5253 located at RA = 13h39m55.96s and Dec. = $-31°38'24.5''$ (J2000; Beck et al. 1996). An example images can be seen in Figure 2.1, with the positions of SN 1972E and SN 1895 marked for reference.

2.3.3 Flux Limits

We did not detect radio emission at the location of either SN 1895B or SN 1972E in any of our images. To obtain flux upper limits, we measured the RMS noise at the locations of the SNe using the `imtool` program within the `pwkit` package [Williams et al., 2017]. These values are listed in Table 2 in the electronic journal version of this chapter. Throughout this manuscript, we will assume 3σ upper limits radio flux from SN 1972E and SN 1895B. In general, the upper limits obtained on the flux from SN 1972E were a factor of ∼2−3 deeper than for SN 1895B. This primarily due to that fact that SN 1895B occurred significantly closer to the radio-bright center of the galaxy (see Figure 2.1). The deepest individual flux limits for both SNe were provided by the December 2016 observation, with 3σ upper limits of $F_\nu < 51$ μJy/beam and $F_\nu < 75$ μJy/beam for SN 1972E and SN 1895B, respectively.

[3]available at: https://github.com/pkgw/pwkit

2.4 Results

2.4.1 Radio Luminosity Limits: Comparison to Previously Observed SNe and SNRs

Upper limits on the radio luminosity to each SNe, computed using a distance of 3.15 Mpc to NGC 5253, are listed in Table 2 in the electronic journal version of this chapter. We find limits ranging from $\lesssim 3 \times 10^{25}$ erg s^{-1} Hz^{-1} in 1981 to $\lesssim 6 \times 10^{23}$ erg s^{-1} Hz^{-1} in 2016. These limits are shown in Figure 2.2, along with observations of previously observed SNe and SNRs for comparison. Each SN or SNR is plotted in a different color, while symbols indicate the frequency of each observation. Upper limits are designated by black arrows.

Figure 2.2 demonstrates the unique timescales and luminosities probed by SN 1972E and SN 1895B. In one of the most thorough reviews of radio emission from Type Ia SNe to date Chomiuk et al. [2016] provided observations of 85 Type Ia SNe within 1 year post-explosion. The deepest limits cited in Chomiuk et al. [2016] correspond to luminosities of $\sim 3{-}6 \times 10^{23}$ erg/s/Hz for SN 2014J between 84 and 146 days post-explosion, and $\sim 4{-}6 \times 10^{24}$ erg/s/Hz for SN 2012cg between 43 and 216 days post-explosion. These are comparable to the limits obtained for SN 1972E and SN 1895B, but at a significantly shorter time post-explosion. In Figure 2.2, we plot the Type Ia SNe with the deepest luminosity limits obtained between 3 months and 1 year post-explosion [Chomiuk et al., 2016; Panagia et al., 2006].

While observations of SNe and SNRs within the Milky Way and other Local Group galaxies can provide deeper constraints on the radio luminosity from Type Ia SNe, such observations have typically been obtained at longer timescales post-explosion. This is demonstrated in Figure 2.2, where we also plot a radio upper limit for SN 1885A in M31 and observed radio luminosities for the Galactic SNRs G1.9+0.3, Tycho, and Kepler, all associated with events of thermonuclear origin [Reynolds et al., 2008].

By co-adding VLA observations in the 4-8 GHz frequency range, Sarbadhicary et al. [2019] produced a deep radio image with RMS noise of 1.3 μJy/ beam at the location of SN 1885A in M31. Some radio emission with 2.6σ confidence is also present, but the association with SN 1885A for this emission is uncertain due to the large amount of diffuse radio emission in the central regions of M31 where the SN is located. The resulting luminosity upper limit of 8.5×10^{21} erg s^{-1} Hz^{-1} at 127 years post-explosion is approximately two orders of magnitude deeper and at timescales just beyond those probed by SN 1895B. In comparison, the Galactic SNR G1.9+0.3 was detected at 1.4 GHz with a flux of 0.74 $\pm$ 0.04 Jy in 1993 [Condon et al., 1998], and 0.935 $\pm$ 0.047 Jy in 2008 [Green et al., 2008], corresponding to ages of $\sim$125$-$140 years post-explosion [Reynolds et al., 2008; Green et al., 2008]. Based on a high absorbing column density in observed X-ray observations, Reynolds et al. [2008] place the distance to G1.9+0.3 to be $\sim$8.5 kpc, with corresponding radio luminosities of $\sim 10^{23}$ erg/s/Hz. Finally, the Catalog of Galactic Supernova Remnants [Green, 2014], lists 1 GHz fluxes of 56 Jy and 19 Jy for Tycho's SNR and Kepler's SNR, respectively. At estimated distances of 2.8 kpc [Kozlova & Blinnikov, 2018] and 6.4 kpc [Reynoso & Goss, 1999], respectively, these translate to radio luminosities of $\sim 5 \times 10^{23}$ erg/s/Hz. However, we emphasize that these SNe are over 400 years old, and have transitioned to the SNR phase.

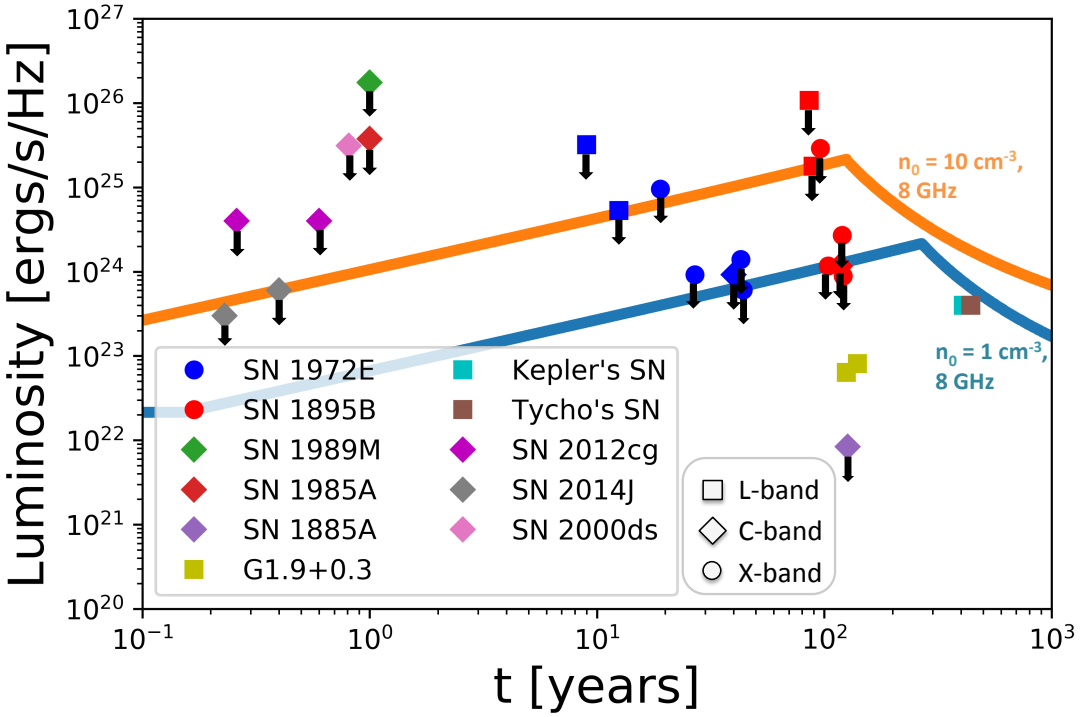

Figuur 2.2 Radio luminosity upper limits for the intermediate-aged Type Ia SN 1972E (blue) and SN 1895B (red) spanning three decades using data from this work. Also shown, for comparison, are observed radio luminosities and luminosity upper limits (black arrows) for Galactic SNRs and other extagalactic Type Ia SNe for a range of times post-SN [Chomiuk et al., 2016; Sarbadhicary et al., 2019; Green, 2014; Condon et al., 1998]. We have distinguished the different observed frequency bands present in this data set as different symbols: squares correspond to L-band (1-2 GHz), diamonds to C-band (4-8 GHz), and circles to X-band (8-12 GHz) observations. For illustrative purposes, we have included solid lines to represent two potential model radio light curves expected for a SN blast wave expanding into a uniform medium with a density of 1 cm^{-3} (blue) and 10 cm^{-3} (orange), assuming our baseline S17 model described in Section 2.4.2.1. See Table 2 in the electronic journal version of this chapter for the precise density limits that can be derived from each point.

Given that the observed luminosities of these Galactic intermediate-aged Type Ia SNe/SNRs are below the luminosity upper limits obtained for SN 1972E and SN 1895B, we also calculate the flux densities that they would be observed with at the distance of NGC 5253. We find that the observed flux densities of G1.9+0.3-like, Kepler-like, and Tycho-like SNRs would be $\sim$2 μJy, $\sim$15 μJy, and $\sim$ 26 μJy in NGC 5253, respectively. These flux levels for Kepler's and Tycho's SNR are within the sensativity limits that can be achieved through dedicated JVLA observations, and the implications for the future evolution of SN 1972E and SN 1895B are discussed in Section 4.4, below.

2.4.2 Constraints on a Uniform Density CSM

The radio emission from a SN expanding into a relatively low density medium is described by a synchrotron spectrum. As the shockwave expands into the CSM, electrons are accelerated to relativistic speeds and interact with shock-amplified magnetic fields [Chevalier, 1982a; Chevalier & Fransson, 2006]. Here, we use a quantitative model for the radio luminosity from a SN blast wave expanding into a constant density CSM and our luminosity upper limits to place constraints on the density of the media surrounding the progenitors SN 1972E and SN 1895B.

2.4.2.1 Radio Light Curve Model

We adopt the radio luminosity model outlined in Sarbadhicary et al. [2017, S17 hereafter, see their Appendix A], based on the radio synchrotron formalism of Chevalier [1998]. This model self consistently treats the evolution of the SN from early (ejecta dominated) to late (Sedov-Taylor) phases, and is therefore ideal for the intermediate-aged SNe considered here. While we refer the reader to S17 for a complete model description, we summarize salient features here.

The luminosity of the radio emission from a Type Ia SN will depend on the density profiles of the outer SN ejecta and CSM, the ejecta mass (M_{ej}) and kinetic energy (E_K) of the SN explosion, the power spectrum of the relativistically accelerated electrons, and the fraction of post-shock energy contained in amplified magnetic fields and relativistic electrons (ϵ_B and ϵ_e, respectively). S17 use standard model assumptions in many cases: adopting a power-law density profile with a "core-envelope" structure for the SN ejecta as defined by Truelove & McKee [1999] with $\rho \propto v^{-n}$ and $n = 10$ in the outer ejecta [Matzner & McKee, 1999], a constant density CSM, and a distribution of relativistic electrons of the form $N(E) \propto E^{-p}$. However, S17 deviate from standard assumptions in their treatment of the magnetic field amplification.

In most analytic models of SN radio light curves, ϵ_e and ϵ_B are free parameters, assumed to be constant. This is generally considered to be one of the most significant uncertainties in converting observed radio luminosities to CSM densities [Horesh et al., 2012, 2013]. In contrast, S17 develop a new parameterization for ϵ_b, as a scaling of the Alfven Mach number of the shock and the cosmic ray acceleration efficiency, based on the results of numerical simulations of particle acceleration [Caprioli & Spitkovsky, 2014]. ϵ_B is therefore determined as a function of time and equipartition is not assumed. As a result, the models of S17 contain five free parameters: p, ϵ_e, M_{ej}, and E_K, and n_0 (the density of the CSM).

Given their ages and the analytic models for SN blast wave dynamics of Truelove & McKee [1999], SN 1972E and SN 1895B should still be in the free-expansion (ejecta-dominated) phase during the VLA observations described above. During this phase, the radius and velocity of the forward shock can be described by:

$$R_s = (1.29 \text{ pc})\ t_2^{0.7}\ E_{51}^{0.35}\ n_0^{-0.1}\ M_{ej}^{-0.25} \tag{2.1}$$

and

$$v_s = (8797 \text{ km/s})\ t_2^{-0.3}\ E_{51}^{0.35}\ n_0^{-0.1}\ M_{ej}^{-0.25} \tag{2.2}$$

where $t_2 = t/(100 \text{ yrs})$, is the time post-explosion, $E_{51} = E/(10^{51} \text{ ergs})$ is the kinetic energy of explosion, $M_{ej} = M/(1\ M_\odot)$ is the ejecta mass, and n_0 is the ambient medium density in units of 1 cm^{-3}.

Using these relations, and equations A1-A11 in S17, we can then calculate the radio luminosity of a Type Ia SN interacting with a uniform density CSM under the assumption that the resulting synchrotron emission is optically thin and the forward shock will dominate the radio luminosity. These assumptions hold for the low density ambient media we consider here.

In Figure 2.2 we plot example S17 light curves for two CSM densities (1 and 10 cm^{-3}), assuming a fiducial "baseline" model with $M_{ej} = 1.4$ $M_\odot$, $E_K = 10^{51}$ erg, $p = 3$, and $\epsilon_e = 0.1$. The latter two values are widely adopted in the literature and are motivated by radio observations of SNe and gamma-ray bursts [Chevalier & Fransson, 2006]. However, we emphasize that both p and ϵ_e may vary based on the source population and ϵ_e, in particular, is subject to significant uncertainty. Observations of young SNRs, such as Tycho, are consistent with a very small ϵ_e ($\lesssim 10^{-4}$; Morlino, 2012; Berezhko, 2006; Berezhko, 2009), while the luminosity function of older SNRs in local galaxies requires an intermediate value ($\epsilon_e \approx 10^{-3}$; S17). Similarly, while young radio SNe are often consistent with $p = 3$ [Chevalier & Fransson, 2006], the spectral index of young SNRs is usually in the range of $p = 2.0 - 2.4$ [Dubner 2005]. We have chosen our baseline values for p and ϵ_e both because SN 1972E and SN 1895B should still be in the ejecta-dominated phase, and to allow for direct comparison to the observational results of Chomiuk et al. [2016] and the hydrodynamic models of SN-CSM shell interaction described in Section 2.4.3. Effects of varying these parameters will be examined below.

From the baseline S17 models presented in Figure 2.2 it is clear the predicted radio luminosity increases steadily during the free-expansion phase—over a timescale of centuries—thus allowing later observations to place deeper constraints on the density of the ambient medium. This is in sharp contrast to a $\rho \propto r^{-2}$ wind environment, where the predicted radio luminosity fades with time as a result of the decreasing density [see, e.g. Chomiuk et al., 2016]. In the uniform CSM scenario, the radio light curve peaks a few hundred years after SN, around the Sedov time, and subsequently the radio luminosity declines throughout the Sedov-Taylor phase (S17).

2.4.2.2 Limits on Uniform Density CSM

We have applied the radio model of S17 to the luminosity upper limits derived for SN 1972E and SN 1895B (Section 2.3.3; Figure 2.2) in order to place limits on the density of any uniform medium surrounding the SNe. In Table 2 in the electronic journal version of this chapter we list the density upper limits that result when assuming our baseline model described above ($M_{ej} = 1.4$ $M_\odot$, $E_K = 10^{51}$ erg, $p = 3$, and $\epsilon_e = 0.1$). For each point, we run a large grid of S17 models and the quoted density upper limit corresponds to the curve which goes directly through the 3σ luminosity limit plotted in Figure 2.2). These density upper limits, which were computed assuming a mean molecular weight of 1.4, range from $\sim$1 to $\sim$15 cm^{-3}, depending on the epoch, frequency, and sensitivity of the observation.

In the top panel of Figure 2.3, we plot example 8 GHz light curves for this baseline model at a range of CSM densities, along with the X-band (8-10 GHz) upper limits for SN 1972E and SN 1895B. For both SNe, our deepest constraints on the density of the ambient medium come from the Dec. 2016 observations, due to a combination of their deeper sensitivity and longer time post-explosion. Assuming our baseline model, these limits correspond to $n_0 \lesssim 0.8$ cm^{-3} for SN 1895B, and $n_0 \lesssim 0.9$ cm^{-3} for SN 1972E. In Figure 2.4 we plot these density limits in comparison

to those for SN 1885A, SNR G1.9+0.3, and the ∼200 observations of 85 extra-galactic Type Ia SN from Chomiuk et al. [2016]. For SN 1885A and G1.9+0.3 we have taken the observed luminosities from Sarbadhicary et al. [2019] and computed new density limits assuming our baseline model, as Sarbadhicary et al. [2019] adopted significantly different values of p=2.2 and $\epsilon_e = 10^{-4}$. Given both the small distance to NGC 5253 and the fact that the radio luminosity of a SN expanding into a uniform density CSM will continue to increase over time, we are able to place limits on the CSM density surrounding SN 1972E and SN 1895B that are several orders of magnitude lower than the bulk of the population presented in Chomiuk et al. [2016].

In Figure 2.3, we also examine the influence on our derived density upper limits if we deviate from our baseline model described above. In the middle panel we plot the 8 GHz light curves that result if we consider an ejecta mass of $M_{ej} = 0.8\ M_{\odot}$, representative of sub-M_{ch} explosions [e.g., Sim et al., 2012]. For these parameters, our best ambient density constraints correspond to $n_0 < 0.38$ cm^{-3} (SN 1972E) and $n_0 < 0.31$ cm^{-3} (SN 1895B). Overall, assuming a sub-M_{ch} explosion yields upper limits on the CSM density that are a factor of ∼2.5 more constraining (assuming $E_{\rm K} =$ is held fixed at 10^{51} erg). Finally, in the lower panel of Figure 2.3 we highlight the influence of varying the adopted value for ϵ_e. Lowering the value of ϵ_e by a factor of 10 will yield a predicted luminosity for a given density that is a factor of 10 fainter, and a density constraint for a given luminosity upper limit that is a factor of ∼7 weaker (for $p = 3$). If we adopt $\epsilon_e = 10^{-4}$ and p = 2.2 as assumed by Sarbadhicary et al. [2019] when modeling SN 1885A (based on values consistent with young SNRs), our best ambient density constraints become ∼17 cm^{-3} (SN 1972E) and ∼16 cm^{-3} (SN 1895B). In this case, the impact of a lower adopted p value partially cancels the effect of a dramatically lower ϵ_e.

The uniqueness of a data set spanning two decades also allows us to place constraints on the density of the CSM as a function of radius from the progenitor star. In Figure 2.5 we plot the uniform density CSM limits obtained for each SN 1972E and SN 1895B observation, assuming our baseline S17 model. On the top axis we also provide the radius probed as a function of time, assuming a constant CSM density of 1 cm^{-3}. We note that the exact radius probed by each point will vary depending on the density of the CSM (see Equation 2.1). These densities and radii are similar to those observed in several known CSM shells. For illustrative purposes, we have provided a simple density profile for two such examples: the inner ring of SN 1987A, and the planetary nebula Abell 39. These density profiles should be associated with the top axis of Figure 2.5, which lists the radius from the SN progenitor star.

The radius and density of for inner ring of SN 1987A are obtained from Mattila et al. [2010b], who provide both upper and lower limits on the ring density (plotted as dashed and dotted orange lines, respectively). For the planetary nebula Abell 39, the radius and density of the shell were obtained via spectroscopic analysis from Jacoby et al. [2001]. We chose Abell 39 because it is the simplest possible planetary nebula: a one-dimensional projected shell that is used as a benchmark for numerical modeling of these structures [Jacoby et al., 2001; Danehkar et al., 2012]. In the case of Abell 39, the shell has a radius of 0.78 pc, a thickness of 0.10 pc, and a density of 30 cm^{-3} [Jacoby et al., 2001]. We have plotted a simple step function where the density is 2 cm^{-3} outside of the shell, consistent with the number density observed within the shell [Toalá & Arthur, 2016]. This illustrative comparison highlights that even the less sensitive luminosity limits obtained for

SN 1972E and SN 1895B are useful in constraining the presence of CSM shells. We consider a more detailed model for the radio emission from a SN interacting with CSM shells below.

2.4.3 Constraints on the Presence of CSM Shells

In addition to placing deep limits on the density of uniform CSM, the multi-epoch nature of our radio observations allow us to investigate the possibility of shells of CSM surrounding the progenitors of SN 1972E and SN 1895B. Here we outline a parameterized radio light curve model for SN ejecta interacting with spherical shells of finite extent, the applicability of these models to the regimes probed by our observations of SN 1972E and SN 1895B, and the types of shells that can be ruled out for these systems.

2.4.3.1 Radio Light Curve Model: Shell Interaction

To constrain the presence of CSM shells surrounding the progenitors of SN 1972E and SN 1895B we use the parameterized light curve models of Harris et al. [2016] (H16, hereafter). H16 model the interaction of expanding SN ejecta with a CSM shell of constant density using the Lagrangian hydrodynamics code of Roth & Kasen [2015] and compute radio synchrotron light curves based on the gas property outputs of these simulations. While these models can be run for a wide variety of ejecta and CSM configurations, for ease of parameterization, H16 also produced a set of fiducial models for a $M_{ej} = M_{Ch} = 1.38\ M_{\odot}$ and $E_K = 10^{51}$ erg Type Ia SN, with a physical set-up that is based off of the self-similar formalism of Chevalier [1982a].

Specifically, for this fiducial model set, H16 adopt power law density profiles for both the SN ejecta and CSM, and set the initial conditions of the simulations such that the initial contact discontinuity radius equals the contact discontinuity radius at the time of impact from Chevalier [1982a]. Following Chevalier & Fransson [1994] and Kasen [2010], the SN ejecta is defined by a broken power law with shallow and steep density profiles ($\rho \propto r^{-1}$ vs. $\rho \propto r^{-10}$) for material interior and beyond a transition velocity, v_t, respectively. The CSM is defined as a shell with a finite fixed width, ΔR, and constant density, n.

In constructing radio synchrotron light curves from the outputs of this fiducial set of models H16 assume that $\epsilon_e = \epsilon_B = 0.1$ and that that the accelerated electrons possess a power-law structure with respect to their Lorentz factor, γ, of the form $n(\gamma) \propto \gamma^{-p}$ with $p = 3$. It is also assumed that the radio emission is dominated by the forward shock and that the resulting emission is optically thin to synchrotron self-absorption, assumptions that were shown to be valid for their model set.

With these assumptions, H16 find a "family" of resulting radio synchrotron light curves that can be defined by three key parameters:

r_1: the inner radius of the CSM shell.

n: the density of the CSM shell.

f: the fractional width of the CSM shell ($\Delta R/r_1$).

H16 provide analytic expressions describing radio light curves as a function of these three parameters.

In Figure 2.6 we plot the resulting radio light curves (lower panels) for various CSM shells (top panels) as each of r_1, n, and f are varied individually. Also shown, for context, are the luminosity upper limits measured for SN 1972E and the radio light curve for a 0.1 cm^{-3} constant density CSM from S17. Overall, the resulting radio light curves are strongly peaked in time, with a rapid decline occurring once the forward shock reaches the outer radius of the CSM shell. For a constant shell density and fractional width (left panels), adjusting the inner radius of the shell will primarily influence the time of impact and therefore the onset of radio emission. Adjusting the density of the CSM shell (center panels) will primarily influence the peak luminosity of the resulting radio emission—although the onset of radio emission will also be delayed slightly for higher density shells (see below). Finally, increasing the fractional width of the shell (right panels) will increase both the overall timescale and peak luminosity of the resulting radio signature as the interaction continues for a longer time period. Thus, a given observed data point will constrain the presence of a thick shell over a larger range of r_1, compared to thin shells with similar densities.

2.4.3.2 Applicability to SN 1972E and SN 1895B

H16 first developed and applied their fiducial models to investigate the case of low-density CSM shells located at radii $\lesssim$ a few $\times 10^{16}$ cm, whose presence would manifest in radio light curves within the first $\sim$1 year post-explosion. We now examine whether the assumptions made in H16 are applicable for CSM shells that would manifest at the timescales of the observations of SN 1972E and SN 1895B described above.

The main assumption that may be violated for the case of shells at the radii probed by the observations of SN 1972E and SN 1895B is that the CSM impacts the *outer* portion of the SN ejecta, which has a steep density profile. For this to hold true, first the total mass swept up by the SN shock prior to impacting the shell should not approach the mass in the outer SN ejecta. For the broken power-law ejecta profile adopted in H16, $\sim$2/9 of the SN ejecta mass is located in the outer ejecta, corresponding to $\sim$0.3 M$_\odot$ for a Chandrasekhar mass explosion. H16 assume that the shell occurs essentially in a vacuum. If we instead assume a low density medium interior to the shell of $<$0.1 cm^{-3} [e.g. Badenes et al., 2007] we find that that mass of the internal material swept up should be $\lesssim$0.002 M$_\odot$ for the shell radii probed by the observations of SN 1972E.

Thus, the CSM shell density and radius are the primary determinants of whether the interaction is with the outer SN ejecta. In setting the initial conditions of their simulations, H16 assume that the "impact", and hence the beginning of the radio light curve, occurs when the ratio of the CSM and SN ejecta density at the contact discontinuity reaches a specific value ($\rho_{\rm CSM} = 0.33\,\rho_{\rm ej}$). This requirement is the cause of the shift in radio emission onset time when considering shells of various densities at a fixed radius. For denser shells, the H16 impact will occur when a slightly denser—more slowly moving—portion of the SN ejecta reaches r_1. Thus, at every radius, there is a density that corresponds to $0.33\,\rho_{\rm ej,vt}$ where $\rho_{\rm ej,vt}$ is the density of the ejecta at the transition velocity, v_t, between the outer and inner density profiles. This is the maximum density of a CSM shell at this radius that does not violate the model assumption that the impact occurs in the outer portion of the SN ejecta. Because the density of the expanding SN ejecta decreases with time, as we consider shells at larger and larger radii, this model assumption will break down for lower and lower densities.

Assuming CSM shells with fractional widths between 0.1 and 1.0, we find that the observations of SN 1972E and SN 1895B will probe CSM shells with inner radii ranging between $[1-15] \times 10^{17}$ cm and $[1.5-4.0] \times 10^{18}$ cm, respectively. In Figure 2.7 we show these ranges in comparison to the model assumption constraints described above. For SN 1972E, we find that there are large swaths of parameter space that can be probed using the parameterized light curves of H16. However, for SN 1895B, we find that only shells with very low densities ($\lesssim 10$ cm^{-3}) will not violate model assumptions.

Finally, we note one other requirement based on the assumption that the interaction primarily occurs in the outer SN ejecta: the total mass in the CSM shell should not exceed the total mass in the outer SN ejecta ($\sim$0.3 M$_\odot$). Parameter space where this requirement is met and violated are discussed in Section 2.4.3.3, below.

2.4.3.3 CSM Shell Models Excluded

Finding that the H16 model assumptions are valid over a portion of the parameter space of CSM shells probed by SN 1972E and SN 1895B, we run large grids of parameterized light curve models for comparison with our observations. For SN 1972E, we run 3,200 models for shell radii spanning $r_1 = [1 - 15] \times 10^{17}$ cm and shell densities spanning $n = 1 - 16,000$ cm^{-3} ($\sim 2.3 \times 10^{-24}$ to 3.7×10^{-20} g cm^{-3}). This grid is chosen to encompass the full range of densities that can be probed without violating the the model assumptions described above. For the highest densities considered these models assumptions are only valid at the smallest radii (see Figures 2.7 and 2.8). For SN 1895B we consider 450 models spanning shell radii of $r_1 = [1.6 - 4] \times 10^{18}$ cm and shell densities of $n = 1 - 15$ cm^{-3}. For each event, we run models for three representative shell widths, chosen to span the range of astrophysical shells predicted surrounding some putative Type Ia SN progenitors (see Section 4.4). Specifically, we consider f values of:

$f = 0.15$: A thin shell based on the based on the observed width of the Abell 39 planetary nebula, and in line with widths predicted for some material swept up in nova outbursts [e.g. Moore & Bildsten, 2012].

$f = 0.33$: A medium thickness shell based on models of "nova super shells" [Darnley et al., 2019].

$f = 1.00$: A representative thick shell.

For each combination of f, r_1, and n, we compute the resulting radio light curve at the frequencies of all of our observations and determine whether any of the flux upper limits described above rule out a shell with those parameters. Results from this process for SN 1972E are shown in Figure 2.8. Shells excluded by the data are displayed in red. For reference, we also plot lines that indicate constant shell masses of 0.01, 0.05, 0.1, and 0.3 M$_\odot$ for each shell thickness. Shells with total masses >0.3 M$_\odot$ violate the H16 requirement that the total shell mass be less than the mass in the outer SN ejecta. Regions where the condition that the initial interaction occurs in the outer SN ejecta is violated are also shown in blue. For the medium-thickness shells considered here, theses two conditions are violated at very similar shell densities, while for thick-shells the constraint that the total shell mass be less than 0.3 M$_\odot$ is the more restrictive requirement (see Figure 2.8; right panel).

Each observed luminosity limit leads to a diagonal line of excluded CSM shells in the density-inner radius plane. This is due to the interplay between the shell density and the onset time of strong interaction that leads to radio emission (see above). For thin shells (left panel) these individual "tracks" of excluded models are visible, while for thicker shells (center and right panels) they broaden and overlap. Thus, excluding a complete set of thin shell models for an individual SN progenitor would require higher cadence radio observations than those available for SN 1972E. In contrast, for thicker shells, we are primarily limited by the depth of individual observations.

Overall, for SN 1972E, we can rule out CSM shells down to masses of $\sim$0.01 $M_\odot$ at a range of radii, which vary depending on the shell thickness. We can also rule out the presence of *all* thick shells with masses $\gtrsim$0.05 $M_\odot$ at radii between 1×10^{17} and 1×10^{18} cm, and most medium-width shells of similar mass at radii between 2×10^{17} and 1.5×10^{18} cm. In terms of raw CSM shell density, our deepest limits come between 1 and 1.5 $\times10^{18}$ cm, where we can rule out shells with densities between 1 and 3 cm^{-3}.

We emphasize that these radii are larger than those probed by most other observations searching for CSM surrounding Type Ia SNe to date, including time-varying absorption features [e.g., Patat et al., 2007] and late-time optical photometry/spectroscopy [e.g. Graham et al., 2019], which tend to constrain the presence of CSM around $\sim10^{16}$ cm. Simon et al. [2009] do find a radius of $\sim$ 3 $\times10^{17}$ cm for the material responsible for time-varying Na absorption lines around the Type Ia SN 2007le. However, the density inferred is much higher ($\sim10^7$ cm^{-3}) and fractional width much narrower ($f \approx 3\times10^{-4}$) than those considered here, possibly suggesting a clumpy or aspherical CSM. Our observations constrain a unique parameter space of CSM shells.

For SN 1895B, we find that essentially all of the shell models that would be excluded by the depth and timing of our observations fall in the regime where the H16 assumption that the CSM impacts the outer SN ejecta is violated. However, a few specific exceptions to this exist. For example, we can rule out the presence of an $f = 0.33$ medium width shell with a density of 6 cm^{-3} at a radius of $\sim 2\times10^{18}$ cm (total shell mass $\sim$0.3 $M_\odot$). These borderline cases demonstrate that the observations of SN 1895B are likely useful to constrain the presence of shells at these radii, but updated models that include interaction with the dense inner SN ejecta are required for a quantitative assessment.

2.5 Discussion

The CSM environment surrounding a Type Ia SN is dependent on pre-explosion evolutionary history of the progenitor system. In this section, we will consider different types of CSM that are both allowed and ruled out by our results (Section 2.4), and what they indicate in the context of various Type Ia SN progenitor scenarios. In Section 2.5.1, we consider the presence of constant density material, the only material expected in DD scenarios with significant delay times. We next consider the presence of shells (Section 2.5.2), as may be expected for SD progenitors if they contain nova shells or planetary nebula and DD progenitors in the case of a prompt explosion post-common envelope. We also consider the presence of other types of CSM (Section 2.5.3). Finally, in Section 2.5.4, we make predictions for the future of both SN 1895B and SN 1972E as the SNe evolve and future observations are taken.

2.5.1 Presence of Constant Density CSM or ISM

Our deepest luminosity limits constrain the density of a uniform ambient medium surrounding SN 1972E and SN 1895B to be $\lesssim$0.9 cm^{-3} out to radii of $\sim 10^{17} - 10^{18}$ cm. This implies a clean circumstellar environment out to distances 1−2 orders of magnitude further than those previously probed by prompt radio and X-ray observations [Chomiuk et al., 2012; Margutti et al., 2014]. Densities of this level are consistent with the warm phase of the ISM in some galaxies [e.g. Ferriere et al., 2001], and we examine whether our density constraints for SN 1972E and SN 1895B are consistent with expectations for the ISM in their local environments within the intensely star-forming galaxy NGC 5253.

Using the HI observations of Kobulnicky et al. [1995], Summers et al. [2004] estimate the ISM density at the location of SN 1972E, which is >1.5 kpc from the central star-forming region, to be $\lesssim$ 1 cm^{-3}—comparable to our radio limits. In contrast, SN 1895B exploded ∼100 pc from the nucleus of NGC 5253, in a complex region with multiple large stellar clusters (Section 2.2). Excluding the dense stellar clusters themselves, Monreal-Ibero et al. [2010] use IFU spectroscopy with VLT-FLAMES to conclude that the ISM density in this central region is < 100 cm^{-3}, and could potentially be 1−2 orders of magnitude lower and the explosion site of SN 1895B, depending on the local distribution of material. Thus, despite some uncertainty, we find that our deepest radio limits constrain the density surrounding SN 1972E and SN 1895B to be at levels comparable to, or below, the local ISM at distances of $\sim 10^{17} - 10^{18}$cm.

Low density media surrounding Type Ia SNe can be achieved through multiple progenitor scenarios. Clean, ISM-like, environments are most commonly evoked for DD models produced by the merger of two WDs. The components of such systems have low intrinsic mass loss rates and current population synthesis models predict that >90% of WD mergers should occur >10^5 years after the last phase of common envelope evolution [Ruiter et al., 2013]. Thus, the material ejected during this phase should fully disperse into the ISM at radii beyond 10^{18} cm by the time of explosion. While WD mergers may also pollute the CSM via a number of other physical mechanisms including tidal tail ejections [Raskin et al., 2013], outflows during a phase of rapid mass transfer pre-merger [Guillochon et al., 2010; Dan et al., 2011] and accretion disk winds in systems that fail to detonate promptly [Ji et al., 2013], this material will be located at radii < a few × 10^{17} cm, unless there is a significant ($\gtrsim$100 years) delay between the onset of merger and the subsequent Type Ia explosion. In this case, the small amount of material ejected via these mechanisms ($\sim 10^{-3} - 10^{-2}$ M$_\odot$) will have either dispersed to densities below our measurements or swept up material into a thin shell [Raskin et al., 2013], whose presence will be assessed below. Thus, we conclude that our low inferred densities surrounding SN 1972E and SN 1895B are be consistent with expectations for a majority of DD explosions due to WD mergers.

However, low density ambient media can also be produced by SD and DD Type Ia SN models in which either fast winds or shells of material are ejected from the progenitor system prior to explosion. This high velocity material will subsequently "sweep-up" the surrounding ISM, yielding low density cavities surrounding the stellar system [e.g. Badenes et al., 2007]. For example, recent hydrodynamical simulations of recurrent nova systems find cavity densities of $10^{-1} - 10^{-3}$ cm^{-3}, far below the density of the ambient ISM [Darnley et al., 2019]. Our radio observations would require a cavity that extends to a few ×10^{18} cm. These distances are consistent with the large (r

$> 10^{19}$ cm) cavities predicted to be carved by fast accretion wind outflows from the WD surface in some SD models [Hachisu et al., 1996], although such cavities may be inconsistent with observed SNR dynamics [Badenes et al., 2007]. In the context of recurrent nova systems such large cavities would require a system that had been undergoing outbursts for $\gtrsim$10,000 years [Darnley et al., 2019]. In the section below, we discuss constraints on the presence of CSM shells surrounding SN 1972E and SN 1895B, and thus further implications for this class of progenitor model if a cavity is the source of the clean CSM environments observed.

2.5.2 Presence of Shells

Several putative progenitor systems for Type Ia SNe predict the presence of shells surrounding the system at distances in the range of those probed by our observations ($\sim 10^{17} - 10^{18}$ cm). These include both SD and DD systems, with examples of shell creation mechanisms ranging from a recurrent nova to common envelope ejections. In Section 2.4.3.3, we utilized the models of Harris et al. [2016] to explore the basic parameter space of shells that can be constrained and ruled out by our data. Here, we discuss the implications of these results for various progenitor scenarios.

2.5.2.1 Recurrent Nova Progenitors

A recurrent nova is a high mass accreting WD system that undergoes repeating thermonuclear outbursts due to unstable hydrogen burning on its surface, ejecting mass from the system every $\sim 1 - 100$ yr. The identification of time variable absorption and blue shifted Na I D lines in some Type Ia SNe [Patat et al., 2007; Blondin et al., 2009; Sternberg et al., 2011; Maguire et al., 2013] have raised the question of a connection between recurrent novae and Type Ia SNe, particularly in light of the discovery of blue-shifted Na I D lines in the recurrent nova RS Ophiuchi (RS Oph) during outburst [Patat et al., 2011; Booth et al., 2016].

Individual nova eruptions eject a small mass of material ($M_{ej} \sim 10^{-7} - 10^{-5}$ $M_\odot$) at high velocities ($v_{ej} \gtrsim 3000$ km/s; Moore & Bildsten 2012; Darnley et al. 2019). However, this material will rapidly decelerate to velocities on the order of tens of km s^{-1} as it sweeps up material from the ISM, CSM, or collides previously ejected shells. The result is a complex CSM structure consisting of of low-density ($n \sim 10^{-1} - 10^{-3}$ cm^{-3}) cavities enclosed by a dense outer shell [e.g. Munari et al., 1999; Badenes et al., 2007]. For a for a 10^4 year recurring nova phase, such as that seen in RS Oph-like stars, the outer cavity wall predicted to be at radii of $\gtrsim 3 \times 10^{17}$ cm [e.g. Dimitriadis et al., 2014], within the regime probed by our observations.

The constraints that our observations can provide on the presence of nova shells surrounding SN 1972E depend primarily on their predicted densities, radii, and thicknesses, which in turn depend on the density of the ambient ISM, the total time the system has been in an active nova phase, and the recurrence timescale between eruptions. Two recent hydrodynamic models for the CSM structure surrounding such systems are presented by Dimitriadis et al. [2014] and Darnley et al. [2019]. The former models nova eruptions with 25, 100, 200 year recurrence timescales expanding into a CSM shaped by winds from a red giant donor star with $\dot{M} = 10^{-6}$ $M_\odot$ and $v_w = 10$ km s^{-1}. The the latter simulated eruptions with both a shorter recurrence timescale (350 days) and a lower density CSM (shaped by a red giant star with $\dot{M} = 2.6 \times 10^{-8}$ $M_\odot$ and $v_w = 20$ km s^{-1}). This model was specifically designed to reproduce the CSM surrounding the

M31 nova system M31N 2008-12a. M31N 2008-12a is particularly interesting system as it is the most frequently recurring nova known, the WD is predicted to surpass the Chandrasekhar limit in <20,000 years [Darnley et al., 2017], and it is surrounded by an observed cavity-shell system with a total projected size of $\sim 134 \times 90$ pc [Darnley et al., 2019].

Dimitriadis et al. [2014] find that the density of individual nova ejections expanding into the main cavity depends on the nova recurrence timescale. For longer recurrence times the densities will be higher, as the donor star has additional time to pollute the CSM. For the donor mass-loss rate and recurrence timescales considered b Dimitriadis et al. [2014] these shells are predicted to have densities $\gtrsim 10^2$ cm^{-3}, while the low density and short recurrence timescale of Darnley et al. [2019] yield individual shell densities below the detection threshold of our observations ($n \lesssim 0.1$ cm^{-3}). However, while our observations can rule out high-density shells from some individual nova eruptions, they are predicted to be too thin ($f \sim 0.01$; Dimitriadis et al. [2014]) for our sparse observations to conclusively rule our a system of shells predicted for any specific recurrence time.

In contrast, the outer cavity wall is expected to be thicker. Darnley et al. [2019] find that this "nova super-remnant shell" converges a width of $f = 0.22$ and density approximately 4 times that of the ISM in their simulations (~ 4 cm^{-3}). Our observations can rule out the presence of even these low-density medium-thickness shells at radii between $\sim 5 \times 10^{17}$ cm and 2×10^{18} cm. Darnley et al. [2019] find that the outer cavity would be located at these radii for nova systems that have been active for between $\sim 10^3$ and 10^4 years (having undergone $\sim$1000 − 10,000 total eruptions). For higher density CSM and longer recurrence times, Dimitriadis et al. [2014] find that the cavities will expand more slowly, and thus our observations will rule out older systems.

2.5.2.2 Shell Ejections in DD Progenitors

There are multiple mechanisms by which DD Type Ia progenitors may also eject shells of material pre-explosion. First, all putative DD progenitor scenarios must undergo at least one episode of CE evolution, in order to yield the requisite tight double WD system [e.g. Ivanova et al., 2013]. For WD merger models, the delay between CE ejection and SN is primarily set by the binary separation post-CE and the gravitational-wave timescale. While current binary population synthesis models predict a majority of WD mergers will occur with a significant delay post-CE, Ruiter et al. [2013] highlight a channel wherein $\sim 3.5\%$ of WD binaries with a massive (>0.9 M$_\odot$) primary will merge between 10^3 and 10^4 post-CE. As described above, assuming expansion velocities of a few tens to 100 km s^{-1}, our observations of SN 1972E constrain shells ejected on these timescales. While the CE mass ejection process is uncertain, the total envelop ejected for putative Type Ia progenitors ranges from a few tenths to $\sim$1 M$_\odot$ (e.g. MacLeod et al. [2017]). We can rule out most CE shells with masses between 0.05 M$_\odot$ and 0.3 M$_\odot$, unless they are very thin ($f \lesssim 0.1$). Thus, it is unlikely that SN 1972E underwent and ultra-prompt explosion, although we caution additional theoretical models are required to quantitatively rule out CE shells with masses of $\sim$1 M$_\odot$.

For DD models that are triggered by the detonation of thin surface layer of helium accreted from a low-mass WD companion (the "double detonation" model; e.g., Shen et al. 2013), the explosion is predicted to occur between 10^8 and 10^9 years after CE [Shen et al., 2013]. As such,

any CE shell will have long since dispersed into the ISM. However, [Shen et al., 2013] outline a model whereby such systems can also eject small amounts of hydrogen-rich material (a few $\times 10^{-5}$ $M_\odot$) at high velocities ($\sim$15000 km s^{-1}) in the hundreds to thousands of years before the SN. Analogous to classical novae, this material will sweep up the ISM, forming a cavity and outer shell structure whose properties (mass, radius, thickness) depend on both the evolutionary history of the WD and the ambient ISM density. For ISM densities of 1 cm^{-3}, [Shen et al., 2013] predict shells with $n \sim 5$ cm^{-3} and widths of $f \sim 0.25$ at radii ranging from $r_1 \sim 5 \times 10^{17}$ cm (for older WD progenitors) to $r_1 \sim 1 \times 10^{18}$ cm (for younger WD progenitors). Our deepest limits just rule out the presence of such shells around SN1972E, although some intermediate ages are permitted. For sparser ambient ISM densities, such shells would be below our detection limits.

2.5.2.3 Tidal Tail Ejections

In WD-WD merger scenarios, a small amount of material (a few $\times 10^{-3}$ $M_\odot$) can be ejected in the form of tidal tails, which are stripped from the system just prior to coalescence [Raskin et al., 2013]. The ultimate location of this material depends on the delay between the initiation of the merger and the ultimate explosion, and the non-detection of Type Ia SN in prompt (t $\lesssim$ year) radio and X-ray observations have been used to argue for either very short ($\lesssim$ 100 s) or long ($>$ 100 years) delays [Margutti et al., 2014]. For a delay time of $\sim$100 year, Raskin et al., [2013] predict that the tidal tails should appears as a wide ($f = 1$) shell-like structure with a density of $n \sim 100$ cm^{-3} at a radius of $r_1 \sim 2 \times 10^{17}$ cm. Our observations rule out such a CSM structure for SN 1972E. From this time onward, the tidal material will sweep-up ISM material, decelerating and narrowing in the process. Thus, our observation likely rule out delay times of a few hundred years for this scenario, with the exact range depending on the ISM density and deceleration timescale. Raskin et al., [2013] predict that by 3000 years post-ejection, the tidal material will be located at a radius of $\sim 8 \times 10^{18}$ cm, well beyond those probed by our observations.

2.5.3 Other CSM Structures

There are several putative Type Ia SN explosion models that predict the presence of CSM, which is neither constant in density nor strictly in the form of shells. Here, we discuss two such cases.

2.5.3.1 Stellar Winds

If the CSM surrounding surrounding the Type Ia SN has a stellar wind-like density distribution ($\rho \propto r^{-2}$), observations from the first $\sim$year post-explosion would provide the deepest constraints on the mass-loss rate of the progenitor system. This density distribution is what is typically expected in SD models that undergo quasi-steady mass-loss due to either winds from a giant (symbiotic) donor star [Seaquist & Taylor, 1990], optically-thick winds from the WD itself during phases of high-accretion [Hachisu, 1996], or non-conservative mass-loss through the second Lagrange point during Roche Lobe overflow for some binary configurations [Deufel et al., 1999]. In all such cases, emission from the CSM interaction would be strongest in the first days after the SN event when the density of the CSM is highest [Chomiuk et al., 2016]. As described in Section 2.2, the deepest limits on the mass-loss rates for SN 1972E and SN 1895B come from the 1984 observations, 12.5 and 8.3 years post-explosion. The constraints of $< 8.60 \times 10^{-6}$ $M_\odot$ yr^{-1} and $< 7.2 \times 10^{-5}$ $M_\odot$

yr^{-1} (for wind velocities of 10 km s^{-1}) rule out a number of Galactic symbiotic systems [Seaquist & Taylor, 1990], but are otherwise unconstraining. We note that these limits depend linearly on the assumed wind speed, and hence for $v_w > 10$ km s^{-1} the mass-loss constraints would be even weaker.

2.5.3.2 Mass Loss from a Radially Extended Envelope

Shen et al. [2012] present updated model for the long-term evolution of the remnants of WD mergers, in which the lower mass WD is disrupted and forms a hot radially extended ($r \sim 10^{13}$ cm) envelope around the central remnant rather than an accretion disk. While the final fate of such remnants are debated, it should persist for $\gtrsim 10^4$ years as a carbon burning shell, ignited off-axis, propagates inward to the core. While they neglect mass loss in their calculations, Shen et al. [2012] note that with a typical escape velocities of 60 km s^{-1}, material lost during this phase in the remnant's evolution could reach radii of $\sim 2 \times 10^{18}$cm, within the radius range probed by our observations.

Subsequently, Schwab et al. [2016] perform updated models and examine the consequences of different mass loss prescriptions on the evolution of such merger remnants. In particular, they note the similarities between the observed properties of these remnants and AGB stars, raising the possibility that a dusty wind may form during an ∼5000 year phase in their evolution. Within this context, we note that our observations rule out mass loss on the level observed in extreme AGB stars ($\dot{M} \sim 10^{-4}$ $M_\odot$) out to radii of a few times 10^{17} cm for wind speeds between 10 and 100 km s^{-1}. However, Schwab et al. [2016] also find that the temperature of the merger remnant will eventually increase, in a process analogous to PN formation in AGB stars. As a consequence of this evolution, any phase of intense dusty mass loss should cease and the increased UV radiation from the central star could yield an ionized nebulae with total mass of ∼0.1 $M_\odot$ at a distance of $\gtrsim 3 \times 10^{17}$ cm. Our observations rule out the presence of such shells over a wide range of radii, unless they are very thin ($f < 0.1$).

2.5.4 The Future: SN to SNR Transition

Our upper limits on the radio luminosity from SN 1972E and SN 1895B are consistent with both SN blastwaves expanding into low density CSM environments out to radii of a few $\times 10^{18}$ cm. Assuming a constant density CSM, the radio emission from both events is predicted to continue rising over time (see Figure 2.2), and we can use our baseline S17 model described in Section 2.4.2.1 to project their future evolution and thus prospects for subsequent radio detections. If we assume that no CSM shells are present, and that the SNe are expanding into ambient densities of 0.7 cm^{-3} (just below our Dec. 2016 limits; Table 2 in the electronic journal version of this chapter), then both SN would peak at a flux level of ∼200 μJy (at 5 GHz) ∼300 years post-explosion. In this scenario SN 1972E and SN 1895B would reach maximum observed brightness in 2272 and 2195, respectively. If we assume that *targeted* VLA observations of each SN could achieve C-band images with RMS noise levels of ∼5−10 μJy (consistent with the sensitivity limits obtained by Chomiuk et al. 2016), then both SN1972E and SN 1895B would currently be detectable at a greater than 5σ level.

However, the ambient density surrounding both SNe may be significantly lower than the upper limits found in Section 2.4. In this case the radio light curve would peak at later times and fainter flux levels (S17; See Figure 2.2). For example, the youngest SN in our own Galaxy, G1.9+0.3, is detected at radio wavelengths at a level consistent ambient density of 0.02 cm^{-3} (Sarbadhicary et al. 2019; adjusted for consistency with our baseline S17 model; see Figure 2.4). If SN 1972E and SN 1895B are expanding into similar CSM environments, then we project that they would peak at 5 GHz flux levels of $\sim$6 μJy $\sim$990 years post-explosion. In such a scenario, their current 5 GHz fluxes would be only $\sim$ 1 μJy and $\sim$ 2 μJy, respectively, and they would never rise above the optimal VLA sensitivity limits described above. This indicates that observations of intermediate-aged Type Ia SNe in nearby galaxies may still be sensitivity limited without significant time investment [10-12 hours; see Sarbadhicary et al., 2019] from current instruments. Limits with future radio telescopes such as the Square Kilometer Array (SKA) and the Next Generation VLA will allow us to study radio emission from Type Ia SNe throughout the local volume, even when they are expanding into low density ($\sim$ 0.1 cm^{-3}) surroundings.

Once additional detections of intermediate aged-SN and young SNRs are made, interpretation of the results will require careful consideration of whether the emission is due to CSM shaped by the progenitor system, or simply the ambient ISM. For example, recent analysis of radio observations of SN 1885A by Sarbadhicary et al. [2019] conclude the density surrounding the system must be approximately a factor 5 lower density that that surrounding G1.9+0.3. However, they argue that the higher density found for G1.9+0.3 may be due to a higher density in the Milky Way's center—as compared to M31's—and does not require CSM from the progenitor. Currently, we cannot distinguish between these scenarios based on our data for SN 1895B and SN 1972E.

2.6 Summary and Conclusions

We have conducted a study of the circumstellar environments of the nearby Type Ia SN 1972E and SN 1895B by analyzing seven epoch of archival VLA observations from obtained between 1981 and 2016. We do not detect emission from the location of either SN in our data set. The most stringent upper limits on the radio luminosity from each event are $L_{\nu,8.5GHz} < 8.9 \times 10^{23}$ erg s^{-1} Hz^{-1} 121 years post-explosion for SN 1895B and $L_{\nu,8.5GHz} < 6.0 \times 10^{23}$ erg s^{-1} Hz^{-1} 45 years post-explosion for SN 1972E. These imply low-density environments with $n < 0.9$ cm^{-3} out to radii of a few $\times$ 10^{18} cm — nearly two orders of magnitude further from the progenitor star than those previously probed by prompt (t $\lesssim$ 1 year) radio and X-ray observations [e.g. Panagia et al., 2006; Margutti et al., 2012; Chomiuk et al., 2012; Russell & Immler, 2012; Margutti et al., 2014; Chomiuk et al., 2016]. These ambient densities are consistent with progenitor scenarios that produce either ISM-like environments or low-density evacuated cavities out to large distances.

Given the multi-epoch nature of our dataset, we also investigate the possibility of shells surrounding the progenitor of SN 19722E. Using the models of H16, we rule out the presence of essentially all medium and thick CSM shells with total masses of 0.05 $M_\odot$ to 0.3 $M_\odot$ located at radii between a few $\times$ 10^{17} and a few $\times$ 10^{18} cm. We also exclude specific CSM shells down to masses of $\lesssim$ 0.01 $M_\odot$ at a range of radii, which vary depending on the shell thickness (see Figure 2.8). Quantitative assessment of the presence of more massive CSM shells will require

updated theoretical models that include the effect of the inner SN ejecta impacting the CSM shell.

These shell constraints rule out swaths of parameter space for various SD and DD Type Ia SN progenitor models including recurrent nova, core-degenerate objects, ultra-prompt explosions post-CE, shells ejections from CO+He WD systems, and WD mergers with delays of a few hundred years between the onset of merger and explosion. Allowed progenitor systems include DD in which the delay from the last episode of CE is long ($> 10^4$ yrs) as well as SD models that exhibit nova eruptions—provided the system has a relatively short recurrence timescale and has been in the nova phase for either a short ($\lesssim$100 yrs) or long ($\gtrsim 10^4$ yrs) time.

It is clear that multi-epoch radio observations of nearby intermediate-aged Type Ia SNe explore useful regions of parameter space for distinguishing between the plethora of theoretical progenitor models. In the future, a statistical sample of such events will provide even more robust discriminating power, as different models predict a range of delay times and hence a variety of locations for CSM material.

2.7 Acknowledgements

We would like to thank C. Harris for their generous assistance in our modeling work and answering our questions and B. Shappee for conversations that inspired this work. Support for this work was provided to MRD through Hubble Fellowship grant NSG-HF2-51373, awarded by the Space Telescope Science Institute, which is operated by the Association of Universities for Research in Astronomy, Inc. for NASA, under contract NAS5-26555. MRD acknowledges support from the Dunlap Institute at the University of Toronto and the Canadian Institute for Advanced Research (CIFAR). LC and SS are grateful for the support of NSF AST-1412980, NSF AST-1412549, and NSF AST-1751874.

The National Radio Astronomy Observatory is a facility of the National Science Foundation operated under cooperative agreement by Associated Universities, Inc. The Dunlap Institute is funded through an endowment established by the David Dunlap family and the University of Toronto.

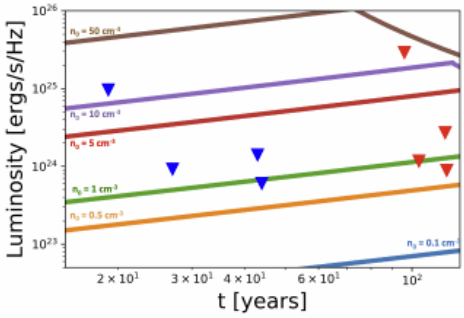

(a) Expected luminosity for various densities for our "baseline" model (M_{ej} = 1.4 $M_\odot$, E_K = 10^{51} erg, and ϵ_e = 0.1, with n_0 ranging from 0.1 − 50 cm^{-3}).

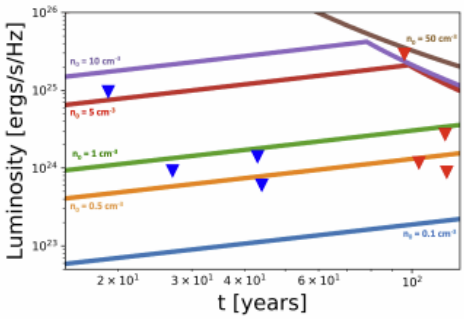

(b) Same as 3(a), but M_{ej} = 0.8 $M_\odot$.

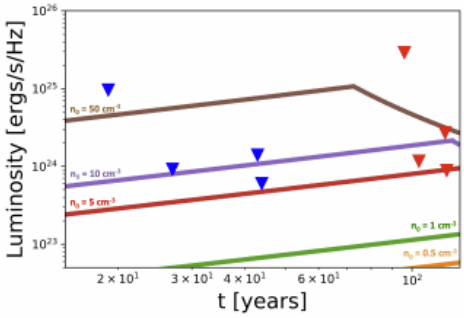

(c) Same as 3(a), but with ϵ_e = 0.01.

Figuur 2.3 Expected 8 GHz radio luminosity over time for S17 models if we vary n_0, M_{ej}, or ϵ_e. X-band upper limits for SN 1972E (blue) and SN 1895B (red) are provided for comparison. See text for details.

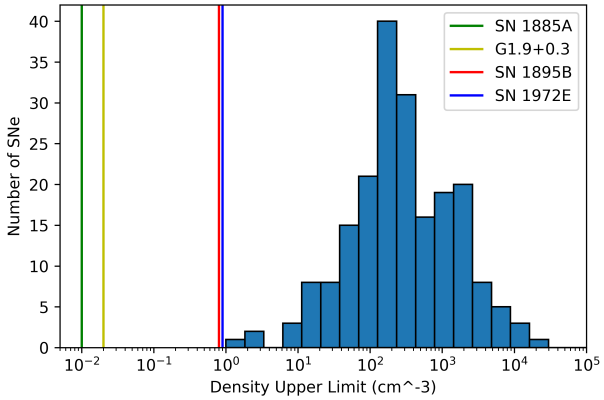

Figuur 2.4 A histogram of the uniform density CSM upper limits for ∼200 radio observations of 85 Type Ia SNe reported in Chomiuk et al. [2016], compared to the deepest limits found in this work for SN 1972E and SN 1895B (red and blue vertical lines, respectively). Also shown is a density upper limit for SN 1885A (green) and a density measurement for G1.9+0.8 (yellow) calculated based on the luminosities from Sarbadhicary et al. [2019] and assuming our baseline model described in Section 2.4.2.1.

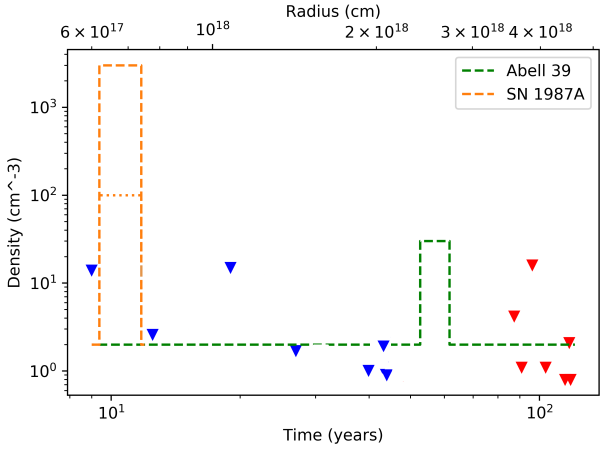

Figuur 2.5 The upper limits on density, in cm^{-3}, obtained for SN 1972E (blue triangles) and SN 1895B (red) assuming our baseline model. The top axis shows the radius probed by each observation, assuming a constant density of 1 cm^{-3}. For reference, we have also provided a simple density profile for the planetary nebula Abell 39 (green dashed line; Jacoby et al. 2001), and the upper and lower limits on the density of the inner ring of SN 1987A (orange dashed and dotted lines, respectively; Mattila et al. 2010b).

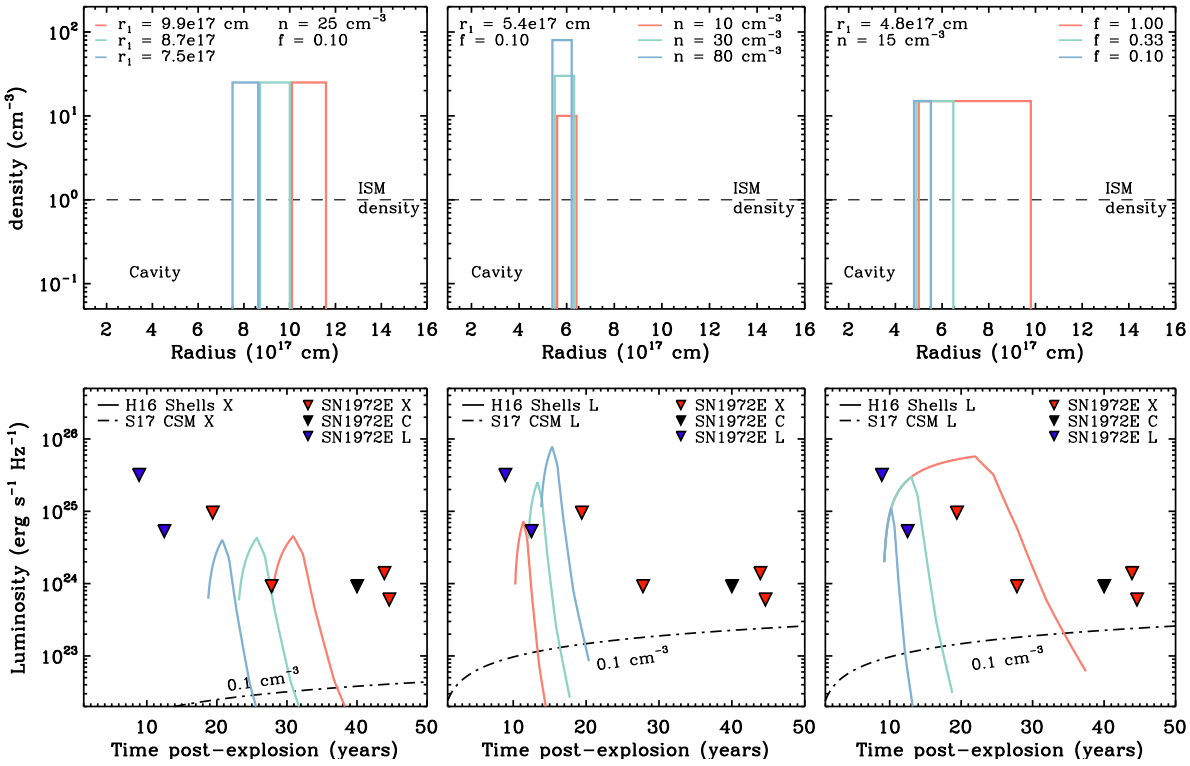

Figuur 2.6 Fiducial H16 light curve models for a SN blastwave impacting a constant density CSM shell. The three top panels show representations of the CSM density structure as a function of each of the three free model parameters, varying shell inner radius (r_1), shell density (n_0), and shell width (f) respectively. A typical ISM density ($\sim$1 cm^{-3}; dashed line) is shown as a dashed line for reference. H16 assume a cavity interior to the CSM shell. The three lower panels show the H16 radio light curves that result when a SN blastwave impacts the density structures shown in the panel immediately above them. Radio upper limits from SN 1972E (downward triangles, colors correspond to observed frequency bands) and a 0.1 cm^{-3} constant CSM density radio light curve from S17 (dash-dot line) are shown for comparison. *Left Panels:* Effect of varying shell inner radius. The onset of the resulting radio emission is delayed. *Center panels:* Effect of varying shell density. Higher densities correspond to brighter radio emission and slightly later rise of the radio light curve (see text for details). *Right panels:* Effect of varying the shell fractional width. Radio light curves initially follow the same evolution, but thicker shells yield a longer-lived and brighter radio transient.

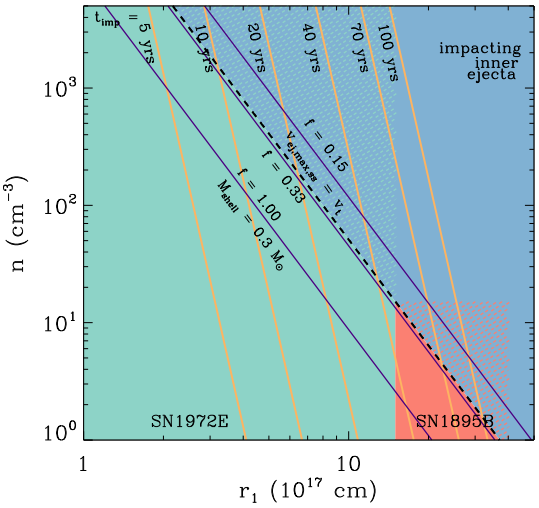

Figuur 2.7 Visual representation of the CSM shell inner radii (r_1) and densities (n) probed by observations of SN 1972E and SN 1895B (aqua and red boxes, respectively) and regions where the model assumptions of H16 are valid. The shaded blue region highlights the parameter space where the assumption that the CSM impacts the outer portion of the SN ejecta is violated. Violet lines indicate densities for which the total shell mass equals the total mass in the outer ejecta ($\sim$0.3$M_\odot$) for fiducial thin, medium, and thick shells. Yellow lines designate the time when the SN ejecta would impact the CSM shell in the models of H16. See text for details.

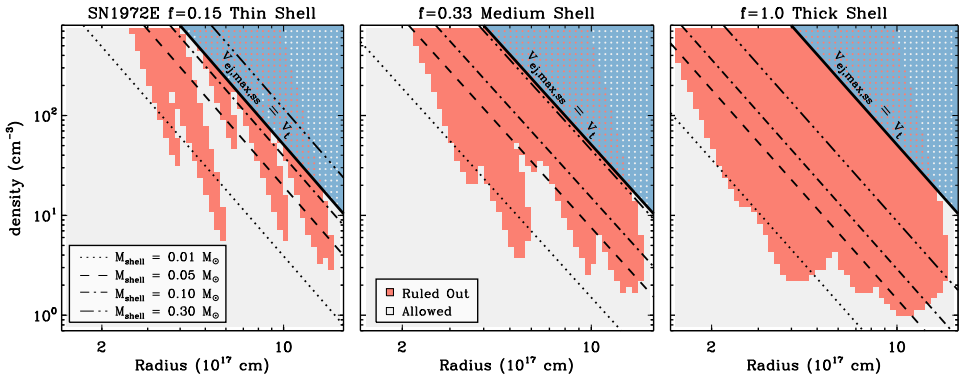

Figuur 2.8 Grid of H16 CSM shell models tested against observations of SN 1972E. Red squares designate the shell radii and densities ruled out for representative thin (left panel), medium (center panel), and thick (right panel) shells. The blue shaded area designates the region where H16 model assumptions are violated. In each panel dotted, dashed, dot-dashed, and triple-dot-dashed lines designate shells with total masses 0.01, 0.05, 0.1, and 0.3 $M_\odot$, respectively. For all shell thicknesses, we can rule out shells with masses down to 0.005$-$0.01 $M_\odot$ for specific radii, and for medium and thick shells our observation exclude the presence of essentially any shell with masses >0.05 $M_\odot$ at radii between 10^{17} and 10^{18} cm. See text for further details.

Hoofdstuk 3

Flagging of Radio Frequency Interference: Implications for Short-Duration Transients

Cendes, Y. et al.,

Astronomy and Computing, Volume 23, article id. 103., 2018

Abstract

With their wide fields of view and often relatively long coverage of any position in the sky in imaging survey mode, modern radio telescopes provide a data stream that is naturally suited to searching for rare transients. However, Radio Frequency Interference (RFI) can show up in the data stream in similar ways to such transients, and thus the normal pre-treatment of filtering RFI (flagging) may also remove astrophysical transients from the data stream before imaging. In this paper we investigate how standard flagging affects the detectability of such transients by examining the case of transient detection in an observing mode used for Low Frequency Array (LOFAR; [van Haarlem et al., 2013b]) surveys. We quantify the fluence range of transients that would be detected, and the reduction of their SNR due to partial flagging. We find that transients with a duration close to the integration sampling time, as well as bright transients with durations on the order of tens of seconds, are completely flagged. For longer transients on the order of several tens of seconds to minutes, the flagging effects are not as severe, although part of the signal is lost. For these transients, we present a modified flagging strategy which mitigates the effect of flagging on transient signals. We also present a script which uses the differences between the two strategies, and known differences between transient RFI and astrophysical transients, to notify the observer when a potential transient is in the data stream.

3.1 Introduction

Modern radio astronomy is particularly suited for the search of many classes of extreme transient object. This is due to a combination of astrophysical and instrumental effects. Astrophysically, extreme objects are often compact, non-thermal emitters, implying they can vary on short time scales and have significant luminosity at radio frequencies. At long radio wavelengths, the blackbody limit severely constrains the allowed luminosity, but often compact objects are seen to have coherent emission at those long wavelengths, which can exceed the (incoherent) blackbody limit by many orders of magnitude. Instrumentally, modern radio telescopes can have very wide fields of view and thus are much more likely than previous instruments to detect rare events. Further, modern computing techniques and hardware infrastructure enable the near real-time processing of the large data streams from these telescopes, and automated generation of alerts to transients. This has enabled rapid multi-wavelength follow-up of candidate transients, essential for understanding the transient source parameters. However, the large data volumes lead to a requirement of automated flagging, which can be pernicious to transient searches.

There are multiple ways of using a radio interferometer to search for transient events. One may use it to image the sky, and search for variations of brightness in the sources detected in the image [Stewart et al., 2016]. One may also add up the signals from all the array elements coherently or incoherently to form a beam on the sky and examine the time series of the signal from that beam [Coenen et al., 2014]. The latter method is preferred for looking at very brief (sub-second) events and periodic signals, and is the method of choice for detecting pulsars and Fast Radio Bursts (FRBs) [Rane & Lorimer, 2017; Lorimer et al., 2007]. When pushed to their limits, both methods require front-line data processing and supercomputing technology in order to cope with the data flow [van Haarlem et al., 2013b]. In response to this, other techniques are now also being developed, such as searching for suspected transient events in raw correlation data products and then imaging very short selected data segments with candidate transients [Bower et al., 2013; van Velzen et al., 2013].

In this paper we focus on the first method, searching for transients in a time series of images. The effectiveness of image domain transient searches has already been demonstrated by the discovery of a bright, low-frequency transient of several minutes duration by Stewart et al. [2016], as well as earlier discoveries by Hyman et al. [2009] and Jaeger et al. [2012]. Interferometers spend a large fraction of their time collecting data in imaging mode, and at the same time sample visibilities initially at order of seconds intervals for the purposes of avoiding time smearing, rejecting bad data, and calibration. This means that a large amount of data are collected in imaging mode that may be used to search for interesting transient sources, thus generating more science at no extra expense of observing time (but considerable extra processing time).

Typical image domain searches for transients of a given duration consist of tracking observations sampled at short timescales, followed by offline flagging and imaging at a much longer timescale in order to increase sensitivity. An example of this is the LOFAR survey mode, in which visibilities are integrated over 10 seconds in real-time, but imaging is carried out in 11 minute snapshots.

A key step in processing such radio data is the removal of Radio Frequency Interference (RFI)– terrestrial, generally human-generated, radio noise that may corrupt celestial signals. In

the large data volumes of e.g., LOFAR, automated algorithms are needed to manage this process in realistic time. Generally these algorithms use the fact that RFI is much stronger than cosmic signals in the data, and usually forms stripes in a dynamic spectrum that are either narrow in frequency or in time, on a smooth, much lower background. Simple removal of these data from consideration is adequate for most radio imaging, and even in a relatively RFI-rich environment like the Netherlands this results in only a few percent data loss [Offringa et al., 2012].

However, a bright and short astrophysical transient may resemble RFI in the data, and thus be filtered out before any image is created. In this paper, we investigate the effect this has on the likelihood of transient detection. We quantify the effect of various RFI flagging techniques on transients by injecting simulated transients into an actual LOFAR observation, then flagging and imaging the data.

The breakdown of the paper is as follows. In Section 2, we will present an overview of current standard methods of RFI flagging, and of potential problems faced while flagging data from transient searches. In Section 3, we will present our observations with the LOFAR Observatory and our transient simulations. In Section 4, we will discuss the effect of various flagging strategies on simulated transients. In Section 5, we will discuss the findings of our transient simulation results, along with a potential solution to identify astrophysical transients mistakenly flagged as RFI. In Section 6, we will present our conclusions from this research.

3.2 RFI Flagging Overview

3.2.1 Radio Frequency Interference and Celestial Radio Transients

Radio Frequency Interference (RFI) from man-made sources is emission that can severely contaminate celestial observations by swamping the comparatively weak sky signal received by a sensitive radio telescope. The signature of received RFI in an observation depends on several factors, including the type of radio telescope (single dish or interferometer), the type of observation (continuum, spectral line, beam-formed or time resolved), and the kind of RFI itself. The latter can range from impulse-like bursts, narrow-band, or wide-band RFI, and can be ground-, air-, or space-based (e.g. terrestrial emitters, airplanes, spacecraft).

Temporally restricted RFI bursts are especially pernicious to transient searches due to their resemblance to celestial transients. These can be both band limited (e.g. Jovian bursts) as well as wide band. Thus, extra care needs to be taken to distinguish such transients from RFI, and special RFI detection strategies have been developed based on the class of transient [Ryabov et al., 2004; Kocz et al., 2012].

Interferometers used for imaging observations possess several natural defences to RFI. A long enough spatial separation of the antennas making up a baseline results in a different RFI environment at each antenna, leading to a natural suppression of the RFI signal. Further, the delay tracking of a fixed location in the sky also leads to a delay decorrelation of the RFI signal. The phase tracking of the interferometer also leads to attenuation via fringe washing. Finally, interferometers usually have high enough spatial resolution to be able to isolate a coherent RFI source in the image plane.

In spite of these effects, interferometric observations can still be sensitivity limited by residual RFI, due to the high sensitivity of the telescopes. Interferometers typically use offline post-correlation flagging methods, which can be applied over multiple passes on the data. Of the available post-correlation methods, flagging using thresholding is by far the most common approach taken due to its ease of implementation and its predictable effect on the image noise, where the thresholding occurs on the visibility amplitude per baseline [Offringa et al., 2010]. Another approach uses filtering techniques, where a parametric model of the RFI signal can be built up and subsequently subtracted from the data, but this is computationally expensive and model dependent [Offringa et al., 2012]. Adaptive interference cancellation using an independent estimate of the RFI signal obtained from reference channels also exist, but may not be as effective as the other methods [Barnbaum & Bradley, 1998]. Spatial filtering can be an effective method, where the RFI source is isolated and subtracted from the visibility data [Raza et al., 2002]. However, this is effective only if the RFI is significantly correlated at the antenna sites. Higher order statistics can also be used for RFI flagging [Fridman, 2001], and Spectral Kurtosis in particular has been tested for transient detection [Nita, 2016; Nita & Gary, 2010]. However, the statistical methods such as Spectral Kurtosis require much more data processing in order to calculate the mean and variance, which is less feasible than thresholding methods for large-scale transient surveys.

For telescopes with large data volumes, such as LOFAR or the Murchison Widefield Array (MWA; Tingay et al. [2013]), automated algorithms are needed to manage this process in realistic time. Generally these algorithms use the fact that RFI is much stronger than cosmic signals in the data, and usually forms stripes in a dynamic spectrum that are either narrow in frequency or in time, on a smooth, much lower background. Simple removal of these data from consideration is adequate for most radio imaging.

Visibility based flagging would eliminate only the transients bright enough to cross a high threshold on a single visibility, leaving weaker transients relatively unaffected, and available in the image domain. The latter could be many more in number, based on existing source counts [Cordon et al., 1984]. However, the current lack of a population of such transients and their unknown origins make the reliable and unambiguous detection of such events important, especially for triggering multi-wavelength observations. Detecting the brightest transients is thus essential in the discovery phase.

An illustration of the effects of thresholding based flagging on a bright transient can be seen in Figure 1, where the visibility amplitudes on a single baseline are visualized in the time-frequency domain. A simulated transient of 30 seconds duration has been injected into the visibilities. Through the sequence described in more detail below, the flagger will flag such a transient automatically as contaminated data. As such an example illustrates, it is crucial to understand whether such transient signals spanning a range of amplitudes could potentially be flagged before the data are even examined by the observer. This aim is also important in light of transients such as the one reported by Stewart et al. [2016], and surveys for FRBs using the MWA such as Tingay et al. [2015] and Rowlinson et al. [2016], which all relied on the RFI flagging algorithm, AOFlagger [Offringa et al., 2012], for their analysis. We analyze the performance of this algorithm via simulations.

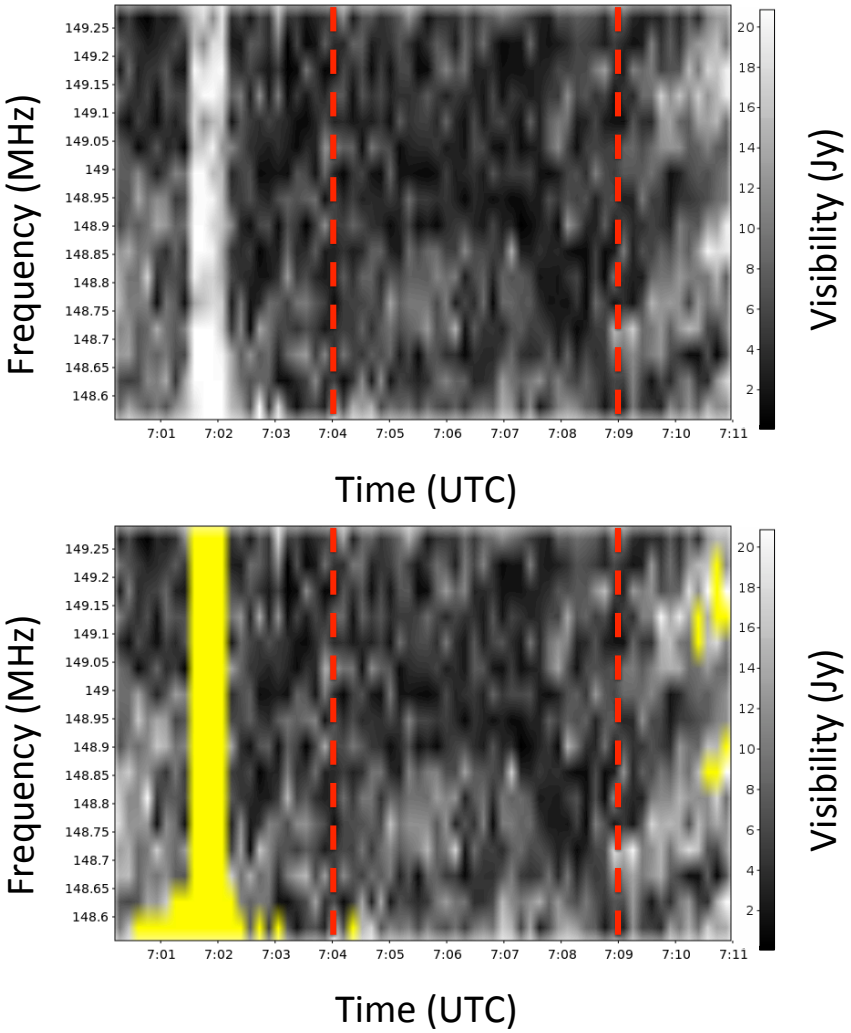

Figuur 3.1 A visual representation of the observed visibility amplitude in the time-frequency domain on the baseline between two LOFAR stations in the visualization program “rfigui,"where the top is an unflagged data set and the lower left has been flagged by AOFlagger (yellow). Here we have an 11 minute LOFAR data set with a 30 second top hat simulated signal of amplitude 10 Jy injected at 07:01:30. This signal was flagged as RFI when the flagging algorithm is run with default parameters, showing the potential perils of using automatic flagging during transient searches. For this baseline, the 10 Jy signal is added on top of the median amplitude values. During the period where no transient is present, indicated as the space between the red dotted lines, when looking at the amplitudes of the visibility time series the data has a standard deviation of $\sim$2.6 Jy and a median value of 5.5 Jy. Here the scale is 20 Jy due to bright amplitude values at the end of a few channels, which are later flagged.

3.2.2 RFI Flagging Algorithms

3.2.3 AOFlagger

The current default RFI flagging software for radio imaging at multiple observatories, which is used routinely during transient surveys such as MWA [Offringa et al., 2015] and LOFAR, is called the AOFlagger. In recent years, AOFlagger has become one of the standard RFI flagging algorithms, and is increasingly used on many radio telescopes. It has been successfully used with data from several interferometric arrays, such as Very Large Array [VLA; Williams et al., 2017], Westerbork Synthesis Radio Telescope [WRST; Adebahr et al., 2017], the Australia Telescope Compact Array [ATCA; Smolčić et al., 2016], the Boolardy Engineering Test Array of the Australian Square Kilometre Array Pathfinder [ASKAP BETA; Allison et al., 2017]. It has also been successfully implemented on single dish telescopes, such as Parkes [Offringa et al., 2012] and Arecibo. [1]

In brief, the AOFlagger is an iterative algorithm which operates on a frequency resolved timeseries of visibilities from a single baseline, and can operate on either a single polarization or a chosen Stokes parameter. It fits a surface to the visibility amplitudes in the time-frequency plane in order to eliminate systematics, e.g., due to fringes from bright sources in sidelobes, and then clips out visibilities with amplitudes crossing a chosen threshold. The flagged visibilities are ignored in the next iteration. The algorithm detects low level RFI using a set of decreasing thresholds, implemented via the SumThreshold algorithm. It has been empirically determined that two iterations of SumThreshold are adequate for flagging [Offringa et al., 2012]. The algorithm consists of the following steps:

- SumThreshold: This is a combinatorial thresholding algorithm where the same dataset is subjected to a set of decreasing thresholds. A threshold χ_M is determined by M, the number of samples in the data set surrounding a candidate data point (visibility amplitude for one time/frequency sample), where M is predefined, and a chosen false detection rate [Offringa et al., 2010]. If the sum of amplitudes of M contiguous visibilities exceeds the threshold χ_M, then all M visibilities are flagged.

  The algorithm processes data in order of decreasing thresholds $\chi_1, \chi_2, ..., \chi_M$, where the thresholds are in units of the visibility amplitude standard deviation, σ. The single sample threshold, χ_1 is the highest, and eliminates really bright and sporadic visibilities. Visibilities flagged by a χ_i threshold are ignored when computing the statistics for applying the next level threshold χ_{i+1}. These lowered thresholds are used to eliminate low-lying RFI not filtered by χ_i. Visibilities comprising such low-level RFI are usually connected to their neighbors in time and frequency, i.e., the connected visibilities form islands of high amplitudes. In the SumThreshold algorithm, the range of applied thresholds depends on the extent of connectivity in all four directions on the time/ frequency visibility amplitude plane.

  For a given baseline, SumThreshold is applied twice in an AOFlagger iteration, first prior to the surface fit in order to ignore RFI when fitting, and then again when the fitting has converged in order to establish the actual flags. The χ_i thresholds are decreased exponentially in every iteration of SumThreshold to increase the sensitivity to low level RFI.

[1] A full list of telescopes which have successfully used AOFlagger, along with the software itself, is available at: https://sourceforge.net/projects/aoflagger/

- **Channel and Time Selection:** Next there is a channel and time selection step which flags problematic channels and time steps which may be fully contaminated but have not yet been flagged. In the case of channel selection, the RMS value of visibilities across channels for a given time slice is computed. The time series of these RMS values are Gaussian smoothed, and the standard deviation, σ, of the difference between the RMS time series and the smoothed time series is computed. Any RMS value found to be $> 3.5\sigma$ results in the entire set of channels for that time slice to be flagged. The same occurs for the time axis. This step, akin to conventional thresholding, is implemented in order to facilitate faster convergence.

- **Surface fitting:** Surface fitting then occurs, which removes fringes caused by strong sources in the side lobes in order to increase accuracy. This is done with a Gaussian kernel sliding window in both time and frequency space, and is a time-consuming step when compared to the other steps.

Overall, for routine data collection and subsequent imaging, the AOFlagger has proven to be a fast and accurate automatic flagger, particularly in the relatively high-RFI LOFAR radio environment [Offringa et al., 2013b], although it can, in some cases, flag data that is not RFI [Offringa et al., 2013b]. Normally, however, this is not an issue in routine observatory observations because mistakenly flagged data are a small percentage of the entire data set [Offringa et al., 2013b, 2015].

A flow chart of AOFlagger can be seen in Figure 3.2.

3.2.4 Concerns for Transient Searches

The aim of this paper is to investigate the effect of AOFlagger on transient observations. As such, in addition to investigating the impact of the default AOFlagger settings on transients, we also focused on modifying the flagger to see whether an automatic RFI flagging method could be adapted for the needs of transient searches. In particular we examined the following:

- One particular concern was that the thresholding algorithm, SumThreshold, works in both the time and frequency domains. This means brief, bright transients that are broadband, and a focus for image-plane surveys, could be flagged due to their sudden increase of power in the time domain.

- Time selection steps that rely on sigma clipping may inaccurately flag data that are not RFI. For example, a sudden, brief transient in an otherwise quiet radio field would have its amplitude suddenly change by a high value compared to the data around it, and it could be mistaken for RFI and flagged at this stage.

- In addition to this, the lowered thresholds in later steps of SumThreshold for data connected in either frequency or time are also a concern for transient searches. This is because such lower thresholds may flag fainter transients which are normally not affected by the high single sample threshold χ_1.

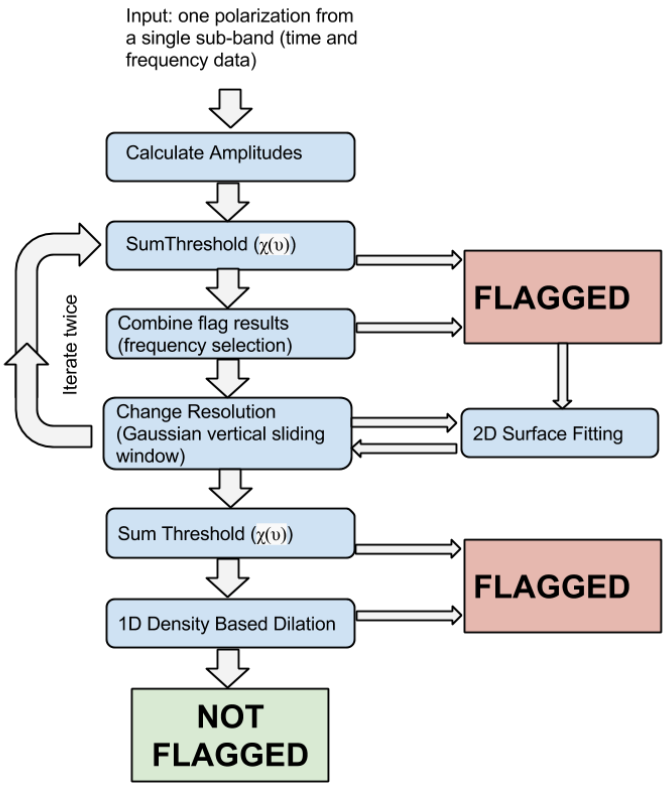

Figuur 3.2 A flow chart of the steps in AOFlagger. The steps that we focused on in particular for our transient specific analysis for modification are the SumThreshold and time selection steps. We should note the input can also be a Stokes parameter of interest.

3.3 Observations and Transient Simulations

3.3.1 Observations

As we were interested in examining the consequences of RFI flagging on real data, we wanted to examine a field observed with LOFAR. For this purpose, we chose data taken with the LOFAR telescope as an extra target observation during routine transient monitoring observations (Fender et al., in prep) using one sub-array pointing of the telescope, where the beam is formed using the innermost antennas from each station. We then focused on a low-RFI 11 minute measurement set, taken on February 10, 2013, using one beam at 149 MHz with a bandwidth of 781 kHz, along with calibrator source Cygnus A.

First, the data were pre-processed using the standard methods with LOFAR: they were flagged for RFI using AOFlagger [Offringa et al., 2012], and the data calibration and imaging were carried out using the method described by Broderick et al. [2016]. We used a model of the source for the calibration of the calibrator sub-bands, and then the gain amplitudes and phases were transferred to the target field data as outlined by Heald et al. [2011]. We also refined the calibration further by performing phase-only self-calibration on the target field, as outlined by van Haarlem et al. [2013b].

For imaging, we used the AWImager [Tasse et al., 2013]; a maximum projected baseline of 6 km was chosen to ensure a reliable image from the given u,v coverage for the 11 min snapshot, leading to an angular resolution of approximately 34 arcsec. This image has a total field of view of 11.35 deg^2 in a circular region. We measure a noise standard deviation of 25 mJy by generating a noise map of the image using the sourcefinding script PySE (Carbone et al., submitted)

3.3.2 Observational Detection Bounds on Transient Fluence

We quantified the effect of a threshold based flagging strategy on a bright transient by simulating the presence of such a transient on a dataset with a realistic noise and RFI instantiation. Assuming no sources in the field, the measured LOFAR System Equivalent Flux Density (SEFD) for a core station in HBA mode is 3 kJy at 150 MHz [van Haarlem et al., 2013b]. To calculate the expected noise on a single visibility amplitude of a single polarization, ΔS, under the assumption of a high SNR, we use the equation

$$\Delta S = \frac{1}{\eta} \frac{SEFD}{\sqrt{2}\sqrt{\delta\nu t_{int}}} \tag{3.1}$$

where $\delta\nu$ is the channel width, and t_{int} is the integration time. For our data, the system efficiency η is assumed to be 1, and the two stations making up the baseline are assumed to have the same SEFD. The subband of 781 kHz was spectrally resolved into 16 channels, with visibility integration times of 10 seconds. This corresponds to a noise ΔS of 3.04 Jy per visibility of a single polarization. Thus, if the time selection threshold is set at its hard-coded default as 3.5σ, we can calculate that any transient signal exceeding $S_{flag} = 10.6$ Jy will be flagged for these observing parameters.

For determining the theoretical flagging bounds, we used the single sample threshold due to its effect on short duration (1 sample) transients. At the single sample level, two thresholds are

applied to the data by AOFlagger: χ_1, and the time selection threshold of 3.5σ. We calculate the flagging bound based on the time selection threshold due to it being the more conservative (lower) of the two.

We estimated the standard deviation of the visibility amplitude over the 11 minute observation for a typical baseline, and this was found to be $\sim$2.5 Jy. We chose to carry out our analysis with the per visibility noise derived from the empirical SEFD due to the expectation of LOFAR sensitivity to be of that order, and the fact that there can be systematics in the visibility time series such as fringes due to bright sources which can bias the measured statistics.

When flagging is applied on high time and frequency resolution visibilities and then transient detection is carried out on the integrated image, transients can be lost due to two reasons:

- The transient flux per visibility exceeds the used flagging threshold, or
- The transient fluence (flux×duration) is lower than the image detection threshold.

Thus, in order to be detected via imaging, transients need to lie in the region where they are bright enough to be visible in the integrated image, but not bright enough to be flagged.

3.3.2.1 Effect of transient duration on its detection

We can compute the duration a transient should have to be visible in an integrated snapshot by limiting the transient flux to be < 10.6 Jy to prevent its visibility flagging. Due to computational limitations, typical searches for these brief signals in the image domain will be in integrated images, such as the 11 minute observations of LOFAR. As outlined by Trott et al. [2013], if an image is longer than the width of the transient signal duration, then we can estimate the minimum transient signal flux density, $S_{min,w}$, that LOFAR is sensitive to using:

$$S_{min,w} = S_{min,11min}\frac{\Delta t}{w} \tag{3.2}$$

where $S_{min,11min}$ is the sensitivity of one snapshot image multiplied by the detection threshold, $\Delta t = 660$ s is the snapshot integration time, and w is the duration of the transient. The background noise of the 11 minute integrated image is 25 mJy beam^{-1}, as measured by our observations, and we set a 5σ detection limit for a source in the image plane, corresponding to a source flux of $S_{min,11min} = 0.125$ Jy in an image with $\Delta t = 660$ s. From Equation 3.1, we showed sources with a flux greater than 10.6 Jy will be flagged. Therefore, using Equation 3.2, we can show that transients with a duration $w \lesssim 8$ s would not be detected due to the channel selection step, although transients of longer duration could also be flagged due to other parts of AOFlagger such as SumThreshold or surface fitting.

3.3.2.2 Fraction of transients lost

We can quantify the fraction of transients lost due to flagging from time selection and fluence by assuming that the number density of transient sources is constant in a Euclidean universe. Therefore, knowing the cumulative flux distribution, $log(N)-log(S)$, of the sources, and assuming a simple power law, $N(> S) \propto S^{-\alpha}$, we can determine the fraction of sources expected to be lost due to flagging via:

$$\frac{N(S > S_{flag})}{N(S > S_{min,11min})} = \frac{S_{flag}^{-\alpha}}{(S_{min,11min}\frac{\Delta t}{w})^{-\alpha}} \tag{3.3}$$

For $w < 8$ s, all transients will be lost. For longer durations, let us take the concrete example of a Euclidean universe, where transient sources are evenly distributed and radio source count for transient sources brighter than a given flux would follow a cumulative distribution for logN-logS $\alpha = 1.5$. For a transient which lasts 5% of the measurement set, or 33 seconds, $\sim 11\%$ of transients detectable in the image will be flagged based on Equation 3.3. These transients are significant because they give the highest S/N, and are the best candidates for multi-wavelength follow up and understanding the physics behind the source population.

The fraction of transients expected to be rejected via a flagging operation is dependent upon the transient duration and the extent of the imaging dwell time. It increases as the transient duration reduces to approach the hard limit of 8 seconds, after which all transients are undetectable. The fraction flagged then decreases as the transient duration increases to that of the snapshot integration. With theoretical boundaries set up, we populated the range of fluences expected to be affected by a default flagging strategy in order to quantify the effect of flagging on transient detection.

3.3.3 Transient Simulations

In order to quantify the effect of a flagging algorithm based on applying a set of thresholds on the visibility amplitude, we added simulated transients onto an actual LOFAR observation which would have a realistic noise and RFI instantiation. We focused our efforts on an observation at 149 MHz consisting of a single snapshot of 11 minutes and with a total bandwidth of 781 kHz, where the visibilities were already calibrated. These data were available at a spectral resolution of 48.8 kHz and a temporal resolution of 10 seconds. As described earlier, data were already flagged once with AOFlagger, and the visibilities calibrated. The tests we describe here involve a secondary RFI flagging step after the transient was simulated and added to the calibrated visibilities, but before imaging. This was done in order to study the effect of the flagger on this one injected transient signal in particular, as this data was very low in the amount of RFI it contained.

For these simulations a transient source was injected in the center of the image by taking a model point source, transforming it to visibility space, and adding this to the recorded visibilities. This was done using BlackBoard Selfcal (BBS) software [Loose et al., 2008] where the temporal profile of the point source was a top hat signal of a given strength and duration in the image's sky model. After this injection, the data were processed as usual through the imaging pipeline described in Section 3.3.1, and the resulting image was then analyzed.

This transient's amplitude was varied from 0.5-10 Janskys in half Jansky intervals, and the duration was varied from one second to 2 minutes on a logarithmic scale. This range, based on estimates laid out in Section 3.3.2, was selected to probe the range of χ thresholds which depend on both the amplitude and connectivity of visibilities. The resulting images for these data were then run through the sourcefinding script PySE where the integrated flux at the location of the injected transient was measured via a forced fit of a point source. We should note that the data we injected the transient into had already been run through RFI processing during pre-processing

when it was first obtained for analysis– that is, the typical RFI processing for LOFAR imaging. The tests we describe here involve a secondary RFI flagging step after the transient was simulated and injected into the data but before imaging in order to study the effect of the flagger on this one injected transient signal in particular, especially as these data contained a very low amount of RFI.

The results of this test before any secondary flagging steps were introduced can be seen in Figure 3.3. Here, we see the brightest detected transients correspond with the brightest simulated transients with the longest duration, and the measured flux of the transient (indicated by the color bar) is consistent with expectations from Equation 3.2. This measured flux then decreases for transients of shorter durations and brightnesses, until they are undetectable because they are either too faint, too brief, or a combination of the two. After this, the same tests were conducted but with an automatic flagging step added after the transient was injected into the data in order to measure the effects of RFI flagging on the transient signal.

We also performed a similar simulation for radio transients of varying brightness but with 2 minute long snapshots, which was the same duration as the Rowlinson et al. [2016] MWA survey for brief transients, flagged and calibrated using 2 minute measurement sets but imaged in 30 second increments. This was done in order to understand how flagging for transients would affect shorter measurement sets, because the number of data samples is much smaller for such observations. For these measurement sets, we focused on transients that were up to 60 seconds duration in the data, or half the length of the observation. Further, we note that because AOFlagger has a recommendation of at least 1,000 time steps to be passed through the flagger, and this is impossible for MWA-length measurement sets, we edited the time window in which the measurement sets are divided for flagging into smaller increments than is recommended.

3.4 Effect of Flagging Strategies on Simulated Transients

3.4.1 Default AOFlagger Settings

We first considered only the effects of the standard AOFlagger settings on the flagging of transients, in order to characterize the typical effects of such flagging on bright transients. In an 11 minute measurement set, we found that if the simulated transient was of a longer duration than two minutes there was no statistically significant difference in the observed flux of the transient—that is, the transient was unaffected by flagging algorithms because its long duration would not trigger the thresholding algorithm. However, when considering brief transients of durations less than two minutes, as seen in Figure 3.3, differences between the two become apparent. If automated flagging is used, very brief transients ($\sim \Delta t < 60$ s) of a detectable brightness will be flagged out altogether by the automated flagging software because of the single sample threshold, χ_1, designed to eliminate very bright and sporadic RFI.

It should be emphasized that the transient signal measured at the end of this procedure would be weaker than the original signal injected, as described by Equation 3.2. Thus, in Figure 3.3, for example, the transient signal flux measured is less than the amount injected.

Longer, brighter transients (60 s $< \Delta t <$120 s), however, are no longer flagged completely by AOFlagger, but do appear to have a lower flux when compared to the original strength of the

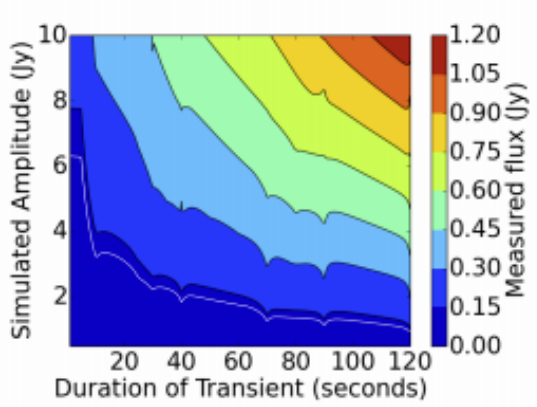

(a) 11 minute measurement set with unflagged data.

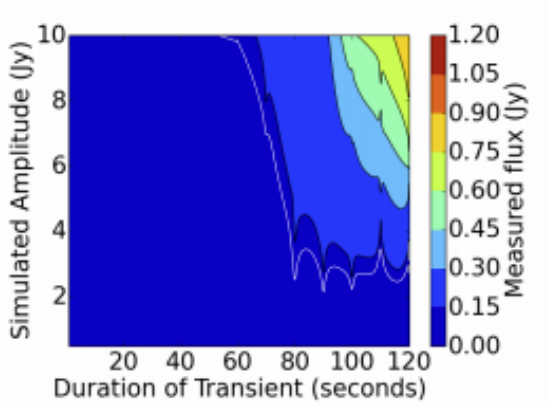

(b) 11 minute flagged with the default flagger.

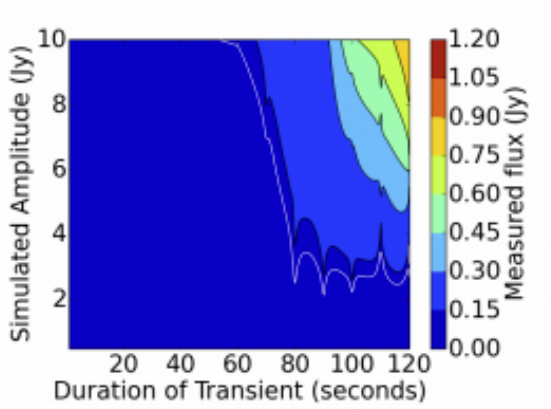

(c) 11 minute flagged data with 6.5σ time selection.

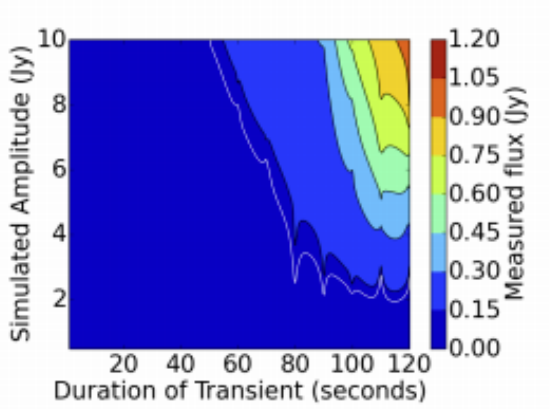

(d) 11 minute flagged data, no time selection.

Figuur 3.3 Observed fluxes for transient signals of a given amplitude and duration in an 11 minute measurement set. Here, the top left plot is with unflagged data, the top right plot is for the default flagger, the bottom left is with the modified flagger with SumThreshold only in the time direction but a time selection $\sigma > 6.5$, and the bottom right is with SumThreshold only in the time direction and with no time selection steps. The unusual contours in the flagged data between levels is due to a sampling effect caused by the sampling window size of the RFI algorithm and brightness of the transient. The white contour corresponds with $S_{min,11min} = 0.125$ Jy, which is the 5σ limit derived from the RMS map of the image.

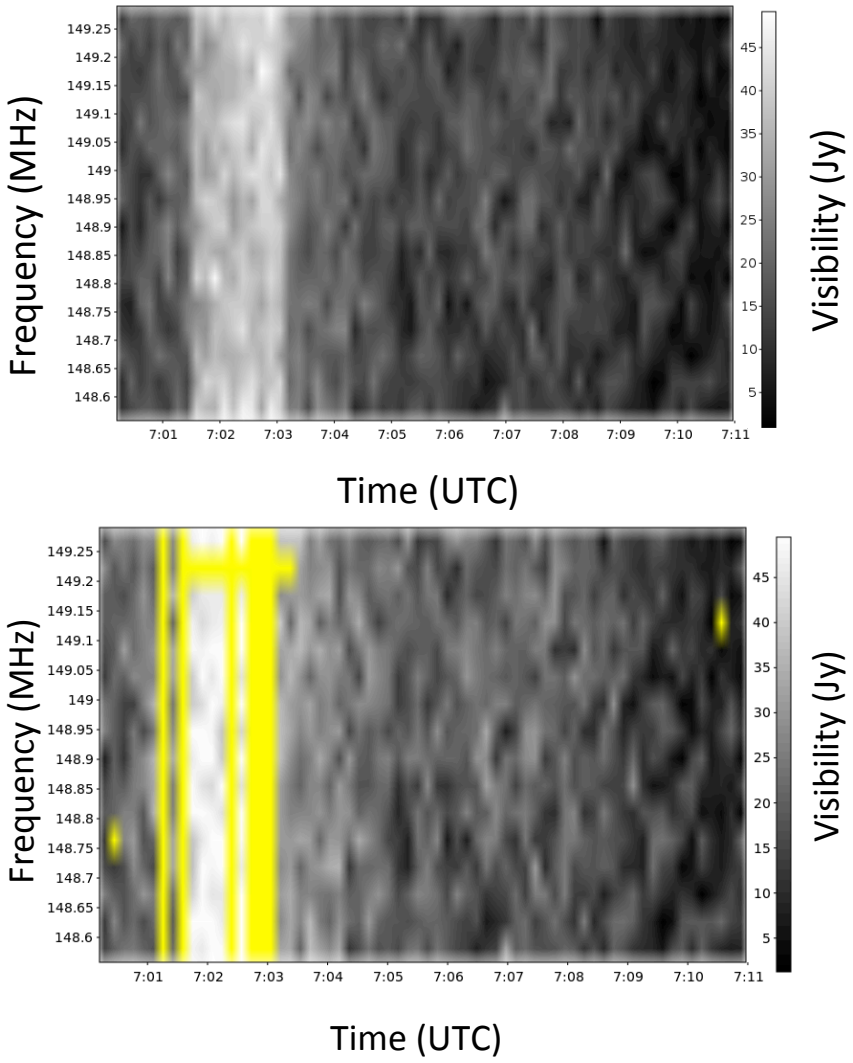

Figuur 3.4 An illustration of "partial flaggingïn the time-frequency domain for two antennas from the program "rfigui,"where the top is an unflagged data set and the bottom has been flagged by AOFlagger (yellow). Here we have an 11 minute data set with a top hat transient from an injected signal with 10 Jy amplitude and 90 seconds duration. A sizeable percentage of the transient is flagged as RFI but not the entire signal. As such, the transient would be detected, but not at its full brightness or duration. We note that some data around the transient which does not contain the injected signal are also flagged.

injected transient. A check of what is being flagged in the visibilities reveals that the transient signals are becoming "partially flagged,"where some, but not all, of the signal is being flagged as RFI. An example of such partial flagging can be seen in Figure 3.4. Exactly how much of the signal is being flagged is dependent on the intensity and duration of the signal. We also note that sections of the non-transient data are also being flagged by the flagger in order to eliminate any potential fringes of RFI within the data due to dilation, which can further affect the measured fluxes in the data stream. For example, for the unflagged data, the 10 Jy transient with 2 minutes duration had a measured flux of 1.24 Jy (Figure 3.3). For the flagged data, the same transient was measured as 1.44 Jy in brightness. This was because while $\sim 30\%$ of the transient signal was flagged, a large fraction of data surrounding the signal which did not contain a transient was also flagged by AOFlagger, making the effective Δt of the measurement set shorter than for the unflagged data. This can have a significant effect: for example, a 4 Jy transient of 100 seconds duration is easily detectable in the unflagged data, but does not exceed the 0.125 Jy detection threshold in the image.

For fainter transients of $\lesssim 3$ Jy, we also see flagging occurring. This is because the connectivity of the data points making up the transient signal trigger the lower thresholds of the SumThreshold algorithm. Excluding the parts of Figure 3.3 where transients are too diluted to be detected, we find that $\sim 10\%$ of transients are flagged due to this underlying connectivity. This percentage was arrived at by taking the ratio of the number of surviving transients to the total number of injected transients.

Similar effects are seen in the measurement sets of 2 minutes duration. These results can be seen in Figure 3.5, where again the upper left plot shows the fluxes measured in unflagged data, and the upper right plot shows results from the flagged data set. We see a similar plot to what was seen before with the longer measurement set in that the briefest transients ($\simeq \Delta t < 25$ s) are all entirely flagged. After this, transients of longer duration (25 s $< \Delta t <$60 s) are visible, but not at their full strengths because they are partially flagged in visibility space. This can have consequences: for example, a 10 Jy, 20 second transient would be detectable in the unflagged data, but would not exceed the detection threshold in the flagged data.

Thus, flagging both template datasets results in loss of the brightest transients, as well as dilution of the recovered flux of unflagged transients.

3.4.2 Modified Flagger Results

In light of the results with default flagging, we carried out modifications of the flagger parameters, and tested the modified flagger on the same data. Specifically, this test focused on two points: adjusting SumThreshold to work “in time direction” only, and to increase the σ cutoff value for the time selection steps. These tests were carried out for both the 2 minutes duration and 11 minutes duration measurement sets.

First, we note that only adjusting one parameter but not the other did not yield a significant difference in flagging results compared with the default AOFlagger settings– that is, if SumThreshold was adjusted the transient would still be flagged as RFI by the $\sigma > 3.5$ time selection step, and vice versa. When adjusting both SumThreshold to only flag “in time directionänd increasing the sigma cutoff for time selection, however, does yield results that are noticeably different

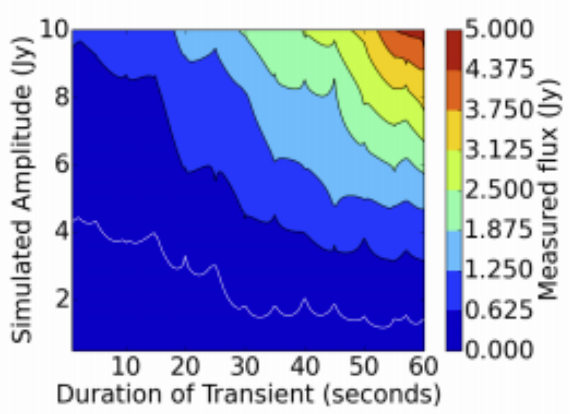

(a) Two minute measurement set with unflagged data.

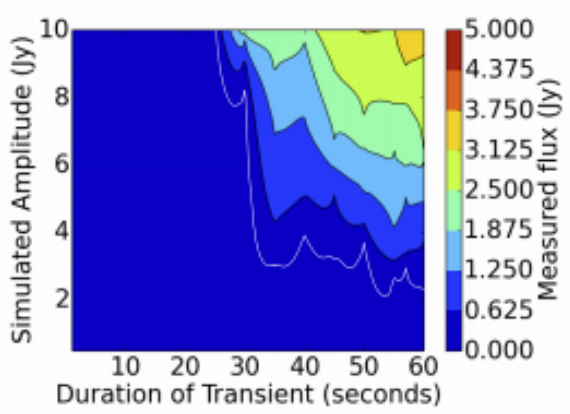

(b) Two minute data flagged with default flagger.

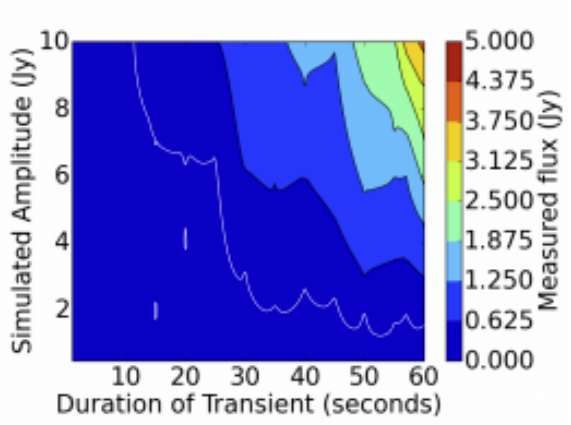

(c) Two minute flagged data with 6σ time selection.

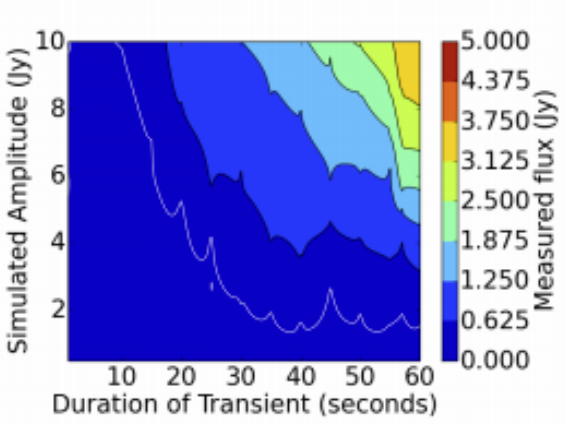

(d) Two minute flagged data, no time selection.

Figuur 3.5 Observed fluxes for transient signals of a given amplitude and duration in a 2 minute measurement set. Here, the top left plot is with unflagged data, the top right plot is for the default flagger, the bottom left is with the modified flagger with SumThreshold only in the time direction but a time selection $\sigma > 6.5$, and the bottom right is with SumThreshold only in the time direction and with no time selection steps. The white contour corresponds with $S_{min,11min} = 0.55$ Jy, as measured from the RMS map as calculated by the sourcefinding script PySE.

from the default AOFlagger settings.

For the 11 minute measurement set, two such examples can be seen in the lower plots of Figure 3.3. In both plots SumThreshold is set to "in time direction" only, but in the lower left panel the time selection step is set to $\sigma > 6.5$, which we chose as an arbitrary cutoff to demonstrate the effect of a higher threshold for time selection. In the lower right plot, the time selection is deleted from the algorithm altogether. We see that although all the transients less than 60 seconds in duration are still flagged, there is some improvement in the number of transients that are visible because they are only partially flagged in both cases. The scenario where the time selection steps are eliminated also shows better results than the panel with a $\sigma > 6.5$ time selection step included. For example, while in the lower left the $\lesssim 3$ Jy signals are all flagged by the lower threshold, in the lower right only the $\lesssim 2.5$ Jy signals are now affected. This can be attributed to the decoupling of the time dimension in the SumThreshold connectivity based thresholding. Further, the 4 Jy, 100 s transient described earlier which was flagged out would now exceed the detection threshold with the modified flagger that had no time selection present in the default AOFlagger, although would still be flagged if 6.5σ time selection was applied.

We see similar results for the 2 minute measurement set, where the modified flagger results are shown in the lower plots of Figure 3.5, with the $\sigma > 6.5$ cutoff on the left hand side plot, and eliminated altogether in the lower right plot. Here, while all transients of a duration less than 20 seconds are still flagged, we have partial flagging occurring on a larger fraction of transients that are of (25 s $< \Delta t <$60 s) duration. Once again, the lower right panel, which contains no time selection step, flags fewer transients than the lower left panel with a time selection step of $\sigma > 6.5$. Here, for example, we see that the 10 Jy, 20 second transient which did not exceed the detection limit with the default flagger now exceeds the detection limit in both modified flaggers.

3.4.3 Observer Alert Script

We have developed a script which can alert the observer when a potential transient is in the data stream. This is based on a comparison on the percentages of data flagged between the two RFI flaggers, and various criteria which are expected to be different between transient RFI and an astrophysical signal. In this script, first the RFI flagger checks the percentage of data flagged for the entire data set in each channel- a standard output given in AOFlagger- for both the default and modified strategies. Although we expect the modified flagger to flag slightly less data than the default flagger, due to less stringent criteria, a transient in the data stream would also create a difference in the percentage flagged between the two methods. As such, the difference between the percentage flagged can then be used to then determine whether a signal is in the data stream which may be worth further examination through further selection criteria.

To illustrate this phenomenon, we show the difference in percentages flagged for a 10 Jy signal of various durations injected into an 11 minute observation in Figure 3.6, illustrated with blue points. We include the difference in percentage between the two strategies when no transient is injected in the data stream (red), and the percentage that would occur if the default flagger fully flagged the transient but the modified flagger did not (yellow), for reference. What we find is even for the shortest duration transient we tested, of 1 second length, there is already a $\sim 1.5\%$ difference between the percentage of the measurement set flagged between the default and modified

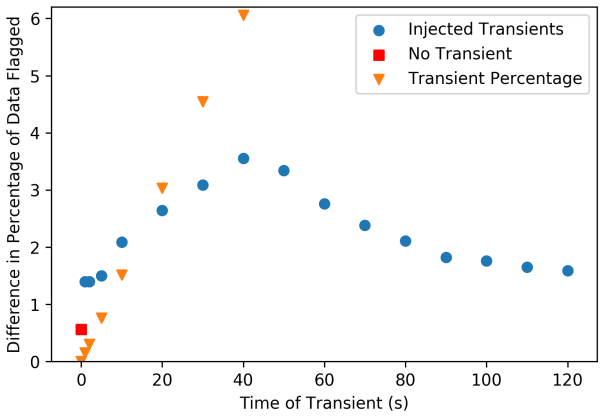

Figuur 3.6 The difference in percentage of data flagged between the default and modified strategies for an injected 10 Jy signal in an 11 minute measurement set, for different durations of time (blue). We provide the difference for the same data set with no injected transient (red) for reference. For the injected flagged transients, the difference between the two strategies steadily increases until it peaks at 40 seconds, and then begins to decrease (there is 1-4% more data flagged by the default flagger, depending on the transient duration). We attribute this decrease to the emergence of partial flagging, described in Section 3.4.1, in transients of this duration and longer. For reference, we also provide the percentage of the transient if it was completely flagged by the default but not at all by the modified flagger (yellow) until 40 seconds, when partial flagging begins to occur. We will note that error bars in the average values in this plot were included, but are too small to be visible.

flaggers, which exceeds the amount seen with no transient (where there is a 0.53% difference). Visual inspection of the data flags in rfigui confirmed this is because while both flaggers will flag these shortest transients in our case (Figure 3.3), the default flagger will additionally flag extra data before and after the transient which is not part of the signal. The percentage flagged will then steadily increase as the percentage of time the signal is in the measurement set increases, until it peaks at 40 seconds, and begins to decrease. This is the duration where partial flagging becomes a factor, where a fraction of the transient signal is flagged instead of the entire signal. This results in the difference in percentages flagged beginning to decrease, although this difference still remains consistently higher than when there is no transient in the data.

Based on these tests, we decided that any difference in percentage of data flagged between the two strategies that exceeds 1% is of interest for further inspection for these transients. For this, we used PYRAP to sort the data by time series and to search for the following:

- First, we searched the data set for baselines where the columns FLAG_ROW were set, which occurs when all the data in a row of visibilities are flagged. We chose this parameter because a broadband transient signal is expected to be visible in all frequency channels in our data set, but a flag in only a few channels is expected to be RFI. We should note that because LOFAR data sets often include a flagged row in the final time step of data, we set our script to disregard the last ten seconds of the measurement set.
- Next, we searched the flagged row by baseline. Specifically, we were interested in occurrences when FLAG_ROW was true for a majority of baselines at a given time. We chose this parameter because a flagged row only present in a small number of baselines is likely caused by local interference, whereas an astronomical signal would be visible in most baselines (although not all, depending on the noise within that specific baseline).
- Finally, if all these criteria are met, the script returns a note to the observer, informing them a potential transient is present in their data.

We tested our script on our transient signals seen in Figure 3.6, which were 10 Jy signals in a 11 minute measurement set. We found that when we used the above criteria, our script returned a potential transient alert for all our signals. However, raising the difference in percentage flagged to 3% only returned a potential transient alert for the transients of 30-50 second duration, and no alert was returned when the difference was set in excess of 4%.

3.5 Discussion

3.5.1 Observed AOFlagger Effects

From our simulation work, it appears that AOFlagger, which is relied on by many radio surveys searching for brief transient signals, could be flagging out existing bright, brief transients in the data stream. In particular, it is possible all bright transients of just a few seconds' duration sufficiently bright to be detected in the integrated images have been flagged in previous surveys such as those of Stewart et al. [2016], if they were present. Re-examination of the data's flagged sections with the observer alert script could aid transient detection. Using the observer alert

script does not require the more computationally intensive imaging steps to identify previously flagged data which merits further inspection, but any astrophysical transient would originate from one point in the sky and converge to a point source upon imaging. RFI, on the other hand, is much more likely to originate from the ground, meaning it would result in a noise-filled image if only affecting a few baselines.

Even when a transient is detected using default flagging methods, however, consideration should be given that the signal can be subject to partial flagging by RFI detection algorithms. Further, some non-transient data is also flagged by the flagger, which can further affect measured fluxes. Checking any candidate transient signals for partial flagging in the data stream (if possible) should be carried out in any transient detection follow up to determine the true flux density.

3.5.2 Effect of the Duration of an Observation

Further, it is important to consider the merits behind searching for very brief transients on the order of a few seconds in an 11 minute observation. Although using such an observation length is not ideal for transients of this duration, often such observations are “piggybacked"for transient searches from observations such as sky surveys. For such a survey, even if imaging is done using shorter timescales than 11 minutes, the data are typically flagged over the full length of the measurement set before it is sliced into smaller increments for imaging in order to obtain a sufficiently large number of data points for flagging to be conducted. This means that even if imaging is done in smaller increments that are more ideal for transient searches, potential transient signals on the order of a few seconds duration would be flagged.

In addition to this, our tests using a 2 minute observation show transients on the order of a few seconds duration are flagged even when flagging is conducted over a shorter time span when using LOFAR data. There are surveys being conducted at these time scales, such as Rowlinson et al. [2016] which sought to constrain the transient rate by searching for signals on the order of a few seconds by taking 2 minute measurement sets from MWA and slicing them into 30 second images. However, due to the differences between the LOFAR and MWA telescopes in SEFD and channel width, while the brightest transient signals would have been flagged, if they existed, it seems likely that fainter transient signals would have survived the flagging process. Repeating the simulations in this work using an MWA measurement set would answer where precisely these cutoffs lie. Further, if the brightest transient signals were flagged, the subsequent transient rate estimates from this and other surveys currently do not incorporate the effects of RFI flagging, and this should be taken into account.

3.5.3 Effects of AOFlagger Modifications and Detection Script

There are some modifications to AOFlagger that can be implemented in order to detect more transients than one would with the default settings (though, it should be emphasized, not all transients). In particular, for AOFlagger, setting SumThreshold to only operate in the time direction, and eliminating all time selection steps (i.e., only use frequency selection), would be advisable when seeking transients of ∼minute long durations within snapshots. For transients on the order of tens of seconds long, flagging on a shorter time scale is advised, but consideration

must be given to the number of time steps and resolution in the length of the data stream to ensure flagger accuracy.

We note that while these modifications to the RFI flagger will still result in automated flagging of narrow-band RFI, and not have significant effects on low-level RFI in general, implementing such a modified flagger opens up the possibility that bright, broadband RFI signals will no longer be flagged.

We have also presented in Section 3.4.3 a potential solution in which the differences between the default AOFlagger and modified version, along with the known distinguishing properties between RFI and transient signals, are used to alert the observer when a transient may be present in the data stream. This script could be further modified depending on the class of transients in which the observer is interested- for example, a search for minutes-long transients such as that described in Stewart et al. [2016] could use a higher difference in percentage flagged than 1%, which would decrease the number of false positives. Further, the data could be examined for the sequential occurance of the script criteria in several time stamps, which would indicate a potential transient of longer duration.

We would recommend that an observer using this method choose their own parameters for the difference in percentages flagged, and the percentage of baselines with completely flagged visibilities at a given time, as these are dependent on the location of the telescope, and the resolution of the data acquired by the observer. In particular, because some transient-like RFI will still meet the criteria outlined above, it is inevitable that a percentage of false positives will be present in the data stream. We will investigate the effects of a modified flagger with alert script on a high-RFI observation with injected transients and different data resolutions in a future publication.

Another possibility could be to also implement the dictionary approach outlined by Czech et al. [2017], which focused on filtering so-called transient RFI (defined in Czech et al. [2017] as non-constant RFI). This work demonstrated the use of Markov models to identify transient RFI as a sequence of sub-events, and could reliably extract transient RFI events from a larger observation. Given the similarities between transient RFI and astronomical sources, investigating the differences between the two categories with this method could provide another useful tool in distinguishing between the two.

3.6 Conclusions

Using the typical LOFAR imaging survey mode as an example, we have investigated the effects of automated RFI flagging on transient signals of astronomical origin. We have demonstrated that RFI flagging with AOFlagger can flag out brief transients < 60 s in duration. Further, we have calculated that all bright transients > 10.6 Jy would be flagged when the integration is 10 s and the frequency integration is 48 kHz. Fainter signals of a few Jy brightness are also affected, depending on the extent of connectivity of the signal in the visibility plane.

For transient signals of > 60 s length in a measurement set of 11 minutes duration, the majority of the expected bright transient signals will survive the flagging process– albeit with diminished flux due to "partial flagging"– and we have a good chance of observing these transients. However,

the original data would need to be reexamined in order to determine whether part of the signal was mistakenly flagged. Reexamining the data may also reveal shorter transients already flagged in the data stream, which face a significant loss. For a shorter LOFAR measurement set of just 2 minutes duration, it is equally likely that 100% of radio transients of up to 20 seconds duration would be flagged. Approximately 60% of transients on the order of tens of seconds or longer will be detected, but partially flagged.

We have presented a script which can be used to alert an observer that the flagged data contains a potential astrophysical transient, which identified our simulated transients which had been flagged. This could be used for any additional investigations into whether there are any transients in already flagged RFI data, in both previous survey data and in any future data preflagged to default settings.

For future transient surveys, in order to minimize the flagging of bright transients in the image plane we recommend modifying AOFlagger by only applying thresholding in the frequency direction, and eliminating the time selection steps in the algorithm that rely on sigma clipping. With these steps in place, a larger fraction of bright transient signals will be seen, though likely partially flagged. We also recommend the implementation of an observer alert system based on the differences between transient RFI and astronomical sources, to allow the correct identification of these signals.

Acknowledgements

We acknowledge support from the European Research Council via the Advanced Investigator Grant no. 24729. This work is also supported in part by European Research Council Advanced Grant 267697. LOFAR, the Low Frequency Array designed and constructed by ASTRON, has facilities in several countries, that are owned by various parties (each with their own funding sources), and that are collectively operated by the International LOFAR Telescope (ILT) foundation under a joint scientific policy. We would like to thank the LOFAR Observatory staff for their assistance in obtaining and the handling of this large data set. We would also like to thank Andre Offringa for answering some initial questions. S.C. acknowledges funding support from the UnivEarthS Labex program of Sorbonne Paris Cité (ANR-10-LABX-0023 and ANR-11-IDEX-0005-02).

Hoofdstuk 4

A Time-Domain Survey of Luminous Local Radio Sources on 25 Year Timescales

Yvette Cendes, Bryan Gaensler, Casey Law

to be submitted

Abstract

We consider 117 extragalactic radio sources as potential transient and variable sources that were listed in a catalog of luminous local (<108 Mpc) radio sources as possible persistent Fast Radio Burst (FRB) counterparts. We used observations from the Very Large Array Sky Survey (VLASS) at 3 GHz and the Faint Images of the Radio Sky at Twenty-cm (FIRST) catalog at 1.4 GHz ∼25 years earlier in order to establish changes in flux over time in our sample, and compiled detailed light curves using data from multiple radio surveys for 19 of these sources. We also included X-ray observations of these sources, both from the ROSAT catalog and from analysis of available Swift XRT images, but our X-ray analysis yielded non-detections. We identified one transient candidate, FIRST J235351.4+075835, which has faded monotonically by a factor of ∼ 2 over 20 years, which may be due to a tidal disruption event (TDE) or neutron star merger. However, this source lacks an optical counterpart, so a definitive conclusion on the nature of the source would require additional optical follow-up observations. We conclude the rest of our sources which display variable behavior are likely caused by low excitation radio galaxies (LERG) with emission caused by low, inefficient accretion onto a supermassive black hole.

4.1 Introduction

Thanks to rapidly advancing detector technology and faster computing speeds, in recent years the discovery of radio transients on short time scales (seconds to months) has become increasingly common. However, considerably less effort has been devoted to finding transients on the longer time scales that last from years to decades. In particular, the lack of extensive sub-mJy data over a significant fraction of sky before large surveys such as the NRAO-VLA Sky Survey [NVSS; Condon et al., 1998] and the Westerbork Northern Sky Survey [WENSS; Rengelink et al., 1997] in the ∼1990s greatly limited the ability to find decades-long transients until sufficient time had passed.

Despite this limitation, the radio sky does have transient and variable sources on these timescales. Bannister et al. [2011] conducted a 22 year survey with the Molonglo Observatory Synthesis Telescope (MOST) at sub-mJy sensitivity at 843 MHz, and discovered several dozen transient and variable radio sources. The Stripe 82 survey [Mooley et al., 2016] using the Very Large Array (VLA) established that ∼3.9% of the thousands of radio sources observed at 3 GHz varied by >30% over a two year period. By comparing the TIFR GMRT Sky Survey Alternative Data Release 1 (TGSS ADR1) and the GaLactic and Extragalactic All-sky Murchison Widefield Array (GLEAM) survey catalogues, taken ∼3 years apart, Murphy et al. [2017] reported the discovery of one transient at these time scales. However, no comprehensive all-sky census on these timescales for transients exists because of the limitations of the data and the long time spans involved.

In the majority of the above cases, the transients and variables discovered are thought to be related to active galactic nucleus (AGN) activity [Bannister et al., 2011; Mooley et al., 2016]. Given that the majority of radio sources in the sky for which S > 1 mJy are AGN at 1.4 GHz [Becker et al., 1994], this is unsurprising. AGN variability on time scales of years to decades is common, and is likely to be due to relatively minor changes in the accretion flow onto a supermassive black hole that lead to a temporary change in luminosity of the non-thermal accretion disk emission [Tadhunter, 2016].

Within the population of AGN, quiescent, low-level AGN activity accounts for ∼60% of all AGN [Padovani et al., 2011], and they reach a peak luminosity in radio of $L_\nu = 10^{27} - 10^{34}$ erg s^{-1} Hz^{-1} at ∼1.5-5 GHz [Woo & Urry, 2002; Mooley et al., 2016]. Compared to this, more exotic long-term transients related to gamma-ray bursts (GRBs), tidal disruption events (TDEs), supernovae (SNe), and others are much more rare [Metzger et al., 2015; Mooley et al., 2016].

The recent discovery of FIRST J141918.9+394036 has provided an intriguing example of one such exotic long-term transient. FIRST J141918.9+394036 was a decades-long radio transient that faded by a factor of ∼50 over 23 years, and was no longer detectable by 2017 [Law et al., 2018]. It is thought the source is the afterglow of an off-axis ("orphan") long GRB.

FIRST J141918.9+394036 is also notable because it was discovered through a search relying on archival data from several previous surveys. First, the source was listed in a catalog of luminous ($L_\nu \leq 10^{28}$ erg s^{-1} Hz^{-1}) persistent radio sources in the nearby universe (defined as z ∼ 0.025, or < 108 Mpc), compiled from the Faint Images of the Radio Sky at Twenty-cm survey catalog [FIRST; Becker et al., 1994] and cross-matching with optical databases [Ofek, 2017]. The motivation behind the Ofek [2017] catalog was to identify nearby radio sources similar to the persistent radio counterpart of the first localized repeating Fast Radio Burst [FRB; Lorimer et al., 2007; Spitler

et al., 2016; Chatterjee et al., 2017], known as FRB 121102, and to establish the number density of bright compact persistent sources in the local universe. Ofek [2017] identified 122 possible candidates, of which 11 were identified as candidates associated with active star formation regions. Follow-up of these latter sources was conducted using available images from the Very Large Array Sky Survey (VLASS; Lacy et al. [2019]), which has recently observed the entire sky as seen from the VLA at 2-4 GHz. This in turn revealed the transient nature of FIRST J141918.9+394036.

Although Law et al. [2018] established that there is at least one interesting source within the Ofek [2017] catalog, the majority of sources from Ofek [2017] that were not associated with star forming regions were not examined in that work. Further, while Law et al. [2018] did measure the fluxes in VLASS for five of the other ten sources whose data was available at the time, the detailed light curves for these sources were not compiled. Here, we present the results of the remaining candidate radio signals in the Ofek [2017] catalog in the available VLASS images. From this analysis, we discuss the discovery of new luminous radio transients, and demonstrate what we can learn about variability in the local universe from studies that take advantage of several decades of existing archival data.

This chapter is divided as follows. In Section 4.2, we discuss the catalog of sources used in this study, their spectral indices, and the method used to identify variable sources. In Section 4.3, we discuss the 19 noteworthy sources identified through our study, including light curves that cover a range of ∼10-30 years, and discuss possible origins for all of them. In Section 4.4, we discuss these sources and how they are classified, including what they can tell us about the local variable radio population for luminous sources, the rate of variable luminous radio sources in this volume, and how our study compares to previous surveys. Finally, in Section 4.5, we discuss the conclusions from this work, and make recommendations for future searches.

4.2 Source Characterization

4.2.1 Catalog of Sources

The Ofek [2017] catalog of sources was compiled on the assumption that at least some FRBs will have luminous, persistent synchrotron radio counterparts similar to that seen for FRB 121102. As such, 122 potential FRB hosts were identified in or near nearby galaxies (< 108 Mpc, or $z < 0.025$) to place an upper limit on the number density of such sources in the local universe. Specifically, these sources had luminosities $> 10\%$ of the FRB 121102 persistent source luminosity, and had counterparts in FIRST, a project designed to produce the radio equivalent of the Palomar Observatory Sky Survey of the North and South Galactic Caps. Previous work by Law et al. [2018] focused on VLASS observations of the six candidates that overlapped with the optical light from a galactic disc or compact star forming galaxies which had been observed by VLASS at the time of publication, which were conditions similar to that found for FRB 121102 [Bassa et al., 2017]. The rest of the sources (85) that were within 1" of the center of the galaxy, and the 26 remaining sources not overlapping with light in a galactic disk, were not examined by Law et al. [2018].

To study these remaining sources, we used VLASS observations, which cover the entire sky as seen from the VLA at 2-4 GHz to 2.5" resolution. Our data included all the first VLASS epoch ("epoch 1"), which covered 100% of the observable sky from the VLA, although some

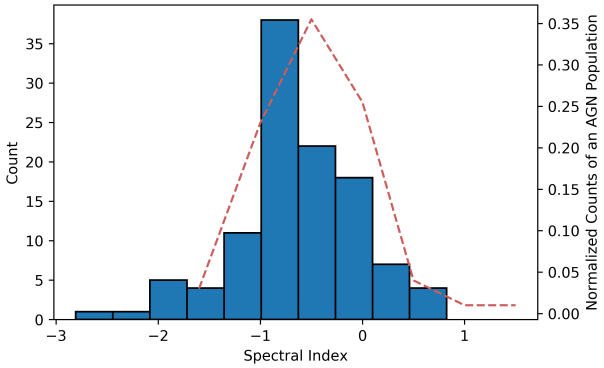

Figuur 4.1 The distribution of spectral indices for the sources in this work. We have overlaid the normalized counts for AGN from Zinn et al. [2012] for reference.

gaps exist due to calibration or noise issues. Epoch 1 is the first of three VLASS epochs, which will be separated by 36 months, with a sensitivity of 120 μJy/beam in a single epoch. Pipeline processed "quicklook" images are made available soon after observations take place, and we used these images to search for counterparts to the Ofek [2017] sources. We found that 117 individual sources were observed from the Ofek [2017] catalog, with two duplicate sources in the original catalog, and visual inspection of the VLASS images confirmed that three individual listings were, in fact, associated with a single extended source[1].

4.2.2 Source Association Between Surveys and Determination of Spectral indices

Our first step was to identify counterparts between the VLASS and FIRST images. As the typical positional error in FIRST images is $\leq$ 0.3"[White et al., 1997], and the VLASS positional error is $\sim$0.5"[Lacy et al., 2019], we defined the association radius between images as 1" in order to identify counterparts.

We obtained the VLASS quicklook images from the VLA archives that contained the sources in the Ofek [2017] catalog. We then used the source finding package Aegean [Hancock et al. (2018)] to create a file containing peak fluxes for all the sources in each VLASS image, and then

[1]The extended Source is located at 12:05:48.207, +20:27:48.27

checked for sources at the coordinates listed for our sources by Ofek [2017]. Once identified, we searched for catalog sources within our defined association radius of 1" from the VLASS sources, and found that all counterparts were within 1" of the source positions. All but three sources were detected to $\geq 3\sigma$ confidence. We discuss these sources in Section 4.3.

Next, we calculated a spectral index (α) for each source (rightmost column, Table 20), defined as:

$$\alpha = \frac{\log \frac{S_F}{S_V}}{\log \frac{\nu_F}{\nu_V}} \tag{4.1}$$

where S_F is the peak flux in FIRST, S_F is the peak flux in VLASS, ν_F is the mean frequency of FIRST (1.4 GHz), and ν_V is the frequency of VLASS (3 GHz). This was done because a spectral index calculation assumes the source has not varied, and thus an extreme or unusual index might be a sign of source variability. We calculated α based on the peak flux of the source in the FIRST catalog at 1.4 GHz, and our obtained VLASS peak source fluxes at 3 GHz.

The histogram distribution of these spectral indices can be seen in Figure 4.1. For the sources not detected in VLASS, we calculated the spectral index limit from the 3σ noise limit at the location of the coordinates, as measured in a forced fit using Aegean.

The coordinates for these sources, as well as their peak fluxes in FIRST, NVSS, VLASS and calculated spectral indices, are available in Table 20. A histogram of the spectral index distribution can be seen in Figure 4.1 as calculated from their peak fluxes in FIRST and VLASS. For reference, we have overlaid the distribution of spectral index for the population of AGN studied by Zinn et al. [2012], who calculated a 1.4 to 2.3 GHz spectral index for 120 AGN. We can see that our population as a whole has a steeper spectral index than the average. We also see there is an excess of sources for which $\alpha < -1.5$ in our source distribution when compared to that of the AGN population, and fewer positive sources than expected when compared to the Zinn et al. [2012] distribution.

4.2.3 Identifying Variability

As our primary interest lies in transient and radio sources, we adopted the variability statistic (V_s) defined by Mooley et al. [2016]. This is based on the flux densities of a source between two epochs and their respective errors:

$$V_s = \left| \frac{(S_1 - S_2)}{\sqrt{\sigma_1^2 + \sigma_2^2}} \right| = \left| \frac{\Delta S}{\sigma} \right| \geq 4.3 \tag{4.2}$$

Our threshold is V_s= 4.3 as defined by the t-statistic lying beyond the 95% confidence interval [see Equation 1 and associated footnote; Mooley et al., 2016].

Because FIRST and VLASS were at different frequencies (1.4 GHz and 3 GHz, respectively), we corrected the VLASS data in ΔS assuming a spectral index of -0.7, as an average value for α typical for nonthermal sources [de Gasperin et al., 2018]. We found that, once corrected, ten of our sources met our definition of variability, which we note in their relevant sections in Section 4.3.

For the ten individually identified sources, we compiled light curves spanning several decades based on existing data beyond what was included in Table 20. Additionally, we compiled light curves for seven sources identified as potential FRB counterparts by Ofek [2017], and two sources which displayed typical spectral indicies (α $\sim$-0.7) for illustrative purposes, for a total number of 19 sources studied in greater detail. The surveys we examined with data in the GHz regime were the high resolution imaging of survey data of Stripe 82 at 1.4 GHz [Hodge et al., 2011], and the Green Bank 4.85 GHz survey [GB6; Gregory et al., 1996]. At lower frequencies, we examined data from the VLA Low Frequency Sky Survey Redux [VLSSr; Peters et al., 2014] at 74 GHz, the 150 MHz TIFR GMRT Sky Survey (TGSS) survey using GMRT [Intema et al., 2017], the WENSS survey using the Westerbork Radio Telescope at 325 MHz [Rengelink et al., 1997], and the GaLactic and Extragalactic All-sky Murchison Widefield Array [GLEAM; Hurley-Walker et al., 2017] covering 72-231 MHz.

In addition to survey data, we examined the VLA archives and obtained several images that contained our sources of interest, stretching from 1984 to 2015. We include details of these images, where they exist, in their respective sections below.

For each of these data sets, we obtained the relevant radio images of the source, and used the sourcefinder Aegean to obtain the peak flux for the total intensity counterpart of the source at the FIRST coordinates. If the source was not detected with this method in the image, we performed a forced fit at the FIRST coordinates to obtain a 3σ upper limit on the radio source. We have starred each source in Table 20, and discuss our findings for each source below. We should also note that, for consistency in the light curve, we also re-measured the peak flux of our sources directly from FIRST images (as opposed to relying on the FIRST catalog values as we did in Section 4.2.2). In all cases, the fitted peak flux measured by the Aegean software was lower than the catalog value, and we include the updated spectral indices for these sources in their respective sections.

We also searched NASA's "GRB-CAT"compilation[2] and the 4Br BATSE gamma-ray burst catalog [Paciesas et al., 1999] for possible GRBs coincident with our radio sources. In all cases, all coincident GRBs had enormous (>20°) positional uncertainties, so we did not find these associations significant in relation to our sources.

We also examined the HEARC X-ray catalog for potential X-ray sources. We found that two sources had ROSAT catalog entries [Voges et al., 1999] coincident with the same location as the radio source. Additionally, we found six sources were coincident with archival Swift X-Ray Telescope [XRT; Burrows et al., 2005] observations, which we reduced and analyzed using standard practices. We discuss these X-ray findings in their relevant sections.

Additionally, we also did a visual inspection of all our sources using optical data from Sloan Digital Sky Survey [SDSS; York et al., 2000]. We include these in Section 4.3 where relevant.

4.3 Noteworthy Sources

The following are the sources that we looked at in greater detail. They are all sources considered interesting due to their variability statistics, as outlined in Section 4.2.3, or because they were

[2]See https://heasarc.gsfc.nasa.gov/grbcat/

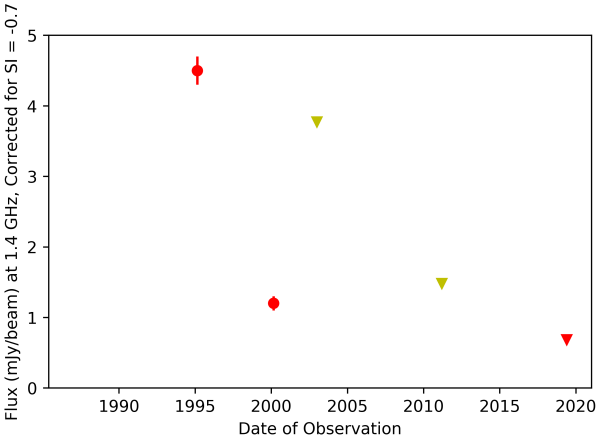

Figuur 4.2 Light curve over time for FIRST J143052.2+060209.6. Light curve for FIRST J143052.2+060209.6, corrected to 1.4 GHz for a spectral index of -0.7. We plot detections from 1.4 to 3 GHz in red, and 150 MHz in yellow, so as to distinguish between high and low frequency bands. Circular points signify detections of the source, and triangles are for the 3σ upper limits for non-detections. Here, we omit the data from Table 4.1 that are non-constraining.

one of the FRB-associated candidates noted by Ofek [2017].

4.3.1 Missing source: FIRST J143052.2+060209.6

FIRST J143052.2+060209.6 is notable in our survey because it was not detected in VLASS, for a 3σ upper limit of <0.4 mJy. This resulted in an implied spectral index of <-1.6. The source was detected by NVSS and FIRST, but was not detected by GB6, VLSSr, VLASS, or TGSS (Table 4.1). The light curve corrected for spectral index is visible in Figure 4.2, where we can see that it has decreased in brightness over time and has not been detected since 2000.

The host galaxy of the source is 2MASX J14305227+0602096, which is 113.2±7.9 Mpc distant [Hernández-Fernández et al., 2012]. This allows us to calculate a luminosity at peak flux in FIRST of $L = 6.9 \times 10^{28}$ erg s^{-1}Hz^{-1}. FIRST J143052.2+060209.6 is located at the center of its host galaxy.

Date of Observation	Peak Flux (mJy)	Observations	Frequency (GHz)
1987	<9	GB6	1.45
1995-02-27	4.5 ± 0.5	NVSS	1.4
2000-02-07	1.2 ± 0.2	FIRST	1.4
2003-09-20	<126	VLSSr	0.075
2011-02-11	<16	TGSS	0.15
2019-05-08	< 0.4	VLASS	2-4

Tabel 4.1 Table of flux values over time for FIRST J143052.2+060209.6. All non-detections are listed as 3σ upper limits.

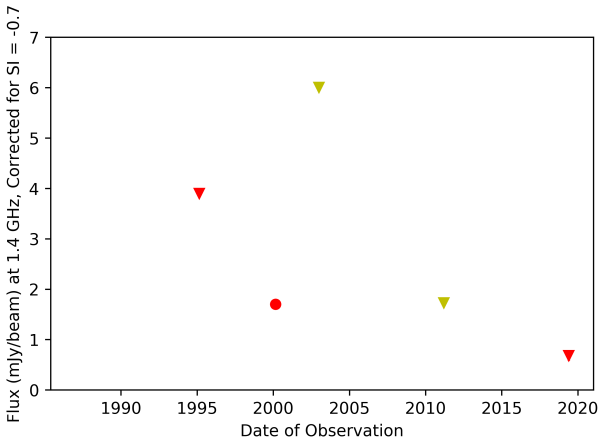

Figuur 4.3 As in Figure 4.2, but for FIRST J141430.5+060955.4.

4.3.2 Missing source: FIRST J141430.5+060955.4

FIRST J141430.5+060955.4 is notable in our survey because it was also not detected in VLASS, for a 3σ upper limit of <0.4 mJy. This resulted in an implied spectral index of <-1.9. The source was detected by FIRST, but was not detected by GB6, NVSS, VLSSr, or TGSS (Table 4.2). The light curve corrected for spectral index is visible in Figure 4.3, fitted to a spectral index of -1.2 because of the nearness in time of the high and low frequency FIRST and VLASS observations, respectively. We can see that this source was only detected once, when it was detected by FIRST as a 1.5 ± 0.1 mJy source.

The host galaxy of the source is LEDA 1295689, which is 92.8±6.5 Mpc distant [de Vaucouleurs et al., 1991]. This allows us to calculate a luminosity at peak flux from the FIRST observation of $L = 3.3 \times 10^{28}$ erg s^{-1}Hz^{-1}. FIRST J141430.5+060955.4 is located at the center of its host galaxy.

Date of Observation	Peak Flux (mJy)	Observations	Frequency (GHz)
1987	<18	GB6	4.85
1995-02-27	<3.9	NVSS	1.4
2000-02-01	1.7 ± 0.1	FIRST	1.4
2003-09-20	<245	VLSSr	0.075
2011-02-18	<20	TGSS	0.15
2019-05-08	<0.4	VLASS	2-4

Tabel 4.2 Table of flux values over time for FIRST J141430.5+060955.4. All non-detections are listed as 3σ upper limits.

4.3.3 FIRST J141043.6+085929

We examined FIRST J141043.6+085929 because it was noted as one of the 11 FRB-associated candidates by Ofek [2017]. The source was detected by NVSS, FIRST, and VLASS, but was

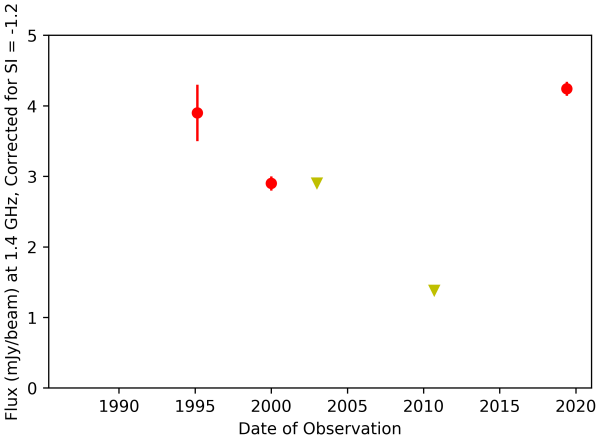

Figuur 4.4 As in Figure 4.2, but for FIRST J141043.6+085929.

not detected by GB6, VLSSr, or TGSS (Table 4.3). The light curve corrected for spectral index is visible in Figure 4.4. We can see that although it is brighter in VLASS than it was during its detection in FIRST, its non-detections by both VLSSr and TGSS indicate the source has fluctuated over time in flux.

The host galaxy of the source is CGCG 074-128, which is 107.3±7.5 Mpc distant [Beers et al., 1995]. This distance allows us to calculate a luminosity at peak flux from the FIRST observation of $L = 5.37 \times 10^{28}$ erg s^{-1}Hz^{-1}. FIRST J141043.6+085929 is located at the edge of a spiral galaxy, 17.7" from the center.

Additionally, we identified several Swift observations where the field of view included FIRST J235351.4+075835. However, none of these images had X-ray counts at its given location. The observation with the longest XRT exposure was observation 00010512023 taken on June 21, 2013, with 513 seconds of XRT exposure.

Date of Observation	Peak Flux (mJy)	Observations	Frequency (GHz)
1987	<80.7	GB6	4.85
1995-02-27	3.9 ± 0.4	NVSS	1.4
2000-01-02	2.9 ± 0.1	FIRST	1.4
2003-09-20	<46	VLSSr	0.075
2010-08-26	<12	TGSS	0.15
2019-05-08	1.7 ± 0.1	VLASS	2-4

Tabel 4.3 Table of flux values over time for FIRST J141043.6+085929. All non-detections are listed as 3σ upper limits.

4.3.4 FIRST J102526.1+171547

We examined FIRST J102526.1+171547 because it was noted as one of the 11 FRB-associated candidates by Ofek [2017]. The source was detected by NVSS, FIRST, and VLASS, but was not detected by GB6, VLSSr, TGSS, or a VLA observation from 1998 from the archives (Table

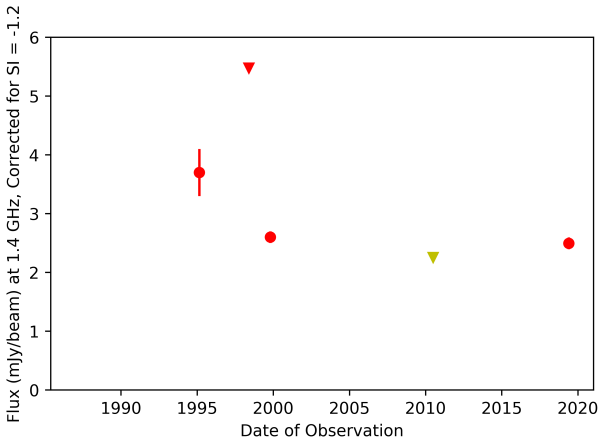

Figuur 4.5 As in Figure 4.2, but for FIRST J102526.1+171547.

4.4). The light curve corrected for spectral index is visible in Figure 4.5, where we can see it has remained relatively steady.

The host galaxy of the source is UGC 05639, which is 86.6±6.1 Mpc distant [Falco et al., 1999]. This distance allows us to calculate a luminosity at peak flux from the FIRST observation of $L = 2.3 \times 10^{28}$ erg s^{-1}Hz^{-1}. FIRST J102526.1+171547 is located in the spiral arm of a galaxy, 7.1" from the center.

Date of Observation	Peak Flux (mJy)	Observations	Frequency (GHz)
1987	<10.5	GB6	4.85
1993-12-06	3.7 ± 0.4	NVSS	1.4
1998-04-24	<5	VLA AM0236	1.51
1999-11-01	2.6 ± 0.1	FIRST	1.4
2003-09-20	<260	VLSSr	0.075
2010-06-15	<6	TGSS	0.15
2019-04-19	1.0 ± 0.1	VLASS	2-4

Tabel 4.4 Table of flux values over time for FIRST J141043.6+085929. All non-detections are listed as 3σ upper limits.

4.3.5 FIRST J105823.6+241355.3

We examined FIRST J105823.6+241355.3 because it was noted as one of the 11 FRB-associated candidates by Ofek [2017]. The source was by FIRST and VLASS, but was not detected by GB6, VLSSr or TGSS (Table 4.5). For the NVSS image, it was determined through the size of the beam fitted by the Aegean software and visual inspection of the NVSS image and comparison to the FIRST image that the NVSS source was unresolved, and in fact comprised of two sources. As such, we did not include this data in our analysis.

The light curve corrected for spectral index is visible in Figure 4.6. The source has decreased slightly in flux from its detections in FIRST to VLASS, assuming $\alpha = -0.7$.

Figuur 4.6 As in Figure 4.2, but for FIRST J105823.6+241355.3.

The host galaxy of the source is NGC 3475, which is 93.3±6.2 Mpc distant [de Vaucouleurs et al., 1991]. This distance allows us to calculate a luminosity at peak flux from the NVSS observation of $L = 2.1 \times 10^{28}$ erg s^{-1}Hz^{-1}. From our VLASS observation, where the source decreased in flux to of 0.7 ± 0.1 mJy, the source decreased to $L = 7.2 \times 10^{27}$ erg s^{-1}Hz^{-1} FIRST J105823.6+241355.3 is located in the spiral arm of a galaxy, 29.8" from the center.

Date of Observation	Peak Flux (mJy)	Observations	Frequency (GHz)
1987	<18	GB6	4.85
1995-12-08	2.1 ± 0.2	FIRST	1.4
2003-09-20	<123	VLSSr	0.075
2011-02-28	<76	TGSS	0.15
2019-06-08	0.7±0.1	VLASS	2-4

Tabel 4.5 Table of flux values over time for FIRST J105823.6+241355.3. All non-detections are listed as 3σ upper limits.

4.3.6 FIRST J140038.9-025122

We examined FIRST J140038.9-025122 because it was noted as one of the 11 FRB-associated candidates by Ofek [2017]. The source was detected by NVSS, FIRST, and VLASS, but was not detected by GB6, VLSSr, TGSS, or a VLA observation from 1983 from the archives (Table 4.6). The light curve corrected for spectral index is visible in Figure 4.7. We can see that the FIRST detection was the highest flux observation, after which the source has been stable at a lower flux.

The host galaxy of the source is NGC 5400, which is 113.7±8.0 Mpc distant [de Vaucouleurs et al., 1991]. This distance allows us to calculate a luminosity at peak flux from the FIRST observation of $L = 2.0 \times 10^{28}$ erg s^{-1}Hz^{-1}. FIRST J140038.9-025122 is located in the spiral arm of a galaxy, 26.4" from the center.

Further, we identified Swift observations which overlapped with the field of FIRST J140038.9-025122. Although there was no source at this location, we can establish an upper limit at 0.2-10

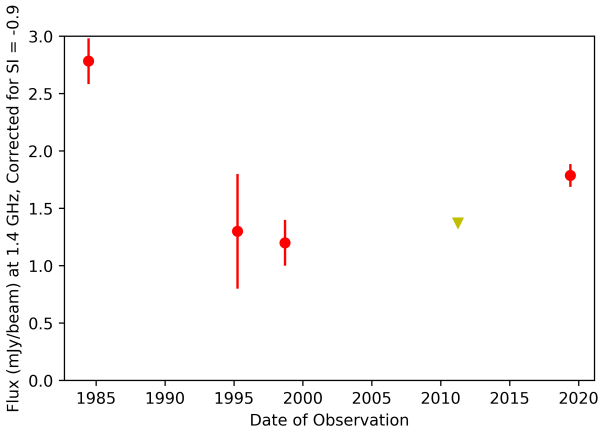

Figuur 4.7 As in Figure 4.2, but for FIRST J140038.9-025122.

keV of 1.0×10^{-3} ct/s (at 90% confidence).

Date of Observation	Peak Flux (mJy)	Observations	Frequency (GHz)
1984-06-10	2.6 ± 0.2	VLA AW0110	1.51
1995-02-27	1.3 ± 0.5	NVSS	1.4
1998-09-04	1.2 ± 0.2	FIRST	1.4
2003-09-20	<360	VLSSr	0.075
2011-03-01	<13	TGSS	0.15
2019-05-01	0.9 ± 0.1	VLASS	2-4

Tabel 4.6 Table of flux values over time for FIRST J140038.9-025122. All non-detections are listed as 3σ upper limits.

4.3.7 FIRST J114529.3+192327

We examined FIRST J114529.3+192327 because it was noted as one of the 11 FRB-associated candidates by Ofek [2017]. The source was detected by NVSS, FIRST, and VLASS, but was not detected by GB6, VLSSr, TGSS, or a VLA observations from 1983, 2000, and 2007 from the archives (Table 4.7). The light curve corrected for spectral index is visible in Figure 4.8. We can see that the FIRST detection was the highest flux observation, after which the source has been stable at a lower brightness. We can see that the source is brighter in VLASS than it was when it was detected in NVSS and FIRST, and underwent a period of non-detection in the interim.

The host galaxy of the source is NGC 3867, which is 104.8±7.87 Mpc distant [Smith et al., 2004]. This distance allows us to calculate a luminosity at peak flux from the FIRST observation of $L = 4.1 \times 10^{28}$ erg s^{-1}Hz^{-1}. FIRST J114529.3+192327 is located in the edge of a galaxy, 33.35" from the center.

Further, we identified Swift observations which overlapped with the field of FIRST J140038.9-025122. Although there was no source at this location, we can establish an upper limit at 0.2-10 keV of 1.5×10^{-3} ct/s (at 90% confidence). However, there is an X-ray source associated with

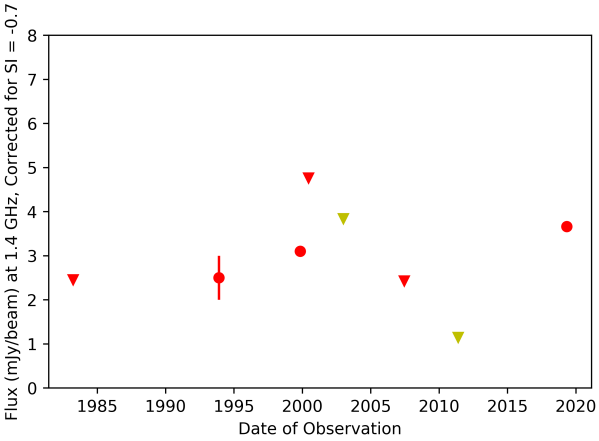

Figuur 4.8 As in Figure 4.2, but for FIRST J114529.3+192327.

FIRST J140038.9-025122. Identified by ROSAT as X-ray source 1RXS J140037.3-025103, the source has a count rate of $1.878 \times 10^{-02} \pm 9.164 \times 10^{-03}$ ct s^{-1} [Voges et al., 1999], and a flux of 4.800×10^{-13} erg $cm^{-2}Hz^{-1}$ [Turriziani et al., 2007]. However, because the ROSAT positional error for this source is 25", and the source is in fact 31" distant from the galaxy, we conclude this is a coincident association.

Date of Observation	Peak Flux (mJy)	Observations	Frequency (GHz)
1983-03-12	<2.4	VLA O34	1.46
1987	<12.6	GB6	4.85
1993-12-06	2.5 ± 0.5	NVSS	1.4
1999-11-01	3.1 ± 0.1	FIRST	1.4
2000-06-15	<4.6	VLA AC540	1.5
2003-09-20	<279	VLSSr	0.075
2007-06-22	<2.4	VLA AC483	1.43
2011-04-15	<12	TGSS	0.15
2019-04-19	2.5 ±0.1	VLASS	2-4

Tabel 4.7 Table of flux values over time for FIRST J140038.9-025122. All non-detections are listed as 3σ upper limits.

4.3.8 FIRST J140255.7+092514

FIRST J140255.7+092514 is notable in our survey because of its extreme spectral index of $\alpha = -1.59$. The source was detected by FIRST, NVSS, VLASS, and a VLA observation from 1983, but was not detected by GB6, NVSS, VLSSr, or TGSS (Table 4.8). The light curve corrected for spectral index is visible in Figure 4.9. We can see that the source increased in brightness from 1983 to its detection in NVSS in 1983, but has decreased in brightness since.

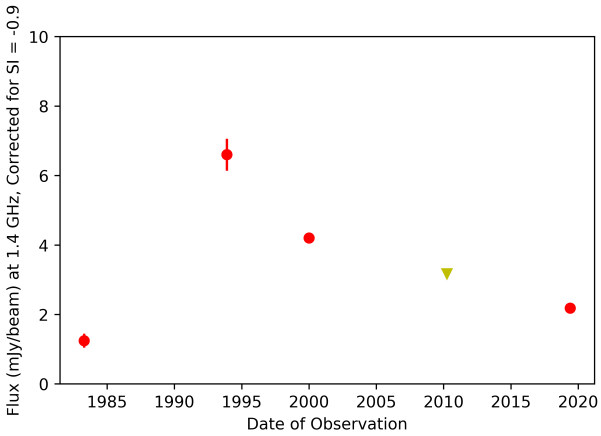

Figuur 4.9 As in Figure 4.2, but for FIRST J140255.7+092514.

The host galaxy of the source is NGC 5424, which is 87.1±6.2 Mpc distant [Falco et al., 1999]. This allows us to calculate a luminosity at peak flux from the FIRST observation of $L = 6.0 \times 10^{28}$ erg s^{-1}Hz^{-1}. FIRST J140255.7+092514 is located at the center of its host galaxy.

Further, we identified Swift observations which overlapped with the field of FIRST J140255.7+092514. Although there was no source at this location, we can establish an upper limit at 0.2-10 keV of 8.5×10^{-4} ct/s (at 90% confidence).

Date of Observation	Peak Flux (mJy)	Observations	Frequency (GHz)
1983-03-16	1.2±0.2	VLA AN0021	1.46
1987	<17	GB6	4.85
1993-12-06	6.6 ± 0.46	NVSS	1.4
2000-01-15	4.2 ± 0.1	FIRST	1.4
2003-09-20	<260	VLSSr	0.075
2010-02-28	<33	TGSS	0.15
2019-05-08	1.1±0.1	VLASS	2-4

Tabel 4.8 Table of flux values over time for FIRST J140255.7+092514. All non-detections are listed as 3σ upper limits.

4.3.9 FIRST J092758.2-022558

We examined FIRST J092758.2-022558 because it was noted as one of the 11 FRB-associated candidates by Ofek [2017]. The source was detected by NVSS, FIRST, and VLASS, but was not detected by VLSSr or TGSS (Table 4.9). The light curve corrected for spectral index is visible in Figure 4.10. We can see that the source has remained fairly steady in flux over this period.

The host galaxy of the source is CGCG 006-045, which is 108.4±7.8 Mpc distant [Jones et al., 2010]. This distance allows us to calculate a luminosity at peak flux from the NVSS observation of $L = 3.2 \times 10^{28}$ erg s^{-1}Hz^{-1}. FIRST J092758.2-022558 is located in the spiral arm of a galaxy, 14.3" from the center.

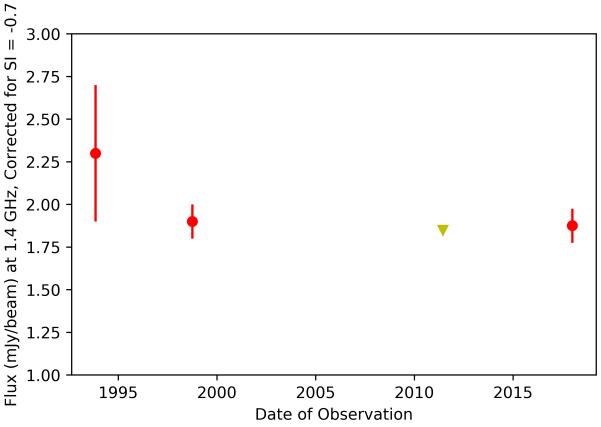

Figuur 4.10 As in Figure 4.2, but for FIRST J092758.2-022558.

Date of Observation	Peak Flux (mJy)	Observations	Frequency (GHz)
1993-11-15	2.3 ± 0.4	NVSS	1.4
1998-09-01	1.9 ± 0.1	FIRST	1.4
2003-09-20	<260	VLSSr	0.075
2011-06-15	<11	TGSS	0.15
2018-01-02	1.1±0.1	VLASS	2-4

Tabel 4.9 Table of flux values over time for FIRST J092758.2-022558. All non-detections are listed as 3σ upper limits.

4.3.10 FIRST J104726.6+060247

We examined FIRST J104726.6+060247 because it was noted as one of the 11 FRB-associated candidates by Ofek [2017]. The source was detected by NVSS, FIRST, VLASS, and TGSS, but was not detected by VLSSr (Table 4.10). The light curve corrected for spectral index is visible in Figure 4.11. We can see that the source has remained steady in flux over this period.

The host galaxy of the source is NGC 3376, which is 91.3±6.4 Mpc distant [Smith et al., 2004]. This distance allows us to calculate a luminosity at peak flux from the NVSS observation of $L = 2.7 \times 10^{28}$ erg s^{-1}Hz^{-1}. FIRST J104726.6+060247 is located away from the center of the galaxy, 5.9" from the center.

4.3.11 FIRST J235351.4+075835

We examined FIRST J235351.4+075835 because it was noted as one of the 11 FRB-associated candidates by Ofek [2017]. The source was detected by FIRST and VLASS, but was not detected by GB6, TGSS or VLSSr (Table 4.11). For the NVSS data, visual inspection confirmed the source was unresolved and had extended emission, so we did not include this data point in our study. The light curve corrected for spectral index is visible in Figure 4.12. We can see that the source has remained fairly steady during this period.

The host galaxy of the source is NGC 7782, which is 74.0±5.2 Mpc distant [de Vaucouleurs

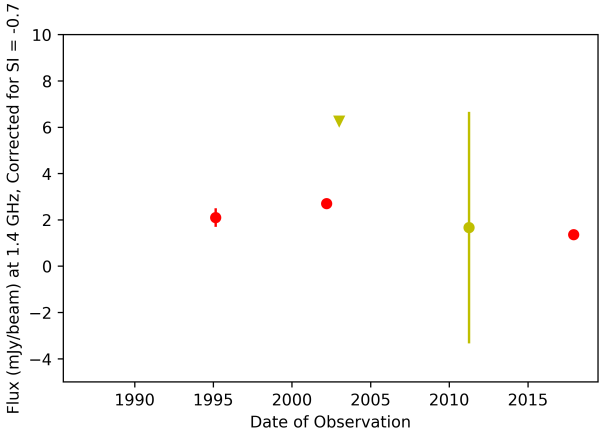

Figuur 4.11 As in Figure 4.2, but for FIRST J104726.6+060247.

Date of Observation	Peak Flux (mJy)	Observations	Frequency (GHz)
1987	<17	GB6	4.85
1995-02-27	2.1 ± 0.4	NVSS	1.4
2002-02-02	2.7 ± 0.1	FIRST	1.4
2003-09-20	<260	VLSSr	0.075
2011-02-28	19±7	TGSS	0.15
2017-11-22	0.8±0.1	VLASS	2-4

Tabel 4.10 Table of flux values over time for FIRST J104726.6+060247. All non-detections are listed as 3σ upper limits.

et al., 1991], which is an early-type spiral galaxy (type Sb) [Pignatelli et al., 2001]. We include an optical image of NGC 7782 with the position of FIRST J235351.4+075835 marked in Figure 4.13. This distance allows us to calculate a luminosity at peak flux from the FIRST observation of $L = 2.5 \times 10^{28}$ erg s^{-1}Hz^{-1}. We include an optical image of NGC 7782 with the position of FIRST J235351.4+075835 marked in Figure 4.13.

Further, we identified Swift observations which overlapped with the field of FIRST J235351.4+075835. Although there was no source at this location, we can establish an upper limit at 0.2-10 keV of 5.9×10^{-5} ct/s (at 90% confidence).

Date of Observation	Peak Flux (mJy)	Observations	Frequency (GHz)
1987	<13	GB6	4.85
2009-04-19	3.9 ± 0.1	FIRST	1.4
2003-09-20	<180	VLSSr	0.075
2010-06-15	<24	TGSS	0.15
2019-05-08	1.1±0.1	VLASS	2-4

Tabel 4.11 Table of flux values over time for FIRST J235351.4+075835. All non-detections are listed as 3σ upper limits.

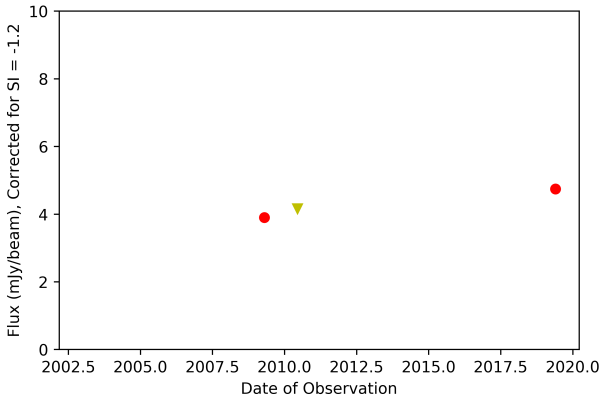

Figuur 4.12 As in Figure 4.2, but for FIRST J235351.4+075835.

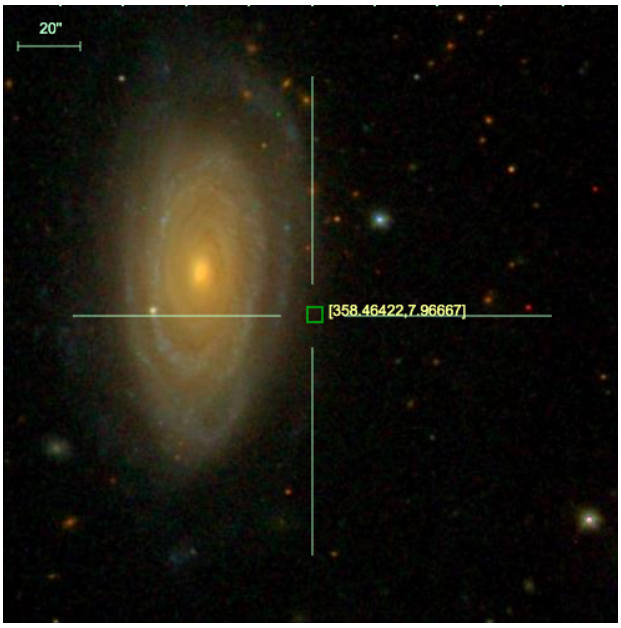

Figuur 4.13 The SDSS image for FIRST J235351.4+075835, including the host galaxy NGC 7782.

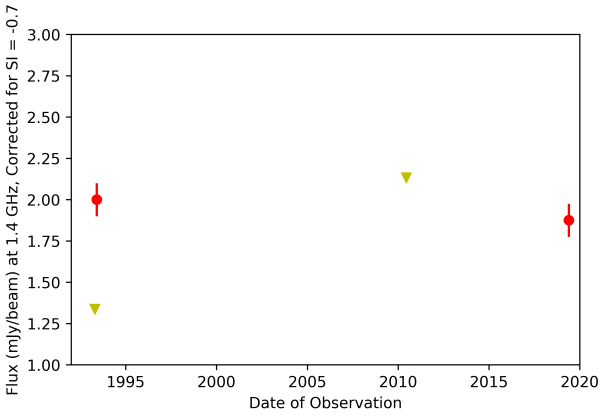

Figuur 4.14 As in Figure 4.2, but for FIRST J131441.9+295959.

FIRST J235351.4+075835 is near a spiral arm, 42.7" from the center of the galaxy. We identified one GRB coincident with this source's position, STK01 08530c, which was a non-triggered event identified after data re-analysis of BATSE data, occurring on October 1, 1991. While the coordinates for this GRB are 40 arcminutes from this source, the error circle for this event is 20.5 degrees. This large error circle means we chose to not associate this source with the GRB.

Further, we identified Swift observations which overlapped with the field of FIRST J235351.4+075835. Although there was no source at this location, we can establish an upper limit at 0.2-10 keV of 5.9×10^{-3} ct/s (at 90% confidence).

4.3.12 FIRST J131441.9+295959

We examined FIRST J131441.9+295959 because it was noted as one of the 11 FRB-associated candidates by Ofek [2017]. The source was detected by FIRST and VLASS, but was not detected by GB6, WENSS, TGSS or VLSSr (Table 4.12). For the NVSS data, visual inspection confirmed the source was unresolved and had extended emission, so we did not include this data point in our study. The light curve corrected for spectral index is visible in Figure 4.14. We can see that the source was not detected by WENSS, but increased in brightness dramatically by the FIRST observation, and has been at the same flux since assuming a spectral correction of -0.7. We also note that the WENSS data were taken at some point during the period of the 23rd of April 1993 and 20th of May 1993, and the FIRST observation was taken May 4, 1993.

The host galaxy of the source is CGCG 160-169, which is 104.8±7.3 Mpc distant [Berlind et al., 2006]. This distance allows us to calculate a luminosity at peak flux from the NVSS observation of $L = 5.0 \times 10^{28}$ erg s^{-1}Hz^{-1}. From the VLASS observation, we can calculate a luminosity of $L = 1.0 \times 10^{28}$ erg s^{-1}Hz^{-1}. FIRST J131441.9+295959 is located at the edge of a spiral galaxy, 20.6" from the galaxy center.

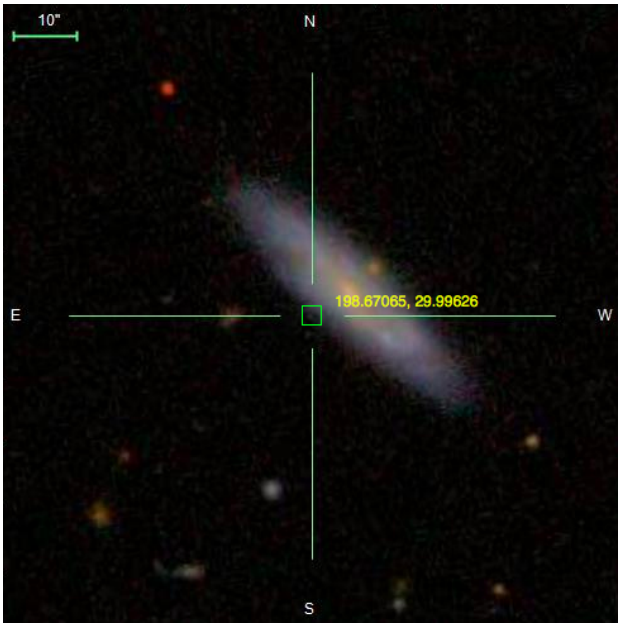

Figuur 4.15 The SDSS image for J131441.9+295959, including the galaxy CGCG 160-169.

Date of Observation	Peak Flux (mJy)	Observations	Frequency (GHz)
1987	<10	GB6	4.85
1993-04-23 to 1993-05-20	<6.5	WENSS	.325
1993-05-04	2.0 ± 0.1	FIRST	1.4
2003-09-20	<230	VLSSr	0.075
2010-06-15	<27	TGSS	0.15
2019-05-08	1.1±0.1	VLASS	2-4

Tabel 4.12 Table of flux values over time for FIRST J131441.9+295959. All non-detections are listed as 3σ upper limits.

4.3.13 FIRST J162244.5+321259

We examined FIRST J162244.5+321259 because it was noted as one of the 11 FRB-associated candidates by Ofek [2017]. The source was detected by NVSS, FIRST, and VLASS, but was not detected by GB6, TGSS, or VLSSr (Table 4.13). The light curve corrected for spectral index is visible in Figure 4.16. We can see that the source has been steadily decreasing in brightness over time.

The host galaxy of the source is 2MASS J16224461+3213007, which is 98.5±6.9 Mpc distant [Berlind et al., 2006]. This distance allows us to calculate a luminosity at peak flux from the NVSS observation of $L = 2.7 \times 10^{28}$ erg s^{-1}Hz^{-1}. FIRST J162244.5+321259 is located away from the center of the galaxy, 5.9" from the center.

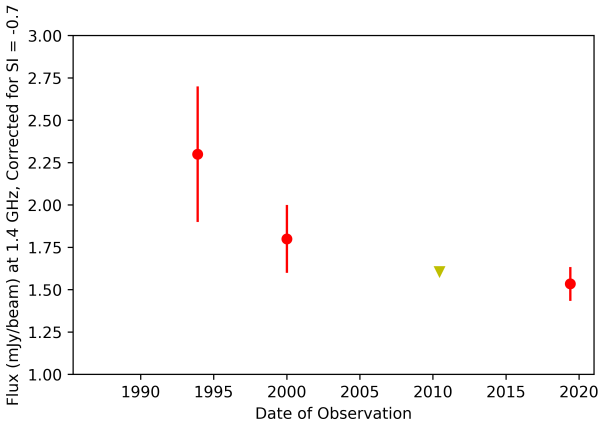

Figuur 4.16 As in Figure 4.2, but for FIRST J162244.5+321259.

Date of Observation	Peak Flux (mJy)	Observations	Frequency (GHz)
1987	<11	GB6	4.85
1993-12-06	2.3 ± 0.4	NVSS	1.4
2000-01-15	1.8 ± 0.2	FIRST	1.4
2003-09-20	<230	VLSSr	0.075
2010-06-15	<18	TGSS	0.15
2019-05-08	0.9±0.1	VLASS	2-4

Tabel 4.13 Table of flux values over time for FIRST J162244.5+321259. All non-detections are listed as 3σ upper limits.

4.3.14 FIRST J141420.8+073058

We examined FIRST J141420.8+073058 because we wanted to include a source with a positive spectral index in our data set. The source was detected by NVSS, FIRST, and VLASS, but was not detected by GB6, TGSS, or VLSSr (Table 4.14). The light curve corrected for spectral index is visible in Figure 4.17. We can see that the source has been varying in brightness over time- it was brightest when observed by NVSS, faintest during FIRST, and then has increased in brightness in VLASS.

The host galaxy of the source is NGC 5519, which is 113.6±8.0 Mpc distant [Hoffman et al., 1995]. This distance allows us to calculate a luminosity at peak flux from the NVSS observation of $L = 3.7 \times 10^{28}$ erg s^{-1}Hz^{-1}. FIRST J141420.8+073058 is located at the center of its galaxy.

4.3.15 FIRST J140031.1-025139

We examined FIRST J140031.1-025139 because we wanted to include a "typical" source in our sample which closely matched the expected spectral index for synchrotron radiation of $\alpha = -0.7$. The source was detected by NVSS, FIRST, and VLASS, and a VLA observation from 1984, but was not detected by GB6, TGSS, or VLSSr (Table 4.13). The light curve corrected for spectral index is visible in Figure 4.18. We can see that the source has been flat over time.

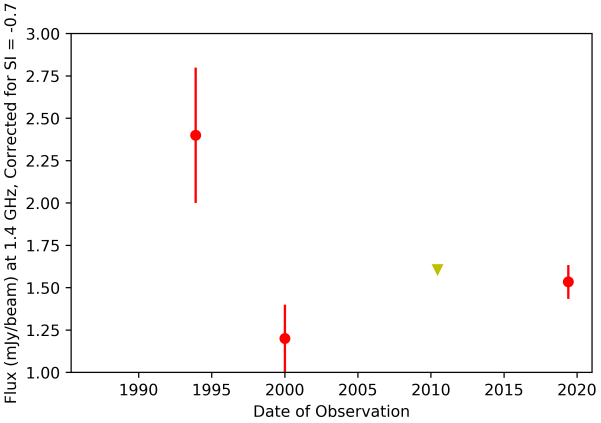

Figuur 4.17 As in Figure 4.2, but for FIRST J141420.8+073058.

Date of Observation	Peak Flux (mJy)	Observations	Frequency (GHz)
1987	<11	GB6	4.85
1993-11-15	2.4 ± 0.4	NVSS	1.4
1998-01-02	1.6 ± 0.1	FIRST	1.4
2003-09-20	<150	VLSSr	0.075
2010-06-15	<18	TGSS	0.15
2018-01-02	0.9±0.1	VLASS	2-4

Tabel 4.14 Table of flux values over time for FIRST J162244.5+321259. All non-detections are listed as 3σ upper limits.

The host galaxy of the source is NGC 5400, which is 113.7±8.0 Mpc distant [de Vaucouleurs et al., 1991]. This distance allows us to calculate a luminosity at peak flux from the NVSS observation of $L = 2 \times 10^{28}$ erg s^{-1}Hz^{-1}. FIRST J140031.1-025139 is located at the center of its galaxy.

Further, we identified Swift observations which overlapped with the field of FIRST J140031.1-025139. Although there was no source at this location, we can establish an upper limit at 0.2-10 keV of 1.0×10^{-3} ct/s (at 90% confidence).

4.3.16 FIRST J033623.0-005257

We examined J033623.0-005257 because it was not detected in the VLASS data. It was also not detected in NVSS data, to a 3σ upper limit of < 0.45 mJy/ beam, nor by VLA project AC0773 in March 2005 when it was <3 mJy/beam at 1.4 GHz. This radio source was detected in FIRST data with a radio flux of 1.3 ± 0.2 mJy/beam, and again in 2013-2014 during an observing campaign for transient radio sources at 3 GHz (VLA project code 13B-370; Kunal et al., in prep) when its flux was 0.571 ± 0.075 mJy (Table 4.16). There were also non-detections in VLSSr, GLEAM, and TGSS at low frequencies. We show the light curve of this radio source along with constraining non-detections in Figure 4.19, where we see the source was only detected during a increase in flux over a few years, and was not detected before or after these epochs.

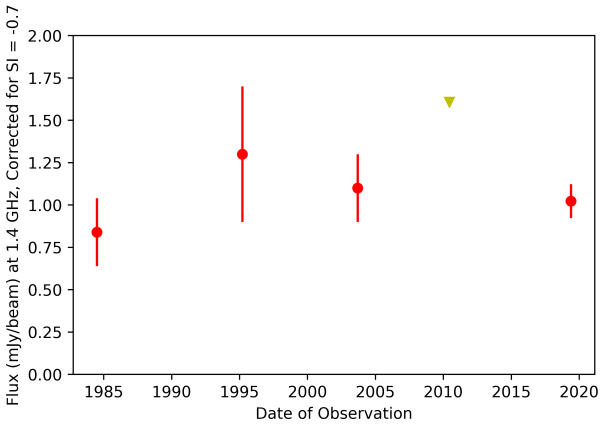

Figuur 4.18 As in Figure 4.2, but for FIRST J140031.1-025139.

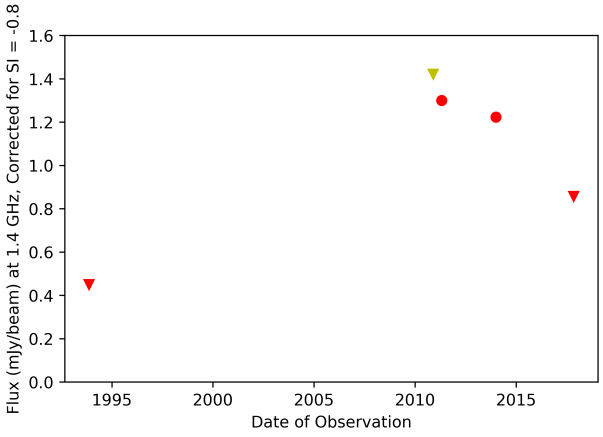

Figuur 4.19 As in Figure 4.2, but for FIRST J033623.0-005257.

Date of Observation	Peak Flux (mJy)	Observations	Frequency (GHz)
1984-06-23	1.2±0.2	VLA AN0021	1.46
1987	<210	GB6	4.85
1995-02-27	1.3 ± 0.4	NVSS	1.4
1998-08-09	1.1 ± 0.1	FIRST	1.4
2003-09-20	<360	VLSSr	0.075
2010-06-15	<18	TGSS	0.15
2019-05-01	0.6±0.1	VLASS	2-4

Tabel 4.15 Table of flux values over time for FIRST J140031.1-025139. All non-detections are listed as 3σ upper limits.

Date of Observation	Peak Flux (mJy)	Observations	Frequency (GHz)
1993-11-15	<0.45	NVSS	1.4
2003-09-20	<486	VLSSr	0.075
2005-03-26	<3	VLA AC0773	1.4
2010-12-14	<13	TGSS	0.15
2011-04-23	1.3 ± 0.2	FIRST	1.4
2013-08-09 to 2014-06-18	<37	GLEAM	0.118
2013-12-19 to 2014-01-14	0.57 ± 0.08	VLA 13B-370	3
2017-12-16	<0.4	VLASS	2-4

Tabel 4.16 Table of flux values over time for FIRST J033623.0-005257. All non-detections are listed as 3σ upper limits.

The position is coincident with the source 2MASX J03362300-0052576, classified as a Seyfert 1 galaxy at redshift z = 0.02 [Toba et al., 2014], and optical images confirm the radio source is coincident with the center of the galaxy (Figure 4.20).

Although the precise timescale is not known, our light curve indicates that FIRST J033623.0-005257 was visible for a period of years, and the optical association with the center of Seyfert galaxy 2MASX J03362300-0052576 allows us to calculate a luminosity at peak flux in FIRST of $L = 1.1 \times 10^{28}$ erg s^{-1}Hz^{-1}.

4.3.17 FIRST J025552.4+010409

The steepest spectral index in our sample was for source FIRST J025552.4+010409, and we show a summary of observed fluxes over time in Table 4.17. This source was first detected in 1993 in NVSS data, and was as bright as 2.8 ± 0.1 mJy in 1995 at 1.4 GHz when it was observed by FIRST as measured with Aegean, but was 0.8 ± 0.1 mJy in VLASS in 2017 at 3 GHz. If we use the flux measured directly from the FIRST image instead of the value obtained from the FIRST catalog (that is, 2.8 ± 0.1 mJy instead of 3.0 ± 0.14 mJy), we obtain a new spectral index of -1.6 (versus $\alpha = -1.8$ from the catalog value). The source was also detected in VLA observations by project 13B-370 (Kunal et al., in prep), and detected at low frequencies in 2011 by TGSS. We also found observations at these coordinates that were non-constraining upper limits, but include

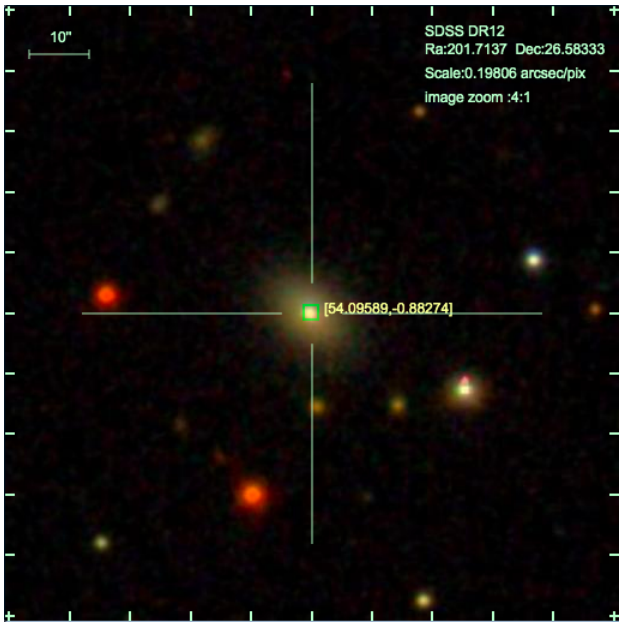

Figuur 4.20 The SDSS image for FIRST J033623.0-005257. This position is coincident with the source 2MASX J03362300-0052576, classified as a Seyfert 1 galaxy.

Date of Observation	Peak Flux (mJy)	Observation	Frequency (GHz)
1990-02-22	<1680	GB6	4.85
1993-11-15	1.5 ± 0.4	NVSS	1.4
1995-10-16	2.8 ± 0.1	FIRST	1.4
2006-06	<360	VLSSr	0.075
2010-12-12	7.0 ± 0.3	TGSS	0.15
2013-12-13 to 2014-01-14	0.82 ± 0.06	VLA 13B-370	3
2017-11-20	0.8 ± 0.1	VLASS	3

Tabel 4.17 Table of flux values over time for FIRST J025552.4+010409.

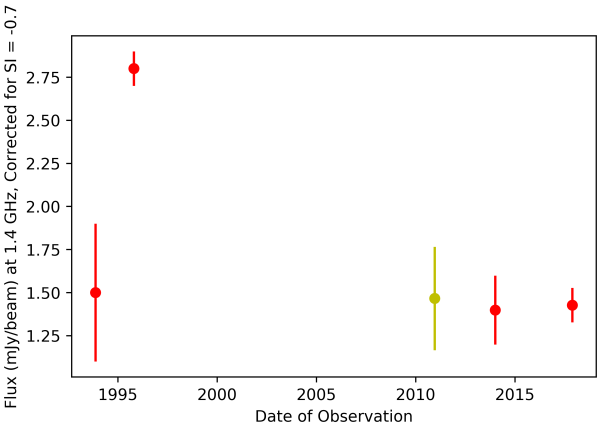

Figuur 4.21 As in Figure 4.2, but for FIRST J025552.4+010409.

Date of Observation	Peak Flux (mJy)	Observation	Frequency (GHz)
2002-3-24	2.1 ± 0.1	FIRST	1.4
2006-06	<366	VLSSr	0.074
2009-01-01 to 2009-01-03	1.81 ± .03	Stripe82	1.4
2010-10-31	<10.2	TGSS	0.15
2013-08-09 to 2014-06-18	<39	GLEAM	0.118
2013-12-13 to 2014-01-14	0.7 ± 0.07	VLA 13B-370	3
2017-11-30	0.6 ± 0.1	VLASS	3

Tabel 4.18 Table of flux values over time for FIRST J020203.2-000518.

them in Table 4.17 for completeness.

The light curve over time for FIRST J025552.4+010409 with the flux corrected for $\alpha = -0.7$ can be seen in Figure 4.21. We used this value for the correction because the 2006 TGSS detection at 150 MHz combined with the 2013 VLA observation are relatively close in time, and this allows us to find the spectral index more precisely than we did for our initial assumption. We found that the source was fairly flat, excepting the high flux measured by the FIRST survey.

Examination of SDSS images confirm that there is no optical galaxy at the coordinates for FIRST J025552.4+010409, although it does appear within 1 arcminute of an edge-on galaxy. Thus, it seems likely that FIRST J025552.4+010409 is at a distance >108 Mpc, and was included in the Ofek [2017] catalog due to chance coincidence. We can place a lower limit on the source's radio luminosity at 1.4 GHz of 4×10^{28} erg s^{-1}Hz^{-1}.

4.3.18 FIRST J020203.2-000518

FIRST J020203.2-000518 was identified due to its extreme variability between FIRST and VLASS observations. We list our compiled data over time in Table 4.18, and provide the light curve of data in Figure 4.22. When using the direct measurement of the flux from the FIRST image instead of the catalog value, we obtain a spectral index for this source of $\alpha = -1.5$. However, when compiling our data in Figure 4.22, we see the detections show a steady decay over ∼20

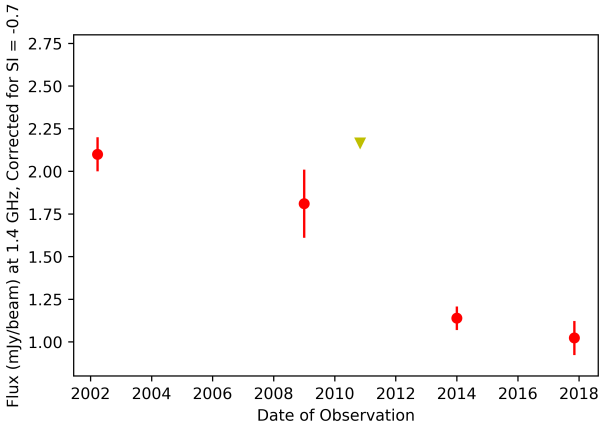

Figuur 4.22 As in Figure 4.2, but for FIRST J020203.2-000518 and corrected for a spectral index of $\alpha = -0.75$.

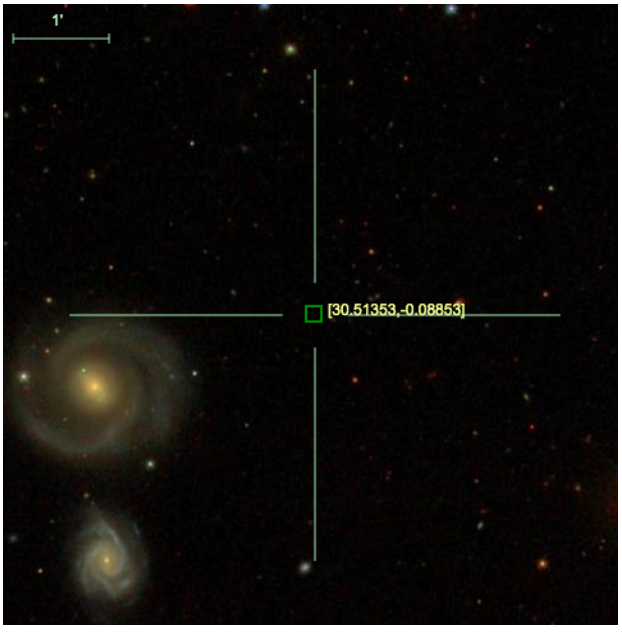

Figuur 4.23 The SDSS image for FIRST J020203.2-000518.

Date of Observation	Peak Flux (mJy)	Observation	Frequency (GHz)
1984-05-30	1.1 ± 0.4	VLA	1.51
1994-01-11	2.1 ± 0.4	NVSS	1.4
1995-11-13	1.1 ± 0.1	FIRST	1.4
2006-06	<360	VLSSr	0.075
2010-12-12	<10	TGSS	0.15
2017-11-25	0.6 ± 0.1	VLASS	3

Tabel 4.19 Table of flux values over time for FIRST J132651.2+263528.

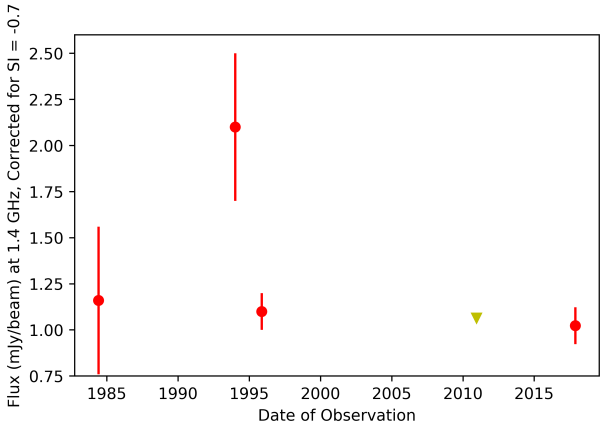

Figuur 4.24 Light curve for FIRST J132651.2+263528.

years, with one constraining non-detection in 2010 from TGSS data. We note that the source was also detected in NVSS, but was unresolved. If we calculate the upper limit for the spectral index when using this observation and the 2009 Stripe82 one, we obtain $\alpha \leq -0.7$.

We see in Figure 4.22 that the light curve consists of a steady decline over the ∼2 decades of observations since it was first detected. Similar to FIRST J033623.0-005257, we find that there is no optical counterpart to the coordinates of this radio source, and instead it is located ∼ 1 arcminute distant from a bright optical galaxy, NGC 799 (Figure 4.23). From this, we can calculate an upper limit its 1.4 GHz luminosity of $L_\nu = 2.6 \times 10^{28}$ erg s^{-1}Hz^{-1}, assuming a distance >108 Mpc.

4.3.19 FIRST J132651.2+263528

FIRST J132651.2+263528 was examined for two reasons: it matched our variability criteria, and the SDSS image for the source confirmed the radio source was near the center of the western of two interacting galaxies, 2MASS J13265127+2635285 and 2MASX J13265125+2635283. Collectively known as Markarian 454 [Mrk 454; Toba et al., 2014], they are undergoing what appears to be a merger process (Figure 4.25). Mrk 454 is located at a distance of 99 Mpc [Skrutskie et al., 2006], and the right (eastern) galaxy in Figure 4.25 is classified as an AGN [Toba et al., 2014].

The compiled data for this radio source can be found in Table 4.19, and the subsequent light curve in Figure 4.24. We can see in the light curve that this source increased in flux in NVSS

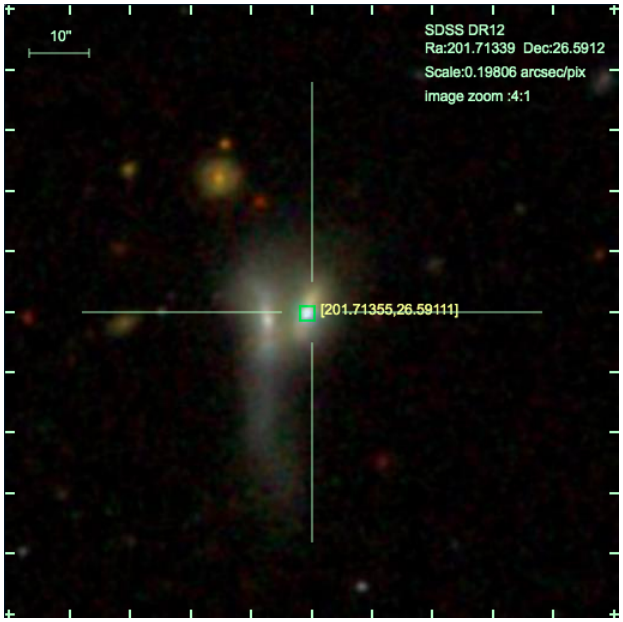

Figuur 4.25 The SDSS image for FIRST J132651.2+263528

data, where it was ∼2 times brighter than all other observations. Further, the source faded significantly in the 23 months between the NVSS and FIRST observations. When we used the directly measured peak flux from FIRST to recalculate the spectral index, we obtained $\alpha = -0.7$.

Because we know the distance to the galaxy, we can calculate the luminosity during this period of variability. We find that at its peak during the NVSS observation, the radio source at 1.4 GHz had a luminosity $L = 2.4 \times 10^{28}$ erg s^{-1}Hz^{-1}, which decreased by almost half to $L = 1.3 \times 10^{28}$ erg s^{-1}Hz^{-1} in ∼670 days.

Further, we identified Swift observations which overlapped with the field of FIRST J132651.2+263528. Although there was no source at this location, we can establish an upper limit at 0.2-10 keV of 1.0×10^{-3} ct/s (at 90% confidence). However, this radio source is also listed in Ofek [2017] as coincident with an X-ray source in the ROSAT catalog of count rate 1.1 ct/ks [1RXS J132640.4+263336; Voges et al., 1999]. However, because the ROSAT positional error for this source is 17", and the source is in fact 85"distant from the galaxy, and because we did not detect any counts from the Swift XRT data, we conclude this is a coincident association.

4.4 Discussion

Our study is important in the context of what we can learn about variability at local distances. In Section 4.4.1, we discuss the categorizations we used to identify our different radio sources. In Section 4.4.2, we cover the sources that we looked at in detail in Section 4.3, including a possible TDE or NS-NS merger candidate (Section 4.4.2.1), sources from low-excitation AGN activity (Section 4.4.2.2), and sources which exhibited non-transient behavior (Section 4.4.2.3. In Section 4.4.4, we compare the variability seen in our study to that seen in other surveys. In Section 4.4.3, we discuss the rate of NS-NS mergers with late time emission, as well as the local volumetric

rate of variable sources. In Section 4.4.5, we compare our sources to those of other transient phenomena in the local universe.

4.4.1 Categorizing Sources

From the information compiled in Section 4.3, we can consider the origins of those sources deemed worthy of further inspection. When categorizing the various sources in our study, we used three factors for each source:

- First, we considered the position of the source. This entailed noting whether the source was nuclear versus non-nuclear in its location within the galaxy, as a nuclear source is most likely to be associated with AGN related activity, or a TDE. We additionally noted if the source did not appear coincident with a galaxy, meaning the source was more likely to be a background source coincidentally included in our study. We also considered what X-ray information exists for the source, either from the lack of detection in the ROSAT catalog or a Swift XRT observation.
- Second, we were interested in the light curve over time for the source. In particular, we were interested in sources that displayed monotonic decay over time versus other behavior, such as flaring, which indicates different physical processes.
- Third, we were interested in whether the source underwent a large change in brightness during our survey. We defined these as sources which increased or decreased by a factor of two in flux during our study.

Once the sources were grouped together, we classified the likely source of emission based on the physical mechanisms underlying their origin. We found that none of the sources in our study met all three of our criteria. However, one source, FIRST J020203.2-000518 (Section 4.3.18), did display some of the criteria listed above, and may be confirmed as a transient with additional follow-up observations. We discuss all our sources in greater detail in Section 4.4.2 below.

4.4.2 Discussion of Individual Sources

4.4.2.1 Possible TDE or SGRB Candidate

FIRST J020203.2-000518 is notable because of its light curve (Figure 4.22). It has steadily decreased in brightness by a factor of ~ 2 since it was first detected in 1993 (assuming a synchrotron spectral index of $\alpha = -0.75$). We have calculated the decay rate of this source (Figure 4.26), and find a decay rate of $\beta = -0.6$ if we set the y-intercept for our fit t_0= 1993. We chose this value because an unresolved source was detected in NVSS at this position in 1993, but showed some extended emission via visual inspection of the data. Thus, we concluded that while we do not have the flux measurement from NVSS, it does seem likely it was already visible at that time. This combined with the monotonic decay leads us to conclude the light curve could be caused by a shocked CSM. Radio propagation phenomena, such as extreme scattering, are typically symmetrical in their light curves [Bannister et al., 2016; Fiedler et al., 1994] so we conclude this is less likely.

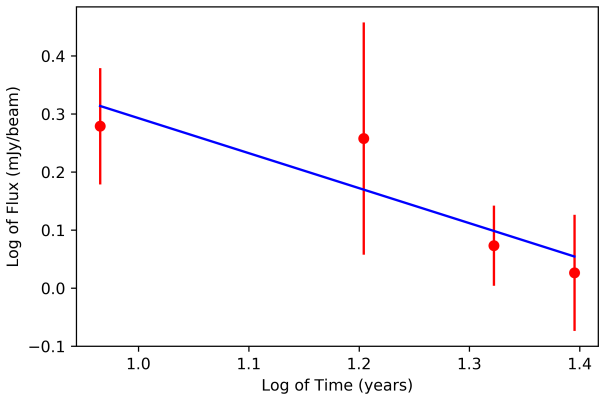

Figuur 4.26 A log-log plot of the flux over time for FIRST J020203.2-000518, assuming $t_0 = 1980$..

However, no optical counterparts coincided with the locations of the source. The reason it was included in the Ofek [2017] catalog is because the search radius from an optical galaxy was based on the optical galaxies galaxy's 25 mag arcsec^{-2} surface brightness semi-major axis listed in the HyperLEDA catalog, which could be very large in the event a nearby optical galaxy was also large. This resulted in an angular distance between the radio source and an optical galaxy for FIRST J020203.2-000518 of 183". If we assume a distance >108 Mpc, we can calculate an upper limit its 1.4 GHz luminosity of $L = 2.6 \times 10^{28}$ erg s^{-1}Hz^{-1}. However, if FIRST J020203.2-000518 is in fact located further, this would correspond with an even greater luminosity. Finally, it is notable that there has been a steady decrease in the light curve over the ∼25 years of data collected for this source, and we obtained an upper limit for X-ray emission from Swift XRT at 90% confidence of 0.2-10 keV of 1.0×10^{-3} ct/s.

We have first considered the possibility that the FIRST J020203.2-000518 source is at a much greater distance than its nearby galaxy host. Our upper limit on luminosity is much lower than what we would expect for an on-axis TDE, which is on the order of $10^{30} - 10^{31}$ erg s^{-1}Hz^{-1} [Metzger et al., 2015; Mooley et al., 2016]. However, an on-axis TDE has an expected light curve duration of ≤3 years at 1.4-3 GHz [Zauderer et al., 2013; Metzger et al., 2015], defined as the time interval over which the flux is within a factor of two of its peak value. If we assume that the NVSS observation occurred near the peak flux for a TDE event, it took >10 years to reach this value, making an on-axis TDE less likely. Although the details of the light curve for an off-axis TDE are not available, it is thought to last for years [Metzger et al., 2015], so this could still be a possible scenario for this event.

The second possibility we considered for FIRST J020203.2-000518 is that it is in fact associated with NGC 799 even though it appears 183" distant. If so, if we assume the source is at roughly the same distance of NGC 799 of distance of 83.2 ± 5.8 Mpc [Theureau et al., 1998], this would correspond with a distance between the center of the host and FIRST J020203.2-000518 of 73.8 kpc. While this exceeds the offsets observed for transients such as LGRB [Blanchard et al., 2016], up to 30% of NS-NS mergers are estimated to take place outside their host galaxies [Belczynski et al., 2006], and 25% of SGRB at ≥ 10 kpc [Fong & Berger, 2013]. Further, [Fong & Berger, 2013] reported the offset of GRB 090515 at 75.03 ± 0.15 kpc from its host galaxy, after using the

Hubble Space Telescope to conduct follow-up observations for counterpart galaxies in the burst's region. This leads us to the conclusion that it is possible that an SGRB occurred at the distance of FIRST J020203.2-000518 from NGC 799. If we assume FIRST J020203.2-000518 occurred at a distance of ∼83.2 Mpc, we find $L = 1.9 \times 10^{28}$ erg s^{-1}Hz^{-1}.

As such, we have considered whether the progenitor source for FIRST J020203.2-000518 could be related to a neutron star merger (NSM), either from an off-axis SGRB where the emission comes from the relativistic jet, or from the ejecta from the kilonova (KN) interacting with an ISM [Hallinan et al., 2017; Alexander et al., 2017; Berger, 2014; Nakar & Piran, 2011]. While the two phenomena are expected to have a similar expected luminosity of $10^{28} - 10^{29}$ erg s^{-1}Hz^{-1} [van Eerten et al., 2010; Metzger & Berger, 2012; Metzger et al., 2015], the radio emission from an off-axis SGRB peaks once the jet material sweeps up its own mass in ISM, whereas the radio emission from the KN ejecta peaks once it has swept up its own mass of ISM. Because the KN ejecta has a larger mass, it expands more slowly, and thus the radio emission takes longer to peak compared to the off-axis SGRB afterglow [Fong et al., 2016; Berger, 2014]. It is predicted that off-axis SGRB emission will peak after a few hundred days, whereas emission from the KN ejecta will peak closer to a decade after the NSM [see Figure 1; Metzger et al., 2015].

Our first concern in this scenario was whether the ISM at a distance of 73.8 kpc from the host galaxy would have a high enough density for corresponding radio emission. Although the ISM is expected to be low at such a distance, a smaller satellite galaxy is possible at these distances. Further, we note that SDSS images have a depth of g' ∼23 mag [York et al., 2000], and if placed at a distance of 83.2 Mpc even a Large Magellanic Cloud (LMC) sized satellite galaxy would not be detectable by SDSS. Therefore, such ISM levels are possible if the location of FIRST J020203.2-000518 is coincident with an unseen satellite galaxy of NGC 799.

A monotonically decreasing light curve of >20 years is more consistent with KN ejecta interaction compared to an off-axis SGRB [Metzger et al., 2015], leading us to conclude this scenario is the more likely of the two if FIRST J020203.2-000518 is located at this distance. However, while radio afterglows from SGRB have been observed [Hallinan et al., 2017; Fong et al., 2016], late-time emission from KN ejecta has not. It is predicted the emission would be highly dependent on the ISM density, and we should note a density of $n \leq 1$ cm^{-3} is the typical density scale inferred from existing SGRB observations [Fong et al., 2016, 2015]. Berger [2014] predicted emission from KN ejecta will peak at 0.15 mJy for a NSM located at 200 Mpc at 1 GHz, on a time scale of 10 years, assuming an ISM density $n = 0.1$ cm^{-3}. In the case of GW 170817, which occurred at a distance of $\sim$ 40 Mpc [Abbott et al., 2018], Alexander et al. [2017] predict emission will peak at $\leq 3\mu$Jy assuming the ISM is $n = 10^{-3}$ cm^{-3}. Both of these density estimates would correspond with luminosities far less than what we see from FIRST J020203.2-000518. Although it is possible the source is embedded in a relatively high density region in a faint satellite galaxy ($n \geq 1$ cm^{-3}), it is also likely to be in a region with very low ISM levels.

We conclude that we cannot definitively classify this transient candidate without additional optical and radio follow-up observations. In optical, such observations would be useful to determine whether there is a small galaxy at $\sim$ 83.2 Mpc distant (which may indicate NSM-related activity), or the center of a much larger galaxy at distance >108 MHz (indicating TDE-related activity). Radio observations in the future will also be useful in determining whether the monotonic

decrease in flux observed in this source continues.

4.4.2.2 AGN Candidates

We first considered the five variable radio sources which coincided with the center of their host galaxies. These are FIRST J143052.2+060209.6 (Section 4.3.1), FIRST J141430.5+060955.4 (Section 4.3.2), FIRST 140255.708+092514.54 (Section 4.3.8), FIRST 033623-005257 (Section 4.3.16), and FIRST J132651.2+263528 (Section 4.3.19). This is because nuclear transients are most likely associated with either AGN or TDE activity [Mooley et al., 2016; Tadhunter, 2016]. To distinguish between the two categories, we looked at the luminosities of the radio sources, which all had a peak luminosity at 1.4 GHz of $L_\nu \sim 10^{28}$ erg s^{-1}Hz^{-1}. This luminosity is fainter than that expected from a TDE, which occurs when a star gets sufficiently close enough to a black hole's event horizon that it is pulled apart by the black hole's tidal forces [Giannios & Metzger, 2011], and is typically associated with luminosities $\geq 10^{30}$ erg s^{-1}Hz^{-1} [Zauderer et al., 2013; Metzger et al., 2015]. We will also note that of these galaxies, only FIRST 140255.708+092514.54 had coincident X-ray observations, resulting in an upper limit of 8.5×10^{-4} ct/s (at 90% confidence).

However, this luminosity is consistent with that of a radio-loud AGN [Woo & Urry, 2002; Kimball et al., 2011]. Given the location of the sources at the center of their host galaxies, and the luminosities we observed, we conclude the variability we observed was due to flaring in the AGN. For example, for FIRST J132651.2+263528 (Section 4.3.19), located in one of the pair of interacting galaxies in Mrk 454, the light curve revealed a flare during the period observed by the NVSS survey (Figure 4.24). Further, the rightmost galaxy in Mrk 454 coinciding with the location of FIRST J132651.2+263528 is listed as an AGN. Finally, radio-loud AGN have been connected to interacting galaxies, which is thought to be triggered by the interactions. From this, we conclude this flare was likely related to AGN activity.

In the case of FIRST J025552.4+010409 (Section 4.3.17), no optical counterpart coincided with the locations of the source. The reason this source was included in the Ofek [2017] catalog is because the search radius from an optical galaxy was based on the optical galaxies galaxy's 25 mag arcsec^{-2} surface brightness semi-major axis listed in the HyperLEDA catalog, which could be very large in the event that a nearby optical galaxy was also large. This resulted in an angular distance between the radio source and an optical galaxy for FIRST J025552.4+010409 of 64". We also confirmed the location of this optical galaxy compared to their sources in SDSS data, and concluded it was a coincidental association.

Finally, we have a handful of sources which have a non-nuclear position that appears to be within a galaxy, and display some variability, but do not show monotonic behavior expected from transients. These sources are FIRST J140038.9-025122 (Section 4.3.6) and FIRST J114529.3+192327 (Section 4.3.7). They appeared at the edges of their respective galaxies, and show a peak luminosity of 10^{28} erg s^{-1}Hz^{-1}, but showed flaring behavior during the period of our study. Although many objects in our Local Group are known to flare (flare stars, pulsars, brown dwarfs, etc), all of these do not have sufficient luminosity to be detectable at these distances [see Table 1 of Mooley et al., 2016]. For example, magnetic flares from active binary stars do not exceed $10^{14} - 10^{22}$ erg s^{-1}Hz^{-1} [Güdel, 2002], and thus cannot explain our candidate signals. Finally, we will note that for both of these sources we obtained upper limits from Swift

XRT observations of the area, indicating neither is likely to be a site associated with high-energy phenomena.

Instead, we are left with two possibilities: that these light curves were caused by interstellar scattering (ISS), or a coincident background. If the variations we observed in these sources are due to ISS, this implies a compact source or component that is being refracted by a turbulent, ionized ISM. Together with the spectral index observed, this implies a classification as a compact steep spectrum source (CSS). Such sources have been detected by transient surveys in the past [Bannister et al., 2011]. Additional spectral information on these sources would help confirm these sources as CSS. Alternatively, these flares could be caused by coincident AGN that are background sources to the host galaxies.

Ultimately, we conclude AGN activity is the most reasonable remaining interpretation for all the variable sources covered in this section because they appear to be inconsistent with other possibilities for transients and variable sources. Given that many of these sources were primarily associated with the nuclei of galaxies, that AGN activity is the most common slow radio transient phenomenon at these frequencies that can be seen on time scales of decades, and that it is thought that all AGN may exhibit variability at some point [Tadhunter, 2016], and radio sources in the local universe are dominated by AGN [Nyland et al., 2016], this is unsurprising. Further, we should note that variability at 1 GHz from AGN is greatest on time scales of 2-5 years [Hancock et al., 2018; Bannister et al., 2011]. In a survey of 159 AGN flares at 22 and 37 GHz, Hovatta et al. [2008] found that the flares last on average 2.5 years and are only slightly longer at lower frequencies, which is also consistent with our observations. Some of our AGN candidates varied on longer periods of >10 years (see FIRST J033623.0-005257, Figure 4.22, for one such example), which has been noted in the past for other variable sources discovered in studies of transient and variable sources as well [Bannister et al., 2011; Mooley et al., 2016]. It is likely that these changes in variability are due to episodes of enhanced accretion onto the black hole, leading to increased jet activity in the AGN [Kunert-Bajraszewska et al., 2006; Frank et al., 2016].

We have also considered how our examined sources fit into what is known about the local AGN population. Best & Heckman [2012] conducted a study of nearby AGN ($z \leq 0.1$) using both SDSS optical spectra and NVSS and FIRST radio data, and found the local galaxy population is dominated at luminosities $L < 10^{33}$ erg s^{-1} Hz^{-1} by 'low-excitation' radio galaxies (LERG), which have very little radiated energy, as opposed to the quasar-like 'high-excitation' radio galaxies (HERG). The emission in LERG is thought to be from advection-dominated accretion flows which are optically thin, whereas HERG emission is driven by a radiatively efficient, optically thick accretion disc [Shakura & Sunyaev, 1973]. It should also be noted that HERG emit radiation over a very broad part of the electromagnetic spectrum, including X-rays, but LERG do not show accretion-related X-ray emission [Elvis et al., 1994; Hardcastle et al., 2007]. Finally, morphological radio studies of low radio luminosity galaxies show most of these sources are compact and lack prominent jets or diffuse lobes [Baldi et al., 2015], which is similar to what we found in our sources.

None of our sources were detected in the ROSAT catalog, which had a brightness limit of 0.1 cts/s at the 0.1- 2.4 keV energy band [Voges et al., 1999], although we have deeper limits for the sources for which Swift observations exist. The lack of X-ray emission combined with the luminosities of our sources ($L \approx 10^{28}$ erg s^{-1} Hz^{-1}) lead us to conclude all our sources categorized

as AGN are LERG. Our detected radio emission in this situation originates from radiatively inefficient flows that have low accretion rates, and changes in variability are due to the changes in density within these flows.

4.4.2.3 Non-Varying Sources

Finally, we will note that eight of our sources- FIRST J102526.1 +171547 (Section 4.3.4), FIRST J105823.6 +241355.3 (Section 4.3.5), FIRST J092758.2 -022558 (Section 4.3.9), FIRST J104726.6+060247 (Section 4.3.10), FIRST J235351.4 +075835 (Section 4.3.11), FIRST J131441.9 +295959 (Section 4.3.12), FIRST J162244.5 +321259 (Section 4.3.14), and FIRST J141420.8 +073058 (Section 4.3.15)- did not meet our criteria as a variable candidate as outlined in Section 4.2.3, and did not meet more than one of our criteria outlined above in Section 4.4.1. Further, in the case of FIRST J141420.8+073058 and FIRST J235351.4+075835, Swift XRT data indicated these sources are not associated with X-rays, and are unlikely to be a high-energy sources. For the sources located at the center of their galaxies (FIRST J162244.5+321259 and FIRST J141420.8+073058), we conclude this emission is likely caused by LERG behavior. The remainder of our sources are also likely due to non-transient emission, from either a local source to the host galaxy such as star formation, or an AGN at greater distance.

4.4.3 Rates

4.4.3.1 NSM Merger Afterglow

Based on our identification of FIRST J020203.2-000518 as a possible NSM candidate, We have calculated the volumetric rate of NSM afterglows detectable in radio, assuming these transients scale with stellar luminosity at distances < 108 Mpc. If we consider sources where $\Delta t_{1.3} = 4000$ days- the longest light curve duration predicted by Metzger et al. [2015] for a NSM- we can use the relationship:

$$R_{var} \approx \frac{1 \text{ event}}{\Delta t \; f_{spec} \; \Delta\Omega (d^3/3)} \tag{4.3}$$

where f_{spec} is the estimated completeness of stellar luminosity in the catalog to this distance [$\sim$30%; Ofek, 2017], and $\Delta\Omega$ is the footprint of the area of sky covered by the FIRST catalog of 10,600 deg^2. From this, we obtain a rate of $\sim$200 Gpc^{-3}yr^{-1}. This is lower than the rate predicted for NS-NS mergers predicted by Abbott et al. [2017] of 1540^{-1120}_{+3200} Gpc^{-3}yr^{-1}, based on the single detection of GW 170817 during the O1 and O2 LIGO science runs. However, we emphasize that the fraction of NS-NS mergers with emission at later times is not yet well established. For example, Nakar et al. [2006] predicted a local SGRB rate of $<$10 Gpc^{-3}yr^{-1} within 100 Mpc, but noted this rate could be several orders of magnitude higher based on factors such as the luminosity function and beaming factor. Further, we know any future KN emission from GW 170817 will be difficult to detect with current instruments [Alexander et al., 2017].

In the future, we expect LIGO will allow us to obtain a more precise rate of NS-NS mergers, both in the local surroundings and at greater distances, especially as the O3 science run is currently ongoing [Abbott et al., 2018]. While GW 170817 was nearby, analysis has suggested that GRB 170817A-like events are rare in the existing SGRB catalogs, and just a few percent of

NS-NS mergers may have accompanying emission [Mandhai et al., 2018], which may explain the discrepancy between our rate and the Abbott et al. [2017] rate of NSM. Detecting more decaying light curves like FIRST J020203.2-000518 may pay a key role in establishing the true rates of radio transients. It would also be useful for when the Square Kilometer Array (SKA) comes online, which is expected to find many more transients, in order to establish long-term transient behavior.

4.4.3.2 Local Volumetric Rate of Variable Sources

We have also obtained a local volumetric rate of variability based on our survey. Using Equation 4.3, if we use the 10 sources that fit the variability statistic in Equation 4.2, we obtain a rate of $\sim$4100 $\mathrm{Gpc^{-3}yr^{-1}}$.

As noted in Section 4.3, two sources that matched $V_s \geq 4.3$ do not have an associated host galaxy. Although it is possible that some of these sources are from transients that were kicked out of their host galaxy systems [Fong & Berger, 2013], it is more likely that the radio source is a false association between the galaxy and a coincident AGN at >108 Mpc. Thus, if we restrict the calculation to radio sources with an optical counterpart that have a high variability statistic, we are left with a rate of $\sim$3300 $\mathrm{Gpc^{-3}yr^{-1}}$.

4.4.4 Comparing Variability in Surveys

We have compared our rate of radio variability to other surveys. Hodge et al. [2013] conducted a study of variability for mJy sources in Stripe 82 [Hodge et al., 2011], and established that 1% of sources had a fractional variability $f_{var} < 3$ between 7 and 22 years. They concluded a majority of these sources were due to AGN. More recently, Mooley et al. [2016] established a variability fraction >4% on time scales of 1.5 years. In our survey, 3% of the sources varied by this amount over the $\sim$25 years of our study, which is consistent with the prevailing view that only a few percent of the sources in the radio sky are variable. In coming years, VLASS will cover the sky at two more epochs, which will allow us to continue monitoring variability in these sources.

At lower frequencies, Bell et al. [2019] have reported on the variability rate of bright (> 4 Jy) radio sources at 154 MHz using the MWA. They found that $\sim 1.6\%$ of radio sources display variability at time scales > 2.8 years, and concluded that this variability is due to interstellar scintillation. They also concluded that synchrotron-driven variability and intrinsic AGN variability can only produce changes at low frequencies on >100 year time scales. As such, it is not clear whether we can draw conclusions on radio observations of these sources at lower ($\sim$100 MHz) frequencies compared to our GHz frequencies on the time scale of our study.

We have also considered the biases inherent in using data from different studies to compile our light curves. One such consideration is that some of our variables could be artificial and due to angular resolution differences between the various surveys we used, particularly if diffuse components were present. For comparison, NVSS had a beam size of 45änd was observed in D configuration [Condon et al., 1998], FIRST had a beam size of 5änd was observed in B configuration [Becker et al., 1994], and VLASS has a beam size of 2.5änd was observed in configurations B and BnA [Lacy et al., 2019]. This means that VLASS and FIRST are missing short spacings compared to NVSS, and because VLASS was taken at a higher frequency compared to NVSS and

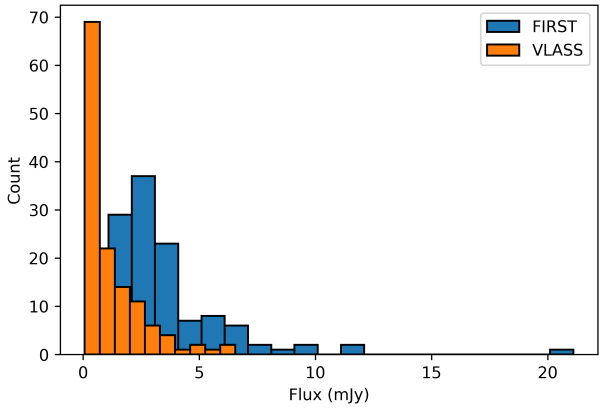

Figuur 4.27 A histogram of flux values for all the sources from Ofek [2017] observed by FIRST (blue), and a histogram of the same values from this study and Law et al. [2018] (yellow). The outlying data point in the FIRST data at ∼20 mJy is FIRST J141919+394036, and the second brightest source is FIRST 105823.641+241355.32.

FIRST (2-4 GHz instead of 1.4 GHz, respectively). It is thus conceivable that this discrepancy can make a source clearly detected in NVSS to appear to fade or disappear altogether in VLASS, even though it has not faded in actuality. Further, due to the differences in resolution it is possible that several radio sources close together would appear as a brighter radio source in NVSS, yielding a bright flux from that observation, but be resolved into multiple sources in a later survey where each appears fainter. We in fact found this to be the case for several sources, both via visual inspection of the images and when examining the 2D Gaussian fit of the source finder and seeing whether the fit exceeded the beam size, indicating an unresolved source. Future studies which compare data from multiple surveys will need to take care when examining observations from different surveys, and how the observations are compared to one another.

4.4.5 Comparison to Other Transient Sources

4.4.5.1 Candidate LGRB FIRST J141919+394036

We can compare our estimated rate of variability to that derived by Law et al. [2018] for decades-long extragalactic radio transients which was derived using the same catalog yielding a volumetric rate assuming $\Delta t = 2000$ days of ∼900 $\mathrm{Gpc}^{-3}\mathrm{yr}^{-1}$. As this value was obtained when only half the sky had been surveyed by VLASS, and we found no transients of this time scale in the second half of the VLASS data, we can update the number of such transients to 450 $\mathrm{Gpc}^{-3}\mathrm{yr}^{-1}$. We conclude that the rate of variable events is in excess of transient events, although more precise rates will require a more analytic approach to a large fraction of VLASS data (Dykaar et al., in prep).

Beyond the occurrence rate, we can also consider how unique the disappearing radio source FIRST J141919+394036 was as an event by comparing it to sources from our study. First, the spectral index limit of FIRST J141919+394036 obtained between FIRST and VLASS is far lower than any we found in our study at $\alpha < -5.1$, and the steepest spectral index we found for one

object was -1.8 (Section 4.3.17). Furthermore, the source that we found missing in VLASS in our study (Section 4.3.16) had a much smaller limit on spectral index, $\alpha < -1.3$.

In simplest terms, this difference in spectral indices is from a bias towards bright sources in FIRST in the design of this transient study. FIRST J141919+394036 had a flux of 20.1 mJy [Law et al., 2018], meaning it was twice as bright in FIRST as any source we measured in VLASS (or, in fact, any other source covered in the full catalog). We provide a visualization of this in Figure 4.27, where we show a histogram of all the FIRST and VLASS flux values for sources in the full Ofek [2017] catalog that were in epoch 1.1 of VLASS. This shows that the discovery of FIRST J141919+394036 was somewhat serendipitous due to the luminosity of the source (L $\approx 7 \times 10^{29}$ erg s^{-1} Hz^{-1}).

Additionally, we note that we may have introduced a bias when correcting our fluxes for a spectral index of -0.7 when calculating variability. This is because if a source has a spectrum of ($\alpha < -0.7$), its calculated spectral index would appear less steep, meaning it might be excluded from our variability criteria. In the future, when multiple VLASS epochs can be compared for transients which will have the same frequency as well as beam size, these biases will be minimized.

4.4.5.2 AGN and FRB Connections

Since the theory of what mechanism causes FRBs is unknown– or even if there are multiple mechanisms– it is not unexpected that there have been efforts to link the origins of FRBs to AGN [Vieyro et al., 2017; Katz, 2017]. This has been particularly interesting as the large and variable rotation measure observed in the FRB 121102 bursts has only been observed to date in the vicinity of black holes [Michilli et al., 2018]. The association between FRBs and AGN is difficult to establish, however, due to the variable nature observed in many AGN [Williams & Berger, 2016; Vedantham et al., 2016].

Vieyro et al. [2017] recently proposed a model for FRBs in which the FRB signals originate from a turbulent plasma hit by a relativistic jet from an AGN. They predicted that this would result in a luminosity at 1.7 GHz of approximately 10^{30} erg s^{-1} Hz^{-1}, which would far exceed luminosities visible in our study. To date, however, we note that the FRB with the lowest dispersion measure (DM), FRB180729.J1316+55, has an estimated distance of ∼300 Mpc, assuming standard cosmological parameters [CHIME/FRB Collaboration et al., 2019].[3] This means that no FRB has as yet been detected from within the local distances covered in this survey. However, the prodigious rate of FRB detection by the Canadian Hydrogen Intensity Mapping Experiment (CHIME) leaves us optimistic that a FRB within this distance will be detected soon. If it does, we expect that the methods used in this study to compile information on a local counterpart's light curve over several decades will be of interest, and we expect that radio catalogs and archival data sets are complete enough that any variability over decades-long time scale could be established.

4.5 Conclusions

We have conducted a survey of 117 radio sources in VLASS that also appeared in the FIRST catalog, and were first listed by Ofek [2017] as potential counterparts to FRBs. We have identified

[3]Distance is from http://www.frbcat.org; see Petroff et al. [2016] for more info.

FIRST J020203.2-000518 as a transient candidate based on its luminosity, monotonic decay, and time scale of the signal, either as a NS-NS merger remnant if at closer distance, or a TDE if at a distance >108 Mpc. Additional optical follow-up observations are needed to confirm the location of this radio source and classify it further, as well as radio observations for long-term monitoring of this transient.

In addition to these sources, we compiled detailed light curves for 18 other sources, but conclude that all are likely related to normal AGN activity and variability. We conclude that the majority of slow transients in the local radio sky at GHz frequencies are AGN, with more exotic phenomena comprising only a small handful of the transients at this distance, and the majority of low luminosity AGN sources at these distances are due to LERGs with low, inefficient accretion rates. We estimate the local rate of variability for luminous radio sources to be $\sim$4100 $\mathrm{Gpc^{-3}yr^{-1}}$. We also expect that in the future, when nearby transient radio phenomena are discovered, the existing archives of radio data will prove useful in compiling the behavior of such sources before the event, in order to establish any prior variability.

4.6 Acknowledgements

We thank Huib Intema for his correspondence regarding TGSS data, Joseph Callingham for his assistance with providing the WENNS observation dates, and Kunal Mooley and Gregg Hallinan for their assistance with providing VLA 13B-370 fluxes. This research has made use of data obtained through the High Energy Astrophysics Science Archive Research Center Online Service, provided by the NASA/Goddard Space Flight Center. The National Radio Astronomy Observatory is a facility of the National Science Foundation operated under cooperative agreement by Associated Universities, Inc. The Dunlap Institute is funded through an endowment established by the David Dunlap family and the University of Toronto. C.J.L. acknowledges support from the National Science Foundation under grant 1611606. B.M.G. acknowledges the support of the Natural Sciences and Engineering Research Council of Canada (NSERC) through grant RGPIN-2015-05948, and of the Canada Research Chairs program.

RA (J2000)	Dec) (J2000)	FIRST Flux (mJy/beam)	NVSS Flux (mJy/beam)	VLASS Peak Flux (mJy/beam)	Spectral Index Spectral Index
*09:27:58.282	-02:25:58.95	1.9 ± 0.1		1.1 ±0.1	-0.7
*10:25:26.189	17:15:47.97	2.6 ± 0.1		1.0 ±0.1	-1.0
*10:47:26.693	06:02:47.72	2.7 ± 0.1	2.4±0.4	0.8 ±0.1	-1.6
*10:58:23.641	24:13:55.32	2.1 ± 0.2		0.7 ±0.1	-1.4
*11:45:29.346	19:23:27.46	3.1 ± 0.2	2.4±0.4	2.5 ±0.1	-0.3
*13:14:41.932	29:59:59.19	2.0 ± 0.1	4.0±0.5	1.1 ±0.1	-0.7
*14:00:38.929	-02:51:22.79	1.2 ± 0.2		0.9 ±0.1	-0.4
* 14:10:43.667	08:59:29.96	2.6 ± 0.2	4±0.4	3.4 ±0.1	0.3
*16:22:44.571	32:12:59.28	1.8 ± 0.2	2.7±0.4	0.9 ±0.1	-0.9
*23:53:51.412	07:58:35.91	3.9 ± 0.1		1.1 ±0.1	-1.6
00:06:28.516	-03:42:58.83	2.4 ± 0.2	2.3±0.4	4.1 ±0.1	-0.6
00:17:27.498	-09:34:26.56	2.5 ± 0.2		5.5 ±0.1	0.0

00:17:59.547	-09:16:00.89	1.6 ± 0.2	2.9±0.5	1.1 ±0.1	-0.9
00:21:51.145	-09:29:32.2	3.3 ± 0.2	5.1±0.5	2.3 ±0.1	-0.5
00:42:39.26	02:44:14.17	3.3 ± 0.1	5±0.5	2.1 ±0.1	-0.6
01:44:43.099	-04:07:46.25	5.2 ± 0.1	10.9±0.6	4.0 ±0.1	-0.2
*02:02:03.248	00:05:18.72	2.1 ± 0.1		0.6 ±0.1	-1.6
02:17:04.793	01:14:39.44	11.1 ± 0.2	11.9±0.6	0.7 ±0.1	-1.2
02:36:23.588	00:42:31.55	1.9 ± 0.1		5.7 ±0.1	-0.7
02:52:42.189	-08:48:15.76	3.1 ± 0.2	4.4±0.5	1.9 ±0.1	-0.1
02:52:51.841	-01:16:29.31	3.1 ± 0.2	5.4±0.6	2.4 ±0.1	-0.1
*02:55:52.403	01:04:09.95	3.0 ± 0.1		0.8 ±0.1	-1.7
*03:36:23.014	00:52:57.85	1.6 ± 0.1		<0.4	<1.8
07:54:26.555	16:13:5.27	9.8 ± 0.1	10.5±0.5	6.6 ±0.1	-0.4
07:58:0.444	52:51:42.18	6.3 ± 0.1	7±0.5	3.3 ±0.1	-0.6
07:59:57.145	35:48:51.54	6.1 ± 0.2	9.2±0.5	2.3 ±0.1	-1.0
07:59:17.875	27:04:40.32	1.8 ± 0.1		1.8 ±0.1	-0.0
08:33:30.775	41:31:31.89	2.9 ± 0.1	2.7±0.4	1.7 ±0.1	-0.5
08:50:56.603	36:20:7.65	1.9 ± 0.2	3.4±0.4	1.0 ±0.1	-0.6
09:16:41.894	30:54:55.35	1.9 ± 0.1		1.7±0.1	-0.1
09:19:45.473	33:44:42.28	3.7 ± 0.1	5±0.4	3.3 ±0.1	-0.1
09:20:02.17	01:02:17.82	11.4 ± 0.2	10.7±0.5	2.8 ±0.1	0.2
09:20:36.948	33:04:29.06	3.2 ± 0.1	4.4±0.4	1.1 ±0.1	-1.1
09:39:17.261	36:33:44.17	4.8 ± 0.2	4±0.4	2.5 ±0.1	-0.6
09:43:2.176	37:49:23.37	2.4 ± 0.1	2.4±0.4	1.1 ±0.1	-0.8
09:47:10.836	23:30:51.86	2.3 ± 0.1		2.3 ±0.1	-0.0
09:50:0.613	37:34:31.4	1.7 ± 0.2	2.8±0.5	0.8 ±0.1	-0.7
09:52:46.77	30:02:20.16	3.8 ± 0.1	3.1±0.4	1.7 ±0.1	-0.1
09:58:40.109	28:52:38.98	3.5 ± 0.2	2.4±0.4	2.6 ±0.1	-0.3
10:11:07.608	46:54:56	3.2 ± 0.2	3.9±0.4	1.8 ±0.1	-0.6
10:13:47.92	38:40:32.19	2.4 ± 0.2	2.8±0.4	1.3 ±0.1	-0.6
10:13:51.543	38:47:2.29	6.2 ± 0.1	3.7±0.4	3.6 ±0.1	-0.5
10:15:1.568	39:39:48.41	1.9 ± 0.1		1.4 ±0.1	-0.5
10:27:25.021	01:14:30.82	3 ± 0.1	3.1±0.4	0.7 ±0.1	-1.4
10:37:22.113	37:04:39.35	2.9 ± 0.1	4.7±0.5	1.9 ±0.1	-0.4
10:37:37.903	37:27:20.27	2.2 ± 0.1	3.4±0.5	1.1 ±0.1	-0.6
10:41:52.953	21:15:9.35	3.1 ± 0.2	2.5±0.4	1.3 ±0.1	-0.9
10:44:18.973	52:46:12.56	7.9 ± 0.1	5.4±0.4	2.7 ±0.1	-0.7
10:44:38.235	56:22:11.18	4.5 ± 0.2	5.2±0.4	2.7 ±0.1	-0.7
10:51:26.328	08:17:55.3	2.2 ± 0.1	2.4±0.4	3.0 ±0.1	-0.1
10:55:6.921	40:34:0.91	2.4 ± 0.1		3.5 ±0.1	0.0
11:11:18.082	35:23:8.26	1.7 ± 0.2		1.1 ±0.1	-0.5
11:24:03.341	-07:47:01.13	2.1 ± 0.1	3.7±0.6	1.2 ±0.1	-0.5
11:39:17.604	09:57:45.03	2 ± 0.1	±	1.1 ±0.1	-0.7

11:39:14.889	17:08:37.41	6.2 ± 0.1	6.6±0.5	4.9 ±0.1	-0.2
11:41:52.959	10:18:15.75	2.1 ± 0.1	2.9±0.4	1.5 ±0.1	-0.2
11:43:02.141	19:38:31.29	8.5 ± 0.1	6.7±0.5	5.4 ±0.1	-0.5
11:44:32.113	20:06:23.67	2.8 ± 0.2	3.1±0.4	1.5 ±0.1	-0.6
11:45:58.38	29:19:57.58	2 ± 0.2	±	1.6 ±0.1	-0.2
11:48:27.531	12:43:38.39	6.2 ± 0.2	8.8±1	0.7 ±0.1	-1.2
11:52:30.543	20:37:31.62	1.8 ± 0.2		0.7 ±0.1	-0.9
11:52:42.608	20:37:52.89	4.5 ± 0.2	5.5±0.4	3.9 ±0.1	-0.1
12:01:44.901	20:19:41.84	2.4 ± 0.1		1.5 ±0.1	-0.6
12:01:52.231	08:29:45.18	2.4 ± 0.1	3.4±0.4	1.2 ±0.1	-0.7
12:02:29.57	00:12:44.64	2.5 ± 0.2		1.4 ±0.1	-0.5
12:03:21.111	04:13:41.29	2.3 ± 0.2		2.5 ±0.1	-0.1
12:05:29.34	20:14:48.23	3.1 ± 0.1	8.4±1.3	2.5 ±0.1	-0.2
12:09:09.831	31:34:10.19	2.5 ± 0.1	4±0.5	2.6 ±0.1	0
12:05:48.207	20:27:48.27	6.9 ± 0.1		2 ±0.1	0.4
12:13:09.305	32:35:47.07	1.7 ± 0.2	2.2±0.4	2 ±0.1	0.2
12:14:53.824	22:08:22.56	2 ± 0.1		2.7 ±0.1	0.3
12:18:08.114	06:08:22.23	6 ± 0.1		3.2 ±0.1	-0.6
12:19:52.969	08:56:15.35	1.8 ± 0.1		0.9 ±0.1	-0.7
12:25:46.309	45:17:24.25	3.3 ± 0.1	3.8±0.4	0.9 ±0.1	-0.5
12:26:3.665	08:15:18.97	5.1 ± 0.2	2.9±0.4	1.7 ±0.1	-1.1
12:32:56.778	11:23:24.64	2.3 ± 0.2		2.1 ±0.1	-0.8
12:35:41.168	26:31:22.78	1.9 ± 0.2		0.7 ±0.1	-1.3
12:38:48.796	31:59:5.63	4.2 ± 0.1	4.8±0.4	2 ±0.1	-1
12:50:08.706	33:09:33.34	3.1 ± 0.2	7.4±1.1	2.1 ±0.1	-0.5
12:50:52.959	34:09:24.54	3.3 ± 0.1	3.3±0.5	2.1 ±0.1	-0.5
12:53:59.118	26:26:38.68	2.4 ± 0.1	4.1±0.5	2.8 ±0.1	0.2
13:07:8.149	46:18:34.24	1.5 ± 0.1		2 ±0.1	0.2
13:11:34.032	44:55:59.05	3.3 ± 0.1		1.7 ±0.1	-1.0
13:12:25.858	28:32:15.74	4.9 ± 0.1	5.1±0.4	3.1 ±0.1	-0.6
13:19:40.071	27:42:21.79	3.2 ± 0.1	6±1.2	2.1 ±0.1	-0.5
13:23:59.882	30:55:56.94	2.5 ± 0.1	2.7±0.5	1.5 ±0.1	-0.7
13:23:45.004	31:33:56.68	3.7 ± 0.1	158.7±5.1	3.2 ±0.1	-0.1
13:24:28.234	04:46:29.54	2.3 ± 0.1		1.6 ±0.1	-0.4
*13:26:51.288	26:35:28.53	1.7 ± 0.1	2.2±0.4	0.7 ±0.1	-1.2
13:29:30.908	11:44:44.77	1.8 ± 0.1		7.4 ±0.1	0.5
13:32:43.365	18:10:34.78	2.7 ± 0.1	3.8±0.4	3.0 ±0.1	0.1
13:34:13.828	09:38:08.01	2.2 ± 0.1		1.2 ±0.1	-0.6
13:34:25.231	34:41:26.07	1.6 ± 0.1	3.6±0.5	3 ±0.1	0.8
13:37:28.941	38:58:13.82	3.2 ± 0.2		1.1 ±0.1	-0.5
13:39:26.009	15:12:46.45	1.9 ± 0.1		1.8 ±0.1	-0.0
13:46:22.224	-03:25:6.81	3.2 ± 0.2	5.5±0.5	2 ±0.1	-0.5

13:56:04.438	38:18:15.27	2.8 ± 0.1	4.8±0.5	1.6 ±0.1	-0.7
*14:00:31.163	-02:51:39.17	1.1 ± 0.2		0.6 ±0.1	-0.8
14:00:37.212	-02:51:28.47	2.9 ± 0.2	6.4±0.5	2.1 ±0.1	-0.5
* 14:02:55.708	09:25:14.54	4.2 ± 0.2	6.9±0.5	1.1 ±0.1	-1.6
14:05:28.328	30:46:2.02	7.8 ± 0.1	7.2±0.5	9 ±0.1	0.2
14:08:04.001	07:19:40.07	2.8 ± 0.2	3.6±0.4	1.5 ±0.1	-0.6
*14:14:20.854	07:30:58.06	1.6 ± 0.2	2.3±0.5	0.9 ±0.1	-0.4
*14:14:30.535	06:09:55.42	1.7 ± 0.2		<0.4	<-1.9
*14:30:52.286	06:02:09.66	1.2 ± 0.1		<0.4	<-1.4
14:36:23.708	35:54:19.16	6 ± 0.1	5.5 ±0.4	3.6 ±0.1	-0.7
15:34:53.723	23:28:16.48	5.1 ± 0.1	4.4±0.4	7.4 ±0.1	0.5
15:39:27.5	24:56:51.51	9.3 ± 0.1	20.1±1	5.7 ±0.1	-0.6
15:59:13.913	19:43:15.09	5.6 ± 0.1	11.3±0.5	1.8 ±0.1	-0.3
16:04:28.18	14:46:56.84	3.7 ± 0.1	2.6±0.5	5.2 ±0.1	0.3
16:29:33.664	21:47:12.34	3.8 ± 0.1	3.7±0.4	3.7 ±0.1	-0.8
22:40:17.262	08:33:57.07	2 ± 0.1	9.4±0.9	3.0 ±0.1	-0.1
23:35:01.071	04:53:51.38	3.1 ± 0.1	8.7±0.5	9.0 ±0.1	0.2
23:35:10.457	04:57:51	5.3 ± 0.1	9.8±0.5	1.5 ±0.1	-0.8

Tabel 20: Table of sources studied in this work, which originally appeared in Ofek [2017], along with calculated peak fluxes and spectral indices. The starred sources are the ones we discuss in more detail in Section 4.3. The 10 sources located off-center within a host galaxy are in the first section before the dividing line, and the second contains either sources located at the center of a nearby galaxy or which appear far from the galaxy.

Bibliografie

B. P. Abbott, R. Abbott, T. D. Abbott, et al., 2017. *ApJ*, 848:L12.

B. P. Abbott, R. Abbott, T. D. Abbott, et al., 2018. *Living Reviews in Relativity*, 21(1):3.

B. Adebahr, M. Krause, U. Klein, et al., 2017. *A&A*, 608:A29.

K. D. Alexander, E. Berger, W. Fong, et al., 2017. *ApJ*, 848(2):L21.

J. R. Allison, V. A. Moss, J. P. Macquart, et al., 2017. *MNRAS*, 465(4):4450–4467.

Dennis Alp, Josefin Larsson, Claes Fransson, et al., 2018. *ApJ*, 864(2):174.

A. Ardeberg & M. de Groot, 1973. *A&A*, 28:295–304.

W. D. Arnett, J. N. Bahcall, R. P. Kirshner, et al., 1989. *ARA&A*, 27:629–700.

T. S. Axelrod, 1980. *Late time optical spectra from the Ni-56 model for Type 1 supernovae*. Ph.D. thesis, California Univ., Santa Cruz.

C. Badenes, J. P. Hughes, E. Bravo, et al., 2007. *ApJ*, 662:472–486.

R. D. Baldi, A. Capetti, & G. Giovannini, 2015. *A&A*, 576:A38.

L. Ball, D. Campbell-Wilson, D. F. Crawford, et al., 1995. *ApJ*, 453:864.

L. Ball & J. G. Kirk, 1992. *ApJ*, 396:L39–L42.

K. W. Bannister, T. Murphy, B. M. Gaensler, et al., 2011. *MNRAS*, 412:634–664.

Keith W. Bannister, Jamie Stevens, Artem V. Tuntsov, et al., 2016. *Science*, 351(6271):354–356.

Cecilia Barnbaum & Richard F. Bradley, 1998. *AJ*, 116(5):2598–2614.

C. G. Bassa, S. P. Tendulkar, E. A. K. Adams, et al., 2017. *ApJ*, 843:L8.

S. C. Beck, J. L. Turner, P. T. P. Ho, et al., 1996. *ApJ*, 457:610.

R. H. Becker, R. L. White, & D. J. Helfand, 1994. In *Astronomical Data Analysis Software and Systems III*, editors D. R. Crabtree, R. J. Hanisch, & J. Barnes, volume 61 of *Astronomical Society of the Pacific Conference Series*, page 165.

Timothy C. Beers, Jeffrey R. Kriessler, Christina M. Bird, et al., 1995. *AJ*, 109:874.

Krzysztof Belczynski, Rosalba Perna, Tomasz Bulik, et al., 2006. *ApJ*, 648(2):1110–1116.

M. E. Bell, T. Murphy, P. J. Hancock, et al., 2019. *MNRAS*, 482:2484–2501.

E. Berger, 2014. *ARA&A*, 52:43–105.

Andreas A. Berlind, Joshua Frieman, David H. Weinberg, et al., 2006. *ApJS*, 167(1):1–25.

P. N. Best & T. M. Heckman, 2012. *MNRAS*, 421(2):1569–1582.

M. F. Bietenholz, N. Bartel, & M. P. Rupen, 2001. *ApJ*, 557:770–781.

M. F. Bietenholz, N. Bartel, & M. P. Rupen, 2002. *ApJ*, 581:1132–1147.
M. F. Bietenholz, N. Bartel, & M. P. Rupen, 2003. *ApJ*, 597:374–398.
M. F. Bietenholz, N. Bartel, & M. P. Rupen, 2010. *ApJ*, 712:1057–1069.
M. F. Bietenholz, A. Kamble, R. Margutti, et al., 2018. *MNRAS*, 475:1756–1764.
Michael F Bietenholz & Norbert Bartel, 2017. *ApJ*, 839(1):10.
Peter K. Blanchard, Edo Berger, & Wen-fai Fong, 2016. *ApJ*, 817(2):144.
J. M. Blondin, P. Lundqvist, & R. A. Chevalier, 1996. *ApJ*, 472:257.
S. Blondin, J. L. Prieto, F. Patat, et al., 2009. *ApJ*, 693:207–215.
C. D. Bochenek, V. V. Dwarkadas, J. M. Silverman, et al., 2018. *MNRAS*, 473:336–344.
C. T. Bolton, R. F. Garrison, D. Salmon, et al., 1974. *PASP*, 86:439.
R. A. Booth, S. Mohamed, & P. Podsiadlowski, 2016. *MNRAS*, 457:822–835.
Geoffrey C. Bower, Brian D. Metzger, S. Bradley Cenko, et al., 2013. *ApJ*, 763(2):84.
D. S. Briggs, 1994. In *The Restoration of HST Images and Spectra - II*, editors R. J. Hanisch & R. L. White, page 250.
D. S. Briggs, 1995. In *BAAS*, volume 27 of *BAAS*, page 1444.
J. W. Broderick, R. P. Fender, R. P. Breton, et al., 2016. *MNRAS*, 459(3):2681–2689.
C. R. Burns, E. Parent, M. M. Phillips, et al., 2018. *ApJ*, 869:56.
C. J. Burrows, J. Krist, J. J. Hester, et al., 1995. *ApJ*, 452:680.
David N. Burrows, J. E. Hill, J. A. Nousek, et al., 2005. *Space Sci. Rev.*, 120(3-4):165–195.
D. Caprioli & A. Spitkovsky, 2014. *ApJ*, 794:46.
S. B. Cenko, H. A. Krimm, A. Horesh, et al., 2012. *ApJ*, 753:77.
S. Chatterjee, C. J. Law, R. S. Wharton, et al., 2017. *Nature*, 541:58–61.
R. A. Chevalier, 1982a. *ApJ*, 259:302–310.
R. A. Chevalier, 1982b. *ApJ*, 259:302–310.
R. A. Chevalier, 1998. *ApJ*, 499:810–819.
R. A. Chevalier & V. V. Dwarkadas, 1995. *ApJ*, 452:L45.
R. A. Chevalier & C. Fransson, 2006. *ApJ*, 651:381–391.
R. A. Chevalier & Z.-Y. Li, 1999. *ApJ*, 520:L29–L32.
Roger A. Chevalier & Claes Fransson, 1994. *ApJ*, 420:268.
CHIME/FRB Collaboration, M. Amiri, K. Bandura, et al., 2019. *Nature*, 566(7743):230–234.
S. M. Chita, N. Langer, A. J. van Marle, et al., 2008. *A&A*, 488:L37–L41.
L. Chomiuk, A. M. Soderberg, M. Moe, et al., 2012. *ApJ*, 750:164.
Laura Chomiuk, Alicia M. Soderberg, Roger A. Chevalier, et al., 2016. *ApJ*, 821(2):119.
N. N. Chugai, 2008. *Astronomy Letters*, 34:389–396.
Thijs Coenen, Joeri van Leeuwen, Jason W. T. Hessels, et al., 2014. *A&A*, 570:A60.
J. J. Condon, W. D. Cotton, E. W. Greisen, et al., 1998. *AJ*, 115:1693–1716.
T. J. Cornwell, 2008. *IEEE Journal of Selected Topics in Signal Processing*, 2:793–801.
J. J. Cowan & D. Branch, 1982. *ApJ*, 258:31–34.
A. Danehkar, D. J. Frew, Q. A. Parker, et al., 2012. In *IAU Symposium*, volume 283 of *IAU Symposium*, pages 340–341.
M. J. Darnley, R. Hounsell, P. Godon, et al., 2017. *ApJ*, 849:96.
M. J. Darnley, R. Hounsell, T. J. O'Brien, et al., 2019. *Nature*, 565:460–463.

F. de Gasperin, H. T. Intema, & D. A. Frail, 2018. *MNRAS*, 474:5008–5022.

Gerard de Vaucouleurs, Antoinette de Vaucouleurs, Jr. Corwin, Herold G., et al., 1991. *Third Reference Catalogue of Bright Galaxies*.

A. de Witt, M. F. Bietenholz, A. Kamble, et al., 2016. *MNRAS*, 455:511–517.

T. DeLaney, B. Koralesky, L. Rudnick, et al., 2002. *ApJ*, 580:914–927.

C. R. Eck, J. J. Cowan, & D. Branch, 2002. *ApJ*, 573:306–323.

D. Eichler, M. Livio, T. Piran, et al., 1989. *Nature*, 340:126–128.

J. J. Eldridge, M. Fraser, S. J. Smartt, et al., 2013. *MNRAS*, 436:774–795.

Martin Elvis, Belinda J. Wilkes, Jonathan C. McDowell, et al., 1994. *ApJS*, 95:1.

Emilio E. Falco, Michael J. Kurtz, Margaret J. Geller, et al., 1999. *PASP*, 111(758):438–452.

R. Fiedler, B. Dennison, K. J. Johnston, et al., 1994. *ApJ*, 430:581.

A. V. Filippenko, 1997. *ARA&A*, 35:309–355.

W. Fong & E. Berger, 2013. *ApJ*, 776:18.

W. Fong, E. Berger, R. Margutti, et al., 2015. *ApJ*, 815(2):102.

W. Fong, B. D. Metzger, E. Berger, et al., 2016. *ApJ*, 831(2):141.

D. A. Frail, S. R. Kulkarni, L. Nicastro, et al., 1997. *Nature*, 389:261–263.

K. A. Frank, S. A. Zhekov, S. Park, et al., 2016. *ApJ*, 829:40.

C. Fransson, J. Larsson, K. Migotto, et al., 2015. *ApJ*, 806:L19.

W. L. Freedman, B. F. Madore, B. K. Gibson, et al., 2001. *ApJ*, 553:47–72.

P. A. Fridman, 2001. *A&A*, 368:369–376.

B. M. Gaensler, R. N. Manchester, L. Staveley-Smith, et al., 1997. *ApJ*, 479:845–858.

B. M. Gaensler, L. Staveley-Smith, R. N. Manchester, et al., 2007. In *Supernova 1987A: 20 Years After: Supernovae and Gamma-Ray Bursters*, editors S. Immler, K. Weiler, & R. McCray, volume 937 of *American Institute of Physics Conference Series*, pages 86–95.

A. Generozov, P. Mimica, B. D. Metzger, et al., 2017. *MNRAS*, 464(2):2481–2498.

D. Giannios & B. D. Metzger, 2011. *MNRAS*, 416:2102–2107.

Ami Glasner, Eli Livne, Elad Steinberg, et al., 2018. *arXiv e-prints*, arXiv:1803.00941.

M. L. Graham, C. E. Harris, P. E. Nugent, et al., 2019. *ApJ*, 871:62.

D. A. Green, 2014. *Bulletin of the Astronomical Society of India*, 42:47–58.

D. A. Green, S. P. Reynolds, K. J. Borkowski, et al., 2008. *MNRAS*, 387:L54–L58.

P. C. Gregory, W. K. Scott, K. Douglas, et al., 1996. *ApJS*, 103:427.

Manuel Güdel, 2002. *ARA&A*, 40:217–261.

S. F. Gull & G. J. Daniell, 1978. *Nature*, 272:686–690.

G. Hallinan, A. Corsi, K. P. Mooley, et al., 2017. *Science*, 358(6370):1579–1583.

P. J. Hancock, B. M. Gaensler, & T. Murphy, 2011. *ApJ*, 735:L35.

Paul J. Hancock, Cathryn M. Trott, & Natasha Hurley-Walker, 2018. *Publications of the Astronomical Society of Australia*, 35:e011.

M. J. Hardcastle, J. H. Croston, & R. P. Kraft, 2007. *ApJ*, 669(2):893–904.

Chelsea E Harris, Peter E Nugent, & Daniel N Kasen, 2016. *arXiv.org*, (2):100.

George Heald, Michael R. Bell, Andreas Horneffer, et al., 2011. *Journal of Astrophysics and Astronomy*, 32:589–598.

E. A. Helder, P. S. Broos, D. Dewey, et al., 2013. *ApJ*, 764:11.

J. D. Hernández-Fernández, J. Iglesias-Páramo, & J. M. Vílchez, 2012. *ApJS*, 199:22.
A. Hewish, S. J. Bell, J. D. H. Pilkington, et al., 1968. *Nature*, 217:709–713.
W. Hillebrandt & J. C. Niemeyer, 2000. *ARA&A*, 38:191–230.
J. A. Hodge, R. H. Becker, R. L. White, et al., 2011. *AJ*, 142:3.
J. A. Hodge, R. H. Becker, R. L. White, et al., 2013. *ApJ*, 769(2):125.
G. Lyle Hoffman, B. M. Lewis, & E. E. Salpeter, 1995. *ApJ*, 441:28.
D. W. Hogg, J. Bovy, & D. Lang, 2010. *ArXiv e-prints*.
S. Holmbo, M. D. Stritzinger, B. J. Shappee, et al., 2018. *arXiv e-prints*.
Assaf Horesh, S. R. Kulkarni, Derek B. Fox, et al., 2012. *ApJ*, 746:21.
Assaf Horesh, Christopher Stockdale, Derek B. Fox, et al., 2013. *MNRAS*, 436:1258–1267.
L. J. M. Houben, L. G. Spitler, S. ter Veen, et al., 2019. *A&A*, 623:A42.
T. Hovatta, E. Nieppola, M. Tornikoski, et al., 2008. *A&A*, 485:51–61.
D. A. Howell, 2011. *Nature Communications*, 2:350.
N. Hurley-Walker, J. R. Callingham, P. J. Hancock, et al., 2017. *MNRAS*, 464:1146–1167.
Scott D. Hyman, Rudy Wijnands, T. Joseph W. Lazio, et al., 2009. *ApJ*, 696(1):280–286.
H. T. Intema, P. Jagannathan, K. P. Mooley, et al., 2017. *A&A*, 598:A78.
N. Ivanova, S. Justham, X. Chen, et al., 2013. *Astronomy and Astrophysics Review*, 21:59.
G. H. Jacoby, G. J. Ferland, & K. T. Korista, 2001. *ApJ*, 560:272–286.
T. R. Jaeger, S. D. Hyman, N. E. Kassim, et al., 2012. *AJ*, 143(4):96.
K. G. Jansky, 1932. volume 20 of *Proceedings of the Institute of Radio Engineers*, pages 1920–1932.
A. H. Jarrett, 1973. *Information Bulletin on Variable Stars*, 828.
Y. Jia, Y. Zou, J. Ping, et al., 2018. *Planet. Space Sci.*, 162:207–215.
D. H. Jones, M. A. Read, W. Saunders, et al., 2010. *VizieR Online Data Catalog*, VII/259.
Eric Jones, Travis Oliphant, Pearu Peterson, et al., 2001. "SciPy: Open source scientific tools for Python." [Online; accessed May 2, 2018].
B.-I. Jun & M. L. Norman, 1996. *ApJ*, 472:245.
Daniel Kasen, 2010. *ApJ*, 708(2):1025–1031.
Robert E. Kass & Adrian E. Raftery, 1995. *Journal of the American Statistical Association*, 90(430):773–795.
J. I. Katz, 2017. *MNRAS*, 467:L96–L99.
Amy E. Kimball, K. I. Kellermann, J. J. Condon, et al., 2011. *ApJ*, 739(1):L29.
R. P. Kirshner & J. B. Oke, 1975. *ApJ*, 200:574–581.
J. Kocz, M. Bailes, D. Barnes, et al., 2012. *MNRAS*, 420(1):271–278.
J. A. Kollmeier, P. Chen, S. Dong, et al., 2019. *MNRAS*, 486:3041–3046.
A. V. Kozlova & S. I. Blinnikov, 2018. In *Journal of Physics Conference Series*, volume 1038 of *Journal of Physics Conference Series*, page 012006.
M. Kunert-Bajraszewska, A. Marecki, & P. Thomasson, 2006. *A&A*, 450(3):945–958.
W. Kunkel, B. Madore, I. Shelton, et al., 1987. *IAU Circ.*, 4316.
Doron Kushnir, Boaz Katz, Subo Dong, et al., 2013. *ApJ*, 778:L37.
M. Lacy, S. A. Baum, C. J. Chandler, et al., 2019. *arXiv e-prints*, arXiv:1907.01981.
C. J. Law, B. M. Gaensler, B. D. Metzger, et al., 2018. *ApJ*, 866:L22.
J. R. Lewis, N. A. Walton, W. P. S. Meikle, et al., 1994. *MNRAS*, 266:L27.

Weidong Li, Ryan Chornock, Jesse Leaman, et al., 2011a. *MNRAS*, 412(3):1473–1507.

Weidong Li, Jesse Leaman, Ryan Chornock, et al., 2011b. *MNRAS*, 412(3):1441–1472.

D. Liu, B. Wang, & Z. Han, 2018. *MNRAS*, 473:5352–5361.

Oliver Lodge, 1900. *The title of the work*. Signalling across space without wires. Being a description of the work of Hertz & his successors, 3 edition.

D. R. Lorimer, M. Bailes, M. A. McLaughlin, et al., 2007. *Science*, 318(5851):777.

K. Maguire, M. Sullivan, F. Patat, et al., 2013. *MNRAS*, 436:222–240.

Soheb Mandhai, Nial Tanvir, Gavin Lamb, et al., 2018. *Galaxies*, 6(4):130.

D. Maoz, F. Mannucci, & G. Nelemans, 2014. *ARA&A*, 52:107–170.

R. Margutti, J. Parrent, A. Kamble, et al., 2014. *ApJ*, 790:52.

R. Margutti, A. M. Soderberg, L. Chomiuk, et al., 2012. *ApJ*, 751:134.

T. A. Matthews & A. R. Sandage, 1963. *ApJ*, 138:30.

Seppo Mattila, Peter Lundqvist, Per Gröningsson, et al., 2010a. *ApJ*, 717(2):1140–1156.

Seppo Mattila, Peter Lundqvist, Per Gröningsson, et al., 2010b. *The Astrophysical Journal*, 717(2):1140–1156.

Christopher D. Matzner & Christopher F. McKee, 1999. *ApJ*, 510(1):379–403.

R. McCray & C. Fransson, 2016. *ARA&A*, 54:19–52.

J. P. McMullin, B. Waters, D. Schiebel, et al., 2007. In *Astronomical Data Analysis Software and Systems XVI*, editors R. A. Shaw, F. Hill, & D. J. Bell, volume 376 of *Astronomical Society of the Pacific Conference Series*, page 127.

A. Menon & A. Heger, 2017. In *The Lives and Death-Throes of Massive Stars*, editors J. J. Eldridge, J. C. Bray, L. A. S. McClelland, et al., volume 329 of *IAU Symposium*, pages 64–68.

P. Mészáros & M. J. Rees, 1997. *ApJ*, 482:L29–L32.

B. D. Metzger & E. Berger, 2012. *ApJ*, 746(1):48.

B. D. Metzger, P. K. G. Williams, & E. Berger, 2015. *ApJ*, 806:224.

D. Michilli, A. Seymour, J. W. T. Hessels, et al., 2018. *Nature*, 553:182–185.

A. Monreal-Ibero, J. M. Vílchez, J. R. Walsh, et al., 2010. *A&A*, 517:A27.

K. P. Mooley, G. Hallinan, S. Bourke, et al., 2016. *ApJ*, 818:105.

K. Moore & L. Bildsten, 2012. *ApJ*, 761:182.

T. Morris & P. Podsiadlowski, 2007. *Science*, 315:1103.

T. Morris & P. Podsiadlowski, 2009. *MNRAS*, 399:515–538.

U. Munari, T. Zwitter, T. Tomov, et al., 1999. *A&A*, 347:L39–L42.

T. Murphy, D. L. Kaplan, S. Croft, et al., 2017. *MNRAS*, 466:1944–1953.

Ehud Nakar, Avishay Gal-Yam, & Derek B. Fox, 2006. *ApJ*, 650(1):281–290.

Ehud Nakar & Tsvi Piran, 2011. *Nature*, 478(7367):82–84.

C.-Y. Ng, B. M. Gaensler, S. S. Murray, et al., 2009. *ApJ*, 706:L100–L105.

C.-Y. Ng, B. M. Gaensler, L. Staveley-Smith, et al., 2008. *ApJ*, 684:481-497.

C.-Y. Ng, G. Zanardo, T. M. Potter, et al., 2013. *ApJ*, 777:131.

G. M. Nita, 2016. *MNRAS*, 458(3):2530–2540.

Gelu M. Nita & Dale E. Gary, 2010. *PASP*, 122(891):595.

K. Nomoto, 1982. *ApJ*, 253:798–810.

K. Nomoto, K. Iwamoto, & N. Kishimoto, 1997. *Science*, 276:1378–1382.

Kristina Nyland, Lisa M. Young, Joan M. Wrobel, et al., 2016. *MNRAS*, 458(2):2221–2268.
Eran O. Ofek, 2017. *ApJ*, 846:44.
A. R. Offringa, A. G. de Bruyn, M. Biehl, et al., 2010. *MNRAS*, 405(1):155–167.
A. R. Offringa, A. G. de Bruyn, S. Zaroubi, et al., 2013a. *A&A*, 549:A11.
A. R. Offringa, A. G. de Bruyn, S. Zaroubi, et al., 2013b. *A&A*, 549:A11.
A. R. Offringa, J. J. van de Gronde, & J. B. T. M. Roerdink, 2012. *A&A*, 539.
A. R. Offringa, J. J. van de Gronde, & J. B. T. M. Roerdink, 2012. *A&A*, 539:A95.
A. R. Offringa, R. B. Wayth, N. Hurley-Walker, et al., 2015. *PASA*, 32:e008.
S. Orlando, M. Miceli, M. L. Pumo, et al., 2015. *ApJ*, 810:168.
W. S. Paciesas, C. A. Meegan, G. N. Pendleton, et al., 1999. *ApJS*, 122:465–495.
P. Padovani, N. Miller, K. I. Kellermann, et al., 2011. *ApJ*, 740:20.
N. Panagia, S. D. Van Dyk, K. W. Weiler, et al., 2006. *ApJ*, 646:369–377.
F. Patat, P. Chandra, R. Chevalier, et al., 2007. *Science*, 317:924.
F. Patat, N. N. Chugai, P. Podsiadlowski, et al., 2011. *A&A*, 530:A63.
R. A. Perley & B. J. Butler, 2017. *ApJS*, 230:7.
S. Perlmutter, G. Aldering, G. Goldhaber, et al., 1999. *ApJ*, 517(2):565–586.
Wendy M. Peters, W. D. Cotton, & N. E. Kassim, 2014. In *American Astronomical Society Meeting Abstracts #223*, volume 223 of *American Astronomical Society Meeting Abstracts*, page 236.05.
E. Petroff, E. D. Barr, A. Jameson, et al., 2016. *PASA*, 33:e045.
E. C. Pickering, 1895. *Harvard College Observatory Circular*, 4:1–2.
M. Pietka, R. P. Fender, & E. F. Keane, 2015. *MNRAS*, 446:3687–3696.
E. Pignatelli, E. M. Corsini, J. C. Vega Beltrán, et al., 2001. *MNRAS*, 323(1):188–210.
P. C. Plait, P. Lundqvist, R. A. Chevalier, et al., 1995. *ApJ*, 439:730–751.
E. Platts, A. Weltman, A. Walters, et al., 2018. *arXiv e-prints*.
T M Potter, L Staveley-Smith, B Reville, et al., 2014. *ApJ*, 794(2):174.
J. L. Racusin, S. Park, S. Zhekov, et al., 2009. *ApJ*, 703:1752–1759.
Akshaya Rane & Duncan Lorimer, 2017. *Journal of Astrophysics and Astronomy*, 38(3):55.
J. Raza, A. J. Boonstra, & A. J. van der Veen, 2002. *IEEE Signal Processing Letters*, 9(2):64–67.
R. B. Rengelink, Y. Tang, A. G. de Bruyn, et al., 1997. *A&AS*, 124:259–280.
S. P. Reynolds, K. J. Borkowski, D. A. Green, et al., 2008. *ApJ*, 680:L41.
E. M. Reynoso & W. M. Goss, 1999. *The Astronomical Journal*, 118(2):926.
Barney J. Rickett, 1977. *Annual Review of Astronomy and Astrophysics*, 15(1):479–504.
A. G. Riess, S. Casertano, W. Yuan, et al., 2018. *ApJ*, 855:136.
Nathaniel Roth & Daniel Kasen, 2015. *ApJS*, 217(1):9.
A. Rowlinson, M. E. Bell, T. Murphy, et al., 2016. *MNRAS*, 458(4):3506–3522.
A. J. Ruiter, S. A. Sim, R. Pakmor, et al., 2013. *MNRAS*, 429:1425–1436.
M. P. Rupen, J. H. van Gorkom, G. R. Knapp, et al., 1987. *AJ*, 94:61–70.
B. R. Russell & S. Immler, 2012. *ApJ*, 748:L29.
V. B. Ryabov, P. Zarka, & B. P. Ryabov, 2004. *Planet. Space Sci.*, 52(15):1479–1491.
S. K. Sarbadhicary, C. Badenes, L. Chomiuk, et al., 2017. *MNRAS*, 464:2326–2340.
S. K. Sarbadhicary, L. Chomiuk, C. Badenes, et al., 2019. *ApJ*, 872:191.
R. J. Sault, P. J. Teuben, & M. C. H. Wright, 1995. In *Astronomical Data Analysis Software and*

Systems IV, editors R. A. Shaw, H. E. Payne, & J. J. E. Hayes, volume 77 of *Astronomical Society of the Pacific Conference Series*, page 433.

R. A. Scalzo, E. Parent, C. Burns, et al., 2019. *MNRAS*, 483:628–647.

B. E. Schaefer, 1995. *ApJ*, 447:L13.

E. R. Seaquist & A. R. Taylor, 1990. *ApJ*, 349:313.

N. I. Shakura & R. A. Sunyaev, 1973. *A&A*, 500:33–51.

K. J. Shen, L. Bildsten, D. Kasen, et al., 2012. *ApJ*, 748:35.

Ken J. Shen, James Guillochon, & Ryan J. Foley, 2013. *ApJ*, 770:L35.

J. M. Silverman, P. E. Nugent, A. Gal-Yam, et al., 2013. *ApJS*, 207:3.

S. A. Sim, M. Fink, M. Kromer, et al., 2012. *MNRAS*, 420:3003–3016.

Joshua D. Simon, Avishay Gal-Yam, Orly Gnat, et al., 2009. *ApJ*, 702(2):1157–1170.

M. F. Skrutskie, R. M. Cutri, R. Stiening, et al., 2006. *AJ*, 131:1163–1183.

Nathan Smith, 2014. *ARA&A*, 52:487–528.

Nathan Smith & Stanley P. Owocki, 2006. *ApJ*, 645(1):L45–L48.

Russell J. Smith, Michael J. Hudson, Jenica E. Nelan, et al., 2004. *AJ*, 128(4):1558–1569.

Vernesa Smolčić, Jacinta Delhaize, Minh Huynh, et al., 2016. *A&A*, 592:A10.

M. Sokolowski, N. D. R. Bhat, J. P. Macquart, et al., 2018. *ApJ*, 867(1):L12.

L. G. Spitler, P. Scholz, J. W. T. Hessels, et al., 2016. *Nature*, 531:202–205.

L. Staveley-Smith, D. S. Briggs, A. C. H. Rowe, et al., 1993. *Nature*, 366:136–138.

L. Staveley-Smith, R. N. Manchester, M. J. Kesteven, et al., 1992. *Nature*, 355:147–149.

A. Sternberg, A. Gal-Yam, J. D. Simon, et al., 2011. *Science*, 333:856.

A. J. Stewart, R. P. Fender, J. W. Broderick, et al., 2016. *MNRAS*, 456(3):2321–2342.

B. E. K. Sugerman, A. P. S. Crotts, W. E. Kunkel, et al., 2005. *ApJS*, 159:60–99.

Lesley K. Summers, Ian R. Stevens, David K. Strickland, et al., 2004. *Monthly Notices of the Royal Astronomical Society*, 351(1):1–17.

C. Tadhunter, 2016. *A&A Rev.*, 24:10.

C. M. Tan, C. G. Bassa, S. Cooper, et al., 2018. *ApJ*, 866(1):54.

C. Tasse, S. van der Tol, J. van Zwieten, et al., 2013. *A&A*, 553:A105.

S. P. Tendulkar, C. G. Bassa, J. M. Cordes, et al., 2017. *ApJ*, 834:L7.

G. Theureau, L. Bottinelli, N. Coudreau-Durand, et al., 1998. *A&AS*, 130:333–339.

S. J. Tingay, R. Goeke, J. D. Bowman, et al., 2013. *PASA*, 30:e007.

S. J. Tingay, C. M. Trott, R. B. Wayth, et al., 2015. *AJ*, 150(6):199.

J. A. Toalá & S. J. Arthur, 2016. *MNRAS*, 463:4438–4458.

Y. Toba, S. Oyabu, H. Matsuhara, et al., 2014. *ApJ*, 788:45.

V. Trimble, 1982. *Reviews of Modern Physics*, 54:1183–1224.

Virginia Trimble, 1988. *Reviews of Modern Physics*, 60(4):859–871.

Cathryn M. Trott, Steven J. Tingay, & Randall B. Wayth, 2013. *ApJ*, 776(1):L16.

J. K. Truelove & C. F. McKee, 1999. *ApJS*, 120:299–326.

S. Turriziani, E. Cavazzuti, & P. Giommi, 2007. *A&A*, 472:699–704.

A. J. Turtle, D. Campbell-Wilson, J. D. Bunton, et al., 1987. *Nature*, 327:38–40.

T. Urushibata, K. Takahashi, H. Umeda, et al., 2018. *MNRAS*, 473:L101–L105.

Hendrik van Eerten, Weiqun Zhang, & Andrew MacFadyen, 2010. *ApJ*, 722(1):235–247.

M. P. van Haarlem, M. W. Wise, A. W. Gunst, et al., 2013a. *A&A*, 556:A2.
M. P. van Haarlem, M. W. Wise, A. W. Gunst, et al., 2013b. *A&A*, 556:A2.
S. van Velzen, D. A. Frail, E. Körding, et al., 2013. *A&A*, 552:A5.
H. K. Vedantham, V. Ravi, K. Mooley, et al., 2016. *ApJ*, 824:L9.
F. L. Vieyro, G. E. Romero, V. Bosch-Ramon, et al., 2017. *A&A*, 602:A64.
W. Voges, B. Aschenbach, Th. Boller, et al., 1999. *A&A*, 349:389–405.
B. Wang, 2018. *Research in Astronomy and Astrophysics*, 18:049.
K. Weiler, editor, 2003. *Supernovae and Gamma-Ray Bursters*, volume 598 of *Lecture Notes in Physics, Berlin Springer Verlag*.
K. W. Weiler, C. L. Williams, N. Panagia, et al., 2007. *ApJ*, 671:1959–1980.
Kurt W Weiler, Nino Panagia, Marcos J Montes, et al., 2002. *Annual Review of Astronomy and Astrophysics*, 40(1):387–438.
R. M. West, A. Lauberts, H. E. Jorgensen, et al., 1987. *A&A*, 177:L1–L3.
R. L. White, R. H. Becker, D. J. Helfand, et al., 1997. *ApJ*, 475:479–493.
P. K. G. Williams & E. Berger, 2016. *ApJ*, 821:L22.
P. K. G. Williams, J. E. Gizis, & E. Berger, 2017. *ApJ*, 834:117.
W. E. Wilson, R. H. Ferris, P. Axtens, et al., 2011. *MNRAS*, 416:832–856.
J.-H. Woo & C. M. Urry, 2002. *ApJ*, 579:530–544.
Donald G. York, J. Adelman, Jr. Anderson, John E., et al., 2000. *AJ*, 120(3):1579–1587.
G. Zanardo, L. Staveley-Smith, L. Ball, et al., 2010. *ApJ*, 710:1515–1529.
G. Zanardo, L. Staveley-Smith, B. M. Gaensler, et al., 2018. *ArXiv e-prints*.
G. Zanardo, L. Staveley-Smith, C.-Y. Ng, et al., 2013. *ApJ*, 767:98.
Giovanna Zanardo, Lister Staveley-Smith, Remy Indebetouw, et al., 2014. *ApJ*, 796(2):82.
B. A. Zauderer, E. Berger, R. Margutti, et al., 2013. *ApJ*, 767(2):152.
B. A. Zauderer, E. Berger, A. M. Soderberg, et al., 2011. *Nature*, 476:425–428.
P.-C. Zinn, E. Middelberg, R. P. Norris, et al., 2012. *A&A*, 544:A38.

Summary

This thesis focuses on the study of transient and variable radio sources in the universe. Transient signals, unlike a source constantly visible, change in their brightness (or flux) over a certain length of time. While there are a plethora of transients over short intervals in radio astronomy that last less than a minute, this thesis will primarily cover those which play out over many years and decades. More information about these sources in general can be found in **Chapter 1** of the thesis.

In **Chapter 2**, we cover a good example of such a source, known as Supernova 1987A (SN 1987A), which was discovered on February 24, 1987, in a satellite galaxy of our Milky Way known as the Large Magellanic Cloud (LMC). A supernova occurs when a star reached the end of its life, and tears itself apart in a fiery explosion that can briefly outshine its host galaxy made up of billions of stars. They are exceptionally rare though- so rare that SN 1987A was the closest observed supernova to Earth since the invention of the telescope. This means SN 1987A has played a crucial role on understanding supernova explosions, and provides us a view in unprecedented detail on how a the event unfolds in the years and decades post-explosion as the supernova shockwave expands into its surroundings.

Radio imaging observations play a crucial role in SN 1987A studies. In particular, this chapter focuses on observations at 9 GHz, taken with the Australia Telescope Compact Array (ATCA), covering a 25 year period (1992-2017). We used computer modeling of the supernova remnant to model where the radio emission is coming from around SN 1987A. We found that the emission appears to be from a torus, or donut, shaped region surrounding the supernova. Further, we find the expansion of the remnant changed its speed at 9,300 $\pm$ 210 days post-explosion from 2,300 $\pm$ 200 km/s to 3,600 $\pm$ 240 km/s. We conclude this corresponds with the shock wave leaving a dense ring of equatorial gas which the shockwave first entered around 5,000 days post-explosion, and re-accelerating as it advances to the area beyond this ring. We also have seen an increase in brightness in the western lobe of the remnant, although the eastern lobe is still the dominant source of emission, unlike what has been observed at contemporary optical and X-ray wavelengths.

In **Chapter 3**, we focus on another kind of supernova explosion called a Type Ia. These supernovae occur in a binary system where one of the two stars is a white dwarf- a stellar core remnant, like what our sun will be someday when it exhausts its fuel. If the mass of the white

dwarf increases past 1.44 times the mass of our sun, it will re-ignite the fusion process and the white dwarf will go supernova. However, just how this mass transfer occurs is not yet understood, although it appears to depend on the type of companion star in the binary. If it is a regular main-sequence star, mass transfer could theoretically create the supernova (called "single degenerate," or SD). If a second white dwarf is present, a merger could also create the explosion ("double degenerate," or DD). It is thought that radio emission may provide the key to the mystery- a shockwave would slam into any material expelled by either star before the supernova- but no emission has been detected to date from any Type Ia supernovae (SNe).

In this chapter, we have imaged over 35 years of archival Very Large Array (VLA) observations of two nearby Type Ia SNe, SN 1972E and SN 1895B, which occurred in the galaxy NGC 5253 ∼11 million light years (3.15 Mpc) distant, and were two of the closest Type Ia SNe to Earth ever recorded. No radio emission was detected, implying a clean circumstellar medium (CSM) surrounding each explosion, with densities $n < 0.9$ atoms/cm^3 out to radii of a few 10^{18} cm (or ∼1 light year) assuming a uniform density medium. We can also constrain the presence of CSM shells surrounding the progenitor of SN 1972E, ruling out thin shells at certain radii down to $<$ 0.01 times the mass of the sun, and thicker shells of various masses over a more broad radius from the explosion site. These constraints rule out large swaths of parameter space for what could have caused the explosions, and provide a data set of repeated observations unlike any other existing so far for a Type Ia supernova.

In **Chapter 4**, we consider a technical problem with transient radio astronomy, which is how to distinguish between a genuine transient signal and manmade ones. Called Radio Frequency Interference (RFI), manmade signals make up the majority of bright radio signals in radio telescopes, particularly in population-dense countries like the Netherlands. While flagging RFI used to be done by hand by astronomers, most modern telescopes like the Low Frequency Array (LOFAR) employ automatic flagging of their data in order to excise RFI before it is looked at by the observer. However, the effects of such automatic flagging on rare astrophysical transients had not been considered in great detail. In this chapter, we investigate how standard flagging affects the detectability of such transients by examining the case of transient detection in an observing mode used for LOFAR surveys. We quantified the fluence range of transients that would be detected, and the reduction of their signal-to-noise ratio (SNR) due to occasional "partial flagging" of the signal. We found that some signals, such as bright transients with durations on the order of tens of seconds, were completely flagged, and for longer transients on the order of tens of seconds to minutes, part of the signal is lost. For these transients, we present in the chapter a modified flagging strategy which mitigates the effect of flagging on transient signals. The chapter also presents a script which uses the differences between RFI flagging strategies and known differences between transient RFI and astrophysical transients to notify the observer when a potential transient is in the data stream.

Finally, in **Chapter 5** we consider a sample of potential transient and variable radio sources that were listed in a catalog of possible persistent Fast Radio Bursts (FRB) counterparts- a relatively new class of transient sources whose origins are not understood. The catalog consisted of 117 extragalactic (that is, from outside our galaxy) radio sources that were considered fairly luminous and within 35 million light years ($<$108 Mpc). We used observations from two sky

surveys- the Very Large Array Sky Survey (VLASS) at 3 GHz and the Faint Images of the Radio Sky at Twenty-cm (FIRST) catalog at 1.4 GHz ∼25 years earlier- in order to establish changes in flux over time in our sample, and compiled detailed light curves using data from multiple radio surveys for 19 of these sources. We also examined X-ray data for these sources, but these yielded non-detections. We identified one transient candidate, FIRST J235351.4+075835, which has faded steadily by a factor of two over 20 years, which may be due to a tidal disruption event (TDE) where a black hole tears apart a star, or the merger of two neutron stars. However, this source lacks an optical counterpart, so it is difficult to conclude what it is without additional observations. We conclude the rest of our sources which display variable behavior are likely caused by the low, inefficient accretion of gas onto a supermassive black hole, known as low excitation radio galaxies (LERG).

Samenvatting

Dit proefschrift richt zich op de studie van kortstondige en veranderlijke radiobronnen in het heelal. In tegenstelling tot constante zichtbare bronnen veranderen kortstondige radiosignalen in helderheid (of flux) gedurende een bepaalde periode. Hoewel er enorm veel kortstondige bronnen zijn die minder dan een minuut duren, zal dit proefschrift zich voornamelijk richten op degene die meerdere jaren of zelfs decennia lang duren. Meer informatie over dit soort bronnen vindt u in **Hoofdstuk 1**.

In **Hoofdstuk 2** behandelen we een goed voorbeeld van dit soort bron, te weten Supernova 1987A (SN 1987A), welke ontdekt is op 24 februari 1987 in een satelliet van ons melkwegstelsel genaamd de Grote Magelhaense Wolk (LMC). Een supernova ontstaat wanneer een ster zijn levenseinde bereikt met een explosie die tijdelijk de felste lichtbron in een sterrenstelsel van miljarden sterren kan zijn. Ze zijn extreem zeldzaam, zo zeldzaam dat SN 1987A de dichtstbijzijnde geobserveerde supernova was sinds de uitvinding van de telescoop. Dit betekent dat SN 1987A een cruciale rol heeft gespeeld in het onderzoek naar supernovae en ons nieuwe inzichten heeft gegeven hoe de gebeurtenis zich voltrekt in de jaren en decennia na de explosie wanneer de schokgolf zich naar de omgeving uitbreidt.

Observaties waarbij radiosignalen worden gevisualiseerd spelen een belangrijke rol bij het bestuderen van SN 1987A. Dit hoofdstuk richt zich specifiek op de observaties bij 9 GHz, genomen met de Australia Telescope Compact Array (ATCA), over een periode van 25 jaar (1992-2017). We hebben computersimulatie van de supernovarest gebruikt om te modelleren waar de radio emissie rond SN 1987A vandaan komt. We zijn erachter gekomen dat de emissie lijkt te komen vanuit een torus- of donutvormige regio rond de supernova. Verder concluderen we dat de expansie van de supernovarest van snelheid is veranderd rond 9.300 $\pm$ 210 dagen van 2.300 $\pm$ 200 km/s naar 3.600 $\pm$ 240 km/s. Wij concluderen dat de schokgolf de dichte ring van gas rond de hemelevenaar verlaat nadat het deze voor het eerst binnengekomen was rond 5.000 dagen na de explosie, en weer versnelt na het verlaten van het gebied buiten deze ring. We hebben ook een groei van de helderheid aan de westelijke kant van de supernovarest gezien, alhoewel de oostelijke kant nog steeds de dominante bron van de emissie is, in tegenstelling tot hedendaagse observeringen in optische en röntgen golflengtes.

In **Hoofdstuk 3** kijken we naar een ander soort supernova genaamd Type Ia. Deze supernovae

komen voor in binaire systemen waarbij een van de twee sterren een witte dwerg is, het restant van een ster, iets wat onze zon ooit ook zal worden nadat alle brandstof is uitgeput. Als de massa van een witte dwerg groter wordt dan 1,44 keer de massa van onze zon dan zal het fusieproces herstarten en ontstaat er een supernova. Hoe de massa groter wordt is iets dat we nog niet begrijpen, maar het lijkt af te hangen van het type van de andere ster in het binaire stelsel. Als dit een normale ster is, zou massaoverdracht theoretisch een supernova kunnen creëren. Als er een tweede witte dwerg in het spel is, zou een samensmelting kunnen leiden tot een supernova. Men denkt dat radio emissies een verklaring zouden kunnen geven voor dit vraagstuk, een schokgolf zou interactie hebben met materie van beide sterren, maar tot op heden is er nog geen emissie gedetecteerd vanuit Type Ia supernovae. In dit hoofdstuk hebben we 35 jaar aan gearchiveerde observaties van de Very Large Array (VLA) gevisualiseerd voor twee Type Ia supernovae, SN 1972E en SN 1895B, beide in het NGC 5253 sterrenstelsel op 11 miljoen lichtjaar (3.15 Mpc) afstand. Dit zijn twee van de dichtst bij de Aarde geobserveerde Type Ia supernovae ooit. Er werden bij beide explosies geen radio emissies gedetecteerd, wat op weinig interstellair medium rond de ster duidt, met dichtheden van < 0.9 atomen/cm^3 tot op een afstand van enkele 10^{18} cm (of 1 lichtjaar) bij een medium van uniforme dichtheid. We kunnen ook bepalen dat er geen schijf van materiaal is rond de oorspronkelijke ster van SN 1972E, dunne schijven met een radius tot $<$ 0,01 maal de massa van de zon zijn uitgesloten, evenals dikke schijven van verschillende massa's over een grotere radius van de oorsprong van de explosie. Door deze bepalingen kunnen we een reeks van oorzaken voor de explosie uitsluiten, en een dataset genereren met herhaalde observaties zoals er nog niet eerder was voor een Type Ia supernova.

In **Hoofdstuk 4** beschouwen we een technisch vraagstuk binnen de radioastronomie, namelijk hoe onderscheid te maken tussen een daadwerkelijk kortstondig signaal en door de mens geproduceerde signalen. Deze signalen door menselijk toedoen, genaamd RFI, zijn verantwoordelijk voor het grootste deel van heldere radiosignalen in de radioastronomie, vooral in dichtbevolkte landen zoals Nederland. Hoewel het markeren van RFI vroeger vaak met de hand werd gedaan voor de astronomen, maken de meeste moderne telescopen, zoals de Low Frequency Array (LOFAR, nabij Exloo), gebruik van automatisch markeren, nog voordat er een astronoom naar de data heeft gekeken. In dit hoofdstuk onderzoeken we hoe de standaard manier van markeren van invloed is op de mogelijkheid tot detectie van kortstondige signalen door te onderzoeken hoe deze detectie normaal gesproken wordt gebruikt binnen LOFAR studies. We kwantificeren het helderheidsbereik van kortstondige signalen die zouden worden gedetecteerd, en de verlaging van hun signaal-ruisverhouding (SNR), door incidentele gedeeltelijke markering van het signaal. We hebben gevonden dat sommige signalen, zoals heldere kortstondige signalen met een duur in de orde van tientallen seconden, volledig gemarkeerd waren, en voor langere kortstondige signalen in de orde van seconden tot minuten een deel van signaal verloren gaat. Voor deze kortstondige signalen stellen we in dit hoofdstuk een aangepaste markeer strategie voor, welke ongewenste effecten van markeren moet tegengaan. Dit hoofdstuk beschrijft ook een computer script dat de verschillen tussen RFI markeer strategieën en bekende verschillen tussen kortstondige RFI signalen en astrofysische kortstondige signalen gebruikt om de waarnemer te attenderen op een mogelijk kortstondige signaal in de observatiedata.

Tot slot, in **Hoofdstuk 5**, beschouwen we een voorbeeld van een potentieel kortstondig signaal en willekeurige radiobronnen die waren opgenomen in de catalogus van mogelijke herhalende korte heldere radio pulsen (Fast Radio Bursts, FRBs), een relatief nieuwe klasse van kortstondige bronnen waarvan de oorsprong nog niet begrepen wordt. De catalogus bestond uit 117 extragalactische (oftewel, van buiten onze Melkweg) radiobronnen die beschouwd worden als vrij helder en binnen 35 miljoen lichtjaar (<108 Mpc). We hebben observaties gebruikt van twee sky surveys (meting van de gehele sterrenhemel), de Very Large Array Sky Survey (VLASS) bij 3 GHz en de Faint Images of the Radio Sky at Twenty-cm (FIRST) catalogus bij 1.4 GHz ongeveer 25 jaar eerder, om geleidelijke wijzigingen in helderheid te kunnen vinden in onze steekproef. We hebben gedetailleerde lichtkrommen kunnen genereren met de data van verschillen radio surveys voor 19 van deze bronnen. We hebben ook röntgen-data voor deze bronnen onderzocht maar dit resulteerde niet tot detecties. We hebben èèn mogelijke kortstondige signaal geïdentificeerd, FIRST J235351.4+075835, welke consistent verduisterd is met een factor 2 over 20 jaar, wat het gevolg zou kunnen zijn van een tidal disruption event (TDE) waar een zwart gat een ster uit elkaar scheurt, of een samensmelting van twee neutronensterren. Echter, deze bron heeft geen optische equivalent, dus het is lastig om conclusies te trekken zonder aanvullende observaties. We concluderen dat de rest van onze bronnen welke variabel gedrag vertonen waarschijnlijk veroorzaakt zijn door een beperkte, inefficiënte ophoping van gas rond een supermassief zwart gat, ook bekend als Low excitation radio galaxies (LERG).

Curriculum vitæ

Five generations ago, a schoolteacher in a village in the eastern wine region of Hungary scraped together enough money to send his son to university. That son- my great-great-grandfather- ultimately got a PhD in law, thus becoming the first Dr. Csendes. And so a family passion was born for education, with each generation's son earning a doctorate. The turbulence of World War II in central Europe cemented this further with the pragmatism of refugees everywhere, who know the only resource you are guaranteed to carry is what is in your own head. Half of the family shifted to Canada during those turbulent years, and the name shifted to Cendes with my father when he later became a US citizen.

It has been a difficult path in many ways, for many people, but what you hold is the fifth generation of a doctoral thesis from a long line of scholars. It is, I hope, noteworthy in many ways, but one of those is how out of all these family doctorates it is the first written by a woman. While it is trendy in some circles these days to suggest these things do not matter, people like my grandmother would disagree- she always said her greatest regret in life was never being able to learn algebra, because while her brother was sent to university to become a doctor she was sent to finishing school. It is a prime reminder to all of us that while talent is universal, opportunity is not, and I have thought of her many times as these pages came together.

But anyway, onto me. Three astronomical things of note happened in the span of a week in late January, 1986, although you are forgiven for not recognizing them all at the time. The first was, of course, the shocking explosion of the *Challenger* space shuttle on January 28, seconds after launch. The second was, on January 24, the closest approach by *Voyager 2* to the planet Uranus and its moons. And the third was, on January 23, my birth in Pittsburgh, Pennsylvania, USA, twenty minutes after my twin brother and almost two years to the day after our older sister. (My mother insists I was a fairly quiet child until I was about four years old, when I realized if I didn't start talking more no one would pay attention to me.) Childhood in Pittsburgh progressed as these things typically do, although with more Hungarian speaking and devouring of books than average. I do remember a great excitement when I was ten years old when my father announced the great comet Hyukatake was in the sky, and we would drive out to the country after dinner for a better look. "Think of me next time you see it," he joked, after telling us of its 70,000 year orbit. I stared with the awe and wonder of someone realizing what a cosmic scale is for the first

time.

However, I would really argue that my life has been divided in two ways: the part before a fateful autumn day in 1999, and everything after. I was 13 years old, and had a tedious hour-long school bus ride each way between home and school. I would pass the time by reading, and one day ran into the library after class with the emergency of nothing to read, and minutes to solve the impending crisis. For whatever reason, I grabbed a general book about astronomy- *From the Big Bang to Planet X* by Terrence Dickinson, with a fetching image of the Andromeda Galaxy on its cover- and my view of the universe was never the same after. I realized that *anyone* who was 13 years old could conceivably grow up to be an astronomer someday- even if you lived in Pittsburgh- and that decision never really wavered since. I am a lover of stories, and the story of the cosmos is the biggest and grandest one we have.

I settled on radio astronomy fairly quickly too, thanks to the book and movie *Contact* by Carl Sagan and essentially deciding at age 15 that I wanted to be Ellie Arroway. I got my amateur ("Ham") radio license soon after turning 16, and my teenage bedroom was defined by my telescope, over a dozen radios (store bought and homemade), and giant maps of the world and North America with pins for all the stations I ever heard. I learned to tease out signals from the noise, and that when radio works it's as close to magic as you can get short of a wand and a bag of salamanders. Years later, I got my first real taste of radio astronomy doing a summer REU program at the SETI Institute working for Jill Tarter, the inspiration for Ellie Arroway herself.

I started university in 2004 at Case Western Reserve University in Cleveland, Ohio, where I did my bachelor's and master's degrees in physics. My research there was in cosmic rays- specifically on GPS timing units for the Pierre Auger Observatory in Argentina, which are vital to sorting out where ultra-high-energy cosmic rays originate from in our universe. (We still don't know.) In 2007, I studied a semester at the University of Auckland in New Zealand, which sparked a love for serious travel. In between my degrees I have backpacked around the world, most of it solo, to over sixty countries. Along the way I have gotten punched by a wild mountain gorilla, visited Everest Base Camp, gazed at Antarctic islands, and many other experiences. I am very lucky to have had so many adventures I always assumed as a child I would only read about.

It is this love of travel that led me to consider PhD programs abroad, and ultimately took me to the Netherlands for my PhD. I am very grateful to have the opportunity to obtain my PhD from Leiden University, and also conducted predoctoral research at the University of Amsterdam and University of Toronto. I will probably always remember September 12, 2019 as the date my thesis was finally approved, and I went to town hall to marry my husband, Floris Gerardus Looijesteijn, so it all worked out in the long run but in the span of an afternoon!

Finally, I have to mention that along the way, I have been a writer- I thought my calling in life was journalism before I discovered astronomy, so it has been rewarding to succeed in both. Over the years, I have written numerous features that have appeared in *Astronomy*, *Sky & Telescope*, *Discover*, *Scientific American*, and others. Online, my comments are read by millions of people regularly on the platform Reddit, many of which have inspired others to pursue their own STEM careers. I firmly believe that science is an act of human expression, no less valid than music or art, and that outreach by scientists is of vital importance in a world held in the increasing sway of ignorance and misinformation.

In October 2019, I began my position as a postdoctoral fellow at the Harvard-Smithsonian Center for Astrophysics in Cambridge, Massachusetts. I cannot wait to see where my life's cosmic adventures lead to next.

Acknowledgments

It is very difficult to stand at the end of a journey as long as a PhD thesis and thank everyone who brought it in the world. You are trying to capture everything about your journey that cannot be read on the previous pages, and when that journey encompasses three institutions on two continents you realize no words will truly acknowledge them all. So, with that, I will summarize it with five thank yous, and hope it covers everyone.

First of all, I would like to thank my family for their unwavering love and support in all the moments of my journey, especially my parents, brother, and sister. A special *köszönöm* to Sári mamama, whose greatest hope was a woman in our family would earn her own PhD instead of claiming a corner of another's diploma. *Sok szeretettel, mindig.*

Second, there are not enough words to describe my thanks to my supervisors, Bryan, Xander, and Maria. Bryan, thank you for your morals and courage to make our science and corner of the world a better place than you found it. I know some will feel it's melodramatic to suggest an adviser can save a student's life, but in I will always feel like you saved mine. Xander, your cheerful pragmatism has saved many as well, and is an example for the kind of scientists we should strive to be. Thank you again for the SOFIA flight! And Maria, thank you so much for our wonderful collaboration. It struck me more than once during our fits of laughter that this is exactly what I hoped science would be like, and that it was worth fighting for.

Third, thank you to my friends, colleagues, and collaborators around the world, especially for our many cheerful moments over various delicious beverages. Special thanks to Casey Law, who is on the first and last research chapters chronologically, and to Dario Carbone who I will always consider my PhD twin. And thank you so much to Adam, Natalie, and Milena for all the times you listened, and for all your solicited and unsolicited opinions and advice.

Fourth, thank you to my editors at my various publications, and the thousands of folowers on Reddit. I am humbled to have such wonderful platforms to share my astronomical passion with others, who regularly remind me of why I fell in love with it in the first place.

Finally, thank you and love to my Floris, without whom this work would not have been completed. I would do it all again if it was the price I had to pay to meet you.

Cambridge, Massachusetts, USA
Autumn 2019